Ph. D Thesis in Physics
presented for the titles of:

DOTTORE DI RICERCA
UNIVERSITÀ DEGLI STUDI DI TORINO
XIX CYCLE
Settore scientifico-disciplinare FIS/04: Fisica Nucleare e Subnucleare

GRADE de DOCTEUR EN SCIENCES DE
L'UNIVERSITÉ PARIS XI- ORSAY

By

Silvia Goy López

Study of the $K^{\pm} \to \pi^{\pm}\pi^{0}\gamma$ decays at the NA48/2 experiment at the CERN SPS.

Defended December 19th 2006 with jury:

B.	Bloch-Devaux	(french supervisor)
R.	Cester	(external referee)
F.	Marchetto	(italian supervisor)
E.	Menichetti	(president of the jury)
A.	Pich	(external referee)
A.	Stocchi	

Introduction and Overview

Study of the $K^\pm \to \pi^\pm\pi^0\gamma$ decays at the NA48/2 experiment at the CERN SPS.

Goy López, Silvia
Ph. D in Physics
Italian supervisor: Dr. Flavio Marchetto
French supervisor: Dr. Brigitte Bloch-Deveaux
December 2006

The $K^\pm \to \pi^\pm\pi^0\gamma$ channel is amongst the most interesting rare charged kaon decays. First, it provides information on some chiral perturbation theory (ChPT) constants; second, it is one of the most sensitive channels for studying the chiral anomaly in the non-leptonic sector and third, it is also sensitive to possible non-Standard Model effects.
Two amplitudes contribute to the $K^\pm \to \pi^\pm\pi^0\gamma$ decay. The dominant comes from Inner Bremsstrahlung (IB) in the $K^\pm \to \pi^\pm\pi^0$ process. The second is given by the Direct Emission (DE) of the photon at the weak vertex from an intermediate state of the decay.
Taking into account parity non-conservation in the weak decay processes, the simplest radiative transitions are electric dipole (E1) and magnetic dipole (M1) The magnetic transition enters at $\mathcal{O}(p^4)$ in chiral perturbation theory, and it is related to the chiral anomaly.
The electric transition may arise at $\mathcal{O}(p^4)$ in ChPT, but it cannot be completely predicted in this framework. Electric amplitudes can interfere with IB, and CP

violation and possible non-SM effects can show up in the corresponding interference term.

The inner bremsstrahlung amplitude enters at $\mathcal{O}(p^2)$ in ChPT, but it is suppressed by the $\Delta I = 1/2$ rule, so DE amplitudes are relatively enhanced in $K^\pm \to \pi^\pm\pi^0\gamma$ decays in comparison to other channels in which suppresions are not present.

The NA48/2 experiment has collected a large sample of $K^\pm \to \pi^\pm\pi^0\gamma$ decays, providing a unique opportunity of precisely studying this channel.

In this work a subsample of the 2003 NA48/2 data has been analyzed. The main results presented are the relative amounts of Direct Emission and Interference with respect to the Inner Bremsstrahlung component.

The outline of the document is the following:

In the first chapter a theoretical introduction to the $K^\pm \to \pi^\pm\pi^0\gamma$ decay is given. In the second, the methods used for extracting the physical results (Maximum Likelihood and Shape Methods) are described. The present experimental status is also summarized.

The third chapter focuses on the description of the NA48/2 experiment. The main characteristics of the beam line are explained and the different components of the central detector (the magnetic spectrometer, electromagnetic calorimeter, etc) and the Trigger System are described in detail.

Chapter four gives more information about the Trigger and Data Taking conditions during the 2003 and 2004 NA48/2 runs.

The event selection of $K^\pm \to \pi^\pm\pi^0\gamma$ events is described in chapter five. The cuts used are listed and the reasons for including each of them in the analysis are specified. The final number of events used for the extraction of the DE and INT components is $\sim 120\ 10^3$, which is more than five times larger than that of previous experiments.

In chapter six the level one (L1) and two (L2) trigger efficiencies are calculated for signal events. Trigger-related corrections to be implemented in the Monte Carlo simulation have been computed as well.

The Monte Carlo (MC) simulation of the NA48 experiment in general and of the $K^\pm \to \pi^\pm\pi^0\gamma$ decay in particular is explained in the seventh chapter. Different samples of simulated events have been produced on a run by run basis independently for IB, DE and INT. Results obtained from the analysis of these samples are reported.

Chapter eigth describes the potential background sources to $K^\pm \to \pi^\pm\pi^0\gamma$ decays. Samples have been generated using Monte CArlo techniques in order to

study the rejection procedure and its performance. Accidental background has also been studied. With the current selection the total background has been estimated to be less than 1% of the expected DE contribution.
Final results and conclusions are given in chapter nine.

Acknowledgements

First of all I would like to thank Donald Cundy and my advisors, Flavio Marchetto and Brigitte Bloch-Devaux.
Don, thank you so much for your continued interest in this analysis, for all your suggestions and all our conversations, in which I felt treated like a colleague rather than like a student. You have taught me a lot of physics, but also you have shown me how a physicist thinks about the problems that come along. I know this work would have certainly not be the same without your help and for all this I will always feel greatly indebted to you.
Flavio, thank you for accepting me as your student in Torino, it has been a wonderful experience. Thank you as well for all your suggestions and for the good example you give with your work and your humanity.
Brigitte, thank you for supporting me so much in the effort to get a cotutored PhD with the DAPNIA group and the University of Orsay, this has not been an easy task and your help has been fundamental. Also thank you for looking into my work with maximum attention and for being always so accessible.

I would like to thank as well the Torino group:
Ezio Menichetti, for your support and your availability to share your incredible amount of knowledge in all physics topics, from electronics to theoretical physics.
Nadia Pastrone, for considering me to be in your group from the beginning and always treating me like a friend as well, making me know I could count on you. Grazie di tutto Nadia.
Marco Clemencic and Roberta Arcidiacono: for all your support and help, especially regarding our lovely Trigger Supervisor. Grazie mille.
Cristina Biino and Sandro Palestini, thank you so much for your continuous hospitality and help, you made me feel at home in Torino, molte grazie di tutto. Cristina, grazie anche per le nostre sessione sportive, dobbiamo assolutamente continuare.
Nicoló Cartiglia, thank you so much for suggesting me joining the Torino group for my PhD, qualche volta si fanno veramente dei bei incontri in ufficio.

And the DAPNIA/SPP-CEA group: to Bernard Peyaud, Edoardo Mazzucato, and especially to Jean Baptiste Cheze.
Jean Baptiste, thank you for spending all that time introducing me to the KABES reconstruction software, with all your patience and kindness. Merci bien.
Also to Philippe Schune, for being mon parrain de these, and introducing me to

the DAPNIA community.

I want to thank as well Mauro Raggi and Nello Nappi in Perugia:
Mauro, The Independent Analyser. It has been a pleasure working with you. Grazie per la disponibilità e per non essere impazzito con le mie domande e richieste. Buona fortuna per tutto.

There are many people at CERN whose support I cannot forget:
Ivan Mikulec, thank you for sharing all your knowledge, experience and intelligence to think about what were to me the most puzzling problems. Thank you as well for the encouragement you gave to me before starting this PhD and for the good times at the collaboration meetings.
Alan Norton, thank you for teaching me so much and for your patience with me when I was a new-comer. I enjoyed very much the time we worked together and I really appreciate the support you have always given to me.
Marco Sozzi, Augusto Cecucci, Vladimir Kekelidze and Heinrich Wahl, for encouraging me to stay in the NA48 experiment and always caring about my career.
Rainer Wanke, the rare decay session coordinator, for being always so optimistic.
Gianmaria Collazuol, the trigger coordinator. Ti ringrazio per avermi fatto fare lo Xilinx una sola volta, ma sopra tutto ti ringrazio tanto per le nostre interessantissime discusioni sulla Fisica in generale e l'effeto cusp in particolare, ho imparato tantissimo.
And to the whole NA48/2 collaboration, for trusting the students with big responsibilities and asking them for the best results. Being in NA48 gave me the chance to participate in the most interesting discussions, to work in a variety of topics, from calibration, to trigger, software reconstruction and data analysis and to face all kind of questions from experienced and intelligent people who were also interested in the work I was doing. I cannot think of a better way to learn.

I want to thank with all my heart my friends at CERN:
A Barbara, Fernando y Ana, Andrés y Teresa, Arturo y Cristina. Me alegro mucho de haber estado aquí para poder conoceros. Sabéis que estáis todos en mi lista de amigos para siempre.
A Marta y Juan Carlos. Marta, gracias por ser buena jefa y amiga. Y sobre todo gracias a los dos por meterme en salsa.
To Anne, thank you for being there all the time, especially in the bad times. Your support then was very important for me. I wish you all the best.
To Robi and Andi. Thank you so much for all those coffees, lunches, dinners, skiing and singing outings, trekking, and for all our holidays together. You have been really my friends at CERN, grazie und danke schon. Robi, sono molto contenta d'essere capitata in ufficio con te.
A Abraham, gracias por todos esos cafés y por haberte siempre interesado por el estado de mi tesis, y sobre todo por hebértela leído.
To the pranzo team: Marco, Giuseppe, Mauro P., Stefano, Paolo. Mangiare al CERN senza di vuoi sarebbe estato sicuramente molto peggio. Marco, moltissime

grazie per avermi fato capire che posso sempre contare su di te.

Quiero agradecerles a mi padre y mi madre, Celso y María Luz, el que siempre me hayan animado a estudiar, dejándome también claro que la salud es lo primero y que el desayuno es la comida más importante del día, a mi hermana Sonia, que ha venido a visitarme allí donde he estado y me ha animado siempre, y a mi madrina Edelmira, que siempre se ha preocupado por mí.
También a mis amigos de Lugo:
Roci gracias por estar siempre ahí y seguir siendo la misma para mí. La próxima vez que vaya a Lugo tenemos que celebrar nuestra bodas de plata de amistad.
Mónica, muchisímas gracias por tratarme como si nunca me hubiera ido, y por venir a verme, me ha hecho realmente mucha ilusión.
Y a mis amigos de Santiago: a Gema, Eva y Lorenzo, porque siempre que nos vemos es como si no nos hubiéramos separado.

Finally, I would like to give my most special thanks to Eduardo Molina Marinas. Edu, muchas gracias por tu apoyo durante todo este tiempo de tesis, que sé que ha sido mucho. Gracias por haber estado siempre ahí y haber sido mi familia. Gracias por tus consejos, por los buenos momentos que hemos compartido y por aguantar mis nervios. Y gracias por enseñarme el buen uso de los tiempos compuestos. Todo lo que has hecho por mí durante estos años te lo agradeceré siempre, espero que tú también guardes un buen recuerdo.

Table of Contents

Chapter

Appendix

Appendix

List of Tables

Table

List of Figures

Figure

Chapter 1

Theoretical Introduction

1.1 Processes Contributing to the $K^{\pm} \to \pi^{\pm}\pi^{0}\gamma$ Decay.

The $K^{\pm} \to \pi^{\pm}\pi^{0}\gamma$ can proceed via two possible mechanisms: Inner Brems strahlung (IB), where the photon is radiated off from the charged mesons and Direct Emission (DE), where the photon is emitted at the weak vertex from an intermediate state of the decay. Diagrams for these two processes are shown in Fig. 1.1.

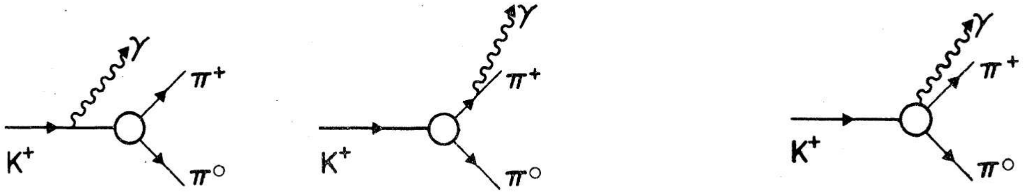

(a)

(b)

Figure 1.1: Diagrams describing the Inner Bremsstrahlung (a) and Direct Emission (b) processes in $K^{\pm} \to \pi^{\pm}\pi^{0}\gamma$

1.1.1 Inner Bremsstrahlung .

In the inner bremsstrahlung process, either the charged kaon $K^{\pm}$ or the charged pion $\pi^{\pm}$ emits a photon. Classically, this radiation can be attributed to a sudden change in the charge when the charged pion is created and leaves. Inner Bremsstrahlung necessarily exists as a consequence of the decay $K^{\pm} \to \pi^{\pm}\pi^{0}$ and its contribution can be directly calculated using standard QED techniques once the amplitude of $K^{\pm} \to \pi^{\pm}\pi^{0}$ is known [1, 2].

Let us consider the case when the bremsstrahlung photon is emitted by the charged pion. In this situation, first the kaon decays through $K^{\pm} \to \pi^{\pm}\pi^{0}$. As the kaon spin is zero and due to conservation of total angular momentum, the two pions must be in a zero angular momentum state ($l_{\pi\pi} = 0$). The wave function of the final state changes under the interchange of the two pions by a factor of $(-1)^{I+l_{\pi\pi}}$. Isospin addition alone tells us that the final state must have I=1 or I=2. As the pions are bosons the sign of the wave function must be plus, so the I=2 combination is chosen. The photon is emitted from the charged pion as it penetrates the centrifugal barrier of the Kaon. Conservation of angular momentum is maintained if the orbital angular momentum of the photon is opposite to its spin, meaning that this is an electric type transition.

In addition, the bremsstrahlung photon could also be emitted by the kaon at the time of the decay. The two contributions to the IB process are shown in figure 1.1 (a)

The amplitude for IB is given in [3]:

$$A_{IB} = A_{2}^{\pm}(K^{\pm} \to \pi^{\pm}\pi^{0}) exp(i\delta_{0}^{2}) \frac{1}{(p_{\gamma}p_{K})(p_{\gamma}p_{\pi})} F_{\mu\nu} p_{\pi}^{\mu} p_{K}^{\nu} \tag{1.1}$$

where $F_{\mu\nu} = p_{\gamma\mu}\epsilon_{\nu} - p_{\gamma\nu}\epsilon_{\mu}$, being p_{π}, p_{γ}, p_{K} the four-momenta of the charged pion, photon and kaon respectively, and ϵ the 4-vector polarization of the gamma ray. $A_{2}^{\pm}$ are the amplitudes for the $K^{\pm} \to \pi^{\pm}\pi^{0}$ decays and δ_{L}^{I} is the phase shift for $\pi^{\pm} - \pi^{0}$ scattering in the channel with total angular momentum L=0, and two pions isospin I=2.

From the amplitude we can get the matrix element and calculate the inner bremsstrahlung differential cross-section:

$$\frac{\partial^{2}\sigma}{\partial\Omega_{f}\partial E_{\gamma}} \alpha \frac{p_{\pi}^{2} sin^{2}(\theta)}{E_{\gamma}} \tag{1.2}$$

Equation 1.2 implies that IB radiation is more probable at high values of the $\pi^{\pm}$ momentum and for small angle θ between the photon and the charged pion. The photon angular distribution is of the form $sin^{2}(\theta)\partial\Omega_{f}$. In addition, the amplitude A_{IB} is bigger at long photon wavelengths, as the volume involved in the emission can then be very large. The photon energy spectrum behaves as dE_{γ}/E_{γ} and therefore, the probability falls off very rapidly with increasing photon energy.

It is also important to note that the $K^{\pm} \to \pi^{\pm}\pi^{0}$ decay proceeds through a

$\Delta I = 3/2$ (or $\Delta I = 5/2$) amplitude, violating the $\Delta I = 1/2$ rule. This suppresses the $K^{\pm} \to \pi^{\pm}\pi^{0}$ decays by a factor of ~ 500 with respect to possible processes with $\Delta I = 1/2$ amplitudes. In fact, as the IB is proportional to the on-shell non-radiative amplitude, it would vanish in the limit where the $\Delta I = 1/2$ rule was exact.

1.1.2 Direct Emission.

Direct photon Emission (DE) (figure 1.1(b)) can be regarded as an electromagnetic transition from the initial $K^{\pm}$ state to final states which then break up into a $\pi^{\pm}$ and a π^{0}. Therefore, DE is sensitive to the Kaon structure.
As parity is not conserved on the weak interaction, direct emission can occur through both electric (E) and magnetic (M) transitions. Since the photon emitted in this process has long wavelength compared to the K radius, only the lowest multipoles contribute significantly, the dipole term being the dominant contribution in the expansion.
In the case of dipole emission the total angular momentum of the photon equals one ($J = 1$, with $J = L + S$). As the photon spin is one, we have $J = l+1, l, l-1$. Electric transitions correspond to $J = l \pm 1$ and magnetic transitions to $J = l$. For fixed J electric and magnetic transitions produce photons of opposite parity. If J is kept at one we must have $l_{\pi\pi} = 1$. Again, as the two pions are bosons $(-1)^{I}(-1)^{l_{\pi\pi}}$ must be one, and therefore the I=1 amplitude is picked.
This has an important consequence: a direct decay into $K^{\pm} \to \pi^{\pm}\pi^{0}\gamma$ can satisfy the ΔI= $\frac{1}{2}$ rule. Therefore the DE contribution can compete with the suppressed IB, even if in principle the rates of direct emission are expected to be small.
We have seen that, for the Inner Bremsstrahlung contribution, no particular assumptions needed to be made, and it could be understood applying basic QED corrections to the $K^{\pm} \to \pi^{\pm}\pi^{0}$ decay amplitude. However, in order to understand the origin of the Direct Emission amplitudes a particular model needs to be considered, given that here the photon is emitted by some intermediate states. To evaluate the values of E and M one needs to construct an effective Hamiltonian which describes the $\Delta S = 1$ radiative decays. A particularly interesting framework is Chiral Perturbation Theory (ChPT), that will be discussed in more detail later. An experimental measurement of E and M is important for differentiating between various models.

1.1.3 The Interference Term.

Given the amplitudes for Inner Bremsstrahlung and the Direct Emission, the total amplitude for the $K^{\pm} \to \pi^{\pm}\pi^{0}\gamma$ decay is just the sum of those:

$$A = A_{IB} + A_{DE(E)} + A_{DE(M)} \tag{1.3}$$

As in any quantum process, these amplitudes are complex and can in principle interfere. In the case of the $K^{\pm} \to \pi^{\pm}\pi^{0}\gamma$ decay, the bremsstrahlung term can interfere with the electric dipole direct emission term, but no interference can be observed with the magnetic term if the photon polarization is not measured.
CP violation could show up in this interference term: a CP violating phase difference between ΔI= $\frac{1}{2}$ structure amplitude and the ΔI= $\frac{3}{2}$ bremsstrahlung amplitude could result in a charge dependent asymmetry in the interference between them.

1.2 The $K^{\pm} \to \pi^{\pm}\pi^{0}\gamma$ matrix element.

The matrix element for $K^{\pm} \to \pi^{\pm}\pi^{0}\gamma$ is given in [4]:

$$M^{\pm}(p_{\pi}, p_{\pi^0}, p_{\gamma}, p_K, \epsilon) =< \pi^{\pm}(p_{\pi})\pi^{0}(p_{\pi^0})\gamma(p_{\gamma}, \epsilon)^{out}|K^{\pm}(p_K) > \tag{1.4}$$

where p_{π}, p_{π^0}, p_{γ}, p_K are the momenta of the charged pion, neutral pion, photon and kaon respectively, and ϵ is the 4-vector polarization of the gamma ray.
In order to calculate this matrix element we need to know the total decay amplitude. Because of the weak nature of the $K^{\pm} \to \pi^{\pm}\pi^{0}\gamma$ decay, the amplitude for this process contains in general two contributions: a vector part A^{μ}_{-}, which is parity violating, and an axial-vector parity conserving part, A^{μ}_{+}. Using Lorentz and gauge invariance, the most general form of these amplitudes is [6]:

$$A^{\mu}_{-} = \alpha \left[\frac{p^{\mu}_{\pi}}{p_{\pi}p_{\gamma}} - \frac{p^{\mu}_{K}}{p_{K}p_{\gamma}} \right] - \beta \left[(p_K p_{\gamma})p^{\mu}_{\pi} - (p_{\pi}p_{\gamma})p^{\mu}_{K} \right] \tag{1.5}$$

$$A^{\mu}_{+} = \gamma \epsilon_{\mu\nu\rho\sigma} p^{\nu}_{K} p^{\rho}_{\pi} p^{\sigma}_{\gamma} \tag{1.6}$$

where α, β and γ are complex numbers.
It is convenient to write the total invariant amplitude as:

$$A = \epsilon_{\mu}A^{\mu} = \epsilon_{\mu}(A^{\mu}_{-} + A^{\mu}_{+}) = A_{IB} + A_{DE(E)} + A_{DE(M)} \tag{1.7}$$

In this way we can identify A_{IB} as the inner bremsstrahlung contribution of eqn. 1.1 and $A_{DE(E)}$ and $A_{DE(M)}$ as the electric (vector) and magnetic (axial-vector) contributions to the DE term, such that $\alpha = A^{\pm}_{2}e^{i\delta^{2}_{0}}$, $\beta = E_1 e^{i\delta^{1}_{1}}$ and

$\gamma = M_1 e^{i\delta_1^1}$, where δ_L^J are the strong rescattering phases for a final state of momentum L and isospin I.

The matrix element can be calculated separately for K^+ and K^-:

$$\begin{aligned} M^+(p_\pi, p_{\pi^0}, p_\gamma, p_K, \epsilon) = \delta^4(p_\pi + p_{\pi^0} + p_\gamma - p_K)(4\pi\alpha)^{1/2}\epsilon^\mu \\ \Bigg(A_2^+ e^{i\delta_0^2}\left[\frac{p_\pi^\mu}{p_\pi p_\gamma} - \frac{p_K^\mu}{p_K p_\gamma}\right] \\ -e^{i\delta_1^1}\frac{E_1}{m_K^4}\left((p_K p_\gamma)p_\pi^\mu - (p_\pi p_\gamma)p_K^\mu\right) - e^{i\delta_1^1}\frac{M_1}{m_K^4}(p_\pi^\nu p_{\pi^0}^\rho p_K^\sigma \epsilon_{\mu\nu\rho\sigma})\Bigg) \end{aligned} \quad (1.8)$$

$$\begin{aligned} M^-(p_\pi, p_{\pi^0}, p_\gamma, p_K, \epsilon) = \delta^4(p_\pi + p_{\pi^0} + p_\gamma - p_K)(4\pi\alpha)^{1/2}\epsilon^\mu \\ \Bigg(A_2^{+\star} e^{i\delta_0^2}\left[\frac{p_\pi^\mu}{p_\pi p_\gamma} - \frac{p_K^\mu}{p_K p_\gamma}\right] \\ -e^{i\delta_1^1}\frac{E_1^\star}{m_K^4}\left((p_K p_\gamma)p_\pi^\mu - (p_\pi p_\gamma)p_K^\mu\right) - e^{i\delta_1^1}\frac{M_1^\star}{m_K^4}(p_\pi^\nu p_{\pi^0}^\rho p_K^\sigma \epsilon_{\mu\nu\rho\sigma})\Bigg) \end{aligned} \quad (1.9)$$

where the amplitude A_2^- for the negative kaon decay satisfies the relation $A_2^- = A_2^{+\star}$ The relevant unknown parameters are $|E_1|$, $|M_1|$, $\delta_1^1 - \delta_0^2$ and the phase difference between A_2^+ and E_1 and between A_2^+ and M_1.

It is convenient to define E and M as follows:

$$\begin{aligned} Ee^{i\phi} &= E_1|A_2^+|/(A_2^+), 0 \leq \phi \leq \pi \\ Me^{i\phi'} &= M_1|A_2^+|/(A_2^+), 0 \leq \phi' \leq \pi \end{aligned} \quad (1.10)$$

If the photon polarization is not observed, no inteference can be seen between the magnetic amplitude and either E_1 or the inner bremsstrahlung contribution. In that case only four parameters are needed to describe the decay: E, M, $\delta_1^1 - \delta_0^2$ and ϕ.

The value of $\delta_1^1 - \delta_0^2$ can be estimated setting $\delta_0^2 = 0$, so δ_1^1 can be obtained from a Breit-Wigner extrapolation from the ρ resonance, giving $\delta_1^1 - \delta_0^2 = 10^0$ [4, 5]. Under this assumption the only parameters to be obtained are E, M and ϕ.

Working in the kaon rest frame and choosing the photon energy and the charged pion energy as the Dalitz plot variables, we obtain the following expression for the Dalitz plot distribution of $K^\pm \to \pi^\pm\pi^0\gamma$ events:

$$\begin{aligned} \frac{d^2R^\pm}{dE_\gamma dE_\pi} = \frac{\alpha}{4\pi^2}\frac{p_\pi^2}{m_K^3} sin^2(\theta)\Bigg[\frac{|A_2^+|^2}{\left(\frac{1}{2}m_K - E_{\pi^0} - \frac{m_\pi^2 - m_{\pi^0}^2}{2m_K}\right)^2} \\ +2cos(\pm\phi + \delta_1^1 - \delta_0^2)\frac{|A_2^+|EE_\gamma}{m_K^2\left(\frac{1}{2}m_K - E_{\pi^0} - \frac{m_\pi^2 - m_{\pi^0}^2}{2m_K}\right)} \end{aligned}$$

$$+(|E|^2+|M|^2)\frac{E_\gamma^2}{m_K^4}\Bigg] \tag{1.11}$$

Where E_{π^0} is the π^0 energy and θ is the angle between the photon and the charged pion. The first term in the sum describes the inner bremsstrahlung contribution. Factorizing it out we get:

$$\frac{d^2R^\pm}{dE_\gamma dE_\pi} = \frac{d^2R^\pm_{IB}}{dE_\gamma dE_\pi}\left[1 + 2cos(\pm\phi+\delta_1^1-\delta_0^2)\left|\frac{E}{A_2^+}\right|\frac{E_\gamma\left(\frac{1}{2}m_K - E_{\pi^0} - \frac{m_\pi^2-m_{\pi^0}^2}{2m_K}\right)}{m_K^2}\right.$$

$$\left. + \frac{(|E|^2+|M|^2)}{|A_2^+|^2}\frac{E_\gamma^2\left(\frac{1}{2}m_K - E_{\pi^0} - \frac{m_\pi^2-m_{\pi^0}^2}{2m_K}\right)^2}{m_K^4}\right] \tag{1.12}$$

1.3 The Dalitz plot variables: W and T_π^*

For the $K^\pm \to \pi^\pm\pi^0\gamma$ decay it is very useful to define another set of Dalitz plot variables: T_π^* and W. T_π^* represents the pion kinetic energy in the kaon rest frame. The less familiar W is defined as:

$$W^2 = \frac{(p_K p_\gamma)(p_\pi p_\gamma)}{m_\pi^2 m_K^2} \tag{1.13}$$

As will be explained later, the distribution of the W variable turns out to be very sensitive to the different components of the $K^\pm \to \pi^\pm\pi^0\gamma$ decay. In addition, W is a Lorentz invariant, so it can be calculated in any frame.

In terms of W and T_π^* the differential decay width of $K^\pm \to \pi^\pm\pi^0\gamma$ can be rewritten as:

$$\frac{\partial^2\Gamma^\pm}{\partial T_\pi^*\partial W} = \frac{\partial^2\Gamma^\pm_{IB}}{\partial T_\pi^*\partial W}\left[1 + 2cos(\pm\phi+\delta_1^1-\delta_0^2)\frac{m_\pi^2}{m_K^2}\left(\left|\frac{E}{A_2^+}\right|\right)W^2 + \right.$$

$$\left.\frac{m_\pi^4}{m_K^4}\left(\left|\frac{E}{A_2^+}\right|^2 + \left|\frac{M}{A_2^+}\right|^2\right)W^4\right] \tag{1.14}$$

From this expression it is obvious that every component of the $K^\pm \to \pi^\pm\pi^0\gamma$ decay has a different behaviour in terms of the W variable. Normalizing by the Inner Bremsstrahlung contribution, the Direct Emission term is proportional to W^2 and the Interference is proportional to W^4. This will be exploited experimentally in order to disentangle the different contributions.

1.4 CP violation.

Symmetry is a fundamental concept in any quantum field theory. In addition to the continuous symmetries, there are the discrete symmetries, like Charge Conjugation (C), Parity (P) and Time reversal (T). Charge conjugation interchanges particles and antiparticles, Parity reverses the handiness of space and T the time coordinate. The combined action of C and P is denoted as CP. From experiment we know that C, P and T are conserved by the strong, electromagnetic and gravitational interactions. The weak interaction violates C and P separately, but it almost conserves CP and T.

The kaon system provided the first evidence for CP-violation. Indirect CP-violation was discovered in K_L, K_S, and can be explained as the mixing between the K^0 and $\bar{K}^0$ by an small component ϵ. However, there is another source of CP-violation, that is not related to any mixing of CP eigenstates, but that occurs directly in the weak transitions. In neutral kaons this is parametrised by the ϵ' parameter, that has been measured by the NA48 [7] and KTeV[8] collaborations. Direct CP-violation has been also observed in the B system.

In the Standard Model the effect of direct CP-violation appears as a complex phase on the mass matrix for the three quark families (the CKM matrix). With three (or more) fermion generations, there is natural room for a parameter that, if non-zero, causes CP-violation.

In charged kaon decays, mixing is not possible due to charge conservation, so any CP-violating effect must be of the direct type, arising from the decay amplitudes themselves.

In order to observe a physical effect from a CP-violating phase, it is necessary to have an interference between at least two different amplitudes that go from the same initial state to the same final state with different scattering phase shifts. Without this interference, all phase information would be lost and no asymmetry would remain.

The main goal of the NA48/2 experiment was the search for direct CP violation in the decays of charged kaons to three pions [10, 11].

Direct CP-violation can in principle also occur on the $K^\pm \to \pi^\pm\pi^0\gamma$ decay. The bremsstrahlung amplitude and internal photon emission amplitude could interfere to produce a difference between K^+ and K^-.

In order to see this more clearly, let us examine again eqn. 1.14. Eqn 1.14 can be rewritten in terms of $cos(\phi)$ and $sin(\pm\phi)$. Considering all $K^\pm \to \pi^\pm\pi^0\gamma$ together, irregardless of the kaon sign, the differential branching ratio can be expressed as:

$$\begin{aligned}\frac{\partial^2\Gamma}{\partial T^*_\pi \partial W} &= \frac{\partial^2\Gamma^+}{\partial T^*_\pi \partial W} + \frac{\partial^2\Gamma^-}{\partial T^*_\pi \partial W}\\ = 2\frac{\partial^2\Gamma_{IB}}{\partial T^*_\pi \partial W} &\left[1 + 2cos(\phi)cos(\delta^1_1 - \delta^2_0)\frac{m^2_\pi}{m^2_K}\left(\left|\frac{E}{A^+_2}\right|\right)W^2 + \right.\\ &\left.\frac{m^4_\pi}{m^4_K}\left(\left|\frac{E}{A^+_2}\right|^2 + \left|\frac{M}{A^+_2}\right|^2\right)W^4\right] \qquad (1.15)\end{aligned}$$

And the difference between the K^+ and K^- differential branching ratios is given by:

$$\begin{aligned}\frac{\partial^2\Gamma_{CPV}}{\partial T^*_\pi \partial W} &= \frac{\partial^2\Gamma^+}{\partial T^*_\pi \partial W} - \frac{\partial^2\Gamma^-}{\partial T^*_\pi \partial W}\\ = 2\frac{\partial^2\Gamma_{IB}}{\partial T^*_\pi \partial W} &\left(2sin(\phi)sin(\delta^1_1 - \delta^2_0)\frac{m^2_\pi}{m^2_K}\left(\left|\frac{E}{A^+_2}\right|\right)W^2\right) \qquad (1.16)\end{aligned}$$

CP violation is indicated by the observation of a non-vanishing asymmetry between the K^+ and K^- decays, either in the rates, or in the Dalitz plot ($\frac{\partial^2\Gamma_{CPV}}{\partial T^*_\pi \partial W}$), or in the energy spectrum of the charged pion ($\frac{\partial\Gamma_{CPV}}{\partial W}$). A prediction for these quantities requires knowledge of ϕ, $\delta^1_1 - \delta^2_0$, E and $|E|^2 + |M|^2$. From the above, the symmetry vanishes if there is not an interference between two different weak amplitudes with different strong rescattering phases ($\delta^1_1 \neq \delta^2_0$) and a relative CP phase. A value of $\phi \neq 0$ can arise from an electromagnetic CP violation in the direct electric dipole transition (which allows $\phi \sim \frac{1}{2}\pi$) or from a small $\Delta I = \frac{3}{2}$ or $\Delta I = \frac{5}{2}$ CP-violating part of the weak interactions affecting the A^+_2 amplitude appearing in the inner bremsstrahlung contribution (yielding $\phi \sim 1$).

There are two different contributions to the imaginary part of E [12]: one from the gluon penguin diagram, and the other from the electromagnetic penguin diagram. These diagrams are shown in fig. 1.2.

In the SM flavor changing neutral currents (FCNC) are forbidden at tree level. Then $s \longrightarrow d$ transitions occur through loop diagrams involving a W boson and a up-type quark, resulting in emission of a photon. The same applies to the gluon penguin, when a gluon is emitted instead of the photon. Following [12], these two diagrams contribute constructively to the CP-odd phase of the electric dipole.

In summary, a possible difference between the positive and negative charged $K^\pm \to \pi^\pm\pi^0\gamma$ decays is sensitive both to electromagnetic CP violation and to CP non-conservation by a small component of the weak interactions allowing $\Delta I > 1/2$. If there is no large electromagnetic CP violation, then CP viola-

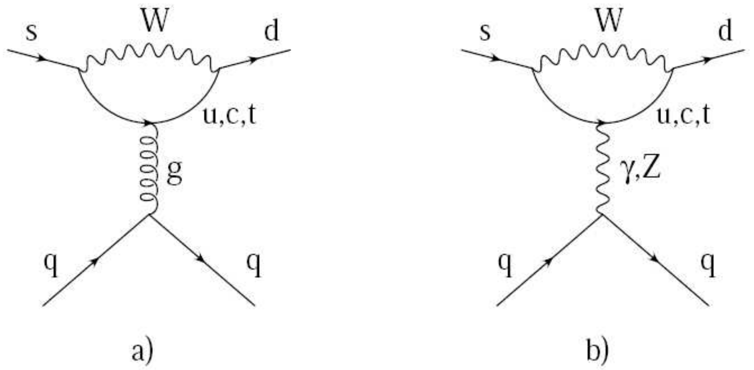

Figure 1.2: Leading diagram contributing to the strong and electromagnetic penguin operators.

tion in these decays provides a measurement of the CP-violating phase difference between the $\Delta I > 1/2$ amplitudes $A_2^{\pm}$, responsible for the $K^{\pm} \to \pi^{\pm}\pi^0$ decays. These effects can be seen thanks to the possible interference between Inner Bremsstrahlung and Direct Emission electric amplitudes.

1.5 Theoretical Frameworks for the Calculation of DE.

As it has been already mentioned, in order to understand the origin of the Direct Emission contribution, we have to consider a particular model. Different approaches have been tried to study the DE term of the $K^{\pm} \to \pi^{\pm}\pi^0\gamma$ decay, such as Chiral Perturbation Theory (ChPT) [13, 14, 15, 16, 17], short-distance effective weak Hamiltonian [6, 3], the vector-meson-dominance (VMD) model and current algebra. Of all these techniques, the most robust is ChPT.

Chiral Perturbation Theory gives a dynamical formulation of the strong interactions among the octet of pseudoscalar mesons, when both quark and gluonic degrees of freedom are integrated out. Our ignorance on the latter step is reflected by the appearance of coupling constants in the effective Lagrangian which are not fixed by symmetry requirements alone and which are not yet directly calculable from QCD.

ChPT uses the Standard Model chiral symmetry in its full generality, so predictions from ChPT are equivalent to Standard Model predictions restricted to the energy range where the characteristic momenta involved in the interactions are small compared to the natural scale of chiral symmetry breaking (~ 1 GeV).

ChPT is therefore an ideal framework to describe kaon decays. Testing ChPT predictions is equivalent to testing the Standard Model at low energies.
The $K^{\pm} \rightarrow \pi^{\pm}\pi^{0}\gamma$ decay can give important information about some of the, for the moment, undetermined chiral constants. In addition, non leptonic radiative kaon decays are sensitive to the chiral anomaly, which is an intrinsic characteristic of any Quantum Field Theory and that translates univocaly into the ChPT framework. The fundamental concepts in ChPT and the Chiral Anomaly are explained in the following sections.

1.6 Chiral Perturbation Theory

Let us begin the explanation of ChPT in the context of the strong interaction. The study of QCD can be divided in three energy regions. At high energies (E $\geq \Lambda_{QCD}$) the coupling is small and we can apply standard perturbation theory as in QED. As we go down in energy the coupling becomes bigger so that at intermediate energies the perturbation technique is no longer applicable. However, at very low energies (E $<$ 1/2 GeV) another kind of controlled approximation is possible, based on the fact that the very soft processes occurring in this region are highly constrained by the symmetry of the underlying theory. The chiral symmetry of the QCD Lagrangian and the mechanism of spontaneous chiral symmetry breaking provide a solid frame to predict the behavior of strong interactions within the meson octet.

1.6.1 Chiral Symmetry

If we ignore all but the lightest quarks u, d and s, the fermionic part of the QCD Lagrangian can be written as:

$$\mathcal{L} = \overline{u}iDu + \overline{d}iDd + \overline{s}iDs - m_u\overline{u}u - m_d\overline{d}d - m_s\overline{s}s \tag{1.17}$$

where u, d and s represent the quark fields, m_u, m_d and m_s their respective masses and D is the covariant derivative. In the approximation of $m_u \sim m_d \sim m_s$, the Lagrangian has isospin symmetry, i.e., it remains invariant under SU(3) unitary rotations mixing the u, d and s fields. In addition, if m_u, m_d, m_s are small, this Lagrangian is symmetric under separate $U(1)_L$ and $U(1)_R$ transformations, because the classical Lagrangian for massless fermions contains no coupling between left and right handed quarks. The overall invariance under $SU(3)_L \times SU(3)_R$ is called chiral symmetry.

Denoting Q as the quark triplet under isospin SU(3), its chiral components Q_R and Q_L can be found using the relevant projection operators $P_L = \frac{1}{2}(1-\gamma_5)$ and $P_R = \frac{1}{2}(1+\gamma_5)$ as $Q_L = P_L Q$, $Q_R = P_R Q$. The currents associated with these symmetries are:

$$j_L^\mu = \overline{Q}_L \gamma^\mu Q_L \quad j_R^\mu = \overline{Q_R} \gamma^\mu Q_R \tag{1.18}$$

$$j_L^{\mu a} = \overline{Q}_L \gamma^\mu \lambda^a Q_L \quad j_R^{\mu a} = \overline{Q}_R \gamma^\mu \lambda^a Q_R \tag{1.19}$$

where λ^a represent the generators of SU(3).
The sum of these give baryon number and isospin vector currents, corresponding to symmetries with $U(1)_R = U(1)_L$. The difference gives the axial vector currents:

$$j^{\mu 5} = \overline{Q} \gamma^\mu \gamma^5 Q \quad j^{\mu 5 a} = \overline{Q} \gamma^\mu \gamma^5 \lambda^a Q \tag{1.20}$$

classically satisfying:

$$\partial_\mu j^{\mu 5} = 0 \quad \partial_\mu j^{\mu 5 a} = 0 \tag{1.21}$$

The vector $SU(3)_V \times U(1)_V$ are manifest symmetries of the strong interactions associated to isospin and baryon number conservation laws. However, the axial vector transformations do not correspond to any obvious symmetry of the strong interactions. Symmetries require particles to appear in multiplets, as symmetry transformations yield states with the same energy. If chiral symmetry were realized one would expect to exist multiplets of particles having same spin and (approximately) the same mass, but with opposite parity. These states do not exist because the chiral symmetry is spontaneously broken down to the vectorial component.

1.6.2 Spontaneous breaking of chiral symmetry.

Hidden symmetry occurs when the Lagrangian is invariant under the symmetry, but the actual ground state is not. This happens because there exists a continuous family of ground states solutions that are related to each other by the symmetry but which are not individually invariant under the symmetry. The symmetry, although still valid, appears to be hidden when one looks at the spectrum. In QCD the ground state is represented by virtual quark-antiquark pairs. Different vacua would have different compositions of left and right handed quarks, so the true chosen vacuum it is not necessarily invariant under a chiral operation.

A direct consequence of spontaneous symmetry breaking is the appearance of Goldstone bosons. These are massless particles that take the available degrees of freedom. In the real world such states are not massless, since exact chiral invariance is broken by the small quark mass terms. Thus, what we have in QCD is an octet of very light pseudoscalar particles, the π, K, η. The important consequence of the symmetry of the theory is that, even if the ground state hides the invariance, symmetry predictions can still be made. Chiral perturbation theory uses chiral symmetry in its full generality. Predictions are those of the theory alone without additional dynamical assumptions. It is a rigorous controlled approximation, however it is limited by the need to determine the low-energy constants phenomenologically. Some models try to overcome this problem making predictions on the low-energy constants.

1.7 Strong and Weak $\Delta S = 1$ Effective Lagrangians and The Chiral Expansion.

In general, if a prediction follows directly from a symmetry, a simple, but non-linear effective Lagrangian can be found that shares the full symmetry of the original theory, and thus encapsulates all the corresponding low energy predictions.

As chiral symmetry is spontaneously broken, there are eight very light pseudo-Goldstone bosons in the pseudoscalar octet. Since these states are much lighter than their hadronic counterparts, an effective field theory can be applied to describe their interactions, provided that the energy-momenta involved are small compared to the 1 GeV scale typical of hadrons.

The lowest order (tree-level) effective strong Lagrangian is [18]:

$$\mathcal{L}_2 = \frac{F_\pi^2}{4} Tr(\partial_\mu U \partial^\mu U) + \frac{m_\pi^2}{4} F_\pi^2 Tr(U + U^\dagger) \tag{1.22}$$

where:

$$U = exp\left(i\frac{\lambda^A \phi^A}{F} \right) \tag{1.23}$$

where λ^A are the Gell-Mann matrices and the field ϕ^A is the pseudoscalar octet in chiral SU(3). This Lagrangian $\mathcal{L}_2$ describes free particles. It is unique and has predictive power. The subscript 2 indicates the derivative order at which we work, equivalent to one power in chiral symmetry breaking (m_π^2) or two powers of external momenta. This can be also expressed as $\mathcal{O}(p^2)$.

It is remarkable that the degrees of freedom are now the meson fields, instead of quarks and gluons. In fact, this is what allowed us to write the matrix elements of the $K^{\pm} \rightarrow \pi^{\pm}\pi^{0}\gamma$ decay directly as function of the momenta of the kaon and the pions.

However, divergences arise when going beyond the tree level. The solution is to absorb these divergences in phenomenological constants, as done in QED.

Electromagnetic perturbations to the strong effective Lagrangian can be taken into account in this context. The explicit structure of the effective chiral Lagrangian for strong and electromagnetic interactions to fourth order in derivatives and masses, $\mathcal{O}(p^4)$, was written by Gasser and Leutwyler [19]. It is denoted as $\mathcal{L}_4$ and can be expressed as:

$$\mathcal{L}_4 = \sum_{i=1}^{10} L_i \mathcal{O}_i \tag{1.24}$$

where O_i are the chiral operators. The constants L_i cannot be determined by chiral symmetry alone. The renormalized values are obtained by appending to these bare quantities the divergent one-loop contributions. Comparing predictions to experiment, empirical numbers can be determined for each of these ten parameters.

ChPT is an iterative procedure. If two-loop amplitudes from $\mathcal{L}_2$ or one-loop corrections from $\mathcal{L}_4$ are calculated, divergences will arise involving six-derivatives. The chiral procedure represents a systematic expansion in energy and momentum. One-loop corrections from $\mathcal{L}_2$ or tree level contributions from $\mathcal{L}_4$ are $\mathcal{O}(E^2/\Lambda^2_{QCD})$ where $\Lambda_{QCD} \sim 1$ GeV is the chiral scale. Thus ChPT is a low-energy procedure. It is only to the extent that the energy is small compared to the chiral scale that is makes sense to truncate the expansion at a given level (or order O). The adequate truncation order depends on the process under consideration.

In this theory the effects of electroweak interactions can be also taken into account under the form of a perturbation to the strong effective Lagrangian. It is clear that these effects cannot be neglected, as at the end, it is the weak interaction which is responsible for the kaon decay.

In the Standard Model, the weak interaction is mediated by a massive vector boson W. The interaction between quarks and the W can be written as:

$$\delta\mathcal{L} = \frac{g}{\sqrt{2}} W_{\mu} \bar{\psi} \gamma^{\mu} (1 - \gamma^5) \psi \tag{1.25}$$

with the boson propagator given by:

$$\frac{-ig_{\mu\nu}}{q^2 - m_W^2 + i\epsilon} \tag{1.26}$$

For momentum transfers small compared to m_W, we can ignore the q^2 in the propagator and write the interaction as the matrix element of the operator:

$$\frac{g^2}{2m_W^2}\mathcal{O}(x) \tag{1.27}$$

where

$$\mathcal{O}(x) = \bar{\psi}\gamma^\mu(1-\gamma^5)\psi\bar{\psi}\gamma_\mu(1-\gamma^5)\psi \tag{1.28}$$

This is a local operator. The interaction is now equivalent to a four-quark vertex. We can say that at distances larger than m_W^{-1}, the W boson can be integrated out. In this framework an effective Hamiltonian can be written using all operators related to $\Delta S = 1$ transitions as:

$$H_{eff}^{\Delta S=1} = -\sqrt{2}G_F s_1 c_1 c_3 \sum_{i=1}^{6} c_i O_i \tag{1.29}$$

where c_i are the so-called Wilson coefficients. $G_F = \sqrt{2}\frac{g^2}{8m_W^2}$ is the Fermi constant, which gives the strength of the weak interactions at energies much less than m_W, and $s_1c_1c_3$ denotes the product of CKM matrix elements $V_{ud}V_{us}^*$ for three generations.

From $H_{eff}^{\Delta S=1}$ a Lagrangian can be found that can also be expanded in the context of ChPT to any order. The effective chiral Lagrangian for equation 1.29 to lowest order in the chiral expansion $\mathcal{L}_2$ can be found in [17]. At next to leading order $\mathcal{L}_4$ is already quite involved. Its full expression is written in [20].

We have now almost all elements needed to understand $K^\pm \to \pi^\pm\pi^0\gamma$ decays in the framework of ChPT. We know how to treat the strong interaction with electroweak perturbations at small energies. There is only one more important point, the so-called chiral anomaly. This subject is treated in [2]. A summary is given in the next section.

1.8 The Chiral Anomaly and the Wess-Zumino-Witten term.

In general theories with massless fermions exhibit chiral symmetry, which implies the separate conservation of the number of left-handed and right handed fermions. However, due to radiative corrections, the $U(1)_A$ symmetry is destroyed, as the conservation of the axial vector current is actually incompatible with gauge invariance. The breaking of a classical symmetry by quantum effects is called anomaly. As the construction of a theory with local gauge invariance relies on the existence of an exact global symmetry, if the symmetry is then broken at quantum level the whole theory is inconsistent. Anomalous terms appear in diagrams with axial currents interacting with background gauge fields where a renormalization cannot be done consistently with the requirement of gauge invariance of the theory. In QED, for example, it can be shown that the axial vector current is not conserved in the presence of electromagnetic fields. The anomalous non-conservation of the four dimensional QED axial current is expressed by the Adler-Bell-Jackiw relation:

$$\partial_\mu j^{\mu 5} = -\frac{e^2}{16\pi^2}\epsilon^{\alpha\beta\mu\nu}F_{\alpha\beta}F_{\mu\nu} \tag{1.30}$$

This equation is correct to all orders in QED perturbation theory.
In the case of QCD, the chiral anomaly has a number of important implications. Let us consider the QCD axial currents written in equation 1.20, interacting with the non-Abelian strong gauge fields. The Adler-Bell-Jackiw equation reads now:

$$\partial_\mu j^{\mu 5a} = -\frac{g^2}{16\pi^2}\epsilon^{\alpha\beta\mu\nu}F^c_{\alpha\beta}F^d_{\mu\nu}tr[\lambda^a t^c t^d] \quad \partial_\mu j^{\mu 5} = -\tfrac{g^2 n_f}{32\pi^2}\epsilon^{\alpha\beta\mu\nu}F^c_{\alpha\beta}F^c_{\mu\nu} \tag{1.31}$$

where $F^c_{\alpha\beta}$ is a gluon field strength, λ^a is an isospin matrix, t^c is a color matrix and the trace is over colors and flavors. Thus, the modification of chiral conservation laws in equation 1.21 due to the coupling of the quarks currents to gluon fields leads to the non-conservation of the isospin singlet axial current $j^{\mu 5}$.
The axial vector isospin currents $j^{\mu 5a}$ have no anomaly from QCD interactions. However they have an anomaly associated with the coupling of quarks to electromagnetism. Coupling now the QCD axial currents to electromagnetic gauge fields, the anomaly is given by:

$$\partial_\mu j^{\mu 5a} = -\frac{e^2}{16\pi^2}\epsilon^{\alpha\beta\mu\nu}F_{\alpha\beta}F_{\mu\nu}tr[\lambda^a Q^2] \tag{1.32}$$

where $F_{\mu\nu}$ is the electromagnetic field strength and Q is the matrix of electric quark charges, and the trace runs over flavors and colors. The flavor trace is non-zero only for $a = 3$ and in this case the electromagnetic anomaly is:

$$\partial_\mu j^{\mu 53} = -\frac{e^2}{32\pi^2}\epsilon^{\alpha\beta\mu\nu}F_{\alpha\beta}F_{\mu\nu} \tag{1.33}$$

Because the current $j^{\mu 53}$ annihilates a π^0 meson, this indicates that the axial vector anomaly contributes to the decay of π^0 to two gammas, which gives a direct measurement of the coefficient of the Adler-Bell-Jackiw relation. The relevant diagram for this process can be seen in fig. 1.3. This constitutes the paradigmatic example of how a decay of a light meson can provide information about the chiral anomaly.

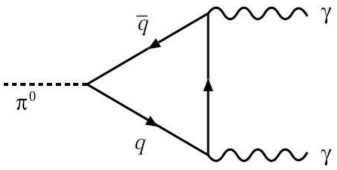

Figure 1.3: Diagram for the $\pi^0 \longrightarrow \gamma\gamma$ decay.

The chiral anomaly affects also the weak interaction.

It is quite remarkable that the anomaly for axial vector weak currents coupling with electromagnetic gauge fields cancels only when considering lepton and quark doublets together. This means that the weak interaction can be consistently combined with QED only because the number of quark doublets is the same as the number of lepton doublets. It is thanks to this cancellation that the Standard Model can be considered as a consistent anomaly-free theory.

The effect of the chiral anomaly can be translated to the effective chiral level in an unambiguous way, free from hadronization problems. The Wess-Zumino-Witten (WZW) term [21, 22] transfers the chiral anomaly from quarks and gluons to the composite level of hadrons. In the chiral counting this enters as an effect at $\mathcal{O}(p^4)$.

As already mentioned, the lagrangian of eqn 1.22 posseses all symmetries of QCD, but in addition it has extra discrete symmetries that do not have a correspondance in the initial theory. In fact, eqn 1.22 is invariant under three separate operations:

- $U \leftrightarrow U^T$, which in terms of pions is $\pi^0 \leftrightarrow \pi^0$ and $\pi^+ \leftrightarrow \pi^-$, corresponding to an ordinary charge conjugation.
- Standard parity operation (P_0 takes $x \leftrightarrow -x$,$t \leftrightarrow t$,$U \leftrightarrow U$)
- $U \leftrightarrow U^{-1}$, that counts modulo two the number of baryons $(-1)^{N_B}$

QCD is invariant only under $P = P_0(-1)^{N_B}$, but not under P_0 or $(-1)^{N_B}$ separately.

In order to solve this problem a higher order term can be added to the chiral lagrangian that respects all proper QCD symmetries but violates P_0 and $(-1)^{N_B}$. For such a term to be Lorentz invariant and violate P_0 it must include the Levi-Civita tensor $\epsilon_{\mu\nu\alpha\beta}$ (contributing therefore to magnetic terms). This is the WZW term.

For the strong, electromagnetic and semileptonic weak interactions, all anomalous Green functions can be obtained from the Wess-Zumino-Witten functional. The chiral anomaly also appears in the non-leptonic weak interactions. Only radiative K decays are sensitive to the anomaly in the non-leptonic sector. The chiral anomaly is a basic feature of quantum field theories with chiral fermions, and thus of the Standard Model. Therefore, experimental tests of the chiral anomaly are crucial for the theoretical basis of particle physics.
Although the anomaly can be interpreted as a short-distance effect, it manifests itself most directly at low energies. As already mentioned, the classical and most precise test is the decay $\pi^0 \longrightarrow \gamma\gamma$. However, there are a number of other processes, all involving either electromagnetic fields (real or virtual photons) or virtual W fields (semileptonic decays) where the anomaly can show. The $K^\pm \to \pi^\pm\pi^0\gamma$ decays is one of these.

1.9 Effective Lagrangian for the $K^\pm \to \pi^\pm\pi^0\gamma$ Decay. Contributions to DE from ChPT.

The total effective Lagrangian relevant for the $K^\pm \to \pi^\pm\pi^0\gamma$ decays is given in [15]:

$$\mathcal{L}_{eff} = \mathcal{L}_{st} - \frac{1}{4}F_{\mu\nu}F^{\mu\nu} + \mathcal{L}_{em} + \sqrt{\frac{1}{2}}G_F s_1 c_1 c_3 (\mathcal{L}_{\Delta S=1} + \mathcal{L}^{em}_{\Delta S=1}) \tag{1.34}$$

where $\mathcal{L}_{st}$ describes the strong interactions among the octet of pseudoscalar mesons, $F_{\mu\nu}$ is the electromagnetic tensor, $\mathcal{L}_{em}$ denotes the hadronic electromagnetic interaction Lagrangian, $\mathcal{L}_{\Delta S=1}$ the nonleptonic strangeness changing weak interactions and $\mathcal{L}^{em}_{\Delta S=1}$ the same weak perturbation in the presence of electromagnetic interactions. The specific form of the various terms has been already discussed on previous sections and can be found in [15].
To lowest order in ChPT $\mathcal{O}(p^2)$ the amplitudes described by equation 1.34 are pure bremsstrahlung . The Direct Emission amplitude described in eqn. 1.6 is three orders in momentum. Therefore, in order to obtain any contribution from

ChPT to the DE term, we need to develop the different terms in the total Lagrangian at least to $\mathcal{O}(p^4)$.

At $\mathcal{O}(p^4)$ we also must include the anomalous WZW terms, describing the chiral anomaly. Anomalous terms have odd intrinsic parity, which means that they are related to the magnetic contribution M to the Direct Emission. The anomalous terms contain the antisymmetric tensor $\epsilon_{\mu\nu\rho\sigma}$ and are even under charge conjugation for one meson and odd for two. This is the opposite behavior to non-anomalous terms.

Two classes of anomalous amplitudes can be identified at $\mathcal{O}(p^4)$: reducible and direct contributions. The source of the reducible amplitude is the WZW term. The direct contribution comes from the $\mathcal{L}_4^{\Delta S=1}$ itself. Unlike for the strong interactions, there are also odd-parity terms in the effective Lagrangian $\mathcal{L}_4^{\Delta S=1}$ of $\mathcal{O}(p^4)$ which have nothing to do with the chiral anomaly. However, the corresponding couplings are expected to be very small, so the magnetic amplitude to $\mathcal{O}(p^4)$ is determined uniquely by the chiral anomaly to good approximation . In any case, the theoretical prediction for direct contributions has big uncertainties, as it is related to unknown constants. A measurement of the magnetic contribution of the Direct Emission is therefore very important.

The WZW term generates long distance contributions to the $K^{\pm} \to \pi^{\pm}\pi^{0}\gamma$ decay. In principle the long-distance contributions arise from nonperturbative corrections to quark diagrams at the scale $\mu < 1$ GeV, which are not calculable in QCD perturbation theory. Long-distance effects are generally treated in pole dominance model, in which poles are the π, η, η' mesons. In chiral perturbation theory the relevant pole diagrams are depicted in figure 1.4.

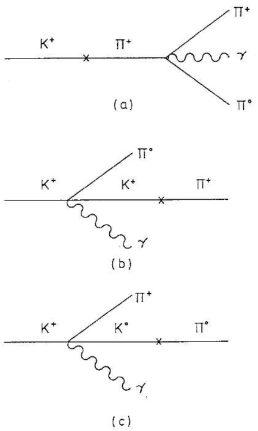

Figure 1.4: Pole diagrams contributing to $K^{\pm} \to \pi^{\pm}\pi^{0}\gamma$. The amplitude c) vanishes.

On the other hand, the $\Delta S = 1$ weak chiral Lagrangian and the $\Delta S = 1$ WZW terms are responsible for the short distance effects. A priori there is no obvious reason why $K^{\pm} \to \pi^{\pm}\pi^{0}\gamma$ should be dominated by long-distance contributions. Calculations have been also made at $\mathcal{O}(p^6)$ [17] that could give contributions to the magnetic amplitude, and not to the electric part. Although there is at present no unambiguous method of calculating these, a so-called weak deformation model predicts that $\mathcal{O}(p^6)$ direct terms completely cancel the previous $\mathcal{O}(p^4)$ direct contributions, so that the magnetic amplitude is completely determined by the anomaly, even after including vector meson exchange to $\mathcal{O}(p^6)$.

Let us now consider the electric part E of the Direct Emission. As indicated, it appears as well at $\mathcal{O}(p^4)$ and is important because it can interfere with the bremsstrahlung amplitude. There are two sources contributing to the electric amplitude. The first is due to the chiral Lagrangian of $\mathcal{O}(p^4)$ $\mathcal{L}_4^{\Delta S=1}$, giving rise to a short-distance contribution to E. Although we do not know the coupling constants which enter, a relatively big amplitude could be expected. Except for small photon momenta, where bremsstrahlung is bound to win, the direct amplitude E cannot be neglected. Measuring the energy spectrum of the photon should allow to isolate this amplitude and determine the coupling constants. For the moment there is no experimental evidence for the electric DE amplitude. The second contribution of $\mathcal{O}(p^4)$ can come from loop amplitudes, but this can be neglected. As loop amplitudes at $\mathcal{O}(p^4)$ are small, contributions at $\mathcal{O}(p^6)$ could be relevant.

In addition, it is important to note that in $\mathcal{L}_{\Delta S=1}^{em}$ appears the leading effective chiral realization of the electromagnetic penguin operator, represented by the diagram in Fig 1.2. As already mentioned, this diagram is specially interesting as it implies a complex coupling due to the CP-violating phase in the KM matrix, with important implications for CP violation.

In summary, we can say that in the context of ChPT, the magnetic amplitude takes long-distance and short-distance contributions, and the electric amplitude only short-distance contributions. The long-distance effects come from the WZW term and can be predicted unambiguously. The short-distance contributions to either the magnetic M or electric E part of the DE term are subject to uncertainties as the theoretical results depend on non measured and for the moment non calculable constants. That is why an experimental measurement of M and E would give a lot of information to ChPT. In addition, CP violation might be observed in the $K^{\pm} \to \pi^{\pm}\pi^{0}\gamma$ decays.

1.10 Theoretical Predictions.

In this section a summary on theoretical predictions for the different contributions to the $K^\pm \to \pi^\pm\pi^0\gamma$ decays is given.
The Inner Bremsstrahlung contribution to the $K^\pm \to \pi^\pm\pi^0\gamma$ decay can be calculated applying well known QED corrections to the $K^\pm \to \pi^\pm\pi^0$ channel, and therefore a very robust theoretical prediction exists for the IB branching ratio. For reasons that will be explained later, the $K^\pm \to \pi^\pm\pi^0\gamma$ decay branching ratio has always been measured in the region 55 MeV $< T^*_\pi <$ 90 MeV. The theoretical prediction for the Inner Bremsstrahlung branching ratio in this range is given in [23]:

$$BR(K^\pm \to \pi^\pm\pi^0\gamma)_{IB} = 2.61 \times 10^{-4} \tag{1.35}$$

In addition, another prediction for the IB branching ratio has been recently made available in [24].

$$BR(K^\pm \to \pi^\pm\pi^0\gamma)_{IB} = 2.84 \times 10^{-4} \tag{1.36}$$

For Direct Emission the predictions have more uncertainties. Under the assumption that Direct Emission is entirely due to reducible anomalous amplitude (magnetic component from WZW term) the branching ratio of DE can be completely predicted at leading order in ChPT using standard $\mathcal{O}(p^2)$ ChPT coupling constants. The result given in [17] is:

$$BR(K^\pm \to \pi^\pm\pi^0\gamma)_{DE} = 0.35 \times 10^{-5} \tag{1.37}$$

The additional contribution of the direct anomalous amplitude can be taken into account only in a model dependent way. For example the factorization model predicts a total DE value of:

$$BR(DE) = 1.94 \times 10^{-5} \tag{1.38}$$

In both previous cases there is not a prediction from ChPT for the electric transition amplitude, which depends on undetermined constants. Again all branching ratios are calculated on the restricted T^*_π range.
A summary of these predictions is shown in table 1.1.

Predictions are also available for CP violation observables. From [12] the magnitude of the CP asymmetry ranges from 2×10^{-6} to 1×10^{-5} for gamma energies from 50 to 170 MeV.

Component	Theoretical Ground	Order in ChPT	Branching
IB	Predictions based on QED	$\mathcal{O}(p^2)$	2.61×10^{-4} 2.84×10^{-4}
DE (M+E)	Assuming only magnetic reducible amplitude	$\mathcal{O}(p^4)$	0.35×10^{-5}
	Magnetic reducible plus direct amplitudes	$\mathcal{O}(p^4)$	1.95×10^{-5}
	Electric amplitude. Non predictable	$\mathcal{O}(p^4)$	
INT (E)	Electric amplitude non-predictable	$\mathcal{O}(p^4)$	

Table 1.1: Summary of theoretical predictions for branching ratios of IB, DE and INT components of the $K^{\pm} \rightarrow \pi^{\pm}\pi^{0}\gamma$

Chapter 2

Measurement of Direct Emission and Interference terms.

2.1 The Measurement Method.

The goal is to extract a very small Direct Emission contribution from the dominant Inner Bremsstrahlung part. For that purpose, the W variable defined in eqn. 1.13 can be used to disentangle the decay components.
The sensitivity of W to the different terms can be most easily explained considering the expresion of W^2 in the Kaon rest frame:

$$W^2 = \frac{E_\gamma^{*2}(E_\pi^* - p_\pi^* cos(\theta_{\pi\gamma}))}{m_K^2 m_\pi^2} \tag{2.1}$$

where E_γ^* is the radiated photon energy, E_π^* and p_π^* are the $\pi^\pm$ energy and momentum and $\theta_{\pi\gamma}$ is the opening angle between the charged pion and the radiated photon.
For Inner Bremsstrahlung , E_γ^* is small, and so is the angle between the charged pion and the emitted γ. Therefore the W distribution will peak at small values for IB events. On the contrary, for Direct Emission events, neither E_γ^* nor $\theta_{\pi\gamma}$ need to be small, so the W distribution will not peak at small W values, but more in the central range. This behavior is illustrated in Fig. 2.1
The E_γ^* , T_π^* and $\theta_{\pi\gamma}$ variables are also very sensitive to the nature of the decay. IB, DE and INT T_π^* distributions are shown in figure 2.2
Two main methods have been used in the literature for measuring the Direct Emission and Interference terms in data: the shape-method and the log-likelihood method.

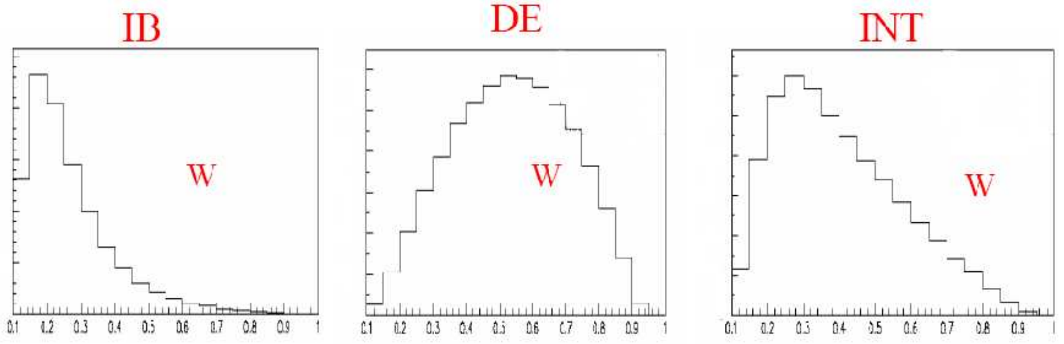

Figure 2.1: Shape of W distributions for Inner Bremsstrahlung , Direct Emission and Interference simulated events.

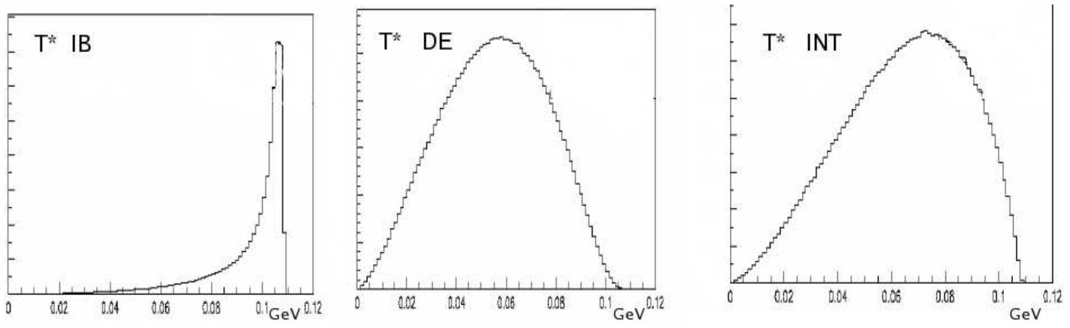

Figure 2.2: Shape of T_π^* distributions for Inner Bremsstrahlung , Direct Emission and Interference simulated events.

2.1.1 The Shape Method

If Direct Emission is present in real data events, it must show up as an excess at high W with respect to a Monte Carlo simulation of Inner Bremsstrahlung only. The experimental distribution can be divided by the simulated Inner Bremsstrahlung distribution and fitted according to Eqn. 2.2 to a simple polynomial function:

$$\frac{\text{W distribution for Data Events}}{\text{W distribution of IB Simulated Events}} = 1 + bW^2 + aW^4 \tag{2.2}$$

The a and b coefficients in this expression are related to the branching ratios of Direct Emission and Interference respectively by:

$$\frac{BR_{DE}}{BR_{IB}} = a\frac{\int \partial T_\pi^* \int W^4 \frac{\partial^2 \Gamma_{IB}}{\partial T_\pi^* \partial W} \partial W}{\int \partial T_\pi^* \int \frac{\partial^2 \Gamma_{IB}}{\partial T_\pi^* \partial W} \partial W} \tag{2.3}$$

$$\frac{BR_{INT}}{BR_{IB}} = b\frac{\int \partial T_\pi^* \int W^2 \frac{\partial^2 \Gamma_{IB}}{\partial T_\pi^* \partial W} \partial W}{\int \partial T_\pi^* \int \frac{\partial^2 \Gamma_{IB}}{\partial T_\pi^* \partial W} \partial W} \tag{2.4}$$

2.1.2 Maximum likelihood method.

In general, if x is described by a probability density f(x,θ) dependent in a parameter θ which true value θ^* is unknown, an estimator for θ^* can be constructed defining the likelihood function as follows:

$$L(x_1, x_2, ..., x_N; \theta) = \prod_{i=1}^{N} f(x_i, \theta) \tag{2.5}$$

where x_i is a set of N independent measurements of x, representing a particular event. The likelihood function gives the probability density of associating θ as the true value of the parameter for that event. The maximum likelihood method consists in adopting as estimator for the parameter the value of θ that maximizes L. As $L > 0$, this is equivalent to maximizing the logarithm lnL.

This method is commonly used in particle physics, in particular to calculate the proportions of different sources needed to describe a given data sample.

As data values are normally binned, it can happen that the number of data points in the bins is small. In that case a normal χ^2 minimization is inappropriate, and a maximum likelihood technique based on Poisson statistics is often used. More information about the general maximum likelihood method can be found in [25]. For $K^{\pm} \to \pi^{\pm}\pi^0\gamma$ we need to estimate the composition of the data based on Monte Carlo simulations of Inner Bremsstrahlung , Direct Emission and Interference events. For that purpose, a code has been used , exploiting as input the W distribution of data events and of simulated IB, DE and INT simulated events. It calculates the fractions of every source needed to minimize the difference between the number of data events and the resulting total number of simulated events in every W-bin. This is described in detail in appendix A

2.2 The Experimental Status.

The $K^{\pm} \to \pi^{\pm}\pi^0\gamma$ decays have been subject to several experimental studies. Previous experiments have always made a cut on the kinetic energy of the charged pion in the kaon rest frame 55 MeV $< T^*_\pi <$ 90 MeV. This minimizes the background contamination arising from $K^{\pm} \to \pi^{\pm}\pi^0$ decays, dominant at T^*_π $>$ 90 MeV, and from $K^{\pm} \to \pi^{\pm}\pi^0\pi^0$ decays, dominant at T^*_π $<$ 55 MeV. The background sources will be explained in more detail in a dedicated chapter.

Six experiments have measured the branching ratio for direct photon emission in this T^*_π range. The first three [26, 27, 28], used in-flight kaons, and found a weighted average of $BR(DE) = (1.8 \pm 0.4) \times 10^{-5}$. The next two [29, 30] used stopped kaons and found $BR(DE) = (0.44 \pm 0.08) \times 10^{-5}$. The discrepancy between these two average values is 3.3 standard deviations. The last result comes from the Istra collaboration [31], that measured $BR(DE) = (0.37 \pm 0.40) \times 10^{-5}$. These results are plotted in Fig. 2.3. In addition the KEK collaboration has presented a preliminary result [32] on a data sample of $\sim 10\ 10^3$ events, obtaining $BR(DE) = (0.38 \pm 0.08) \times 10^{-5}$, which is in agreement with its previously published result. A summary of all previous experimental results is given in table 2.1 There has also been several attempts to measure CP-violation and an interference term in $K^\pm \to \pi^\pm \pi^0 \gamma$ decays [34, 27], however evidence for neither of these effects has been found. Actually, all previous experiments have explicitly set the value of the Interference term to zero in their fits in order to extract the Direct Emission component.

The NA48/2 collaboration can make an important contribution in this respect, as it has more than ten times more events than any of the previous experiments.

Experiment		Technique	Kaon sign	Number of events	BR(DE) × 10^6
BNL	1972 [26]	in-flight	$K^\pm$	2100	$15.6 \pm 3.5 \pm 5$
CERN	1976 [27]	in-flight	$K^\pm$	2461	23 ± 32
Dubna	1987 [28]	in-flight	K^-	140	$20.5 \pm 4.6\ ^{+3.9}_{-2.3}$
BNL E787	2000 [29]	stopped	K^+	2×10^4	$4.7 \pm 0.8 \pm 0.3$
KEK E470	2003 [30]	stopped	K^+	4434	$3.2 \pm 1.3 \pm 1.0$
Protvino	2004 [31]	in-flight	K^-	930	$3.7 \pm 3.9 \pm 1.0$
KEK E470	Prel [32]	stopped	K^+	10154	$3.8 \pm 0.8 \pm 0.7$
BNL E787	Prel [33]	stopped	K^+	20571	$3.5 \pm 0.6\ ^{+0.3}_{-0.4}$

Table 2.1: Summary of previous measurements of Direct Emission in $K^\pm \to \pi^\pm \pi^0 \gamma$ decays.

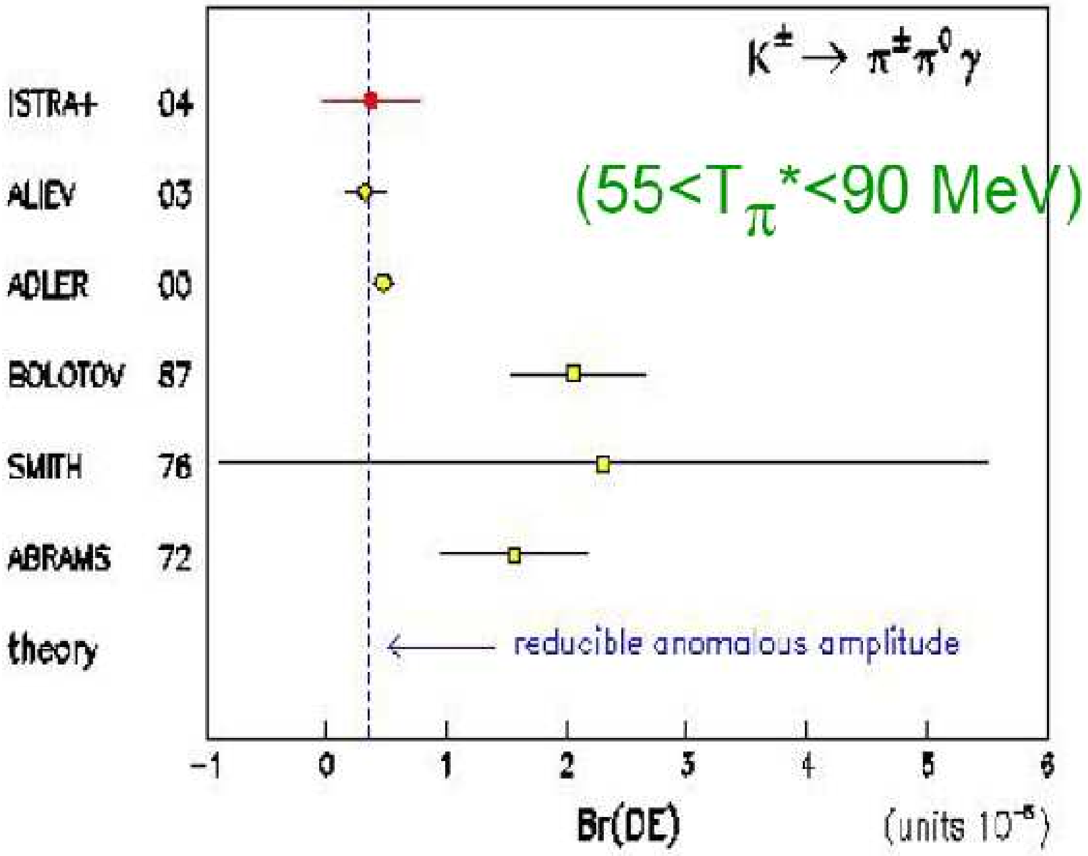

Figure 2.3: Experimental status of the DE branching ratio measurement for $55 < T_\pi^* < 90$ MeV. Vertical line corresponds to theory prediction in ChPT framework under the assumption of reducible anomalous amplitude only. Author and year of publication are shown on the vertical axis.

Chapter 3

The NA48/2 experiment.

3.1 Introduction

NA48/2 was the successor of NA48 and NA48/1, all fixed target experiments situated in the North Area of the CERN-SPS accelerator.
The NA48 experiment was designed to measure direct CP-violation in the neutral kaon system with accuracy of 0.02 %. NA48 took data from 1997 to 2001, when it published its final result [7]:

$$Re(\epsilon'/\epsilon) = (14.7 \pm 2.2) \times 10^{-4} \tag{3.1}$$

The NA48/1 experiment took data on 2002. The NA48 detector had to be upgraded and the beam line was changed in order to measure the branching of the very rare decay of $K_S^0 \to \pi^0 e^\pm e^\mp$, which was found to be [9]:

$$BR(K_S^0 \to \pi^0 e^\pm e^\mp, m_{ee} > 0.165\, GeV/c^2) = (3.0^{+1.5}_{-1.2}(stat) \pm 0.2(syst)) \times 10^{-9} \tag{3.2}$$

The main goal of NA48/2 was the search for direct CP violation in charged kaons decays to three pions. Results on the slope asymmetries on $K^\pm \to \pi^\pm\pi^+\pi^-$ [10] and $K^\pm \to \pi^\pm\pi^0\pi^0$ [11] have been recently published:

$$A_g(K^\pm \to \pi^\pm\pi^+\pi^-) = (1.7 \pm 2.9) \times 10^{-4} \tag{3.3}$$

$$A_g(K^\pm \to \pi^\pm\pi^0\pi^0) = (1.8 \pm 2.6) \times 10^{-4} \tag{3.4}$$

For NA48/2, data were collected in 2003 and 2004, using basically the NA48 detector with a changed beam line providing simultaneous and collinear K^+ and

K^- beams. The improved NA48/2 set-up includes, in addition to the new beam line, two new detectors (KABES and Beam Monitor), an extended decay region, the remapping of the drift chamber electronics in order to be left-right symmetric and changes on the level 2 charged trigger system (MBX). In this chapter a detailed description of the apparatus and the data taking strategy is given.
For what follows the coordinate system will be given by the following convention: z runs in the beam direction, y vertically from bottom to top and x horizontally in the direction to define a right-handed system.

3.2 The Beam Line

The NA48/2 beam line was able to deliver simultaneously K^+ and K^- particles of practically same momentum, with almost the same geometrical acceptance and with the possibility to permute their paths. This created a unique capability to perform high precision comparisons of K^+ and K^- decays under the same experimental conditions and to minimize systematic bias due to eventual local imperfections in the experimental setup.
The main characteristics of the beam line can be seen on Fig. 3.1.

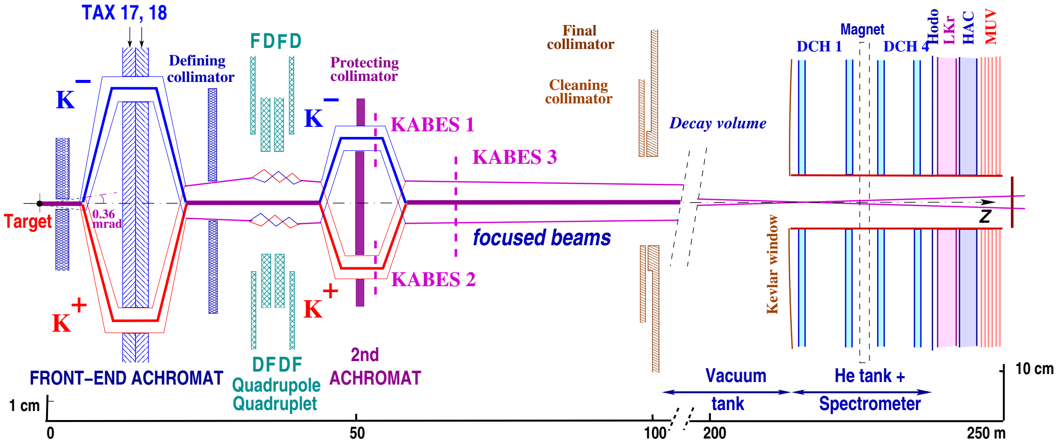

Figure 3.1: The NA48/2 beam line and detector

The primary beam consisted of 400 GeV protons impinging on a Beryllium target of 2 mm diameter and 400 mm length, corresponding to one interaction length for protons. The angle of impinging protons was zero degrees relatively to the experimental beam line and its intensity was 7 × 10^{11} protons per cycle, with a 4.8 s flat spill and 16.8 s cycle. Beams of negatively and positively charged particles were produced after the interaction.

About 14 m away from the target a copper collimator absorbs large angle secondary particles in the beams. The acceptance angle is ± 0.36 mrad in both planes.

Two vertically deflecting magnets, with opposite-sign fields, separate the beams which then pass through a pair of collimators (TAXes) with variable openings. A defining collimator makes the two beams collinear.

Beams were focused so that their transverse dimension is 5 mm r.m.s. at the spectrometer position. In this way the effect of any transverse structure in the beam spot has been minimized. The beam focusing has been realized with a system of four quadrupoles of alternate polarity, giving a small angle of convergence to the beams of $\sim$ 0.04 mrad.

Downstream of the focusing quadrupoles, at about 40 m away from the beryllium target and 50 m before the NA48 decay zone, a second achromat system again separates and recombines positive and negative beams, so they are oriented onto a common axis towards the NA48 detectors. It also incorporates a collimator in the center, that cleans the beams from neutral and many charged particles with momentum out of a given selected range that were produced on the defining collimator. The momentum of the remaining beam particles, passing through such an achromat, does not depend any more on their direction or position. After this a narrow band spectrum of 3.8 % width around the nominal value of 60 GeV/c is selected.

The detectors of the experiment are further protected against background around the beams by a cleaning collimator at $\sim$ 110 m and a final collimator ending at 114 m from the target.

Just upstream the last collimator, small steering dipole magnets allow the two charged beams to be perfectly aligned in both planes as they enter the decay region, so that finally, positive and negative kaon beams traveled through a 114 m vacuum tank superimposed with a precision of about 1 mm.

The final kaon flux is 2.2 10^6 K^+/cycle and 1.3 10^6 K^-/cycle. A series of magnetized-iron sweeping elements around the beam line upstream of the final collimator were used to limit the muon flux.

The beam spot shape as a function of momentum was similar for both beams in 2004, while a small difference was observable in 2003 for one of the beam lines (see figure 3.2).

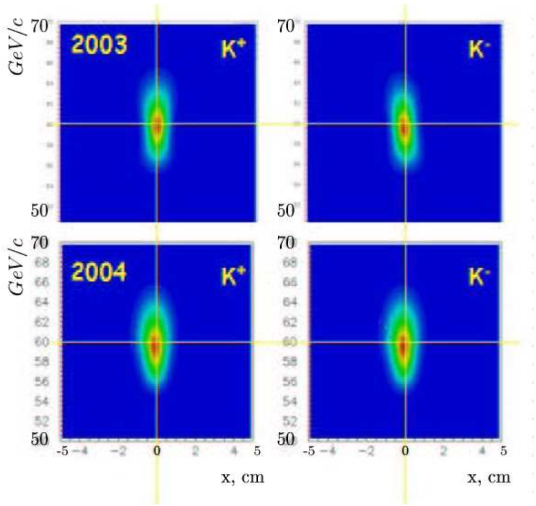

Figure 3.2: Momentum dependence on beam position (X-coordinate on the first spectrometer drift chamber) for 2003 and 2004 runs.

3.3 The KABES Detector

The KAon BEam Spectrometer (KABES) was conceived to provide individual kaon tagging and momentum measurement, with spatial and momentum resolutions of about 100 μm and 1 % respectively.

KABES consists of a set of two stations, located on the upper (Station 1u) and lower (Station 1d) arms of the second achromat and on its exit (Station 2). The upstream station ((1u) and (1d)) is located at the position where the K^+ and K^- beams are separated in the achromat, and allows the sign of the charged tracks to be identified. The downstream station (2) is positioned 8 m away along the beam axis from station 1, in a place where the positive and negative particles are collinear, so it has to sustain the rate from both beams. Layout of the KABES detector is shown in figure 3.3

Each KABES station contained a pair of Micromegas type detectors, with opposite drift directions. The MICROMEGAS detectors operate as Time Projection Chambers (TPC). In this way multiple scattering effects and parasitic interactions of the beam particles with the detectors are minimized, as the beams cross only thin windows confining the gas volume of the MICROMEGAS chambers. The use of the MICROMEGAS technology is justified by its very high rate capabilities. A detection station is shown in figure 3.4

A chamber consists of a conversion gap and a small amplification gap separated by a thin grid. On their passage in the conversion gap the beam particles liberate

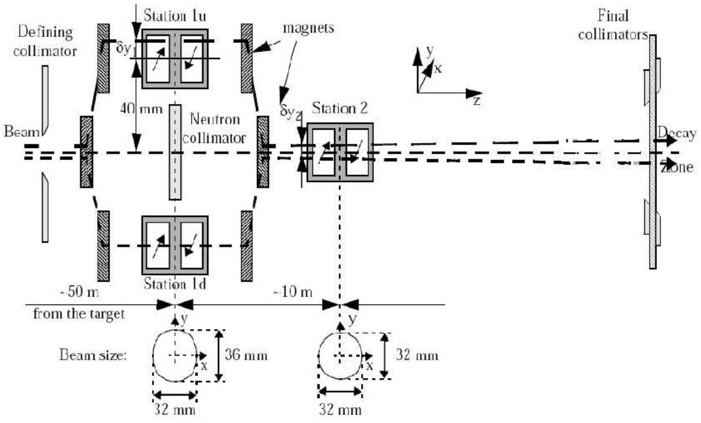

Figure 3.3: Layout of KABES detector

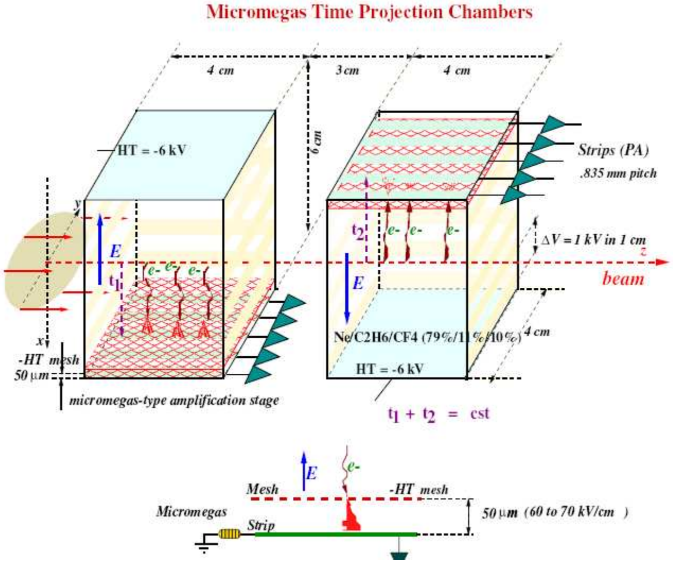

Figure 3.4: Schematic view of a detection station and MICROMEGAS chambers. Note that the x, y axes are rotated in this figure.

ionization electrons in the gas, which drift towards the amplification gap. Field cages provide a constant gradient of 0.83 kV/cm resulting in a uniform drift velocity of 8 cm/μs. Two of them are mounted in each station. They operate with opposite polarity and are separated by a distance of 2 cm. The longest drift distance in the conversion gap of the chambers is 6 cm which corresponds to the maximum drift time less than 1 μs.

The detectors installed in the beam have to withstand $\sim$ 20 MHz of charged hadrons concentrated in a few cm^2 and to meet these requirements, a Micromegas mesh with a 50 μm amplification gap has been chosen.

In the amplification gap each ionization electron creates an avalanche of electrons, which is collected by 48 read-out strips of $\sim$ 4 cm oriented along the beam axis, with $\sim$ 1 mm pitch.

The gas in the detector is a typical mixture with three components premixed in compressed bottles with Ne (79%) + C_2H_6 (11%) + CF_4 (10%) The sensitive gas in the TPC represents the largest contribution to multiple scattering

This configuration with only two longitudinal positions has to rely on the focusing properties of the beams to obtain the momentum of individual K^+ and K^- particles from the difference between the vertical coordinates recorded in stations 1u/1d and in station 2.

Measurement of coordinates in the bending (vertical) direction is given by the active strips. Within the station, the δy deviation of the particle direction from the central beam axis is determined by averaging the measured y_1 and y_2 positions in the first and second chambers of the station. The vertical positions allows one to calculate the $(p - p_0)$ deviation of a particle momentum p from the central momentum of the beam ($p_0 = 60$ GeV/c). This is achieved by correlating the station measurements with positional constraints from the measurement of the beams focusing points. In order to obtain the required 1% precision in the particle momentum, a position measurement resolution of 0.25 mm is necessary.

The arrival times of ionization electrons in first (t_1) and second (t_2) chambers allow to calculate the horizontal particle position x, and its arrival time.

Because there is no deflection in the horizontal plane (x, z), the particle impact points in the drift direction x in station 1 and 2 should be aligned. This fact is used in the kaon track reconstruction algorithm. A sub-nanosecond resolution is required for the time measurements to solve the ambiguities due to the very high intensity of the beams and to achieve a probability of wrong association to be less than few percent.

More details on the KABES detector are given in [36]

Front End and Read Out Electronics

Each strip of the MICROMEGAS chambers is connected to a front-end card containing a pre-amplifier and an amplifier stage followed by a shaper and a discriminator. A common programmable threshold voltage was supplied to the discriminator circuit on every channel front-end in order to get rid of the spurious signals due to electronic noise. The measurements of individual strip signals can be disabled if needed.

Time measurements of the strip signals must contain information about both leading and trailing edges of the signals. The former relates to the particle drift time and the latter to the time over threshold ToT. Fast time measurement capability of the digitizing devices, with very small dead time, is necessary to cope with the high fluxes, which induce chamber signal activity rates of up to several Mhit/s. This is important in order to perform precision measurements with the required low dead time. The detector pulses are digitized by 6 high performance TDC's. A fast first level trigger was used to perform initial selection. In this way only those time measurements which were preselected by a pipelined L1 trigger are stored in the buffer memories. The trigger matching functionality of TDCs is activated. For each L1 trigger, it selects time measurements of the corresponding 1 μs drift time interval, packs them into an event data record and makes the record ready for read-out. General purpose processors decrease further the event data bandwidth and volumes executing data compression and finer selection algorithms. The throughput of the KABES data, selected and compressed in such a way, does not exceed 4 Mbyte/s, which during the 5 s spill accumulates to an acceptable 20 Mbyte volume of storage information.

Reference [37] gives more information on KABES Read-Out System.

3.3.1 Performance

At the nominal proton intensity of 7×10^{11} ppp spatial resolutions of $\sim$ 100 μm have been achieved in the horizontal drift direction, and of $\sim$ 130 μm in the vertical direction using the strips. A time resolution of 0.65 ns has been measured.

The pion momenta from $K^{\pm} \to \pi^{\pm}\pi^{+}\pi^{-}$ decays are measured with the NA48 spectrometer. The resulting kaon momentum is compared to the K momentum measured by KABES. The convolution of the resolutions of the two spectrometers is found to be 1.1% . From this number, the momentum resolution of KABES alone is inferred to be 0.8%. The same 3π event sample is used to control the mistagging level introduced by a charge or momentum mismatch, which is measured to be less than 5%. The fraction of events found without track at nominal proton intensity is less than 1%.

3.4 Decay Volume

The fiducial decay region is contained in a vacuum tank of 1.9 m to 2.4 m diameter and 114 m long. The tank (called the blue tube) was enlarged by 24 m in the upstream direction for the NA48/2 experiment, allowing the acceptance for charged kaon decays to be increased by ~30 %. The pressure after evacuation is $< 10^{-4}$ mbar, avoiding that the kaon decay products interact with matter before being detected.

The tank is closed in the downstream region by a thin Kevlar window, separating the vacuum from the volume of the magnetic spectrometer, filled with helium at atmospheric pressure. The thickness of the window is of 0.9 mm, corresponding to $3\ 10^{-3}$ radiation lengths. Downstream the Kevlar window the beam continues in vacuum through a carbon fiber beam pipe of 152 mm diameter and 1.2 mm thick, that crosses all the central detectors in the middle. Figure 3.5 shows the NA48/2 decay region.

For the charged kaon system it is highly important to take into account the presence of all magnetic fields in the event reconstruction. Any non-reversing constant magnetic field coupled with a non-symmetric detector response would fake a charge asymmetry on the Dalitz plot distributions of K^+ and K^-. Also an asymmetry on the magnetic field seen by negative and positive charged particles would play a similar role. For this sake a campaign was made to precisely measure

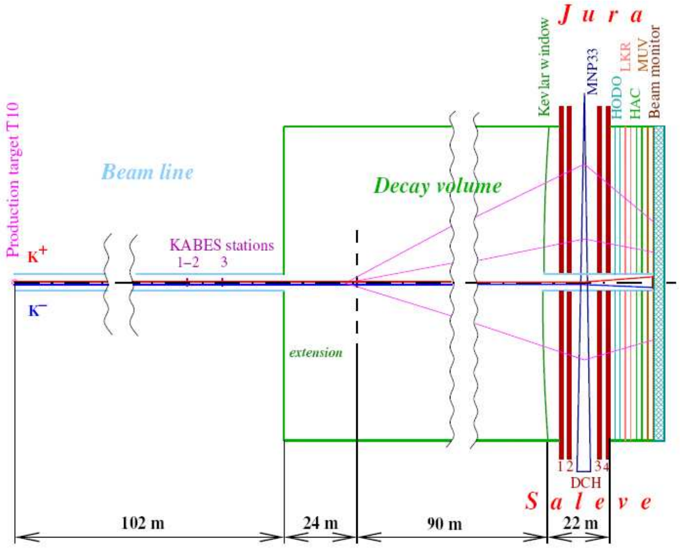

Figure 3.5: The NA48/2 decay region.

the remanent field on the main particle decay volume. The measured field was found to be not homogeneous in the decay volume, arriving to values of up to 200 μT. This non-uniformity could be due to magnetization of the tank itself prior to installation in the NA48 experiment. The measured maps are taken into account at the reconstruction stage and input in the simulation. Measurements of the field components along the blue tube are shown in figure 3.6. For a charged particle crossing the whole length of the vacuum tank on the central axis, the transverse coordinate deflection would be $\sim$ 1.5 mm.

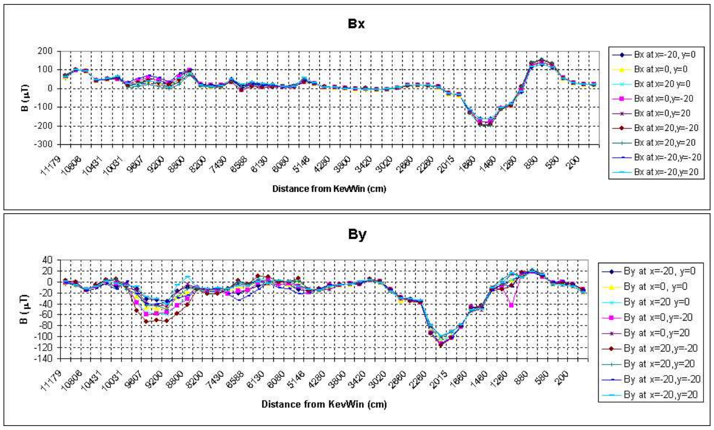

Figure 3.6: Components of residual magnetic field along the vacuum tank at different transverse positions.

In addition, a set of Hall probes was installed to monitor the magnetic field inside the spectrometer magnet.

3.5 The Anti Counters

The Anti Counters (AKLs) were designed to control three body backgrounds for the $Re(\epsilon'/\epsilon)$ measurement. A system of photon veto counter rings was constructed, containing 7 counters (pockets), six on the vacuum tank and two in the spectrometer volume. The AKL positions are shown in figure 3.7 The ring acceptance was complementary to the active detector for kaon decays originating from the middle of the former K_S^0 decay region during NA48 data taking.

Every ring is made of 2 scintillator layers preceded by an iron block 3.5 cm wide, in order to guarantee photon conversions. The light signal is readout at the two ends of the counters. The AKL pockets provide fast signals that can be included at the early trigger level. The time resolution was found to be $\approx 550\,ps$. The geometrical veto efficiency, taking into account the conversion probability, is around $\sim 95\%$

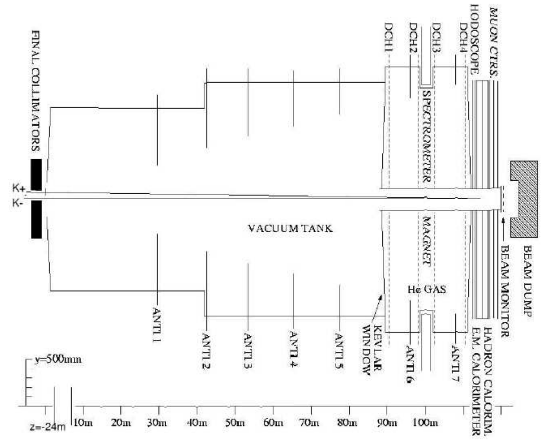

Figure 3.7: Decay region and AKL rings positions.

3.6 The Central Detector

The main components of the NA48 detector are a magnetic spectrometer, a charged hodoscope, a liquid Krypton electromagnetic calorimeter, a hadronic calorimeter and a muon detection system. A layout of the central detector is shown in Fig. 3.8.

3.6.1 The Spectrometer.

The magnetic spectrometer of the NA48 experiment consists of four drift chambers (DCHs). Two of them are located upstream of the magnet, and provide the measurement of the decay vertex position. The other two are used for the bending angle determination of the tracks and therefore for the momentum calculation. To reduce effects of multiple scattering, the entire spectrometer is contained in a large tank of stainless steel filled with helium at atmospheric pressure, so that the DCHs do not have to stand high pressure gradients. The radiation length of He at normal pressure and temperature is 5.3 Km.

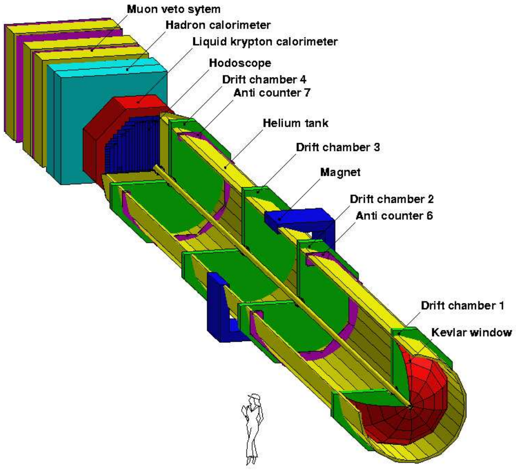

Figure 3.8: The NA48/2 detector

The total length of the spectrometer is about 22 m. A schematic view of the spectrometer layout is shown in figure 3.9.

The spatial resolution in NA48/2 was 150 μm and the momentum resolution could be parameterized as:

$$\frac{\sigma(p)}{p} \simeq (1.02 \oplus 0.044\,p\,)\% \tag{3.5}$$

where the particle momentum p is measured in GeV/c. The first term is related to the multiple scattering, while the second one is due to the accuracy of the space point measurement. The resolution on the kaon mass from $K^{\pm} \to \pi^{\pm}\pi^{+}\pi^{-}$ decays is about 1.7 MeV/c^2

The Magnet

The NA48 magnet consists of a rectangular iron frame with two poles and two pairs of bedstead coils. Its outer dimensions are 4.40 m × 4.00 m × 1.30 m and it has an aperture of 2.45×2.40 m^2, matching the electromagnetic calorimeter acceptance. The main field component is in the vertical y direction.

The magnet can be operated at different currents. Complete maps of one quadrant have been measured for currents of the "master" power supply equal to 1200 A. In addition, partial maps were measured for 1150 A and 500 A. For intermediate current values the field can be calculated by interpolation. The field map is

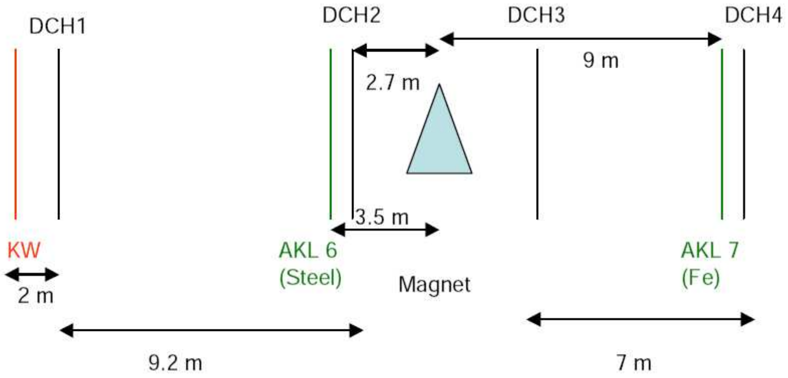

Figure 3.9: Layout of the NA48 spectrometer.

used in the reconstruction of tracks and as input on the Monte Carlo simulation. The actual value of the magnetic field was chosen to optimize the acceptance of the detector to the decays modes under study.

For the NA48/2 experiment the current was set to I=540A. For the proposed beam momentum of 60 GeV/c the integral of the magnetic field was limited to provide 120 MeV/c of momentum kick. The current polarity was reversed on daily basis during 2003 and every 30 10^6 collected triggers ($\sim$ 3 hours) during 2004.

The crossing of the helium tank and the magnet defines an active fiducial region of 2.37 m diameter. The field uniformity in this region is better than 10%, which allows an easy momentum calculation for the fast trigger.

More details on the spectrometer magnet can be found in [38].

The Drift Chambers

The four drift chambers have an octagonal shape with a transverse width of 2.9 m. Their fiducial area is about 4.5 m^2. The knowledge of the absolute transverse dimensions of each chamber to better than 10^{-4} is necessary to keep the systematical uncertainty on the energy scale of the experiment to that level. All chambers have a central hole of 160 mm diameter for the beam pipe, that requires careful construction and positioning of an ensemble of rings on which the central wires of the different planes are soldered.

Each chamber contains eight planes of 256 grounded sense wires. The planes are arranged in four views, each one oriented in a different direction orthogonal to the beam axis: 0^0(X-view),90^0 (Y-view), - 45^0 (U-view) and $+45^0$ (V-view).

Every view is made of two staggered sense planes distant by 12 mm along the beam axis, used to resolve left-right ambiguities. The electric field is produced by two field wire planes located on each side of the sense wire plane at a distance of 3 mm. The transverse spacing between two wires, both on the field and the sense wire planes, is 10 mm. The maximum transverse drift distance in a cell is 5 mm, corresponding to a drift time of 100 ns. This short drift time contributes to the high-rate capability of this detector. The scheme of one view is shown in figure 3.10

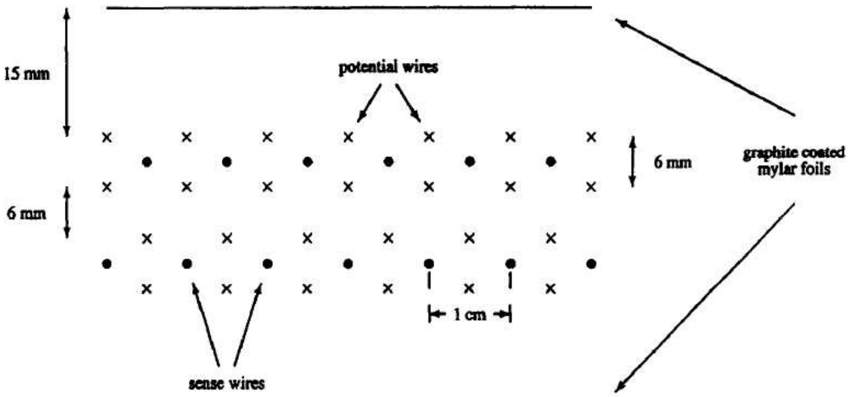

Figure 3.10: Drift cell geometry.

Each view is isolated from the next by two 22 μm thick graphite coated mylar foils placed at a $\pm$24 mm distance from the center plane of the view. The mylar foils are connected to high voltage and are used to reduce the electric field intensity on the field wires. The high voltage applied to the field wires and the mylar foils is respectively -2250V and -1405V.

Two 50 μm thick mylar windows separated by 2 cm along the beam direction are mounted on both ends of the chamber to hold an aluminum ring of 160 mm diameter which is used as a flange for the beam pipe.

The drift chambers are operated with a standard Argon (50%)-Ethane (50%) gas mixture with a small addition of water vapour ($\leq$1%) to slow down aging processes. The drift velocity is 50 μm/ns. The gas gain obtained with these operation conditions is about 6×10^4.

The space resolution obtained with these chambers is about 110 μm in each projection (X or Y) and is almost insensitive to the beam intensity.

The thickness of a chamber corresponds to 4.3×10^{-3} X_0 while the total contri-

bution from the helium gas contained in the tank is about 4×10^{-3} X_0.
Reference [39] gives more information on the drift chambers characteristics.

Front-End and Readout Electronics

Each sense wire is connected to ground via a preamplifier circuit. The front-end amplifiers and discriminators were placed directly on the chamber's frame. The discriminator output is shaped and the output pulses are then transported to central time-measuring circuits (TDCs).
For NA48/1 a new readout system was designed and built to comply with the rate of $\sim 10^{12}$ protons per SPS accelerator pulse expected for the high-intensity beam. This readout system allows for continuous sensitivity, i.e., concurrent data recording and readout during bursts. It sustains single wire rates up to 400 kHz and is able to accept up to 64 simultaneous hits per plane without dead time.
Signals are discriminated and then digitized by a 40 MHz TDC with a 25 ns/16 fine time. Finally, the digitized signals are stored in a 204.8 μs deep memory ring buffer (RB).
In order to obtain drift times, both the arrival time of the ionization cloud at the anode wire and the time of passage of the charged particle are measured with respect to a common clock. The arrival time of the charged particle is obtained from a scintillation counter hodoscope, described in the next section.
The NA48 trigger system will be explained in detail later on. However, some basic concepts must be given here in order to understand the principles of the DCHs read out. NA48/2 trigger is a multilevel system. The first level (L1) is a hardware, pipelined trigger synchronous to the general 40 MHz clock. The second level (L2) is a software asynchronous trigger, based on the response of fast processors. All the acquisition systems in all detectors are synchronized with a 40 MHz clock and all read out systems must contain a memory buffer more than 204.6 μs deep, in order to allow time for level 1 and level 2 decisions. The complete trigger system is controlled by the Trigger Supervisor (TS).
In the case of the DCHs, data can be extracted separately from this buffer for level 1 and 2 timestamps in a nondestructive manner. For L1 triggers the data are given to the L2 processors. For L2 the data are sent to the PC-farm. This extraction proceeds also in parallel for all planes.
The synchronous L1 triggers are queued and dispatched only when the L1 drift chamber readout is ready. An XOFF signal blocking the L1 trigger system is generated internally if the FIFO gets full or if it is collected from a downstream

system. The asynchronous L2 triggers are immediately dispatched without queuing them. An internal timeout checking the busy lines of the readout generates an XOFF blocking signal to the Trigger Supervisor.
During 2003 the readout sustained up to 150 kHz L1 trigger rate with a L2 rate up to 14 kHz. The efficiency was greater than 97 % for all chambers.
The fast rise time of the pulses and the response of the time-to-digital converter are such to allow a time resolution of 0.7 ns.
Particulars on the DCH's read-out system are given in [40, 41]

3.6.2 The Charged Hodoscope

An hodoscope (HOD) placed downstream the Helium Tank and in front of the LKr calorimeter, gave the timing for charged events with a resolution of 250 ps. It consisted of two planes, separated by 75 cm. Every plane contains 64 NE-110 scintillator counters, horizontally arranged in the first plane and vertically in the second. Each counter is 2 cm thick, corresponding to 0.05 X_0. The length varies from 60 cm to 121 cm and the width from 6.5 cm to 9.9 cm. The distance of the second plane with respect to the calorimeter was 80 cm, chosen in order to reduce the effect of possible back splash from the calorimeter front face. Four quadrants can be defined per plane, with 16 counters each.
This layout allows to define a set of fast logical signals from the discriminated pulses, that can be used by the trigger. In particular the logical signal Q1 is defined as a geometrically compatible coincidence in both planes in a single

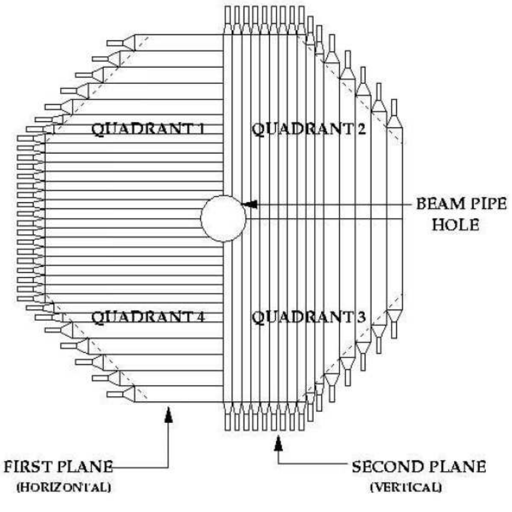

Figure 3.11: Charged Hodoscope layout.

hodoscope quadrant. The Q2 signal corresponds to a double coincidence of both planes in two quadrants.

3.6.3 The Electromagnetic Calorimeter

The NA48 experiment measured direct CP-violation in the $K^0\overline{K^0}$ system with very high accuracy. This imposed strong requirements on the design of the NA48 electromagnetic calorimeter. In particular, energy and spatial resolutions had to be good enough to obtain a high suppression factor on the background coming from CP-conserving $K^0_L \to \pi^0\pi^0\pi^0$ decays, which is about 200 times higher than the signal $K^0_L \to \pi^0\pi^0$.

The energy resolution was required to be of the order of $3\%/\sqrt{E}$ with a constant term smaller than 0.5%. This includes resolution induced by all the passive material upstream of the calorimeter, that amounts for about 0.85 radiation lengths. The space resolution should be better than 1 mm and two photons farther apart than about 4 cm should be distinguished. This advocated for an homogeneous calorimeter with high transverse segmentation.

In order to keep the constant term of the energy resolution under control, precise charge calibration was required, together with long-term stability. The pulse height response had to be calibrated and stable to better than one per mil. To be able to stand single rates of about 1 MHz, the time resolution should be better than 1 ns.

The choice was to build a quasi-homogeneous calorimeter, using liquid krypton (LKr) as active medium and with very thin read-out electrodes, in order to ensure the excellent energy resolution required. Table 3.1 shows some relevant properties of liquid krypton.

The slight radioactivity (^{85}Kr is a β^- emitter with 670 keV maximum energy and 10.74 years lifetime) has no noticeable effect on the noise in the detector.

Calorimeter structure.

The NA48 calorimeter has an octagonal shape, with the radius of the inscribed circle being 125 cm. It is 27 radiation length in depth, minimizing longitudinal leakage. It contains $\sim$ 10 m^3 of LKr. The beam of undecayed particles passes through the vacuum pipe in the center of the calorimeter.

The signal produced by the electromagnetic showers is read-out in a tower structure with 13212 cells. Each cell is formed by two drift gaps sharing the

Z	36
A	84
ρ (g/cm^3), density at 120 K	2.41
X_0 (cm), radiation length	4.7
R_M(cm), Molière radius	4.7
W (eV/pair), energy to create one ion-electron pair	20.5
λ_I (cm), nuclear interaction length	60
T_b (K), boiling point at 1 bar	119.8
T_m (K), melting point	116.0
v_d^e (mm/μs), electron drift velocity at 1 (5) kV/cm	2.7 (3.7)
E_c (MeV), critical energy	21.51

Table 3.1: Physical properties of liquid krypton.

collection electrode and read out by the same preamplifier. The two cathodes are 10 mm away from each side of the anode. The central anode is kept at a high voltage (HV) of 5 kV while the cathodes are grounded. For this value of the HV the drift gap of 10 mm corresponds to a drift time of about 2.8 μs. The cathodes are shared between horizontally adjacent cells. Vertically, the electrodes are aligned along planes set at the same voltage. The distance between electrodes in the vertical direction is 2 mm. The transverse size of each cell is 20×20 mm^2, to be compared to the LKr Molière radius of 4.7 cm. On average about 37% of the electromagnetic shower energy is deposited in just one cell.

The cells increase in transverse dimensions as a function of the distance from the front of the calorimeter up to a maximum of 1.1 % at its back.

The electrodes define a projective geometry of the calorimeter pointing at about 90 m in front of it, inside the decay region. This particular geometry has been realized in order to achieve the best possible accuracy in the measurement of the angle between the flight path of photons and the beam direction.

In order to keep the energy independent term in the resolution less than 0.5 % the precision of the drift gap must be ensured to be better than 100 μm.

To avoid non-uniformity problems, the read-out structure is based on ribbon electrodes stretched between two end plates. The electrodes are 1268 mm long, 18 mm wide, and 40 μm thick, and are made of copper-beryllium alloy.

The exact position of the electrodes is given with an accuracy of ± 45 μm, by five spacer plates of fiberglass reinforced epoxy, located at equal distances of 21 cm along the beam direction. These spacer-plates push the ribbons alternatively from right and left side, positioning them at angles of about ± 50 mrad from the

detector axis.
A general view of the calorimeter structure and a detailed view of the ribbons are shown in figure 3.12

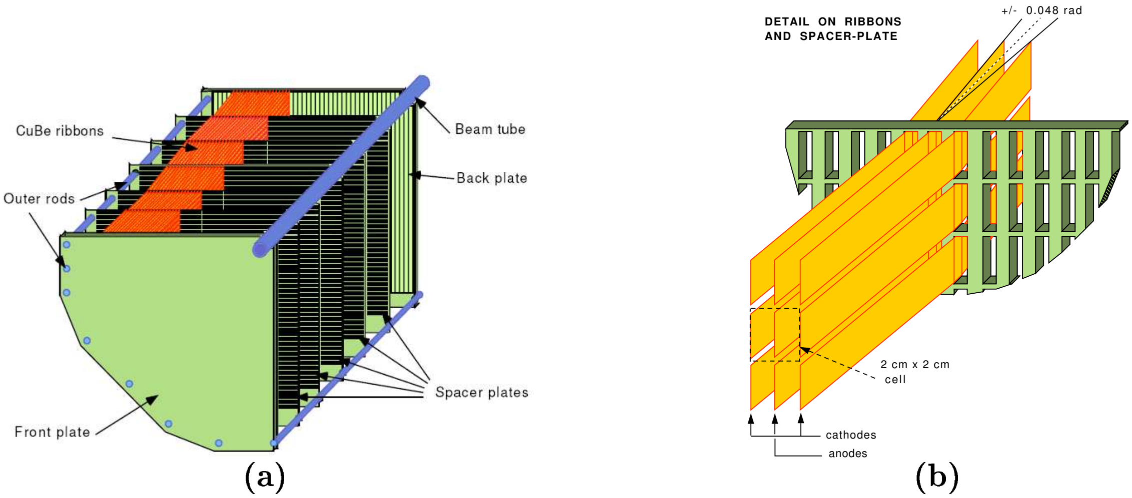

Figure 3.12: (a) Electrode structure of the LKr calorimeter. (b) Calorimeter ribbon and spacing plate detail.

In this way the cells follow a zig-zag instead of an straight path along the original line of particles. Due to the small Molière radius, electromagnetic showers in krypton are characterized by a narrowcore, which, if placed close to the anode, would generate a smaller signal for the shower. The zig-zag geometry reduces the depth inside the detector along which a shower core might be close to an electrode.

The end-plates are 50 mm thick and the spacer-plates 5 mm. Despite of the relatively short radiation length of the material, the thickness of the spacer-plates is small enough not to affect the performance of the detector.
The calorimeter is enclosed in a cryostat, composed by an outer aluminum vessel and a vacuum insulated inner stainless steel container, which keeps the temperature of the LKr calorimeter stable at 121 K to within± 0.1 K.
More details can be found in [42]

Front End electronics

The front-end electronics must stand a high rate of particles and provide good time resolution. Low capacitance detector cells of about 70 pF and the use of cold preamplifiers with very short connections result in a high speed read-out.

The initial current read-out technique is used, with a pulse shaping of 100 ns rise time and a total width of about 200 ns (the total drift time across the gap is 2.8 μs)
There was an undershoot with an amplitude of about 5 % of the peak signal.
The noise performance of the front end electronics is an important issue for high precision measurements. Therefore, low noise charge preamplifiers, optimized for operation at low temperature, are mounted directly on the electrodes.

The LKr read-out system

The signal readout consists of a differential receiver for analog signals, with a 14 bit dynamic range, followed by a fast shaper. The analog signals coming from the calorimeter cells are fed and digitized inside the Calorimeter Pipelined Digitizers (CPD) FASTBUS modules. Digitized signals are stored in a 3.2 μs deep pipeline memory for each cell.
In parallel with the digitizing process for every event the analog signal is sent as well to a non-linear Flash Analogic-Digital Converter (FADC), which is able to choose among 4 different gain ranges. Gain switching increases the effective range of signal digitization.
The triggers delivered by the trigger supervisor (TS) reach the Trigger Input Card (TIC) module, where on-line code handles and sends all the read-out operations to the rest of the system. At the request of the TIC program, the digitized data selected by the trigger are extracted from the CPDs' memories and sent to the Data Concentrator (DC) to be zero suppressed and then transfered to the Digital Read-out Input-Output (DRIO) modules. The DRIOs produce the binary data streams to be sent to the 8 PCs, containing the event information (event number, time-stamp, trigger word) and the channels read. The read-out scheme of the LKr calorimeter is shown in Fig. 3.13
The Data Concentrator (DC) performs the signal zero suppression and a cluster finding algorithm to cells above threshold. For every channel a threshold is set to the pedestal value of that channel plus a certain offset. Only information from cells with a signal greater than its threshold is stored and past through the RIOs to the online PCs. In this way it is possible to reduce to $\sim$ 100 the number of cells read out per shower. The zero suppression induces a non-linearity in the calorimeter response, that can be appropriately modeled and accounted for on the later stages of the analysis.

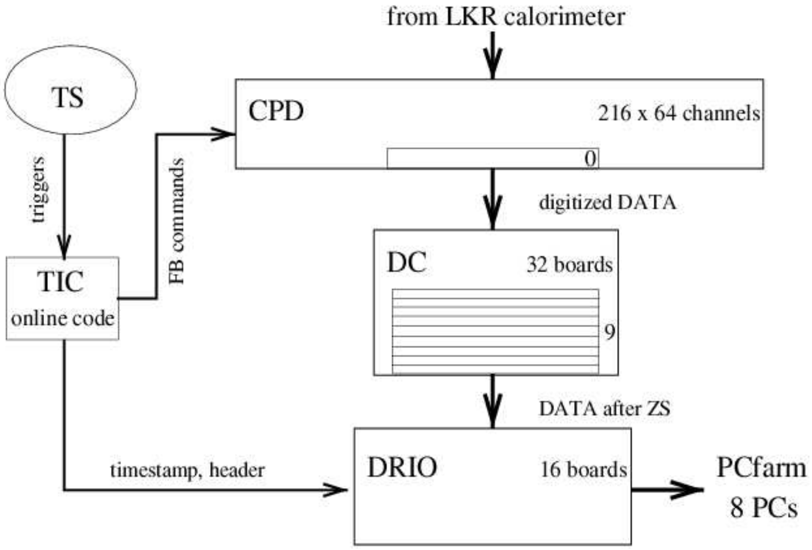

Figure 3.13: Read-out scheme of the LKr calorimeter.

In addition, the DC is the main bottleneck in the DAQ system. In 2002, the read-out technique was changed in order to collect two consecutive triggers before sending the data to the DC. Eight samples of 25 ns were extracted for every event, instead of 16 timeslots, which was the design value. In this the trigger rate could be almost doubled, because the DC receives half the requests. In this way 60000 triggers per burst could be collected, which is the limit of the other sub-detectors.

Calibration

In principle, the calibration of a LKr calorimeter is simple, since the gain stages (charge preamplifier and shaping amplifier) and the read-out electronics can be precisely calibrated by charge injection. Calibration pulses of initial current values determined by an input DC voltage are produced with a DMOS-FET switch and a RC circuit on the preamplifier motherboard. All the capacitances and resistances of the calibration system were measured at room temperature and at liquid nitrogen temperature. By interpolation, they are known at LKr temperature to better than 1% accuracy. The factor used to convert ADC counts to initial current in μA is determined using the calibration system. Pulse samples of different amplitudes give the ADC to current conversion factor under the range of interest.

Calibration triggers were recorded after the bursts, allowing an almost on-line detection and correction of possible jumps on cells response. In addition, a set of random triggers is taken during the burst. These triggers are not physical and are basically used to determine the cells pedestals. For every cell the averaged signal on all random triggers is taken as measurement of its pedestal, a value which already takes into account the effect of undershoot from previous events. Cell pedestals can also be estimated from the first time sample of any event selected by any physical trigger.

During the calibration process sets of so-called dead cells are identified. These are channels with electronic faults preventing their correct calibration and utilization. Their number is in the order of 60 (out of 13212) and the most common problems are faulty preampliers, no calibration, bad pedestal and/or a very unstable response to calibration pulses. Dead cells are included in a data-base so that their signals are masked during reconstruction. They are also taken into account in the Monte Carlo simulation.

Calorimeter performance.

Offline the signal is reconstructed from the sampled data and both, the time and amplitude of the signal are determined using digital filters. The filters assign a set of weights for each of the data samples, derived from the pulse itself. Separated sets of weights are used for the time and for the amplitude measurements. Each data sample is multiplied by the corresponding weight and the sum of the multiplications gives the final value.

$$E = \sum a_i \times s_i \tag{3.6}$$

$$T = \sum b_i \times s_i / E \tag{3.7}$$

where s_i are the three samples around the pulse maximum and a_i and b_i the corresponding coefficients of the digital filters. The filters must be properly calibrated, but once this is done they are very stable.

An electromagnetic shower typically covers a large number of cells. To optimize the relative error contribution from the sampling term (which can be reduced by reading out more cells) and the noise term (which increases with the number of cells), about 100 cells on a radius of about 11 cm are used to calculate the energy. Time and position are calculated only from the information of the most energetic central cells.

Uniformity and Energy resolution.

As already mentioned, the response uniformity and stability of the electronics is permanently checked by injecting calibration pulses into the calorimeter. Moreover, for the calibration of the calorimeter K_{e3} events are used ($K_L^0 \to e^{\pm}\pi^{\mp}\nu_e$ for NA48 and $K^{\pm} \to e^{\pm}\pi^0\nu_e$ for NA48/2). For these decays the electron momentum is measured with the magnetic spectrometer. For an ideal detector, it should equal the energy deposited in the calorimeter (i.e., one should get $E/p = 1$, when neglecting the energy loss of about 45 MeV before the calorimeter). By using these decays, energy variations both within individual cells and from cell to cell have been measured and corrected for.

If an electron enters the calorimeter very close to an anode, part of the deposited charge may drift during a time that is less than the integration time, thus reducing the signal. As the anodes are vertical, this gives rise to a horizontal response variation. The accordion geometry makes this effect small and easy to correct. Small vertical variations are due to the narrow vertical gap between the two anodes. After corrections residual response variations within a cell are not more than 0.1%

The cell-to-cell response uniformity can be checked by means of calibration pulses. As the charge injected for a given DAC value is also subject to a small error (1%), this intercalibration procedure is complemented by a calibration using K_{e3} events and cross-checked with photons from decays of π^0 and η particles produced during special runs by a proton beam impinging on a small, low-Z target. The long-term uniformity of this complex intercalibration procedure is better than 0.1%.

In 1997 the energy resolution of the calorimeter was also tested with an electron beam of 0.1 % momentum bite and adjustable central value.

The energy resolution is defined as the ratio of the width to the mean ($\frac{\sigma}{\mu}$) of a Gaussian fit to the measured current distribution summed in a shower box of 11 × 11 cells around the shower maximum. The 11 × 11 shower box response is corrected as a function of the impact point within the cell by an uniformity correction common to all the cells and slightly energy dependent. The result obtained from the analysis of K_{e3} events is:

$$\frac{\sigma(E)}{E} = \frac{3.2\%}{\sqrt{E}} \oplus \frac{9\%}{E} \oplus 0.42\%.$$

The noise contribution (about 40 MeV) is evaluated from the calibration data fluctuations. The constant term is smaller than 0.5% demonstrating that there are no major non-uniformity problems. A major contribution to the statistical term of the energy resolution is due to the shower lateral leakage outside the shower box, accounting for about $2.5\%/\sqrt{E}$. For 25 GeV photons the energy resolution is better than 1 %.

Position resolution.

The position resolution of the calorimeter has been measured by extrapolating electron tracks from the magnetic spectrometer. The space resolution was obtained by comparing the position of the center of gravity (COG) of the shower in the calorimeter with the electron impact point as reconstructed by the drift chambers. The COG is calculated using a 3×3 shower box and corrected for the non-linear dependence on the impact point within a cell. The space resolution as a function of the beam energy is parametrized as:

$$\sigma_x = \left(\frac{4.2}{\sqrt{E[GeV]}} \oplus 0.6\right) \text{ mm} \tag{3.8}$$

$$\sigma_y = \left(\frac{4.3}{\sqrt{E[GeV]}} \oplus 0.6\right) \text{ mm} \tag{3.9}$$

$$\tag{3.10}$$

For 25 GeV photons the position transverse resolution is better than 1 mm.

Time resolution

The timing resolution was measured using kaon decays with π^0s where the gammas converted or Dalitz decayed. The calorimeter time was compared with the time of the electron measured in a scintillator hodoscope situated in front of the calorimeter. The final time resolution is then determined applying the resulting weights in the offline filter to an independent data sample not used in the training procedure. The time resolution is also determined from the rising edge of the pulse using a parabola fit to determine the maximum amplitude. This method needs several corrections predicted by Monte Carlo, including the impact point dependence of the shower within the drift gap, the correlation of the phase with the sampling clock and the time slewing effect. Both analysis yield similar results. While the time resolution for a single photon is around 500 ps, it can be reduced to 250 ps for a kaon decay, by using the information from all photons.

Detailed information on the LKr calorimeter performance can be found in [43].

3.6.4 The Neutral Hodoscope

To improve the time measurement of the detected photons, scintillator fibers have been inserted vertically in the liquid krypton at a depth of 9.5 X^0, corresponding to the maximum of the longitudinal shower development for 25 GeV photons. The hodoscope is divided in four quadrants. The fibers have a diameter of 1 mm and are ganged in bundles of about 25, that are accurately positioned between ribbons. The scintillator fibers are instrumented with 32 Hamamatsu-1355 photo multipliers also located in the liquid krypton.

The time resolution achieved with these scintillator counters is better than 250 ps for shower energies greater than 15 GeV. The signal from the neutral hodoscope is also used as minimum bias trigger (called T0N), independent of the LKr calorimeter response and essential for the control of the neutral trigger efficiency.

3.6.5 The Hadronic Calorimeter

The hadronic shower leakage from the LKr calorimeter is measured by a hadronic calorimeter (HAC) consisting of scintillator slabs separated by iron blocks. It is divided longitudinally into two stacks and contains in total 49 layers of scintillator slabs oriented either horizontally or vertically. The active area of the calorimeter is 2.7×2.7 m^2. Each iron plane is 2.5 cm thick, resulting on a total length of 1.2 m or $\sim$ 7 interation lengths. The energy resolution obtained is:

$$\frac{\sigma(E)}{E} = \frac{65\%}{\sqrt{E[GeV]}}$$

3.6.6 The Muon Veto System

The Muon Veto System (MUV) is made of three layers of plastic NE-110 scintillation counters separated by 80 cm of iron. The first two planes have 1 cm thick scintillators oriented horizontally and vertically respectively. The time resolution is $\sim$ 700 ps, which is adequate to be used in the trigger logic. The third plane has thinner (6 mm) scintillators and less channels. It is mainly used to monitor the detection efficiency of the first two planes. The efficiency of the Muon Veto System is better than 99 % for muons above 5 GeV.

3.6.7 The Beam Position Monitor.

The beam position monitor has been designed and built in order to satisfy the need of a fast feedback of the beam steering and of an on-line check of the two beams position and geometry. The monitor is composed of two 8×8 matrices of plastic scintillator blocks. Each pixel is 6 mm × 6 mm in transverse dimension and 9 mm thick. The light from the scintillators is collected by two 8×8 multi-anode PMTs. The detector is able to measure displacement of the center of gravity of the beam at the level of 0.1 mm.

3.7 Trigger System

All the NA48 experiments were designed for high rates, in order to make precision measurements on the kaon system and study very rare kaon decays. The readout had to be completely pipelined and dead time free for two main reasons. First, very high statistics is required so, any sizable loss of events due to dead time must be avoided. Second, to prove with the required accuracy that losses and inefficiencies do not bias the results, they must be kept very small, as it is only possible when dead time is zero or negligible.

Dead time in the readout due to cable lengths and trigger processing time is avoided by using a continuous data recording and filtering system.

Individual sub-detectors store the local information for a limited time in buffers, while the trigger system looks at the data and decides whether to accept or reject events.

A readout command is issued from the trigger supervisor to all sub-detectors for each accepted event, causing them to readout from their local buffers. The Time Stamp (TSt), defined as the arrival time of the event as measured in the charged hodoscope with respect to the burst start, is used in the command in order to identify the event.

A common 40 MHz clock is distributed among all sub-detectors. Time is defined for all subsystems by a reference clock in units of 25 ns.

As already mentioned, the NA48 Trigger system is organized in two levels. The level one (L1) which is based on fast detector signals is completely synchronous with the experiment clock. After L1 selection the rate is reduced from the 1 MHz in the detectors to less than 170 kHz. The level two (L2) is partially asynchronous. It is based on software calculations done fastly by a processor using signals from the magnetic spectrometer. The L2 output has a rate of the order of 10 kHz. In addition there is also a so-called level three (L3). The L3 is not really part of the trigger system. It is a semi-on-line code that performs a software selection on the completely built events, deciding whether to keep them depending on the response of different software filters. During 2003 and 2004 the L3 rejection was not active.

When the level one trigger (L1) spots a candidate event at a given TSt, it prompts the acquisition system to send the data taken around that TSt to the level 2 trigger (L2C, level 2 charged). The L2C processes the candidate event and, if the required conditions are satisfied, produces a single Trigger Word (TW) containing the TSt and a trigger code that specifies the main characteristics of the event. This TW is transmitted to the Trigger Supervisor that, depending on the trigger pattern, decides to read out the corresponding data or to dump it.

The sum of the maximum time level 1 and level 2 trigger systems may need to take a decision is 204.6 μs. All sub-detectors must have a buffer big enough to store the data.

The trigger system is composed of a Neutral Chain, a Charged Chain and the Trigger Supervisor, that has to process, select and tag the events to be read out within the $\sim$200 μs data persistence time.

The neutral trigger is a 40 MHz dead time free pipeline which provides trigger information based on signals from the Liquid Krypton calorimeter. The full NT chain produces a trigger decision every 25 ns after a fixed delay of 3.2 μs from the event time.

The charged trigger chain is a mixed hardware and software real-time system, partly pipelined. The chain is composed by a fast first level trigger, followed by a computing engine (L2C).

The first level logic uses signals from the neutral trigger, the hodoscopes, the veto systems and the first drift chamber. This is done inside the fully pipelined Level 1 Trigger Supervisor (L1TS). This continuously receives these signals, performs a time alignment and produces a 3-bit identification code to be transferred to the L2C upon finding the conditions satisfied. A 30-bit timestamp is also attached, carrying the event time information.

The L2C is an asynchronous queued system, partly pipelined, with massive parallel processing capability. For each L1 trigger, it computes hit coordinates, space points, tracks, vertexes and invariant masses. The computing time, although guaranteed not to exceed a fixed upper limit of 100 μs varies on an event-by-event basis.

The logic layout of the trigger chain is shown in figure 3.14

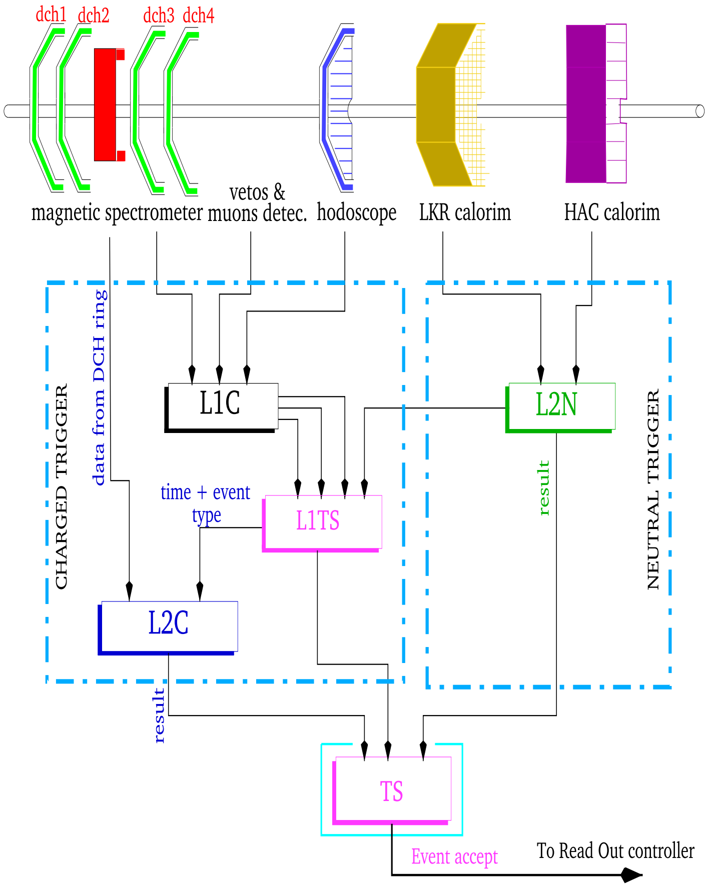

Figure 3.14: The trigger system chain.

3.7.1 The Neutral Trigger (NT)

The Neutral Trigger is extensively discussed in [44]

This system reconstructs the total energy, the Center Of Gravity (COG) and the number of peaks in the horizontal and vertical calorimeter projection on-line every 25 ns and performs a cut on these physical quantities. In order to calculate these quantities, the calorimeter single-cell information is reduced to two orthogonal views of projective calorimeter information.

The first step is to add the calorimeter signals from 16 (2 × 8) single cells with analogue-sum circuits to form super-cells. The information from a single calorimeter cell is used twice to get two orientations (x-view and y-view). This is done in the Calorimeter Pipeline Digitizer (CPD) system.

The digital super-cell signals are summed up into 64 vertical and 64 horizontal projections to gain coarser granularity (4 cm wide strips).

For all steps the digital information is stored in the PMB system and recorded with for every accepted event. This allows the online monitoring of the neutral trigger and an off-line comparison between the information of the calorimeter readout and the information in the neutral trigger.

The Peak Sum System (PSS) computes the energy sum (m0), the first and second moments of the energy (m1 and m2), and the number of peaks for each projection every 25 ns. The energy moments of order n with respect to the coordinate j=x,y are defined as:

$$m_{j,n} = \sum_{0<i\leq N_{cells}} j_i^n E_i \quad 0 \leq n \leq 2 \tag{3.11}$$

A peak is defined as a maximum in space and time which are above an adjustable threshold.

The Look-Up Table (LUT) system combines the results of the two views to reconstruct the relevant physical quantities and to take the final trigger decision. The LKr energy (E_{LKr}) is computed from three time-slices around the maximum in time, using a parabolic interpolation and averaging the energies from both views.

The center of gravity and the decay vertex are computed as:

$$COG = \sqrt{\frac{m_{1,x}^2 + m_{1,y}^2}{E_{LKR}}} \tag{3.12}$$

$$z_v = \frac{\sqrt{E_{LKR}(m_{2,x} + m_{2,y})(m_{1,x}^2 + m_{1,y}^2)}}{m_K} \tag{3.13}$$

If an accidental is identified, the number-of-peaks cut is not applied. Every 25 ns a trigger decision is passed on to the trigger supervisor (TS).

3.7.2 The Charged Trigger

The charged trigger consists of a chain of a fast first level trigger (L1C) and a second level trigger (L2C). The fully pipelined synchronous L1C trigger hardware uses simple criteria that require loose consistency between the neutral branch of the trigger, the hodoscopes, the veto detectors and the first drift chamber. It reduces the initial beam intensity rate to a ~ 100 kHz input rate to L2C trigger.

The L2C is based on partially pipelined hardware and a small processing farm. It uses all the hits produced in DCH1, DCH2 and DCH4 to compute the coordinates, tracks and kinetics of each event it receives. With this information it flags the event according to different criteria. This flag is sent to the Trigger Supervisor, that decides whether or not to issue the read out command to the detectors. A scheme of the charged trigger chain is shown in figure 3.15. The

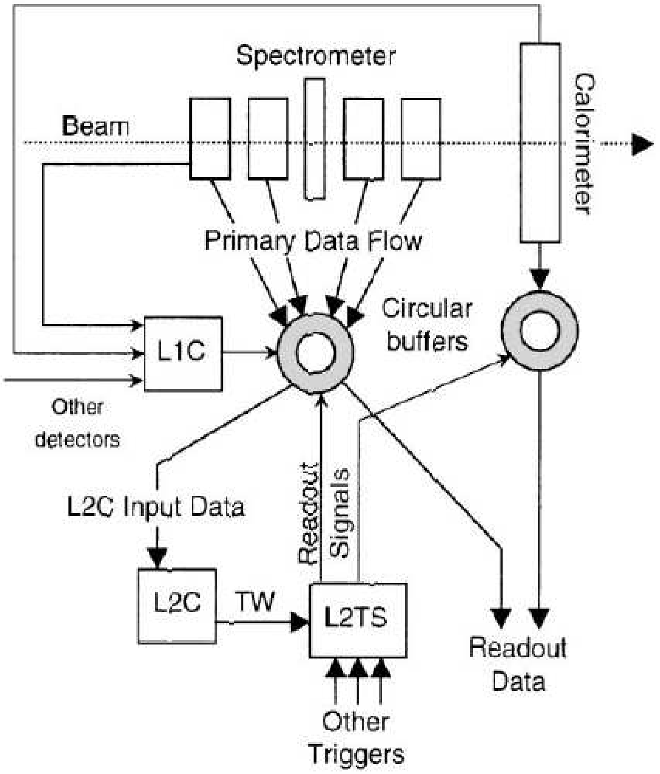

Figure 3.15: Block diagram of the Charged Trigger System.

computation time is variable depending on the event. For events with accidental hits, this time could be too long. An upper limit of 100 μs is imposed to allow readout of all sub-detectors in the remaining 100 μs of storage. If the processing of an event takes more than 100 μs, then the event is flagged as Not In Time and the system discards it.

In order to control the queuing levels, the L2C includes an XON/XOFF mechanism. When queues reach a critical level, the L2C asserts an L1OFF signal, turning off the L1C. Once the queues are absorbed by the system, the L2C releases the L1OFF, allowing the L1C to resume its activity. The dead time generated by this mechanism must not exceed 1%.

The L2C is sufficiently flexible to allow for algorithmic changes, but its performance depends on the selection of a suitable pretrigger.

Different algorithms have been implemented during 2003 and 2004 data taking in order to select the interesting decay channels. These will be explained in the next chapter.

The L2C associates x and y coordinates and produce the space-points of each DCH. In order to reconstruct a space point, at least 3 of the 4 coordinates must be consistent. A space point is reconstructed if one of the following conditions is satisfied within a tolerance of 1.5 mm: $(u = (x+y)/2$, $v = (y-x)/2$, $(y = u+v)/2)$

Given the list of space points, all combinations are checked to form tracks. A vertex is reconstructed if the closest distance of approach of two tracks is below 5 cm.

Then the reconstructed tracks are extrapolated to DCH4, spotting possible deflections by comparing the extrapolated spacepoints to DCH4 data. At this moment the associated invariant mass can be computed. Due to its capability of computing invariant masses, the processor farm is called Mass-BoX (MBX)

When all computations are finished, it sends the Trigger Word to the Trigger Supervisor.

The high beam intensities in the NA48/2 experiment placed heavy demands on the trigger system. In particular, the MBX performance is highly important for charged beams, and it could become a bottleneck under increased rate of events passing the L1 selection. Potential problems were overcome by an upgrade on the processor farm for the NA48/2 experiment, increasing the upper limit of input events from 120 kHz to 170 kHz. More details on the Charged Trigger system are given in [45].

3.7.3 The Trigger Supervisor (TS)

The NA48 Trigger Supervisor is a fully pipelined 40 MHz digital system which correlates and processes the information from the local trigger sources L2C, NT, L1TS. It provides the final trigger word, including a timestamp indicating the event real time, whenever a required condition is fulfilled, and it broadcasts it to all Read Out Controllers (ROCs) within the data persistence (~200 μs). The last stage is derandomized, in order to guarantee a minimum interval between two consecutive readout requests. The TS also performs trigger counting, downscaling and recording, dead-time control and trigger monitoring. The block diagram of the Trigger Supervisor is shown in figure 3.16

The input stage is structured as four identical sub-detector cards, each dedicated to a different trigger source (L1TS, L2C, NT and one used for mis-

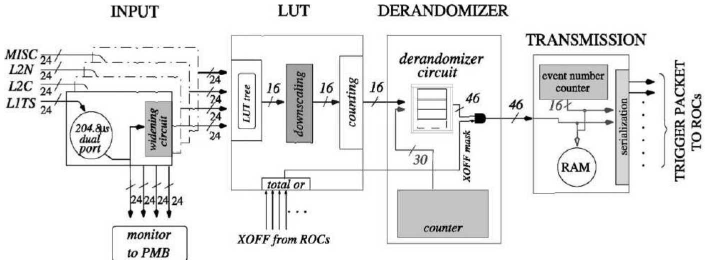

Figure 3.16: Block Diagram of the NA48 Trigger Supervisor.

cellaneous signals). Each source provides the TS with up to 24 bits of data, synchronized with the system clock, together with a strobe used for data validation, at a maximum rate of 40 MHz.

Asynchronous trigger sources, like L2C, provide their own time-stamp together with the data, while for synchronous ones (L1TS, NT) the timestamp is derived by 40 MHz counters located on the TS.

Data from each trigger source are continuously stored into fast RAMs, addressed by the 13 low-order bits of the timestamp. Simultaneously with the writing, the memories are read out sequentially via the second port after a fixed (programmable) delay of $\sim$ 100 μs. This delay is the maximum time budget given to the L2C for its computations.

A general problem arising in a sampled system, superimposing a fixed time binning on a continuous event flow, is the possibility that an event occurring close to a time slice boundary is assigned to different time bins by independent trigger systems. To overcome this potential source of inefficiency, the following scheme has been implemented. Whenever a coincidence between different conditions is required, the signal used as time reference is left unchanged while all the others are widened by two time slots, one preceding and the other following the actual position. In this way, signals displaced by one time slot in either direction are still effective in the trigger decision, allowing for greater efficiency.

For encoding the final 16-bit trigger word, any subset of the 96 input bits can be used by the decision logic. This is achieved by a routing and combining network, implemented in FPGAs and RAMs.

Each bit of the final trigger word can be individually downscaled using programmable synchronous downscalers implemented in FPGAs. The extensive use of downscaled trigger bits, with looser requirements, is mandatory in order to get accurate measurement of the various trigger efficiencies.

The 16 trigger bits are used to generate a validation bit, called the strobe. Every possible bit combination can be selected to generate the strobe. This scheme allows to temporarily disable any individual trigger type already produced by the decision logic.

Whenever the strobe signal is present, the trigger word and a locally generated 30-bit timestamp, are written into the output Trigger Queue Buffer (TQB). The purpose of the TQB is to buffer fast sequences of triggers and to allow for a fixed minimum time interval Δt between the broadcast of two consecutive triggers. The TQB has a FIFO-like structure, whose depth N is tuned according to the subdetectors memory depth (204.8 μs), the ROCs readout time Δt and the maximum L2C computation time (TL2C)

A trigger word is extracted from the queue whenever the minimum time interval from the previous dispatching has elapsed, if a XOFF condition (see below) is not active. A sequential, burst-based event number (16 bit) is attached to the data, and the information is passed to the transmission stage.

The resulting trigger packet consists of 64 bits, 16 bits for event number, another 16 bits for the trigger word and 30 bits plus 2 spare for the timestamp. The trigger packet is sent to 10 destinations simultaneously, over fast dedicated serial links.

A L1 splitter card was added for NA48/2 in order to logically decouple the MBX and the KABES L1 triggers, allowing to individually mask some of them from either system.

Even if the NA48 trigger system is basically dead time free, two basic dead-time sources still exist, the so-called XOFFs and FIFO full. A simple XON/XOFF protocol is used to pause trigger dispatching by the TS whenever a ROC is unable to cope with the read out request rate. Each ROC system asserts its XOFF line whenever the amount of data in its output buffers exceeds a predefined upper limit. The TS responds to XOFF by simply blocking the transmission stage, while trigger data are still being received, processed, stored and extracted from the TQB. When all XOFF signals become unasserted, trigger transmission is resumed with the triggers which happen to be stored inside the TQB at that time.

The second dead-time source in the system is due to the limited FIFO depth in the TQB. Trigger rate fluctuations may result in the TQB being filled up, so that a new valid trigger cannot be stored. Both, XOFF and FIFO full conditions are properly controlled and monitored by the Trigger Supervisor.

The Trigger Supervisor System is treated in [46].

3.8 The Pipeline Memory Boards

The deadtimeless readout of the charged particle hodoscope and other scintillation counters of the experiment was performed using a general purpose module, the Pipeline Memory Boards (PMBs), developed for the experiment. The basic module provides, for 8 channels of 24 bits, a continuous storage of the 40 MHz input in an 8 K circular buffer. An important application of the PMBs is its function as Pattern Units (PUs). The PUs store digital data produced by external trigger related sources and all decisions taken by the trigger supervisor at all steps. Analysis of PUs data allows the offline reconstruction of the trigger logic results from the stored input signals.

3.9 Data Acquisition and Format

The NA48 online DAQ system was able to process 400 MB/burst assuming a spill length of 2.5 s and a SPS duty cycle of 14.4 s. For the NA48/1 high intensity K_S^0 run the data acquisition system needed to be upgraded. The change on the SPS cycle in 2001 increased the data volume by a factor of 2.5. In addition, the trigger rate was increased. The upgrade of the PC farm allowed doubling the data throughput.

In Fig 3.17 the network setup of the on-line PC-farm is shown. Data coming from the read-out systems arrive into the 11 Sub-detector PCs (SPC). They are then distributed to eight Event Building PCs (EBPC) via a switching network. Inside the EBPCs the data is processed, the event fragments from the various subdetectors are merged into complete events (event building) and consistency checks are performed. This raw data is then forwarded to the Central Data Recorder (CDR) via a Giga-switch connection.

In the CDR, the raw data coming from the PC farm are stored on 10 disk servers of 1 TB average capacity installed in the IT division of CERN. At full efficiency $\sim$ 3 TB of data are produced per day. From the raw data, the third level software trigger (L3) produced several compact output streams corresponding to different event types. The L3 runs on the CERN batch system. In the computer center the burst fragment files were combined into burst files. The action of the program consisted of reading these raw burst data files, calling a set of decoding and reconstruction routines, performing a series of cuts and splitting or copying events to different output streams. The real time reconstruction uses the standard offline routines with the best known calibration constants at that time.

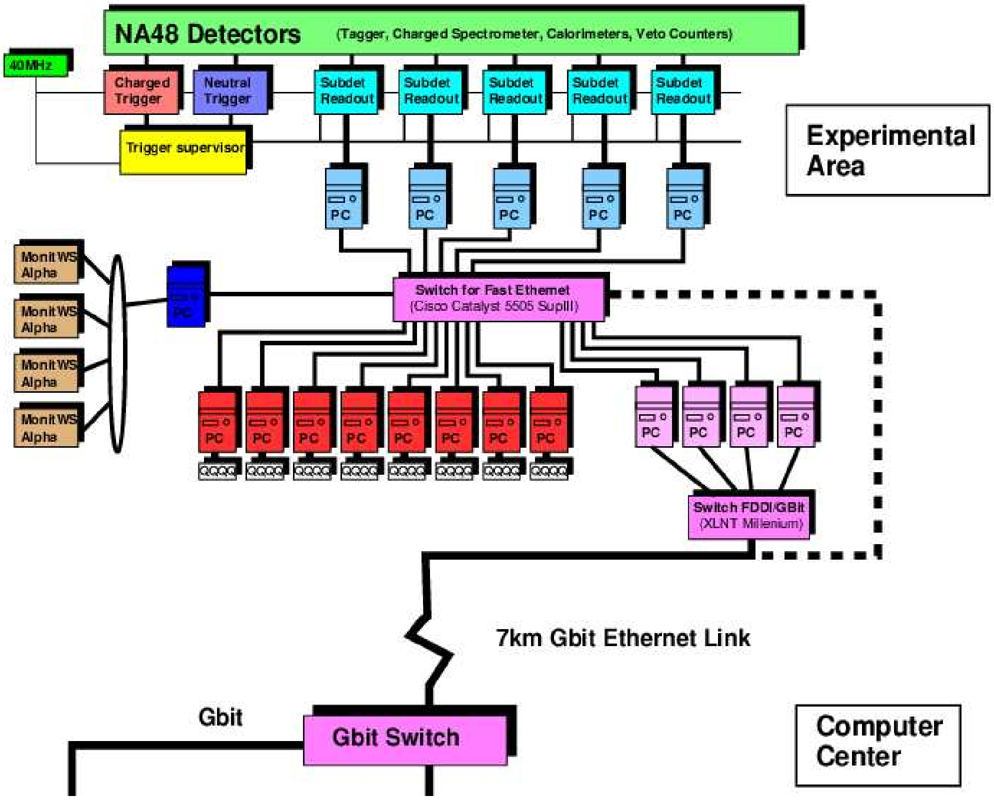

Figure 3.17: PC farm scheme.

Eventually, raw burst files and the results of the reconstruction (COMPACT files) were written to tape. The typical size of one burst of raw data is $\sim$ 500 MB, while a typical Compact file is $\sim$ 120 MB. Reprocessing of Compact files is redone offline later on, once the best set of calibration constants is defined for the relevant detectors on every data taking period. In addition further filtering is done a posteriori.

Chapter 4

Data Taking and Trigger Logics

4.1 Data Taking in 2003 and 2004

NA48/2 collected data in two runs, from June 12 to September 8 in 2003, and from May 15 to August 8 in 2004.

In order to minimize systematic uncertainties for the asymmetry measurements, the magnetic fields in the spectrometer and beam line magnets were alternated regularly. The spectrometer magnet current was reversed on daily basis during 2003 and every ∼ 3-4 hours in 2004. All the beam line magnets were cycled and inverted once per week during the machine development pauses. A complete set of data, with all possible combinations of spectrometer and beam line magnet current signs, was accumulated over a two-week period. This was called a supersample.

During 2003 three straight muon runs, with the spectrometer magnet demagnetized, were taken to monitor the alignment of the spectrometer. From the analysis of $K^{\pm} \rightarrow \pi^{\pm}\pi^{+}\pi^{-}$ events a significant slow drift was detected in the DCH alignment in a period were no muon data was available. Due to this, muon runs were taken more frequently (around twice per month) during 2004. The spectrometer alignment was then found to be stable to ± 20 μm.

The DCHs misalignment could be corrected offline using $K^{\pm} \rightarrow \pi^{\pm}\pi^{+}\pi^{-}$ events. This will be explained in detail in chapter 5.

Of the total of 80 days available in 2003, about 30 were spent in tuning the beam and the upgraded parts of the detector, or lost because of absence of beam, cooling problems and effects of power cuts. In the remaining ∼ 50 days, from August 6 to September 7 data of two complete supersamples (SS1 and SS2) and a smaller one (SS3) were collected in stable conditions. This is the data sample (SS123) analyzed in this thesis.

The data in 2004 were taken in two periods separated by two special runs: one at 25 ns and a scrubbing run, which are not useful for data taking. During the first period trigger and readout conditions were kept as in 2003. During the second period, the read out of the calorimeters was modified to discard calorimeter data for a fraction of the $K^{\pm} \to \pi^{\pm}\pi^{+}\pi^{-}$ and K_{e4} events. The quality of the $K^{\pm} \to \pi^{\pm}\pi^{+}\pi^{-}$ analysis was not affected by this change, but in turn allowed a big gain in bandwidth. This allowed to collect more control triggers and enhance the L1 selection, as it will be explained in detail in the next section. Five super-samples (SS4 to SS8) of different duration were recorded in 2004.
Table 4.1 shows statistics and data volumes for the NA48/2 data taking periods.

	2003	2004
Total number of triggers	$7\ 10^{9}$	$11\ 10^{9}$
Number of bursts	$2.2\ 10^{5}$	$3\ 10^{5}$
Raw Data total size	80 TB	120 TB
Compact Data total size	20 TB	25 TB

Table 4.1: Statistics and data volumes at different stages.

4.2 Trigger Configurations in 2003 and 2004 runs

The NA48 trigger system could be used with almost no modifications to perform efficient selection, with significant background rejection, for candidate events for the NA48/2 experiment.
For the *charged decays* ($K^{\pm} \to \pi^{\pm}\pi^{+}\pi^{-}$, K_{e4}) the charged chain of the trigger logic required, at the first level (L1) a coincidence of hits in different quadrants of the hodoscope (Q2 signal as defined in chapter 3) and the absence of signals in the anti counters (called $\overline{\text{AKL}}$ or !AKL).
At the second level (L2) at least two compatible vertexes in the fiducial decay region had to be identified by the massbox.
The decays with predominantly neutral particles or gammas in the final state ($K^{\pm} \to \pi^{\pm}\pi^{0}\pi^{0}$, $K^{\pm} \to \pi^{\pm}\pi^{0}\gamma$) were initially selected (at L1) by the neutral branch of the trigger requiring more than two peaks in at least one projection of the electro-magnetic calorimeter (loose NT-PEAK signal).

The massbox algorithm (at L2) for this type of events computed a sort of missing mass, using as input the spectrometer information on the charged track and assuming the parent kaon with energy of 60 GeV and traveling along the beam axis. Events were selected if the computed mass was far from the $K^{\pm} \to \pi^{\pm}\pi^{0}$ peak, efficiently collecting $K^{\pm} \to \pi^{\pm}\pi^{0}\pi^{0}$ and $K^{\pm} \to \pi^{\pm}\pi^{0}\gamma$ decays and suppressing the $K^{\pm} \to \pi^{\pm}\pi^{0}$ background.

In 2003 about 50000 events were collected per burst.

In the second period of 2004 a 20% larger effective bandwidth was obtained by reading out the calorimeter information only for a fraction of 70 % of the three tracks events. This allowed for some additional 10000 events per burst, giving a total of 60000 events per burst. Additional triggers were used:

At L1:

- To enhance the pre-trigger for one-track events, allowing a gain in efficiency.

At L2:

- To provide a control trigger for one track events based only on LKr calorimeter information. This trigger did not need to be downscaled, so it could be used for the precise measurement of the main one-track trigger efficiency.
- To provide a dedicated trigger for $K^{\pm} \to \pi^{\pm}\nu\overline{\nu}$ studies.
- To allow a dedicated trigger for events with no tracks detected in the spectrometer, useful for collecting $K^{\pm} \to \pi^{\pm}\pi^{0}\pi^{0}$ events where the $\pi^{\pm}$ was out of acceptance.
- To provide control triggers for various other channels.

4.2.1 First level (L1) logic and configurations

During the beginning of 2003 data taking, different trigger conditions were tested. A stable L1 configuration was implemented from July 10 (beginning of SS0) and kept to the end of the run.

A summary of relevant signals that can be used at L1 is shown in table 4.2

In table 4.3 L1 strobe signals for this configuration are shown. Events satisfying one of the strobe conditions were passed to the massbox for computation.

The first bit (Bit 0) was intended for pre-selection of predominantly neutral decays, such as $K^{\pm} \to \pi^{\pm}\pi^{0}\pi^{0}$ and $K^{\pm} \to \pi^{\pm}\pi^{0}\gamma$. It is given by the logical OR of three conditions, the first two being the more important for the $K^{\pm} \to \pi^{\pm}\pi^{0}\gamma$ signal (see chapter 6). The signal NUT(npeaksloose) is also called loose NTPK or NT-PEAK, and is given by the logic condition of (n_x >2 OR n_y >2), were n_x, n_y are the number of peaks found by the neutral trigger system in the X, Y projections respectively. The NUT(LKrmbias) signal requires an energy deposit seen by the neutral trigger in the LKr calorimeter greater than 10 GeV (E_{LKr} > 10 GeV) This signal is useful to define a minimum bias sample to check the NT-PEAK collection efficiency. The NUT(KMU3-PRE) was intended for the preselection of $K^{\pm} \to \mu^{\pm}\pi^{0}\nu_{\mu}$ events and it is not relevant for $K^{\pm} \to \pi^{\pm}\pi^{0}\gamma$ analysis.

The second bit (Bit 1) was primarily intended for the pre-selection of leptonic decays, $K^{\pm} \to \mu^{\pm}\nu_{\mu}$ and $K^{\pm} \to e^{\pm}\nu_{\mu}$.

The third bit (Bit 2) made the pre-selection of three track events, mainly through the Q2!AKL signal. This signal has the disadvantage that the hodoscope Q2 is slightly inefficient, as it requires the coincidence of two planes. The advantage is that it makes it possible to collect also the events in which one of the charged pions is outside the detector acceptance. The inefficiency of $Q2\overline{AKL}$ is dominated by random veto in the $\overline{AKL}$ condition.

The (Q1+Q2) signal gives the fine time to all strobe bits, providing accurate time information.

Part of the less selective triggers are downscaled in order not to saturate the massbox with uninteresting events. These signals are in any case needed in order to increase the collection efficiency and to have a set of minimum bias events for trigger efficiency calculations. The initial default configuration was D1=10, D2=100, D3=100, D4=100.

During 2003 an unexpected failure of part of the neutral trigger chain led to the loss of a few days of 1-track triggers. During this period control and rare decay triggers were increased to saturate the bandwidth. The existence of so-called bad NT-PEAK periods is not limited to these few days, and a correct treatment of these data is of vital importance for the $K^{\pm} \to \pi^{\pm}\pi^{0}\gamma$ analysis. This will be explained in detail in chapter 6.

At the beginning of 2004, the trigger conditions were kept basically equal to 2003. The only difference at L1 was the removal of pre-selection of leptonic and semileptonic decays to be sent to the massbox. The most important trigger change during 2004 ocurred from SS6 on. Taking advantage of the bigger bandwidth available, and after some trigger tests performed at the end of June 2004, a new signal (NT-NOPEAK) was inserted in OR on the first strobe bit 0. The corresponding change was also made at L2 as explained in next section. The new trigger configuration was inserted from July 7. New strobe bits to MBX are shown in table 4.4

The NT-NOPEAK condition consisted on a coincidence of three signals calculated in the neutral trigger.

$$\mathrm{NUT(nopeak)} = NUT(COG_{LKr} < 30cm\ Zvn < 95m\ E_{LKr} > 15GeV) \quad (4.1)$$

The first signal (COG$_{LKr}$ $<$ 30 cm) requires that the energy deposited in the LKr is compatible with a non two-body kaon decay along the z-axis. The second signal (Zvn $<$ 95 m) requires that the vertex reconstructed with the neutral variables is within the experimental decay volume. The exact definition of the COG variable and of the neutral vertex computation will be given in chapter 5. The third signal (E$_{LKR}$ $>$ 15 GeV) requires that the total energy deposited in the electromagnetic calorimeter is greater than 15 GeV.

The addition of NT-NOPEAK at bit 0 supposed an increase in the rate of events to be received as input by the MBX of $\sim$ 40 k events/burst, out of a total input of $\sim$ 450 k events/burst.

In addition, at bit 1 a signal for study of $K^{\pm} \to \pi^{\pm}\nu\overline{\nu}$ decay was added, requiring only one hit in the charged hodoscope (Q1) and activity in the DCHs compatible with one track only.

4.2.2 Second level (L2) logic and configurations

The L2 trigger configuration for 2003 is shown in figure 4.2.2.

At L2 we can distinguish between trigger bits coming from the massbox response (trigger name starting with MB) and triggers coming directly from the detectors response. In general, massbox triggers were of great importance for the NA48/2 experiment, as the main L2 triggers for event selection were given by some type of massbox response. The MBX block diagram scheme is shown in figure 4.2.2.

The basic algorithm for the selection of events with more than one charged track was to look for two compatible vertexes in the fiducial region. This was called MB-2VTX and was the first trigger bit (0 or 0x0001) in the L2 configuration. This is rather insensitive to the imperfections of the spectrometer and the use of raw uncalibrated data from drift chambers.

A second algorithm was operating in cascade with this one. It looked for a single vertex with a reconstructed two-pion invariant mass compatible with the kinematic limit for 3π events. It was called MB-1VTX and was the second L2 trigger bit (1 or 0x0002). This combination of triggers had an overall inefficiency for $K^\pm \to \pi^\pm\pi^+\pi^-$ of ~ 1 %. Events were selected also at L2 satisfying the same conditions as the charged L1 pre-trigger. This trigger was called C-PRE (from charged-pretrigger) and was heavily downscaled (by a factor of 100) in order not to saturate the bandwidth. The C-PRE trigger was useful as control trigger for the efficiency determination of other charged (MBX) triggers. This was the fourth trigger bit (3 or 0x0008)

The selection of neutral decays was based on the computation of an effective missing mass. This was called MB-1TRK-P or MFAKE trigger, and was the fifth L2 bit (4 or 0x0010) The massbox algorithm needed to allow for a highly efficient selection of $K^\pm \to \pi^\pm\pi^0\pi^0$ events, rejecting the dominant $K^\pm \to \pi^\pm\pi^0$ background. By assuming the flight direction of the kaon along the beam axis and its energy to be 60 GeV, an effective missing mass cut rejecting 2-body decays with a π^0 can be implemented. The MFAKE variable, is given by:

$$\begin{aligned} \mathrm{MFAKE}^2 &= m_K^2 - m_\pi^2 - MM^2 && (4.2)\\ &= 2(< E_K > E_\pi - < p_{zk} > p_{z\pi}) && (4.3)\\ &= 2E_\pi^* m_K && (4.4) \end{aligned}$$

The first equation shows the MFAKE definition, where m_K is the nominal kaon mass, m_π is the nominal π mass and MM^2 is the square of the missing mass, corresponding to the π^0 mass for the $K^\pm \to \pi^\pm\pi^0$ decay hypothesis. The second equation shows how MFAKE can be calculated from the charged track and kaon parameters. Here $<\mathrm{E}_K>= 60$ GeV/c^2 represents the average kaon energy, E_π is the pion energy, that can be calculated from the spectrometer information, $<\mathrm{p}_{zK}>= 60$ GeV/c represents the kaon momentum along the z axis, and $\mathrm{p}_{z\pi}$ the charged π momentum along the z direction, as computed as well from DCHs data. The last equation shows the relation between the MFAKE variable and the energy of the pion in the center of mass (CM) system E_π^*. This relation shows easily how the MFAKE cut corresponds to a cut on the pion kinetic energy in the CM of $T_\pi^* < 90$ MeV.

The actual correspondence between MFAKE, T_π^* and p_π^* given by the following equations:

$$\begin{aligned} T_\pi^* &= E_\pi^* - m_\pi && (4.5)\\ p_\pi^* &= \sqrt{E_\pi^{*2} - m_\pi^2} && (4.6)\\ \mathrm{MFAKE}^2 &= 2E_\pi^* m_K && (4.7) \end{aligned}$$

(4.8)

In table 4.5 the equivalence between MFAKE, p^*_π and T^*_π variables is given for different relevant values of one of them.

The actual algorithm implemented on the on-line processors is the following: First, a fake track, aligned with the beam axis, and with exactly 60 GeV/c momentum, is introduced in the massbox. A vertex is found if the closest distance of approach between tracks is within 5 cm. If there is one vertex computed between the accepted z range, built from a real and the fake track, the ZFAKE massbox bit is set and allows the computation to continue. For each space-point combination in DCH4 the MFAKE variable is computed on-line in the massbox assuming a $K^\pm \to \pi^\pm\pi^0$ decay, using equation 4.9

$$\mathrm{MFAKE}^2 = \frac{1}{|\Delta x_F \Delta x_T|}[P^2_{Kick}(z_{DCH4}-z_{MAG})^2\theta^2+M^2_\pi|\Delta x_T|^2+M^2_K|\Delta x_F|^2] \quad (4.9)$$

where θ is the opening angle, Δx_F is the magnet to DCH4 displacement of the real track and Δx_F is the (constant) displacement for the fake track:

$$\Delta x_F = \frac{P_{Kick}}{60GeV/c}(z_{DCH4} - z_{MAG}) \quad (4.10)$$

The MFAKE resolution for $K^\pm \to \pi^\pm\pi^0$ events was $\sim$ 7.5 MeV on-line (as seen by the MBX) and $\sim$ 4 MeV offline.

The trigger cut was set to MFAKE $<$ 475 MeV/c^2 during 2003. This was very efficient for $K^\pm \to \pi^\pm\pi^0\pi^0$ as these events have a maximum at $\sim$ 438 MeV, far away from the massbox MFAKE cut. However, due to resolution effects, the L2 MFAKE trigger is bound to be inefficient for events with $T^*_\pi \sim 90$ MeV, affecting in particular the $K^\pm \to \pi^\pm\pi^0\gamma$ decay. To get rid of this edge effect in $K^\pm \to \pi^\pm\pi^0\gamma$ analysis the cut was tightened on the offline selection to $T^*_\pi < 80$ MeV, as will be explained in 5.

The MFAKE cut was changed to 480 MeV/c^2 from 2004, inducing $\sim$ 5 % more event rate.

The 2003 L2 configuration included other triggers of interest for the $K^\pm \to \pi^\pm\pi^0\gamma$ analysis: NT-NOPEAK, T0N and NT-PEAK. Signals starting with NT come from response of Neutral Trigger system.

The NT-NOPEAK trigger was the bit 8 (0X0100) and consisted of exactly the same condition described above for NUT(nopeak). This was downscaled by a factor of 80. The N-MBIAS or T0N trigger was the L2 bit 9 (0X0200) and is based on signals from the neutral hodoscope as described in chapter 3. Its downscaling factor was 200. The NT-PEAK trigger repeated the conditions sent to the massbox at L1 by the NUT(npeaksloose) signal and it was downscaled by 50. This was trigger bit 10 (0x0400). All these triggers were intended for efficiency determination, as will be explained in detail in chapter 6.

A summary of L2 trigger bits useful for $K^{\pm} \rightarrow \pi^{\pm}\pi^{0}\gamma$ analysis of 2003 data is given in table 4.6

During 2004 the L2 configuration was modified. The most relevant change was the insertion in L2 bit 10 of the NT-NOPEAK signal in logical OR with NT-PEAK. In this way this bit contained exactly the same information as the one sent to the massbox at L1, as needed in order to evaluate the efficiency of the imposed condition. In addition the signal used at L1 for preselection of $K^{\pm} \rightarrow \pi^{\pm}\nu\overline{\nu}$, was also sent as L2 ouput after application of a heavy downscaling factor.

Standard trigger rates for 2003 and 2004 runs are shown in table 4.7.

Name	Meaning
Q1	Coincidence in the two views of one quadrant in charged hodoscope .
Q2	Double coincidence in two quadrants in charged hodoscope.
AKL	Requires a time coincidence between the two layers of at least one AKL pocket. Signals from pocket 1 and pocket 7 are not used in the trigger logic.
1μ	One hit in muon veto system.
NUT(npeaksloose)	At least two clusters seen by neutral trigger system on x or y projections ($n_x > 2$ or $ny > 2$)
NUT(LKrmbias)	Energy deposited in the LKr greater than 10 GeV.
NUT(KMU3-PRE)	Energy deposited in the LKr greater than 15 GeV.
NUT(KMU2-PRE)	Energy deposited in the LKr less than 10 GeV.
NUT(KE2-PRE)	Logical AND of three conditions: Energy deposited in the LKr greater than 15 GeV and energy deposited in the hadron calorimeter smaller than 10 GeV and a condition on the energy distribution compatible to one cluster only.

Table 4.2: Summary of some signals available at L1. First four (Q1, Q2, AKL, 1μ) come directly from the detectors. Signals starting with NUT come from neutral trigger response.

Bit 0	[(NUT(npeaksloose) + Q1/D1*NUT(LKrmbias))+ (Q1 * !Q2 * 1u * !AKL/D4)*NUT(KMU3-PRE)] (Q1 + Q2)
Bit 1	[(Q1* ! Q2 * !1u * !AKL/D3)*NUT(KE2-PRE)+ (Q1 * ! Q2 * 1u *!AKL/D4)*NUT(KMU2-PRE) + Q1/D2] (Q1 + Q2)
Bit 2	[Q2 * !AKL + Q1/D2] (Q1+Q2)

Table 4.3: L1 configuration from July 10th 2003. The downscaling values were D1=10, D2=100, D3=100, D4=100.

Bit 0	[(NUT(npeaksloose) + Q1/D1*NUT(LKrmbias))+ NUT(nopeak)](Q1 + Q2)
Bit 1	[Q1/D2 + PRE-PNNB/D3](Q1 + Q2)
Bit 2	[Q2 * !AKL + Q1/D2] (Q1+Q2)

Table 4.4: Main L1 configuration used in 2004. NT-NOPEAK signal is added to strobe bit 0. A pretrigger for $K^{\pm} \rightarrow \pi^{\pm}\nu\overline{\nu}$ events is added to strobe bit 1. Downscaling values were D1=10, D2=100, D3=8.

Default trigger word (after June 25th, 2003)

Code	Name	Trigger	D
0x0001	MB-2VTX	2-vertex	1
0x0002	MB-1VTX	1-vertex with mass cut	1
0x0004	MB-WDOG	MB(NOT IN TIME) $\cdot L1 \cdot L1_{on}$	1
0x0008	C-PRE	$Q2 \cdot \overline{AKL} + Q1/100$	100
0x0010	MB-1TRK-P	anti-$\pi^+\pi^0$ cut	1
0x0020	MB-1TRK-3	anti-K_{l2} cut	20
0x0040	MB-1TRK-2	K_{l2} cut	20
0x0080	MB-ZFAKE	Downscaled for debugging	200
0x0100	NT-NOPEAK	$NUT(COG < 30cm \cdot Z < 9500cm \cdot ELKR > 15GeV)$	80
0x0200	N-MBIAS	$T0N$	200
0x0400	NT-PEAK	$NUT(NX > 2ORNY > 2)$	50
0x0800	KMU3-PRE	$Q1 \cdot \overline{Q2} \cdot 1\mu \cdot \overline{AKL} \cdot NUT(ELKR > 15GeV)$	50
0x1000	LKR-CAL-NZS	Not zero supp.	1
0x2000	LKR-CAL-ZS	Zero supp.	1
0x3000	PULSE	HAC/PMB pulser	1
0x4000	2BODY-PRE	KE2-PRE/D + KMU2-PRE/D	50
0x8000	RND	K_L monitor OR $K^{\pm}$ monitor random	5
KE2-PRE	$Q1 \cdot \overline{Q2} \cdot \overline{1\mu} \cdot \overline{AKL} \cdot NUT(ELKR > 15GeV \cdot EHAC < 10GeV \cdot M2 = M1 * *2)$		
KMU2-PRE	$Q1 \cdot \overline{Q2} \cdot 1\mu \cdot \overline{AKL} \cdot NUT(ELKR < 10GeV)$		
KMU3-PRE	$Q1 \cdot \overline{Q2} \cdot 1\mu \cdot \overline{AKL} \cdot NUT(ELKR > 15GeV)$		

Figure 4.1: L2 trigger word from 25th June 2003.

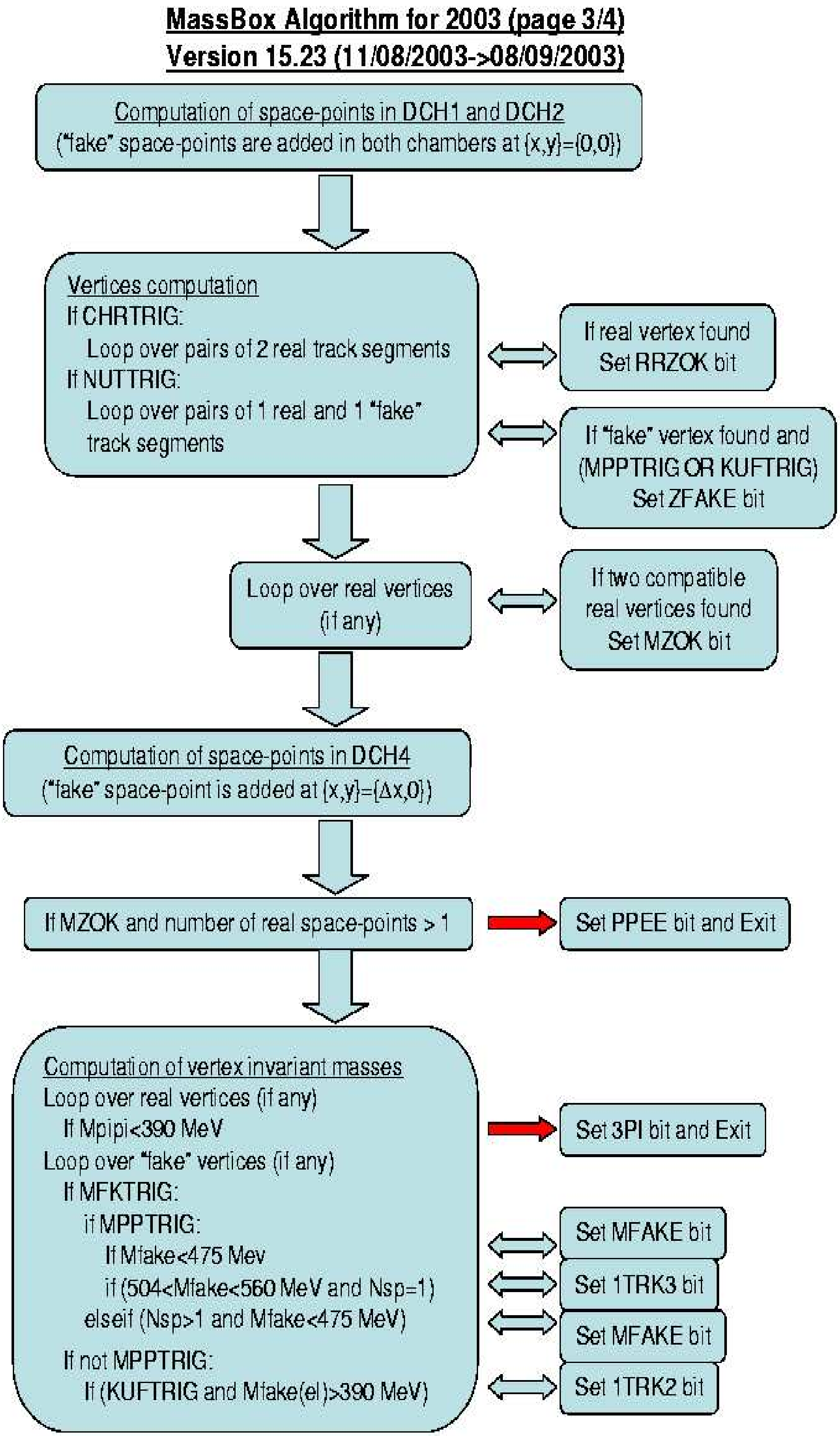

Figure 4.2: Diagram representing the MBX algorithm.

MFAKE (MeV/c^2)	p$^*_\pi$ (MeV/c)	T^*_π (MeV)
495	205	108
475	181	89
480	187	94
466	170	80
438	136	55
476	182	90
460	163	75

Table 4.5: Correspondence of relevant values of MFAKE, p$^*_\pi$ and T^*_π

Bit	Name	Meaning
4 (0x0010)	MB-1TRK-P or MFAKE	Cut on MFAKE against $K^\pm \to \pi^\pm\pi^0$
8 (0x0100)	NT-NOPEAK	Requirements on neutral COG, zvn and energy
9 (0x0200)	N-MBIAS or T0N	Signal from neutral hodoscope
10 (0x0400)	NT-PEAK	Requirements on projections n$_x$>2 or n$_y$>2

Table 4.6: Relevant trigger bits for $K^\pm \to \pi^\pm\pi^0\gamma$ analysis of 2003 data. MFAKE is the main L2 trigger. The others are used to calculate efficiencies of different conditions.

	2003	2004
Protons per pulse	6.5-7 10^{11}	
Rate at detectors	1 MHz	
Triggers per burst at L1	$\sim$ 450 K (410 K)	$\sim$ 490 K (450 K)
Triggers per burst at L2	$\sim$ 52 K	$\sim$ 60 K

Table 4.7: NA48/2 rates at different stages.

Chapter 5

Event Selection and Reconstruction

5.1 General event reconstruction in NA48/2

The reconstruction of NA48/2 events is performed on several steps.

First raw files are produced, containing all detector information collected in one burst. For each detector a reconstruction program has been developed that elaborates the raw information from the read-out into physical quantities. From every raw data file a compact data file is produced by the level three software (L3). Compact files are ~ 4 times smaller than the original raw files. This procedure is done almost in line with the data taking.

Compact files can be read by the compact-reader program [47]. This program is an official NA48 package able to read, filter and write compact files [1] . It also applies a set of corrections to the data, and provides an environment for the user to insert their own corrections and selection routines.

After data taking raw or compact files are analyzed by the detector experts for calibration purposes. Calibration constants are then inserted into data bases that are readable by the NA48 official software, and lists of bad bursts or runs are supplied.

Once calibration constants are available the compact data is reprocessed. Time offsets between detectors are also calculated, so associations between data coming from different detectors can be made. This is done, for example, with MUV hits and reconstructed tracks. The compact-reader program sets a flag if there is a hit in the MUV in the slab corresponding to the extrapolated track position. This association is used in the $K^{\pm} \rightarrow \pi^{\pm}\pi^{0}\gamma$ analysis, as it constitutes a very efficient veto against muons.

---

[1] The compact-reader program can also perform the same operations to supercompact files, which contain just a subset of the compact variables

From reprocessed compact files, supercompact files are made containing less information per event. One supercompact file contains the information from typically ten bursts, with a size reduction factor of ~ 3 with respect to the original compact files. The advantage of supercompact files is that, being fewer in number and smaller in size, the reading by the selection program is much faster.

For analysis of the $K^{\pm} \rightarrow \pi^{\pm}\pi^{0}\gamma$ decay a filter was implemented. This filter reads supercompact files and performs a loose selection of potential $K^{\pm} \rightarrow \pi^{\pm}\pi^{0}\gamma$ candidates. Filtered supercompact files are ~ 13 times smaller than the original ones.

In this chapter the initial reconstruction of the relevant physical quantities, like tracks and clusters, the $K^{\pm} \rightarrow \pi^{\pm}\pi^{0}\gamma$ preselection filter and the final selection of signal events are described.

5.1.1 Track reconstruction

The track reconstruction program uses DCH's data. The output of the program consists of a list of tracks with attributes (like electric charge, momentum, etc) and a list of vertices.

Each time a particle crosses a chamber close to a given wire a hit is generated. Contiguous hits in the two staggered planes constitute a cluster. Clusters made of two hits (one on each plane) are called doublets. If the plane is not fully efficient some doublets can be reconstructed only as singlets (clusters with one hit only). Clusters made of three hits are called triplets.

Tracks are reconstructed from clusters in DCH1, DCH2 and DCH4. Information from DCH3 is added only if the interpolated track trajectory at DCH3 gives a prediction for a space point position compatible with a measured one.

Tracks can be rejected if the hits used in the reconstruction have very different drift times. In addition, a quality variable is computed using the definition from equation 5.1. The value of this track quality ranges from 0 to 1, good tracks having a quality close to 1.

$$\text{Quality} = \frac{\text{Number of hits belonging to doublets and triplets}}{\text{Total number of hits belonging to the track}} \tag{5.1}$$

For *charged events* the program computes vertices from the intersection of three tracks.

For events with only one track, a charged vertex can also be defined from the intersection of the track with the beam line. The longitudinal position of the charged vertex is denoted as $z_{\rm CDA}$. This one-track type of vertex is not an output of the standard track reconstruction program, but can be esily calculated by the user, as described in section 5.4.3

For more details on the NA48 track and vertex reconstruction programs see references [48, 49].

5.1.2 Shower reconstruction

The main characteristics of the cluster reconstruction have been explained in chapter 3. More details on the cluster finding procedure are given in [50, 51] and summarized here.

At the beginning of the reconstruction program all cells are read in order to find candidate cluster seeds. If the cell under consideration is not dead, the average value of the first time samples is subtracted from the rest, in order to correct the energy measurement of showers sitting under the undershoot of a previous accidental. Cells with enough energy ($E > 200$ MeV) are declared cluster seed candidates. One single LKr cell can define two seeds if there are two maxima in the read out window.

Once potential cluster seeds have been identified, clusters are defined if one of these cells is a local maximum:

$$E(seed) > E(all\ surrounding\ cells)$$

and if its energy is above a cut defined by the average energy in the eight surrounding cells:

$$E(seed) > (0.18 + 1.8E(average))\ GeV$$

At this stage all clusters have been identified, along with the first estimates of their energy, time and position.

If a cell receives energy from two or more clusters, the energy of this cell is shared among the clusters according to the expected energy profile, taken from a GEANT Monte Carlo simulation.

The energies of all cells within a clustering radius of 11 cm are then added, giving new estimates for the cluster energy and position.

For reconstructing the energy in one cell belonging to a certain cluster, a well defined pulse maximum is needed. If the pulse signal from a given cell does not have at least two well measured time samples the energy of the cell is set to zero.

The status word of the cluster is defined to keep track of gain switching pathologies. For clusters with status ≥ 4 there was at least one cell were the energy could not be reconstructed. These clusters are normally excluded by the selection criteria.

5.2 Event preselection for $K^{\pm} \rightarrow \pi^{\pm}\pi^{0}\gamma$ decays.

In order to process the data more efficiently, a preselection was done using loose requirements. The final size of the filtered data was 310 GB for SS0, 227 GB for SS123 and $\sim$ 680 GB for SS5-SS8. A reduction factor of $\sim$ 13 was achieved with respect to the input supercompact files. This data volume was small enough so that filtered files could be permanently staged on the NA48 disk pool. As the files were already on disk, no time was lost on transferring the files from CASTOR [2] tapes, speeding up the file reading process.

The conditions required for an event to be selected by the filter are summarized in table 5.1 and described in detail in the following.

The event should contain at least 1 track satisfying:
Radius at LKr $\geq$ 13 cm Radius at DCH1 $\geq$ 10 cm Track quality $\geq$ 0.6
And at least three good clusters satisfying:
STATUS $<$ 4 Emin $\geq$ 2.85 GeV Dist dead cell $\geq$ 2 cm Radius at LKr $\geq$ 13 cm Distance to track $\geq$ 15 cm (for events with one track only) Distance between clusters $\geq$ 10 cm (for events with three clusters only)

Table 5.1: Summary of cuts applied at the preselection stage.

First, events were rejected if they belonged to bursts flagged as bad for at least one of the central detectors (LKr, DCH, NUT, MBX and HODC) or if they came from runs where the NT-PEAK trigger was not working properly. Actually, supercompact files containing only runs belonging to bad NT-PEAK periods (as defined in chapter 4) were not read at all by the filtering program.

---

[2] CASTOR stands for CERN Advanced STORage manager. This is the CERN standard system for storing experimental data.

This avoided producing filtered files without useful events.

Trigger bits are checked in order to accept only events coming either from the main L2 trigger, or from selected control triggers, ie, MB-1TRK-P, NT-PEAK, T0N, NT-NOPK bits.

Events with any number of tracks are taken at this stage. However it must be noted that the trigger bit condition rejected already most events coming from *charged decays*, so that only *neutral events* are left.

From all tracks in the event, there must be at least one that passes some quality requirements. This track constitutes the charged pion candidate.

First, the position of each track at DCH4 is extrapolated to the LKr front face, using the slopes measured with the DCHs located after the spectrometer magnet. To assure a good reconstruction of the electromagnetic energy associated to the track, it is required that the distance between its extrapolated impact point on the calorimeter and the LKr center is greater than 13 cm. This guarantees that no energy is missed due to the presence of the vacuum pipe hole.

In order to avoid misreconstruction due to possible edge effects, the radial track position at DCH1 must be greater than 10 cm.

In addition, the track quality variable must be greater than 0.6.

If the considered event does not contain any track satisfying these conditions, this event is not eligible as $K^{\pm} \to \pi^{\pm}\pi^{0}\gamma$ candidate.

Due to the presence of a charged pion in the final state, no cut can be done on the total number of clusters seen in the electromagnetic calorimeter, as showers produced by hadrons are characterized by a fluctuating number of reconstructed clusters. In addition, these clusters can sometimes be located quite far away from the track impact point. However, a $K^{\pm} \to \pi^{\pm}\pi^{0}\gamma$ event should contain at least three clusters that could be considered as gamma candidates. These potential photon clusters must meet some quality requirements.

First, they must have a value of the status variable smaller than 4, so that their energy has been properly reconstructed.

Second, the gammas minimum energy must be greater than 2.85 GeV. The measurement of small clusters energies can be very much affected by non-linearity problems and has a worse intrinsic resolution. The standard NA48 energy cut is set at 3 GeV, however, at this stage, not all the corrections to the energy measurement have been applied (see below). The value of 2.85 was set in order not to loose events at 3 GeV once the appropriate corrections are made.

In addition, gamma clusters must be 2 cm away from any dead cell and 13 cm away from the calorimeter center, so that no important fraction of their energy has been missed.

Energy mismeasurement could also be due to sharing with other clusters. For events with only one track it was required to have at least three clusters more than 15 cm away from the track extrapolated position at the calorimeter front face, in order to avoid overlapping of the electromagnetic gamma showers with the hadronic shower.

For events with three clusters only, those should correspond to gamma clusters. Those events were selected only if the distance between all clusters was greater than 10 cm.

5.3 Corrections

A set of corrections is applied to the reconstructed Simulated and/or Data events at several stages in the selection procedure. The LKr non-linearity and projective corrections, and the so-called alpha-beta corrections for the spectrometer response are described here. The blue field correction will be explained in the next section 5.4.

In addition, a trigger correction exists, which is applied only to simulated events after reconstruction and selection. This will be explained in detail in chapter 9.

Table 5.2 summarizes which corrections are applied to Simulated events and which to Data events.

CORRECTION	DATA	SIMULATION
Non-linearity	X	-
Projectivity	X	X
Alpha-Beta	X	X
Blue Field	X	X
Trigger	-	X

Table 5.2: Summary of corrections applied (X) to $K^\pm \to \pi^\pm \pi^0 \gamma$ events in Data and in Monte Carlo simulation. The symbol - is used if the correction is not applied.

5.3.1 LKr Non-linearity

Due to the Data Concentrator (DC) Threshold applied to the LKr calorimeter cells at the readout, a non linear relation develops between the value of the energy deposited in the calorimeter and its actual measurement. This non linear response is relatively more important for small clusters energies. The Monte Carlo simulation is not able to reproduce the size of the effect, even if the zero suppression has also been implemented at the reconstruction stage of simulated events.

Figure 5.1 (a) shows the reconstructed π^0 mass versus the minimum photon energy in the π^0 decay for SS3 $K^\pm \to \pi^\pm\pi^0\gamma$ data events, together with the Monte Carlo simulation for the same period. A clear effect of ~ 0.4 % can be seen in data at energies of ~ 3 GeV.

Using $K_S^0 \to \pi^0\pi^0$ decays from the 2002 run a correction has been developed to be applied to clusters with energies smaller than 11 GeV. This can be used for 2003 and 2004 data, where the Data Concentrator Threshold was kept at the same value as in 2002.

Figure 5.1 (b) shows the same data after this correction has been applied. The value of the reconstructed π^0 mass does not show any more any dependency on the gamma energy.

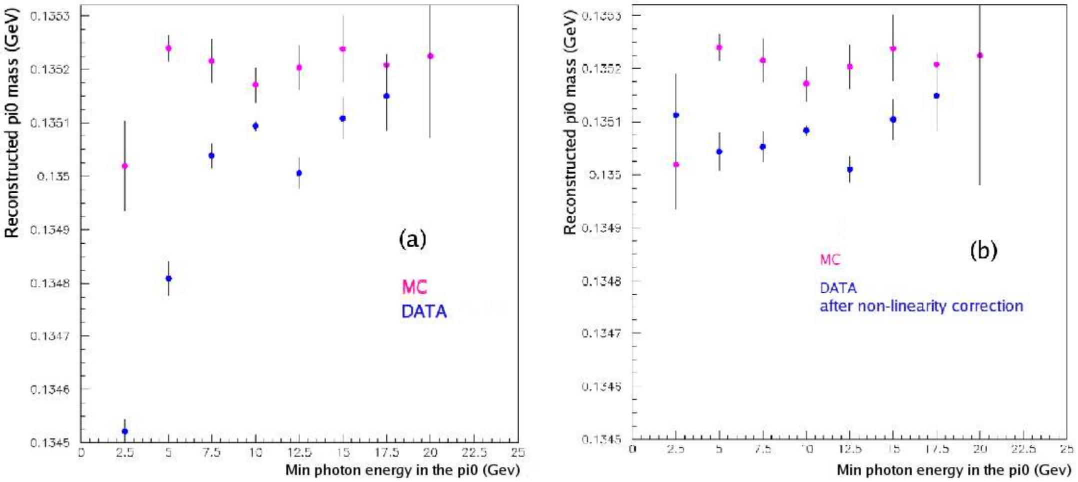

Figure 5.1: (a) Reconstructed π^0 mass for SS3 simulated (pink) and data (blue) $K^\pm \to \pi^\pm\pi^0\gamma$ decays as a function of the minimum gamma energy in the π^0 decay. The effect of non-linearity can be seen for data at small photon energies. (b) Same plot where the LKr non linearity correction has been applied to SS3 data (blue). The dependency on the minimum photon energy in the decay is reduced after the correction.

5.3.2 LKr Projectivity

As already mentioned, the LKr calorimeter has been built such that the cells have projective geometry, pointing at 110 m from the calorimeter front face into the decay region. The x, y cluster positions given by the NA48 standard reconstruction program are extrapolated to the calorimeter front face, assuming that the shower developed along the projective direction. However, if the photon was produced at a position different from the projective point, this assumption no longer holds, and a correction to the cluster transverse position has to be applied. The angle α of the shower development with respect to the projective direction can be calculated knowing the distance z of the the actual decay position from the projective point (z_0) and the approximative shower transverse position at the calorimeter front (x):

$$\alpha = x\left(\frac{1}{z_0 - z} - \frac{1}{z_0}\right) \tag{5.2}$$

For a given photon shower energy E_γ, the shower depth inside the LKr structure can be calculated as [3] :

$$z_{\text{depth}} = 20.8 + 4.3 * \log(E_\gamma(\text{GeV}))\ \text{cm} \tag{5.3}$$

New effective x, y clusters positions at the LKr front face must be modified according to the measured particle direction as:

$$x_{\text{corr}} = x_{\text{standard}}(1 + \alpha z_{\text{depth}}) \tag{5.4}$$

For a photon shower coming from a decay 50 m away from the projective point position and with a shower depth of 30 cm, the amount of this correction is of the order of 5 mm ($\sim$ 5 per mil)

In addition, if no projective correction was applied, the reconstructed π^0 mass would depend on the decay point along the beam axis, as the transverse position enters directly in its computation (see equation 5.8) and this is mismeasured differently as a function of the decay position along z.

This is equivalent to a shift on the neutral vertex value (see equation 5.9) as a function of the true vertex position.

The projective LKr geometry has been implemented in the simulation, and must be therefore accounted for also there. Figure 5.2 shows the difference between neutral vertex (section 5.4.4) and charged vertex (section 5.4.3) as a function of

---

[3] Different constants would be needed in order to calculate the shower depth for electron showers.

the reconstructed charged vertex for SS123 simulated events, before and after the LKr projectivity correction was applied. The correction makes the slope smaller by a factor of four.

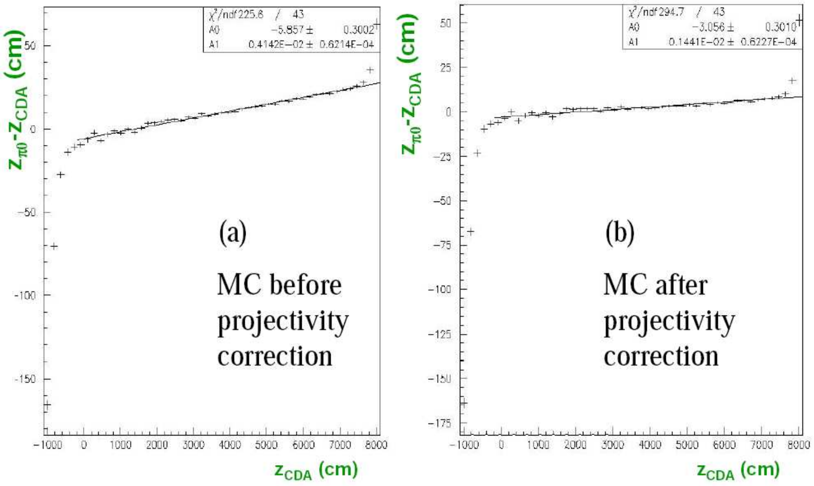

Figure 5.2: Difference between neutral and charged vertex longitudinal positions as a function of the reconstructed charged vertex z coordinate for simulated events before and after the LKr projectivity correction was applied.

5.3.3 Alpha-Beta spectrometer corrections

When analyzing $K^{\pm} \to \pi^{\pm}\pi^{+}\pi^{-}$ events it was observed that the reconstructed kaon masses were different for K^{+} and K^{-}, and both different from the nominal kaon mass M_K (in PDG [52], M_K =0.493677 GeV/c^2) Such effects could only be due to imperfections in the momentum measurement by the magnetic spectrometer. A model was built [53], assuming only two sources affecting the reconstructed momenta: miscalibration of the spectrometer magnetic field B, and misalignemnt of one of the DCHs located downstream the magnet.

Miscalibration of the spectrometer field induces a momentum misreconstruction, as ΔB/B= Δp/p. For $K^{\pm} \to \pi^{\pm}\pi^{+}\pi^{-}$ events this leads to mismeasurement of the reconstructed kaon mass value m, as (m-M_K)/M_K $\approx$ 0.2 ΔB/B. The momentum measured by the spectrometer can be corrected for such effect.

Defining β = ΔB/B=(M_K-m_{aver})/(0.2 × M_K), and m_{aver}=0.5 × (m_{K^+}+m_{K^-}) the corrected momentum p is given by:

$$p = p_0(1 + \beta) \tag{5.5}$$

where p_0 is the uncorrected momentum.

Misalignment of one of the DCHs after the magnet would affect the measurement of deflections of charged particles in the plane of the magnet transverse kick, implying therefore a momentum mismeasurement. For a given magnet polarity, this mismeasurement depends on the charge of the particle, as tracks of opposite charges are deflected in opposite directions. As the K^+ is reconstructed from two positive and one negative track, its mass is shifted in opposite direction compared to the K^-, that is reconstructed from one positive and two negative tracks.

The corresponding momentum correction can be parameterized as:

$$p = p_0(1 + \alpha p_0 q) \tag{5.6}$$

being q the charge of the reconstructed track, and α = (m$_{K^-}$-m$_{K^+}$)/1.7476

If the magnet polarity is changed, the sign of the mass splitting (sign of alpha) is changed as well. So the explicit dependence of the correction and α determination with the B field sign can be omitted from (5.6)

The $K^\pm \to \pi^\pm\pi^+\pi^-$ decays can be used to monitor the spectrometer behavior. Reconstructed K^+ and K^- masses are introduced on a data base, accessible to the reconstruction program on a burst by burst basis. Corresponding values of α and β corrections are computed. The user can decide whether or not to apply these corrections to the reconstructed momenta for any given event in any decay mode. These corrections have been used for $K^\pm \to \pi^\pm\pi^0\gamma$ analysis.

A typical value of the β correction is of the order of a few per mil with negative sign, both for 2003 and 2004 data. This amounts to $\sim$ 500 keV/c^2 shift on the reconstructed kaon mass.

The value of the α correction varies with time. In the worst period, at the beginning of 2003 data taking (SS0), a typical value for α is of -2.1 10^{-4}, corresponding to a 250 μm translation of DCH4 along the x direction. This amounts for a difference in the m$_{K^+}$ and $_{K^-}$ of the order of 350 keV/c^2. For later periods, the value of α is at least one order of magnitude smaller. It must be stressed that the constructed model does not provide a realistic explanation for these changes, which disappeared spontaneously.

The overall calibration is accurate to a few keV/c^2 level in the good periods and around 15 keV/c^2 for SS0.

This model has been used in the simulation in order to introduce the distortions observed in data. At generation level the field in the spectrometer magnet was scaled by a factor $(1 - \beta)$ and the DCH4 was displaced in x direction accord-

ingly to the corresponding α value. A database table containing the K^+ and K^- masses for Monte Carlo on a run by run basis could be used to apply the corresponding corrections to simulated events.
The effect of DCH misalingment on the kaon masses can be seen in figure 5.3 for 2003 data. For this plot the reconstructed K^+ and K^- masses were averaged over a pair of day-samples, where every day sample has an opposite spectrometer magnet polarity with respect to the previous one. For this plot, data has been reprocessed with the position of DCHs adjusted to give equal K^+ and K^- masses for the first day-sample. After the first day-sample the mass differs between kaons deflected to Jura side and kaons deflected to Saleve side. These differences can be attributed to gradual displacements of DCH4 along the x-axis, of ~ 4 μm per day. Simulation studies have shown that a mass split of 70 keV/c^2 in the K^+, K^- reconstructed masses could be induced by a DCH4 position shift of 50 μm.

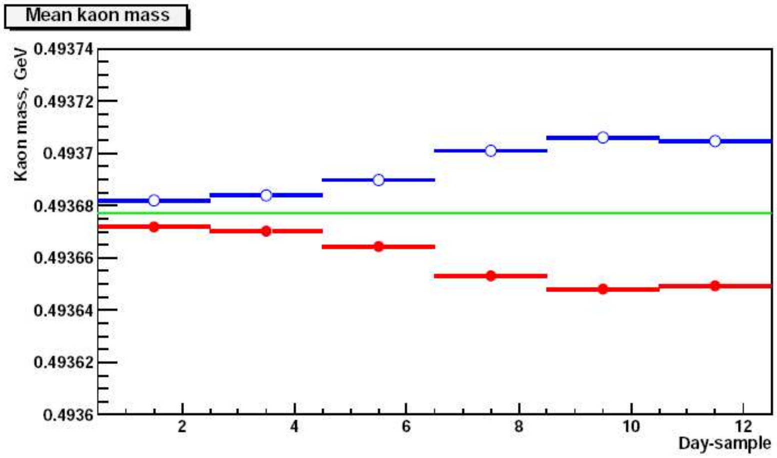

Figure 5.3: Kaon masses reconstructed from different pairs of day-samples. Red circles represent kaons deflected to Saleve side and blue circles kaons deflected to Jura side. The green line shows the nominal PDG value for the kaon mass.

5.4 Selection of $K^\pm \to \pi^\pm\pi^0\gamma$ data events

The main selection of $K^\pm \to \pi^\pm\pi^0\gamma$ events is based on the identification of one good quality track compatible with a pion, and at least three good quality clusters, all lying in the detector fiducial volume. Out of the reconstructed clusters, there must be three photons well separated from the pion impact point at the LKr.

After all decay products have been identified, the vertex position can be reconstructed and the 4-momentum of all particles calculated. The event is selected if the reconstructed invariant mass of the system is compatible with the PDG kaon mass.

The whole selection procedure is described in detail in the following. Cuts applied in the preselection have been either repeated (in that case they will not be mentioned again) or tightened at this stage. A summary of all cuts is shown in table 5.3.

5.4.1 Selection of charged pion track and gamma clusters

To consider an event as a potential $K^{\pm} \rightarrow \pi^{\pm}\pi^{0}\gamma$ candidate, at least three clusters must be reconstructed in the LKr calorimeter within a time window of 100 ns to 154 ns[4] . As already explained, there is no cut on the total number of electromagnetic clusters.

Non-linearity correction is applied to all electromagnetic clusters' energies for data events.

For each event, every combination of three clusters is analyzed and the mean and sigma of their times computed. The three-cluster combination with the smallest sigma is kept as the precise LKr time reference. To refine the selection a new window is opened selecting only clusters within 3 ns around this precise LKr time. This condition defines the number of clusters in time, which must be at least three.

In addition, there must be only one reconstructed track in the DCHs. The track time is given by the charged hodoscope if availabe [5] and by the DCHs otherwise. It is required to be within 116 ns and 154 ns[6] and within 4 ns from the precise LKr time reference.

The selected track must lie within the detector fiducial volume. This is defined by a set of geometrical cuts assuring that the track impact point is far from the edges of the relevant detectors (DCH's, MUV, HODC, LKr) and from the beam

---

[4] The limit values depend on the average time shift of the LKr with respect to the other detectors and their absolute values are not significant.

[5] The hodoscope time may not be available for one track, if more than one hit were present for that event.

[6] Absolute values are not significant.

pipe. The values of the geometrical cuts are specified in table 5.3.

Tracks with associated muon hits are not accepted. This condition rejects background from $K^{\pm} \rightarrow \pi^{\pm}\pi^{0}\pi^{0}$ events where the π decays in flight to a muon (see chapter 8).

At this moment alpha-beta corrections are applied to the track momentum. The corrected value is required to be greater than 10 GeV, in order to avoid inefficiencies from the MUV response.

The minimum track quality is required to be 0.7.

Given the track position and direction at DCH4, the track impact point at the LKr front face can be calculated. An electromagnetic cluster is associated with the track if it lies within 5 cm radius from the extrapolated track position.

Once the associated cluster is found, the E/p variable is calculated as the ratio between the associated LKr cluster energy and the track momentum measured in the spectrometer. The associated cluster must be 2 cm away from any dead cell, must have a status smaller than 4 and be at a radial position in the LKr calorimeter greater than 15 cm. All these conditions assure a good energy reconstruction.

If the track was an electron it would deposit all its energy in the electromagnetic calorimeter, and the value of the E/p variable would be close to 1. Pion tracks (and hadronic tracks in general) do not deposit all their energy in form of electromagnetic showers and many times they do not even have an associated cluster in the electromagnetic calorimeter. In order to reject electron tracks but keeping pion tracks, a cut is made on the track E/p to be less than 0.85.

Once the pion and a set of electromagnetic clusters have been found, potential photons must be identified. A photon is defined as a LKr cluster separated by more than 35 cm from the extrapolated π track position at the calorimeter.

Events are selected with three gamma clusters only. Extra clusters are only allowed if they come from the π shower (within 35 cm from the π track extrapolated position at the LKr) or if they are not at the same time (outside 3 ns window with the precise LKr time).

Gammas must satisfy standard quality requirements. They must also lie within the external LKr octagonal shape. To avoid energy sharing gamma clusters must separated by more than 10 cm from any other in time cluster.

Finally, the gamma energy was required to be between 3 and 100 GeV.

If any of the gamma clusters does not satisfy these requirements, the event is rejected.

5.4.2 Calculation of COG

At this moment all particles belonging to the event have been identified and global event variables can be calculated. The center of gravity (COG) is defined as the energy weighted position at the LKr calorimeter front face of the decay particles in the event.
For events with three gammas and one track it is calculated as follows:

$$COG = \sqrt{(\frac{\sum_{i=1}^{4} x_i E_i}{\sum_{i=1}^{4} E_i})^2 + (\frac{\sum_{i=1}^{4} y_i E_i}{\sum_{i=1}^{4} E_i})^2} \tag{5.7}$$

For i=1,3 x_i and y_i are the x, y coordinates of the ith gamma cluster at the LKr, and E_i is the corresponding gamma energy. For i=4, x_4 and y_4 represent the x, y coordinates of the extrapolated track position at the LKr and E_4 is the pion energy. For this calculation, the track position at the LKr is given by the extrapolation of the slopes and positions measured in the DCH's before the magnet. The pion energy is computed from the momentum measured at the DCH's assuming the pion mass for the track.
If no energy has been lost in the event, the COG calculated in this way must coincide with the radial position of the parent kaon at the LKr front face if it did not decay. As the kaon beam direction is along the z axis and the beam size is very small, a cut on the reconstructed COG position can be made, allowing only events with COG at the LKr smaller than 2 cm. Figure 5.4 (b) shows the COG distribution for $K^{\pm} \to \pi^{\pm}\pi^{0}\gamma$ simulated events. A cut at 2 cm rejects $\sim$ 1 % of the signal.

5.4.3 The CDA and the charged vertex ($z_{\rm CDA}$)

The decay vertex of the kaon decay can be approximated as the intersection point of the charged pion trajectory with the beam line. Assuming the kaon line of flight along the longitudinal axis, the z coordinate of the charged vertex (z$_{CDA}$) is defined at the point of closest distance of approach (CDA) between this axis and the pion direction. Taking this point to be on the kaon trajectory, the complete charged vertex coordinates are (x=0, y=0, z=z$_{CDA}$)
Figure 5.4 (a) shows the distribution of the closest distance of approach between the z axis and the track direction for $K^{\pm} \to \pi^{\pm}\pi^{0}\gamma$ simulated events. A cut is made for CDA $>$ 6 cm, which rejects a negligible amount of the signal.

5.4.4 The π^0 reconstruction and the neutral vertex (z_{π^0})

Given the three selected photons, two of them must be associated to the π^0 decay. The remaining one is identified as the radiated gamma, also called the odd gamma, which carries the relevant information about the nature of the decay (see chapters 1 and 2). Therefore, a wrong assignment of the photons to the π^0 decay implies a wrong assignment of the radiated gamma, distorting the gamma energy and therefore, the W distribution. This constitutes the mistagging problem, that will be treated in detail in chapter 7.

For every pair of photons with indexes (i, j), its invariant mass can be calculated under the hypothesis that they come from a π^0 decaying at the z_{CDA} position along the z axis:

$$m_{\pi^0}^{ij} = \frac{\sqrt{((x_i - x_j)^2 + (y_i - y_j)^2)E_iE_j}}{z_{\mathrm{LKr}} - z_{\mathrm{CDA}}} \tag{5.8}$$

where x, y are the cluster's coordinates on the LKr surface, E_i, E_j the cluster's energies and z_{LKr} is the z position of the LKr calorimeter.

With three gammas, three combinations are possible for $m_{\pi^0}^{ij}$. The pair providing the $m_{\pi^0}^{ij}$ value closest to the PDG π^0 mass (M_{π^0}) is selected.

Once the best pair (i, j) has been identified, the π^0 decay position (z_{π^0}) can be computed from neutral variables as:

$$z_{\pi^0} = z_{\mathrm{LKr}} - \frac{\sqrt{E_iE_jr_{ij}^2}}{M_{\pi^0}} \tag{5.9}$$

where r_{ij} is the distance between the two selected photons.

The variable z_{π^0} is called neutral vertex.

Figure 5.4 shows the distribution of the difference between charged and neutral vertex positions for $K^\pm \to \pi^\pm\pi^0\gamma$ simulated events. This distance is required to be less than 400 cm, rejecting ~ 1 % of the signal.

The neutral vertex for the gamma pair giving the second best agreement with the nominal π^0 mass is also stored. This is used in order to reduce the mistagging probability , requiring that the distance between the neutral vertex for the second best combination ($z_{\pi^0}^{second}$) and the charged vertex must be greater than 400 cm. The sample is reduced by ~ 20 % after this last cut.

At this point the projectivity correction is applied to provide the best estimate for the neutral vertex and the photons coordinates at the LKr.

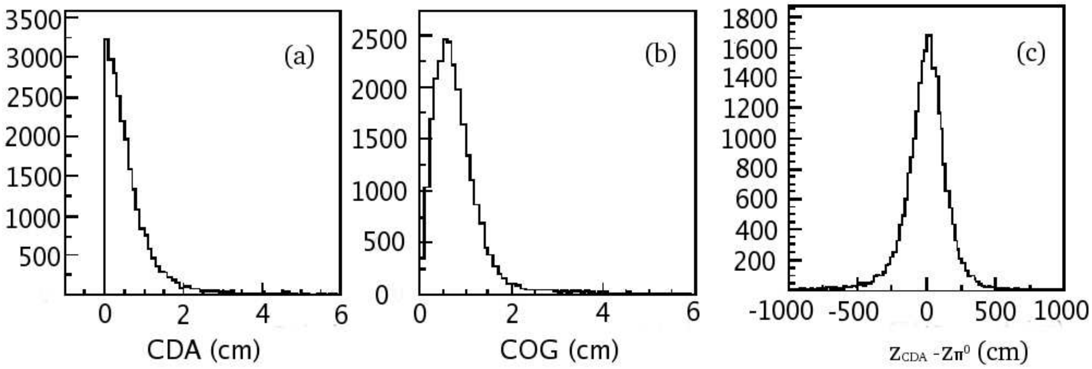

Figure 5.4: Simulated distribution of relevant variables. Figure (a) shows the closest distance of approach (CDA) between the pion track and the z axis. A cut at 6 cm is imposed in the $K^{\pm} \to \pi^{\pm}\pi^{0}\gamma$ selection. Figure (b) shows the center of gravity of signal events. In the selection the COG is required to be smaller than 2 cm. Figure (c) shows the difference between charged and neutral vertices, which must be less than 400 cm for accepted candidates.

5.4.5 Cut against interactions in DCH1

For decays occurring at a z position close to DCH1 it is possible that a photon passes through the vacuum pipe or impinges on the DCH1 flange before reaching into the electromagnetic calorimeter. Due to this interaction of the photon, there is a high probability of showering that could be not well enough modelled in the simulation.

Knowing the position of the DCH1 flange, a direction for photons coming into the LKr from this ring can be computed. This allows to reject gamma clusters whith a radial position in the LKr compatible with this hypothesis.

Defining $\mathrm{z}_{\pi^0\mathrm{res}} = z_{\pi^0} + 400$ cm [7] , then the slope needed for a photon to impact on the DCH1 flange is:

$$\frac{dR^{flange}}{dz} = \frac{11\mathrm{cm}}{z_{\mathrm{DCH1}} - z_{\pi^0\mathrm{res}}} \tag{5.10}$$

where 11 cm is the DCH1 flange radial position.

Extrapolating from this direction, the radius of the resulting gamma cluster in the calorimeter would be:

$$R^{\mathrm{flange}}_{\mathrm{LKr}} = \frac{dR^{\mathrm{flange}}}{dz}\Delta z = \frac{dR^{\mathrm{flange}}}{dz}(z_{\mathrm{LKr}} - z_{\pi^0\mathrm{res}}) \tag{5.11}$$

Events are selected only if the radial position of the three gamma clusters at LKr surface R is greater than $\mathrm{R}^{\mathrm{flange}}_{\mathrm{LKr}}$.

---

[7] The 400 cm are added in order to take into account resolution effects

This condition removes 5 % of the statistics.

5.4.6 The pion direction and the blue field correction

The pion direction is given by the measuremed charged track slopes at the DCHs located upstream the magnet. However, the direction of the charged track at the DCHs is not the same as the direction at the decay point, due to the action of the blue field. The blue field has been already defined in chapter 3 as the remanent field in the vacuum tank which hosts the fiducial decay volume. This field will obviously bend charged tracks, changing their direction along their path. The slopes at the vertex are the ones used in the kaon mass calculation and in the determination of the W variable value.

5.4.7 Vertex coordinates

The blue field must also be taken into account in the computation of the vertex coordinates. The assumption was made that the charged z position (z_{CDA}) would not change appreciably including the blue field correction. However, the effect of the blue field on the vertex transverse coordinates (x, y) cannot be neglected.

Up to this point, the vertex transverse coordinates were assumed to be (0,0), and the decay to occur along the theoretical kaon flight direction, defined by the z axis. A better estimation of the vertex x,y positions can be done in the following way. Let us take the track position and slope as measured in DCH1, and extrapolate this slope in the blue field up to the neutral vertex longitudinal position. The integral of the blue field is computed on steps, providing in every point new values for the track slope and position at the considered z coordinate. The newly computed transverse position of the track at the z_{π^0} point defines the final values of the decay point transverse coordinates, and all gamma directions will be computed from them. Final vertex coordinates are therefore given by $(x_{\mathrm{bf}}, y_{\mathrm{bf}}, z_{\pi^0})$, where $x_{\mathrm{bf}}, y_{\mathrm{bf}}$ are the x, y position of the pion at z_{π^0} once the π direction is corrected by the blue field effect.

The decay vertex position z_{π^0} is required to be between -1000 and 8000 cm. The lower cut minimizes effects from the presence of final collimators, that could not be modelled well enough in the simulation. The upper cut rejects events decaying too close to the main detector to be properly reconstructed. Actually the acceptance for $K^{\pm} \to \pi^{\pm}\pi^{0}\gamma$ events dies rapidely close to 8000 cm.

5.4.8 Calculation of momenta and final variables

Once the charged π and all three photons have been identified, and the vertex coordinates have been computed, the values of the kinematic variables of all decaying particles can be calculated.

For the π, all relevant quantities have been computed already at previous stages. To summarize, the momentum is given by the DCH's measurements, applying alpha-beta corrections. The energy can be simply calculated once the momentum is known, assuming the π mass for the track. The π direction is given by the DCH's measurements and corrected by the blue field effect.

The energy of the gammas is also known: it is given by the LKr measurement corrected by the non-linearity effect. The direction of the gammas can only be computed once final vertex coordinates are available. The photons directions are calculated from the final vertex coordinates and the cluster's positions at the LKr, that have been corrected by projectivity.

The kaon four momentum is given by the sum of the four momentum of the π and the photons. The total kaon energy is required to be within 54 to 66 GeV, i.e., compatible with the beam properties. From the four momentum, the invariant mass of the system can be calculated. It is required to be within 10 MeV from the nominal kaon mass.

The T^*_π is computed using a boost routine from the CERN libraries. Loren4 performs a Lorenz boost along the kaon direction, once the total kaon energy is known.

Finally, the W variable is calculated using equation 1.13 from the computed four momenta of the π, kaon and odd gamma, the reconstructed kaon mass and the nominal π mass (from PDG)

5.4.9 Cuts against background

A set of cuts has been implemented in order to reduce the background contribution to the final sample. Some of these cuts have been already described in another context, like the E/p, COG, kaon mass and MUV cuts. It must be stated that, as the MUV detector is inefficient for tracks with small momentum, it is required that the pion momentum is bigger than 10 GeV/c. This cuts about 10 % of the events.

In addition, there are some cuts that are really specific to background rejection. A cut against gammas overlapping in the LKr from $K^\pm \to \pi^\pm\pi^0\pi^0$ decays is specially relevant, as it allows dropping the standard requirement of previous experiments of $T^*_\pi > 55$ MeV, gaining in sensitivity to Direct Emission events. All these cuts will be explained in detail in chapter 8

5.4.10 Trigger related cuts

In order to increase the L1 trigger efficiency and make sure that it does not introduce any significant distortion to the W distribution it was required that the energy of all photons in the event should be greater than 5 GeV. This rejects ~ 30 % of the data statistics.
In addition a cut has been implemented on the distance between clusters seen by the neutral trigger projections.
To get rid of edge effects of the L2 trigger, it was required that $T^*_\pi < 80$ MeV. These cuts will be explained in detail in chapter 6

5.5 Illustration of the selection procedure.

Figure 5.5 shows the effect of a series of cuts on the invariant mass of the system ($\mathrm{M}_{\pi\pi^0\gamma}$). A small data sample of SS123 has been used. In particular, the power of the COG requirement on the rejection of $K^\pm \to \pi^\pm\pi^0\pi^0$ with one missing gamma can be clearly seen in figure (c).

Figure 5.6 (a) shows the final reconstructed kaon mass for $K^\pm \to \pi^\pm\pi^0\gamma$ events in SS123. The kaon mass resolution is ~ 2 MeV. The plot is presented with a cut of 10 MeV around the nominal kaon mass (rejecting $K^\pm \to \pi^\pm\pi^0\pi^0$ events) and a cut of 5 GeV on the minimum gamma energy in the event.
The number of reconstructed events is $\sim 150\ 10^3$, which is almost 8 times more than previous experiments. As will be explained in chapter 8 the background contribution entering the sample is negligible.
Figure 5.6 (b) shows the final reconstructed W distribution for the same events. As expected, its shape is clearly dominated by the Inner Bremsstrahlung contribution.
For the extraction of the Direct Emission and Interference components of the decay a cut has been applied on the W variable requiring 0.2<W<0.9. The lower cut minimizes the effect of difference in resolution between data and simulation, which is especially important for small W events due to the sharp rise of the W distribution. The upper cut avoids excursion in a region of very small acceptance in W. This final cut on the valid W range reduces the useful sample to ~ 120

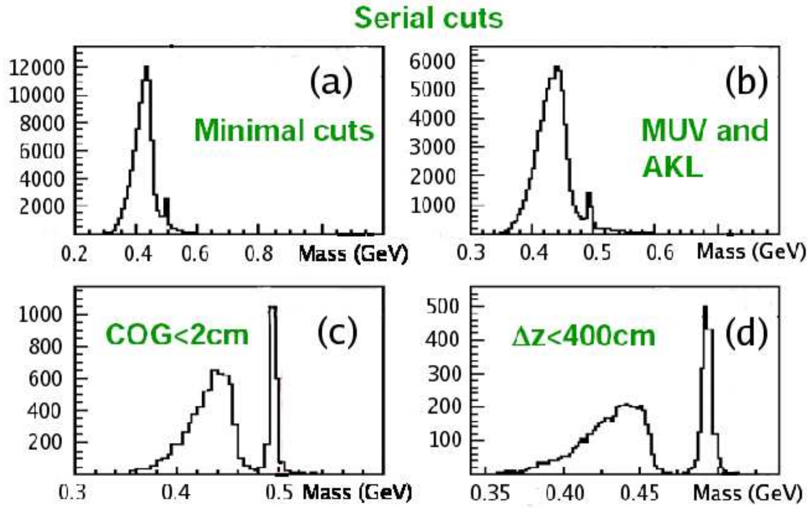

Figure 5.5: Reconstructed kaon mass for a sub-sample of the SS123 data after a series of cuts sequentially applied. Figure (a) shows the invariant mass distribution $M_{\pi\pi^0\gamma}$ when only fiducial geometric cuts have been applied to the track and the gammas. Most of the events at this stage come from $K^\pm \to \pi^\pm\pi^0\pi^0$ decays with only three photons reconstructed in the electromagnetic calorimeter. A small peak at ~ 0.5 GeV is due to the $K^\pm \to \pi^\pm\pi^0\gamma$ signal. Figure (b) shows the effect of requiring that there is no hit in the AKL counters or in the MUV. This cleans the sample from accidental activity and from misreconstructed tracks due to π decay in flight to μ. In figure (c) the cut on COG < 2 cm has been applied. This rejects most of $K^\pm \to \pi^\pm\pi^0\pi^0$ events with missing energy. Figure (d) shows how the cut on $|z_{\pi^0} - z_{\mathrm{CDA}}| < 400$ cm further separates the signal from the background.

10^3 events.

5.6 Selection of $K^\pm \to \pi^\pm\pi^0\gamma$ simulated events

The selection of simulated events is basically the same as for data. The main differences are that the LKr non linearity correction is not applied, and that time cuts are not required, as accidental effects are not included in the simulation. In addition, no trigger bits selection is needed for simulated events, unless for specific trigger studies. The simulation of the trigger logic and the use of trigger bits will be explained in chapter 6.

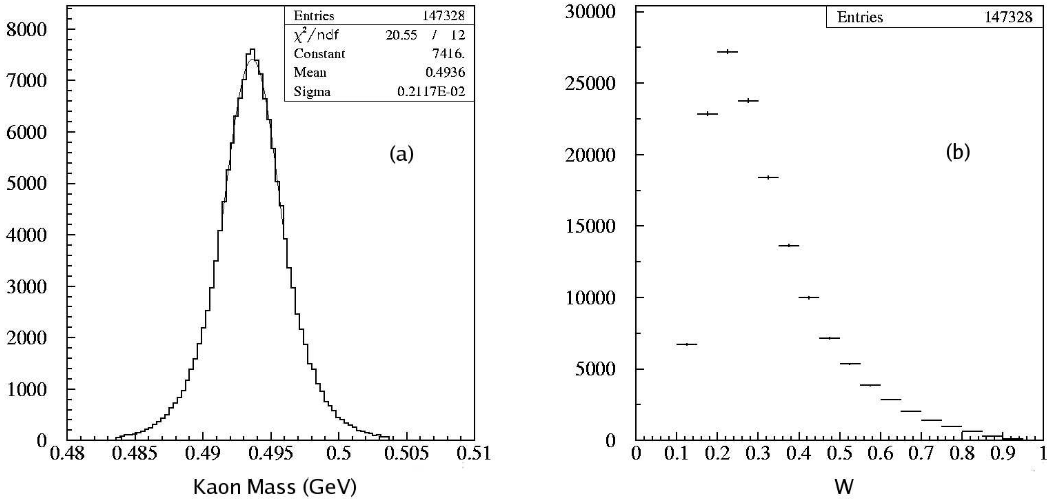

Figure 5.6: Reconstructed kaon mass (a) and W distribution (b) for the final SS123 data sample. The number of events satisfying all requirements is 147 10^3

CLUSTERS.
At least 3 clusters inside in $100 - 154$ ns At least 3 clusters within 3 ns from average LKr time. Recompute precise LKr time Apply complete non-linearity correction to data events.
TRACKS.
Select events with only 1 reconstructed track Track time within $116 - 154$ ns Track within 4 ns with respect to precise LKr time from clusters Geometrical fiducial volume: 12 cm $<$ Radius at DCH's $<$ 150 cm 15 cm $<$ Radius at LKr $<$ 110 cm 12.5 cm $<$ Radius at MUV $<$ 135 cm Quality > 0.7 Apply alpha-beta corrections. Require π momentum > 10 GeV E/p< 0.85 Veto if association to muon track.
CLUSTER ASSOCIATED TO TRACK.
Associated clusters at distance from $\pi < 5$ cm Radial distance at LKr > 15 cm Distance to dead cells > 2 cm Status < 4
GAMMAS.
Unassociated clusters at distance from $\pi > 35$ cm Only 3 gamma clusters allowed Status < 4 Within LKr octagon Radial distance at LKr > 15 cm Distance to dead cells > 2 cm Distance between gamma and any other cluster > 10 cm Energy > 3 GeV at first stage. Changed to > 5 GeV after trigger studies Apply projective correction to gamma clusters Cut against interactions in DCH1
CENTER OF ENERGY.
COG of the event < 2 cm.
VERTEX.
$z_{\rm CDA}$ vertex from intersection of track with z axis. CDA < 6 cm Select combination that gives best π^0 mass. Get z_{π^0} vertex Vertex dist $\lvert z_{\rm CDA} - z_{\pi^0}\rvert < 400$ cm Vertex dist $\lvert z_{\rm CDA} - z_{\pi^0}^{second}\rvert > 400$ cm Neutral vertex position -1000 $< z_{\pi^0} <$ 8000 cm

MOMENTA AND MASSES.
Apply blue field correction. Calculate vertex coordinates (x_{bf}, y_{bf}) Compute gamma directions using $(x_{bf}, y_{bf}, z_{\pi^0})$ vertex Compute kaon mass and momentum and direction Final kaon energy in range $54 < \mathrm{E}_K < 66$ GeV Kaon mass within 10 MeV of PDG mass. Calculate T^*_π
BACKGROUND.
Cut against gammas overlapping in electromagnetic calorimeter.
TRIGGER CUTS.
L1 trigger: Projection cut at 10 cm Emin > 5 GeV L2 trigger: T^*_π <80 MeV

Table 5.3: Summary of reconstruction of $K^\pm \to \pi^\pm \pi^0 \gamma$ events and complete list of cuts used in the analysis.

Chapter 6

Trigger Efficiency and Trigger-Related Corrections

As described in chapter 4, the trigger chain for collection of decays with only one charged particle in the final state consists of two stages: the L1, which is fired by electromagnetic clusters (L1 bit 0) and the L2, which is fired by the charged track (MFAKE bit).
It must be kept in mind that the trigger logic was designed to take $K^{\pm} \rightarrow \pi^{\pm}\pi^{0}\pi^{0}$ events with a maximum efficiency and a minimum systematic bias. Therefore, some of the implemented conditions are not optimal for $K^{\pm} \rightarrow \pi^{\pm}\pi^{0}\gamma$ decays.
To make sure that there is no bias introduced by the trigger in the extraction of the Direct Emission and Interference components, special care must be taken in the monitoring of all possible trigger dependencies on the kinematical variables, as these could distort the measured W distribution.
For that purpose, L1 and L2 efficiencies have been measured from control data samples recorded through minimum bias triggers.
For the L1, the trigger efficiency dependency on the clusters energies and relative positions has been studied using events with three gammas in the calorimeter. As a result, a cut has been added in the selection of $K^{\pm} \rightarrow \pi^{\pm}\pi^{0}\gamma$ events, which checks on the minimum distance between gamma clusters as seen by the Neutral Trigger projections. In addition, a correction has been computed as a function of the photons energies and applied to simulated events.
For the L2, the effect of the trigger on the T^{*}_{π} distribution has been studied using data and Monte Carlo simulation, leading to the implementation of a cut at T^{*}_{π} $<$ 80 MeV in the final $K^{\pm} \rightarrow \pi^{\pm}\pi^{0}\gamma$ selection.
The whole procedure is described in detail in the following sections.

6.1 Trigger efficiency measurement

The method used for the calculation of the efficiency of a generic trigger T consists in the following steps. First, a control sample must be defined, selecting all recorded events from a specific L2 bit. This control sample should not have any correlated inefficiencies with the trigger T under study and should constitute a so-called minimum biased data set. Then, a selection of signal events is performed on the control sample. Finally, a check is done on whether the trigger T condition was satisfied or not for the selected signal candidates. Normally the information stored in the Pattern Units (see chapter 3) is used for this purpose. The trigger efficiency is defined as the ratio of the number of signal events satisfying the T conditions with the total number of signal events reconstructed in the minimum biased control sample.

Two main problems can arise in this procedure. Minimum bias triggers are usually heavily downscaled so that the read-out bandwidth is not saturated with uninteresting events. As a consequence the size of the control sample available is often smaller than desired, giving rise to large statistical errors in the trigger efficiency calculation. Especially when dependencies of the trigger efficiency on specific variables need to be checked, statistical issues are very often the limiting factor in order to decide whether a dependency is present or not. In addition, care must be taken to assure that there are not correlated inefficiencies between minimum biased triggers and the trigger under study.

Once the trigger efficiency ϵ is calculated, its error is determined by the binomial distribution as:

$$\sigma(\epsilon) = \sqrt{\frac{\epsilon(1-\epsilon)}{N}} \tag{6.1}$$

where N is the number of events in the control sample.

6.2 The Level One (L1) Trigger Efficiency: NT-PEAK and (Q1+Q2) signals

In order to study the L1 efficiency, signal events passing through the L2 MFAKE trigger have been selected. Using the information stored in the pattern units it is possible to reconstruct the logic conditions satisfied by these events as seen by the trigger system.

It was expected that $K^{\pm} \to \pi^{\pm}\pi^{0}\gamma$ events would access the data sample through the NUT(npeaksloose) condition inserted in the bit 0 of the L1 signal. Indeed, it was found that 99.9 % of the selected events had fired the L1 bit 0. Out of those, 98.9 % fired the NUT(npeaksloose) signal. The percentage of events firing the different L1 bit 0 conditions is summarized in table 6.1

Logic signal within L1 bit 0	Percentage of events (%)
NUT(npeaksloose)	98.9
Q1/D1*NUT(LKrmbias)	11.4
L1 KMU3-PRE signal	Negligible

Table 6.1: Percentage of $K^{\pm} \to \pi^{\pm}\pi^{0}\gamma$ events collected through the main L2 trigger bit (MFAKE) satisfying the three possible L1 bit 0 conditions. Almost all signal events pass the NUT(npeaksloose) requirement.

As the NUT(npeaksloose) signal is dominant in the acquisition of $K^{\pm} \to \pi^{\pm}\pi^{0}\gamma$ events, its behavior determines the sample's composition and must be carefully studied.

Note that all L1 signals are actually in coincidence with the (Q1+Q2) requirement, which provides the fine-time information to the MBX processors. Therefore, the efficiency of this signal must also be investigated.

6.2.1 Bad NT-PEAK periods

The NT-PEAK behavior was thoroughly studied in the main NA48/2 analysis of the $K^{\pm} \to \pi^{\pm}\pi^{0}\pi^{0}$ charge asymmetry. $K^{\pm} \to \pi^{\pm}\pi^{0}\pi^{0}$ events allow to precisely monitor the Neutral Trigger System behavior.

In figure 6.1 the NT-PEAK inefficiency as measured with a confirmed sample of $K^{\pm} \to \pi^{\pm}\pi^{0}\pi^{0}$ events is shown [54].

During the beginning of the 2003 run the inefficiency for $K^{\pm} \to \pi^{\pm}\pi^{0}\pi^{0}$ decays was found to be less than 1 %. This continued through SS1, except for a short period when it rose to very high values ($\sim$ 70 %). After an intervention in the NUT, the inefficiency went back to normal value.

Another problem arose at the end of SS1, extending up to beginning of SS2. During that time the NT-PEAK trigger bit had a huge rate. For this reason the bit was switched OFF from the L1 strobe to MBX, and also from the L2 for some time. During this period the inefficiency was again very high.

In order to cope with the high rates, the NT-PEAK condition was tightened from the OR of the peak signal in both projections ($n_x > 2$ OR $n_y > 2$) to a requirement on the Y projection only ($n_y > 2$). With this condition the inefficiency was $\sim$ 40

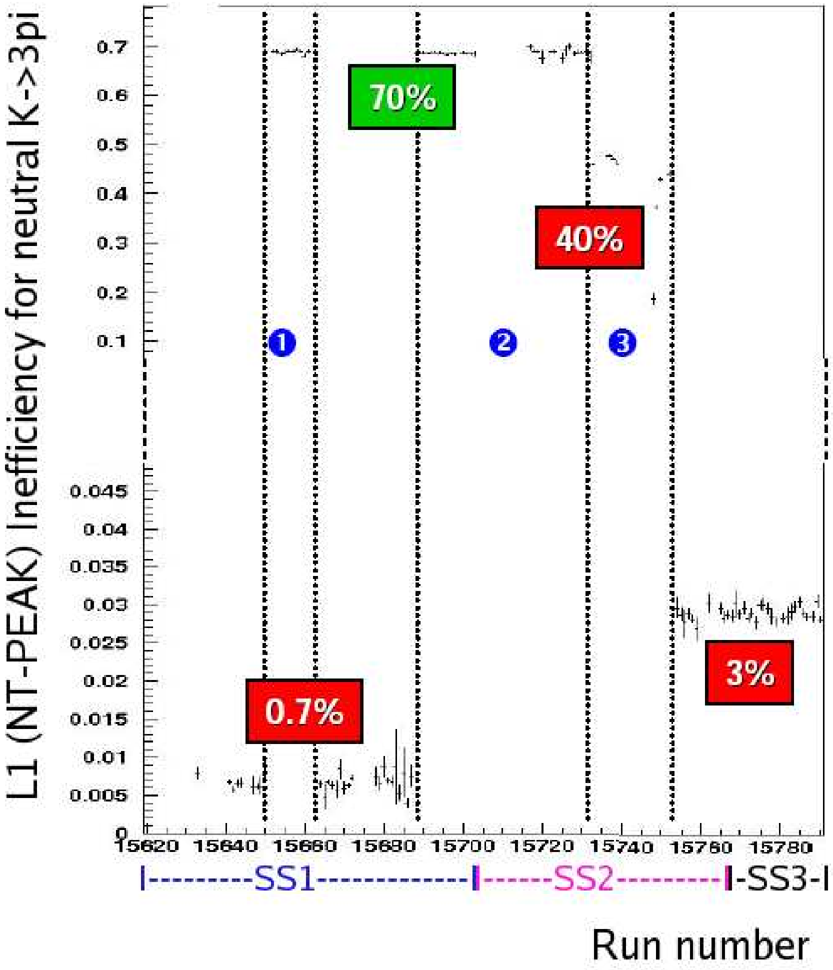

Figure 6.1: L1 (NT-PEAK) trigger inefficiency computed for $K^\pm \to \pi^\pm\pi^0\pi^0$ events in the NA48/2 main analysis [54]. MFAKE&LKrmbias (see section 6.2.3) is used as control sample. Three periods with high inefficiencies can be clearly distinguished. These have been discarded in the $K^\pm \to \pi^\pm\pi^0\gamma$ analysis.

%.

Finally, another hardware intervention in the Neutral Trigger System recovered most of the inefficiency, which then remained at the 3 % level. However, the initial value of less than 1 % was never recovered.

All problematic periods for the NT-PEAK signal have been excluded from the $K^\pm \to \pi^\pm\pi^0\gamma$ sample used in this work.

6.2.2 The NT-PEAK condition

The NT-PEAK signal has been already discussed in chapter 4 as given by the logic condition of (n_x >2 OR n_y >2), were n_x, n_y are the number of peaks found by the neutral trigger system in the X, Y projections respectively.
Figure 6.2 shows an example of how two different kinds of three-clusters events would be seen by the NT-PEAK trigger. The two octagons represent the X and Y views of the LKr calorimeter. On each projection two calorimeter cells are readout together, defining a 4 cm × 4 cm grid. The number of peaks in a given projection is given by the number of 4 cm strips firing for that particular event. The plot illustrates how an event (in orange) with three well separated clusters in the calorimeter, can be seen as only two peaks by at least one of the neutral trigger projections. This effect produces an inefficiency of a geometrical type. In addition, if one of the clusters is not energetic enough to fire the corresponding projection, then an energy-dependent inefficiency is produced.

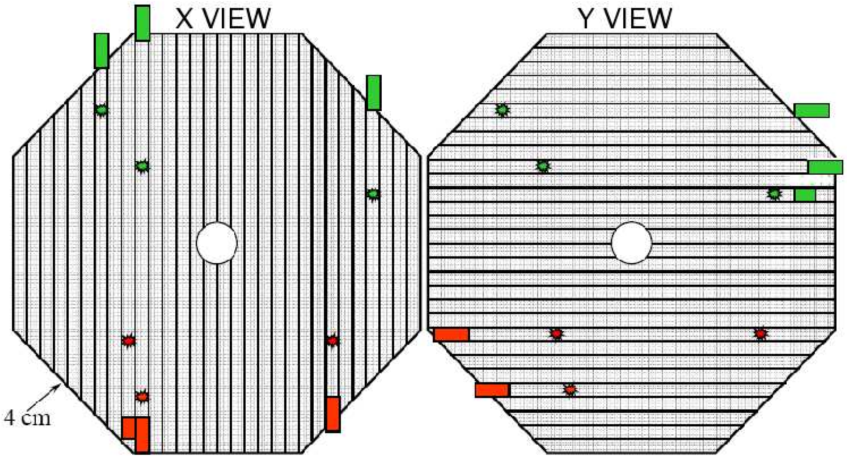

Figure 6.2: X and Y projections defined by the Neutral Trigger on the LKr calorimeter. For the event depicted in green, three peaks can be separated in the X projection (n_x=3) and three peaks in the Y projection (n_y=3). However, for the event in orange, the Neutral Trigger System is able to distinguish only two peaks in Y (n_y=2), even if there are three clusters well separated in the Lkr.

6.2.3 Selection of Control Sample for NT-PEAK in $K^{\pm} \to \pi^{\pm}\pi^{0}\gamma$ analysis

In order to study the NT-PEAK efficiency, there are several possible choices for the control sample.
One possibility is to select events for which the L2 MFAKE trigger bit was ON, and that had passed through the LKrmbias part of the L1 bit 0. The coincidence of these two signals will be denoted as MFAKE&LKrmbias. The L1 condition is checked using the Pattern Units.
As the MFAKE was the main trigger for the collection of *neutral events*, it was not downscaled. This allows for large statistics in the control sample. Events collected at L1 by the LKrmbias bit form an unbiased subsample, as the only requirement in the LKrmbias signal is that the energy deposited in the LKr is greater than 10 GeV.
Another option for the control trigger is to use the NT-NOPEAK bit. However, this signal had a big downscaling factor (80), resulting in a very small statistical power for the trigger efficiency calculation. In addition the NT-NOPEAK condition required that the total energy deposited in the calorimeter was bigger than 15 GeV, so it cannot be used to study effects at low energies.
Another possibility for the control sample is to select events collected through the T0N trigger, but this bit was also heavily downscaled (by a factor of 200) and correlated inefficiencies were found between the T0N signal and the NT-PEAK signal for events with low energy.
This effect is shown in table 6.2. where data from the last half of SS3 has been analyzed. $K^{\pm} \to \pi^{\pm}\pi^{0}\gamma$ decays have been selected with a cut on the minimum gamma energy greater than 3 GeV and with the T0N or MFAKE&LKrmbias L2 bits ON. This condition defines two control samples of 234 and 3176 events, with NT-PEAK efficiencies of 97 ± 1 % and 94.4 ± 0.4 % respectively. The projection cut has been already applied in the selection (see section 6.2.5)
The same procedure has been repeated setting the minimal photon energy to 5 GeV. The T0N sample is reduced by ~ 23 % (from 234 to 181), while the MFAKE&LKrmbias sample is reduced by ~ 30 % (from 3176 to 2225) with respect to the previous energy cut. This means that the T0N sample contains relatively less events with low energy photons than the MFAKE&LKrmbias sample. In addition, the NT-PEAK efficiency almost does not change when computed using the T0N sample (from 97 ± 1 % to 96 ± 1 %). This is in contradiction with the expectation that the NT-PEAK will be more efficient for high energy

photons. However, the NT-PEAK efficiency clearly improves with the cut at 5 GeV when MFAKE&LKrmbias is used as control trigger (from 94.4 ± 0.4 % to 97.3 ± 0.3 %)

This can be explained by the fact that T0N and NT-PEAK signals are both inefficient for the same kind of events, which is called correlated inefficiency. In other words, the T0N sample does not contain already the type of events for which the NT-PEAK is inefficient, biasing the NT-PEAK efficiency measurement towards higher values.

Therefore, only the MFAKE&LKrmbias signal is an adequate control sample for the measurement of the NT-PEAK efficiency for $K^{\pm} \rightarrow \pi^{\pm}\pi^{0}\gamma$ decays.

	Efficiency(%)	
Control Trigger	E>3GeV	E > 5 GeV
T0N	97 ± 1 (234)	96 ± 1 (181)
MFAKE&LKrmbias	94.4 ± 0.4 (3176)	97.3 ± 0.3 (2225)

Table 6.2: NT-PEAK efficiency calculated from two control samples (T0N and MFAKE&LKrmbias) with two different cuts on the minimum photon energy (E>3 GeV and E>5 GeV). $K^{\pm} \rightarrow \pi^{\pm}\pi^{0}\gamma$ decays have been selected from last half of SS3. Number of events in the control sample are indicated in brackets. T0N sample looses 23 % of events with E > 5 GeV while MFAKE&LKrmbias looses 30 %. As expected, the NT-PEAK efficiency calculated from MFAKE&LKrmbias significantly improves for higher energies. However, its value does not change when using T0N as control trigger. This indicates a correlated inefficiency between T0N and NT-PEAK signals for events with low energetic photons.

6.2.4 Determination of NT-PEAK efficiency dependencies. The use of three-gamma events.

The number of $K^{\pm} \rightarrow \pi^{\pm}\pi^{0}\gamma$ events in the MFAKE&LKrmbias sample in SS123 is indeed big enough for a measurement of the overall NT-PEAK efficiency with an absolute error of the order of 0.1 %. However, it is still too small for studying possible dependencies, especially if different data taking periods need to be considered separately.

Figure 6.3 shows the shape of the NT-PEAK efficiency as a function of W for $K^{\pm} \rightarrow \pi^{\pm}\pi^{0}\gamma$ events in SS3. The minimum required photon energy is 3 GeV and none of the L1 trigger-related cuts specified in table 5.3 have yet been applied. The shape of the NT-PEAK efficiency is found to be compatible with a flat distribution, however the statistics are too small to give a precise statement, specially at high W. However, one must keep in mind that the NT-PEAK efficiency does not directly depend on W, but on the clusters energies and positions. Events from $K^{\pm} \rightarrow \pi^{\pm}\pi^{0}\gamma$ decays must have at least three clusters in the calorimeter, coming from the three photons in the final state. The interaction of the charged pion in the LKr may produce one or more clusters, or no clusters at all. In order to simplify the study of the NT-PEAK efficiency only the gamma clusters will be considered.

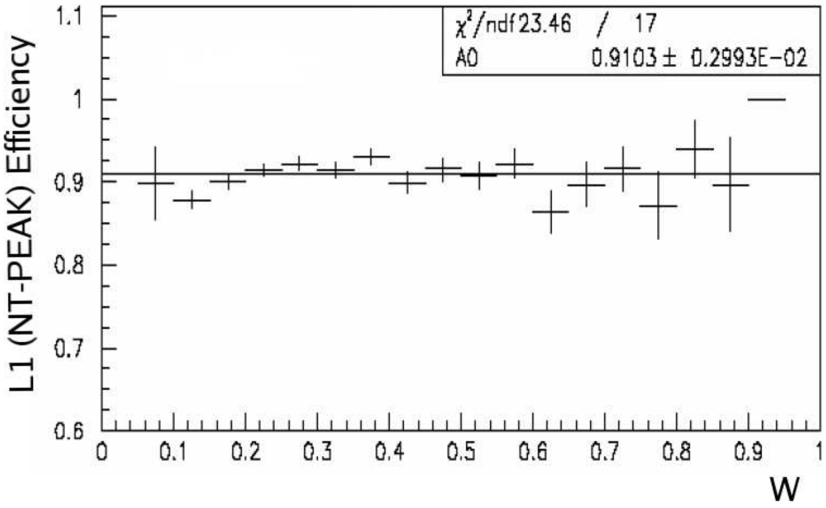

Figure 6.3: L1 (NT-PEAK) efficiency as a function of the W variable for $K^{\pm} \rightarrow \pi^{\pm}\pi^{0}\gamma$ events in SS3. Events satisfying the MFAKE&LKrmbias are used for the control sample. The measured NT-PEAK efficiency is 90.5 ± 0.4 %

Under this assumption, the condition of (n_x >2 OR n_y >2) will be fulfilled only if:

- The gamma clusters are separated enough in at least one of the projections, so that they can be disentangled by the neutral trigger system. The relevant variables are the distances between pairs of clusters in X and Y views.
- The three gamma clusters are energetic enough so that they fire the corresponding strip signal. The relevant quantity is the energy of the less energetic photon in the event.

In order to extract the dependencies of the NT-PEAK signal with these variables, there is no need to use only $K^{\pm} \rightarrow \pi^{\pm}\pi^{0}\gamma$ events; all events with three gammas can be used.

Therefore, the control sample available for trigger efficiency computation can be increased by a factor of $\sim$ 100, just by releasing the standard COG and kaon mass cuts and selecting, in addition to $K^{\pm} \to \pi^{\pm}\pi^{0}\gamma$, all $K^{\pm} \to \pi^{\pm}\pi^{0}\pi^{0}$ decays with one gamma out of the acceptance. This allows to compute geometrical and energy trigger-related corrections with negligible statistical error.

6.2.5 Projection Cut and Energy Dependence from all events with three gammas.

In order to study the geometrical dependencies of the NT-PEAK signal some notation has to be introduced. Let us denote the distance between any two photons (i,j) at a given coordinate in the calorimeter x,y as dist_X^{ij} and dist_Y^{ij}. Let us also define dist_{NUT}^{min} as the minimum distance between clusters required by the Neutral Trigger System in order to disentangle the two signals in any given projection.

For three clusters the condition $\text{n}_X > 2$ ($\text{n}_Y > 2$) is satisfied only if the minimum of the three possible dist_X^{ij} (dist_Y^{ij}) values is greater than dist_{NUT}^{min}. In other words, if any of the photon pairs (i,j) has a distance in one of the projections smaller than dist_{NUT}^{min}, then that pair cannot be separated by the NUT system, and the condition for detecting more than 2 peaks cannot be fulfilled in that view.

This can be expressed as:

$$\text{If } \text{dist}_X^{min} > \text{dist}_{NUT}^{min} \text{ then } n_X > 2 \longrightarrow \text{NTPEAK geometrically efficient}$$

$$\text{If } \text{dist}_Y^{min} > \text{dist}_{NUT}^{min} \text{ then } n_Y > 2 \longrightarrow \text{NTPEAK geometrically efficient}$$

As the NT-PEAK logic requires the OR of the conditions in the projections ($\text{n}_X > 2$ OR $\text{n}_Y > 2$), either one must be satisfied for the event to be taken. This is equivalent to demanding that the maximum of the minimum distances in the two projections $\text{Max}(\text{dist}_X^{min},\text{dist}_Y^{min})$ is greater than dist_{NUT}^{min}.

Figure 6.4 (a) shows the distribution of $\text{Max}(\text{dist}_X^{min},\text{dist}_Y^{min})$ for events in the first period in SS1. Figure 6.4 (b) shows the L1 (NT-PEAK) trigger efficiency as a function of this variable. A clear drop can be observed in the efficiency for distances smaller than 10 cm.

In order to exclude the inefficient region a cut in $\text{Max}(\text{dist}_X^{min},\text{dist}_Y^{min}) > 10$ cm has been included in the final $K^{\pm} \to \pi^{\pm}\pi^{0}\gamma$ selection, reducing the statistics by 3 %.

The energy dependency of the NT-PEAK signal has also been checked in this

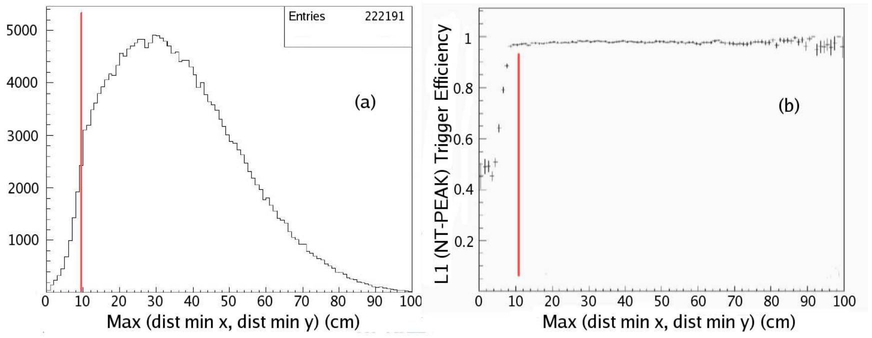

Figure 6.4: (a) Distribution of the maximum of the minimum distances between photon pairs in X and Y for all three-gamma events in first period of SS1. A cut at 10 cm reduces the statistics by 3 %. (b) L1 (NT-PEAK) trigger efficiency versus the maximum of the minimum distance in X and Y for same events. A clear drop in the efficiency is seen for distances smaller than 10 cm.

sample. Figure 6.5 (a) shows the NT-PEAK efficiency as a function of the minimum gamma energy in the event before applying the projection cut (black) and after applying a cut at 10 cm (purple) and at 20 cm (blue). A big dependency can be seen for small energies, followed by a plateau after $\sim$ 5 GeV. The projection cut at 10 cm increases the global efficiency by $\sim$ 2 %, but the shape of the efficiency curve versus minimum energy does not basically change. A projection cut at 20 cm does not improve the global efficiency any further. The same procedure

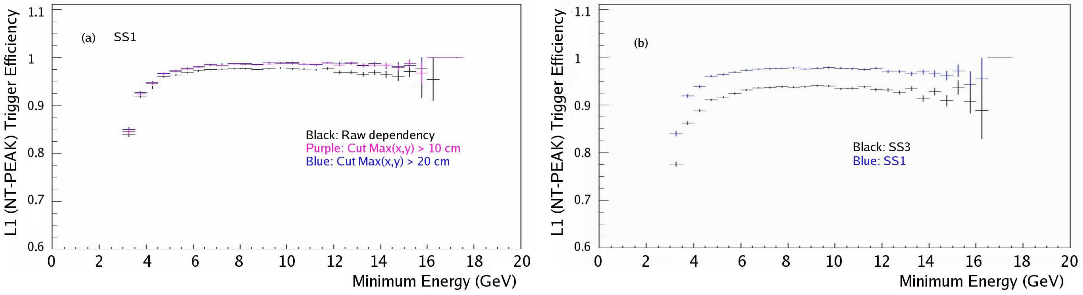

Figure 6.5: (a) L1 (NT-PEAK) trigger efficiency for all three gamma events in first part of SS1 versus the minimum energy of the gammas in the event for different values of the projection cut. A clear dependency can be seen for energies below 5 GeV. (b) L1 (NT-PEAK) trigger efficiency for all three gamma events in first part of SS1 (blue curve) and in SS3 (black curve) versus the minimum energy of the gammas in the event. No projection cut was applied to any of these samples. There is a global decrease of the L1 efficiency in SS3.

was repeated for data events in SS3 and a smaller global NT-PEAK efficiency was found. Figure 6.5 (b) shows the NT-PEAK efficiency as a function of the minimum gamma energy in the event before the projection cut was applied, for events in SS1 and in SS3. The shape of the efficiency curve is rather similar in both cases, but a global decrease is seen for events in SS3. The source of this decrease needed to be investigated, in order to ensure a proper treatment of the problem.

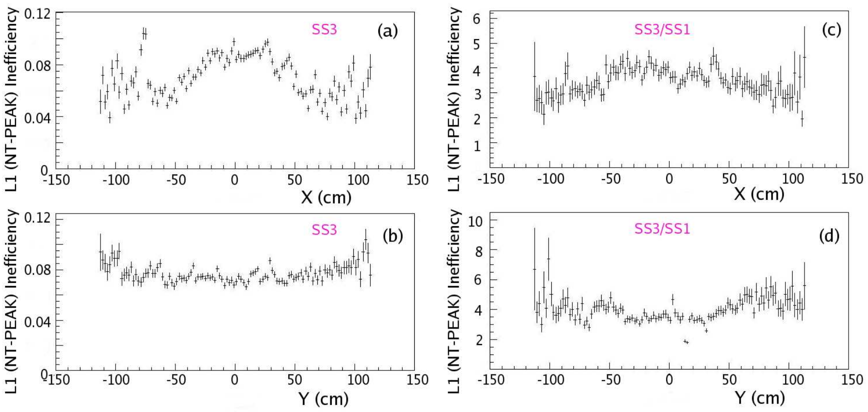

Figure 6.6: L1 (NT-PEAK) trigger inefficiency for all three gamma events in SS3 versus its x (a) and y (b) coordinates at the LKr. No dependency of the trigger inefficiency on the position can be seen from these plots. Figures (c) and (d) show the ratio of inefficient events in SS3 with respect to ones in SS1 as a function of its x, y coordinates in the LKr. The ratio is flat, indicating that the inefficiency showing up in SS3 does not arise from local effects.

Tests were performed in order to check whether there was a localized problem in a certain region of the calorimeter. This is illustrated in figure 6.6. The x, y coordinates of clusters in all inefficient events have been plotted. No particular region of the calorimeter seemed to be affected. In addition, these distributions were divided by the corresponding ones using events in SS1. This ratio is flat, showing that there are no new local effects in SS3.

The behavior in the two projections was also studied. The NT-PEAK efficiency is expected to drop only when both dist_X^{min} and dist_Y^{min} are smaller than 10 cm. In that case neither the $n_X > 2$ nor the $n_X > 2$ condition would be satisfied. This is indeed the behavior observed in SS1. However, a different behavior was observed in SS3. This is explained in detail in the following and shown in figure 6.7.

Let us require the dist_X^{min} to be greater than 35 cm. In that case the $n_X > 2$ condition must have been satisfied, and the NT-PEAK trigger should be effi-

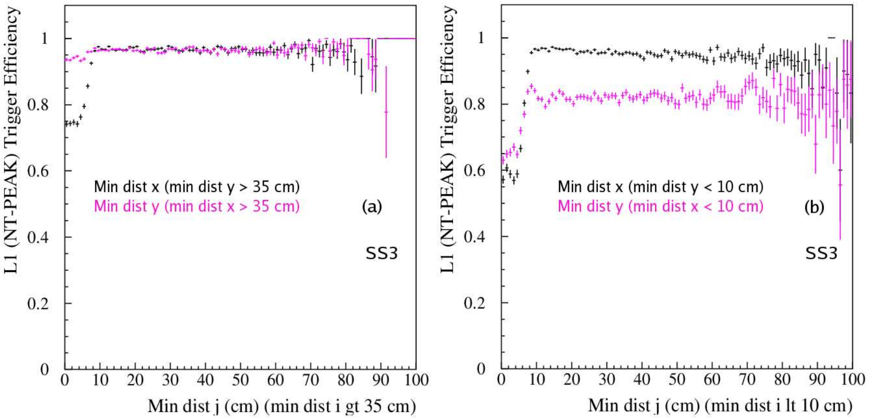

Figure 6.7: L1 (NT-PEAK) trigger inefficiency for all three gamma events in SS3 as a function of the minimim distance in projection j (j=x,y) under two different conditions: (a) requiring in the projection i (i=y,x) a minimum distance between photon pairs greater than 35 cm, (b) requiring in the projection i (i=y,x) a minimum distance between photon pairs smaller than 10 cm. The plots show a global inefficiency in the NUT Y projection.

cient regardless of the dist_Y^{min}. This is shown in the purple curve of figure 6.7 (a), where the NT-PEAK efficiency versus the dist_Y^{min} is plotted for events with $\mathrm{dist}_X^{min} > 35$ cm. This curve is flat and no dependency of the efficiency is found as a function of dist_Y^{min}, as expected. Let us now perform the same procedure in the other view. This is shown in the black curve. The NT-PEAK efficiency versus the dist_X^{min} is plotted for events with $\mathrm{dist}_Y^{min} > 35$ cm. In this case the $\mathrm{n}_Y > 2$ condition should be automatically satisfied and the NT-PEAK signal should be efficient independently of the value of dist_X^{min}. However the black curve shows a clear drop for $\mathrm{dist}_X^{min} < 10$ cm. This indicates a problem in the Y projection of the NUT system, that is only recovered when the $\mathrm{n}_X > 2$ condition has been satisfied.

Another test can be done requiring dist_Y^{min} to be less than 10 cm. In that case the Y projection of the NUT will most probably not have fired and the NT-PEAK efficiency should be dependent only on the dist_X^{min}. This is shown in the black curve in figure 6.7 (b), where the NT-PEAK efficiency versus the dist_X^{min} is plotted for events with $\mathrm{dist}_Y^{min} < 10$ cm. The trigger signal is more than 95 % efficient for $\mathrm{dist}_X^{min} > 10$ cm, as expected. Let us now require the dist_X^{min} to be less than 10 cm. This is shown in the purple curve. The NT-PEAK efficiency versus the dist_Y^{min} is plotted for events with $\mathrm{dist}_X^{min} < 10$ cm. Even for $\mathrm{dist}_Y^{min} > 10$ cm, the NT-PEAK efficiency is never completely recovered, and it reaches a value of ~ 80 % only. This confirms the hypothesis of a global inefficiency in the Y projection of the Neutral System.

Figure 6.8 shows the distribution of events in SS3 as a function of the dist^{min} variable for both X (a) and Y (b) NUT views. The curve in black represent all events in the control sample, the curve in purple only the events satisfying the NT-PEAK condition. There is a lack of efficient events for $\text{dist}_X^{min} < 10$ cm.

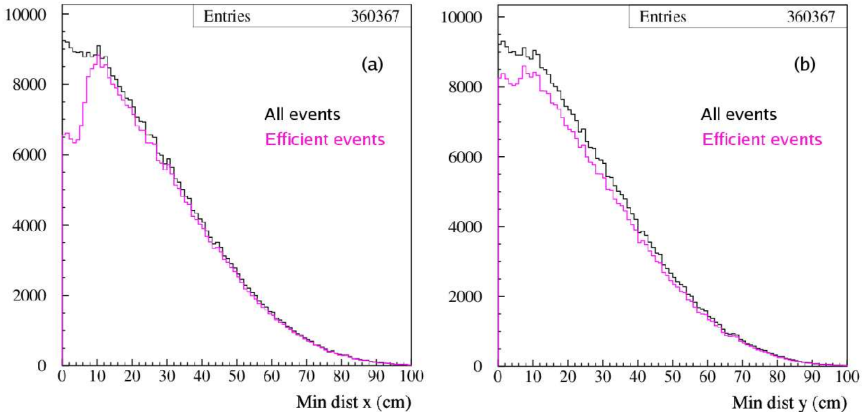

Figure 6.8: Distributions of dist_X^{min} (a) and dist_Y^{min} (b) for all three gamma events in SS3. All events in the control sample (black) are plotted together with the ones satisfying NT-PEAK condition (purple). A clear drop in the efficiency can be seen for $\text{dist}_X^{min} < 10$ cm.

Therefore the projection cut has been changed from the requirement applied in SS1 of $\text{Max}(\text{dist}_X^{min},\text{dist}_Y^{min}) > 10$ cm, to a condition in the X projection only of $\text{dist}_X^{min} > 10$ cm. This cut rejects 20 % of the events in that particular subsample.

Table 6.3 shows the final set of cuts implemented in the $K^\pm \to \pi^\pm\pi^0\gamma$ selection related to L1 trigger efficiency studies.

In addition, the dependency of the NT-PEAK efficiency on the minimum gamma energy has been recomputed after the projection cut has been applied. The resulting curve has been implemented as a correction to the gamma energies in the Monte Carlo simulation, in order to properly take into account any possible energy distortion caused by the L1 trigger.

The NT-PEAK efficiency for $K^\pm \to \pi^\pm\pi^0\gamma$ events in the whole SS123 sample has been calculated after all these cuts have been applied. Figure 6.9 shows the results for every run. A global efficiency of 97.4 ± 0.1 % has been obtained from a control sample of 15896 events.

Cut	Run 15620 to 15752	Run 15753 to 15790
Projection cut	Max(dist_X^{min},dist_Y^{min})$>$ 10 cm	dist_X^{min}>10 cm
Minimum energy cut	(E > 5 GeV)	

Table 6.3: Cuts implemented in the $K^{\pm} \to \pi^{\pm}\pi^{0}\gamma$ selection related to L1 trigger efficiency studies. A difference in the behavior of the NUT Y view was found from run 15753, so the implementation of the projection cut needed to be changed.

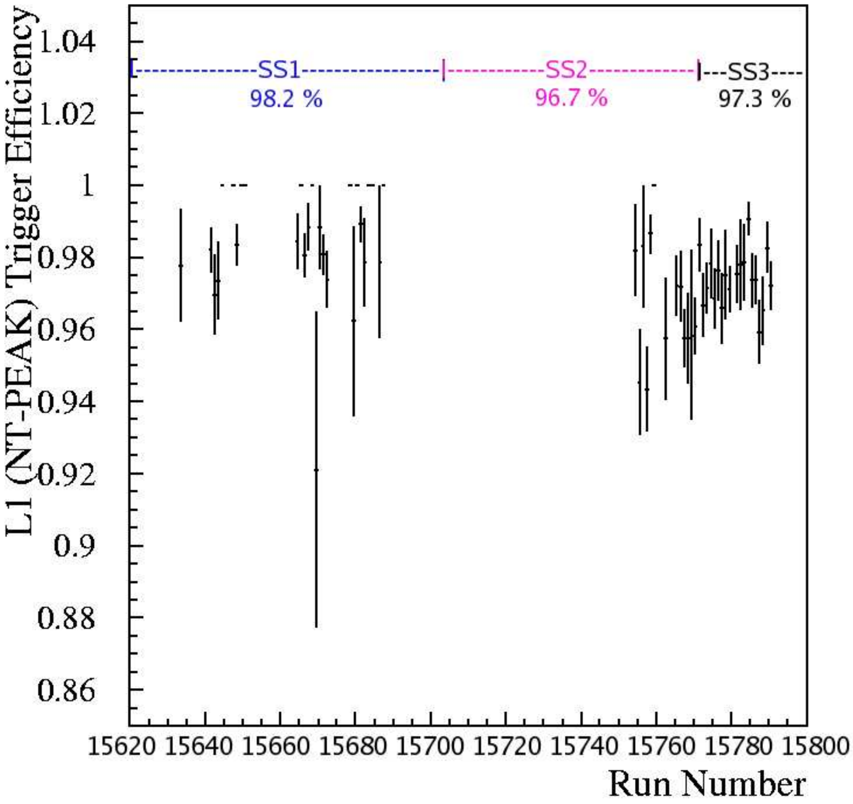

Figure 6.9: L1 (NT-PEAK) trigger efficiency for every run in SS123 after all cuts. The final NT-PEAK is ∼ 97 % and only variations of ∼ 1 % remain.

6.2.6 The (Q1+Q2) efficiency

For events with only one track, the (Q1+Q2) signal is dominated by the Q1 condition.

The Q1 efficiency for $K^{\pm} \to \pi^{\pm}\pi^{0}\gamma$ events has been also checked, using the NT-PEAK L2 bit for defining the control sample. From a control sample of 1024 events no inefficient events were found. This sets a limit in the Q1 efficiency of $>$ 99.7 % at 90 % confidence level.

6.3 The Level Two (L2) Trigger Efficiency: MFAKE condition

As explained in chapter 4 the main trigger for collection of $K^{\pm} \rightarrow \pi^{\pm}\pi^{0}\gamma$ events was the MB-1TRK-P or MFAKE trigger. This trigger was designed to reject $K^{\pm} \rightarrow \pi^{\pm}\pi^{0}$ decays, effectively requiring that $T^{*}_{\pi} < 90$ MeV. Due to resolution effects, the trigger condition modifies the T^{*}_{π} distribution for values in the vicinity of 90 MeV.

As shown in figures 2.1 and 2.2, there is a strong correlation between the T^{*}_{π} and the W variables. Distortions in the T^{*}_{π} distribution for high values of T^{*}_{π} will directly translate into distortions of the W distribution for small W values, affecting the extraction of the fractions of DE and INT components.

The behavior of the MFAKE trigger was studied both with data events and with simulated events.

6.3.1 L2 Studies with Data Events

In order to study the MFAKE efficiency for $K^{\pm} \rightarrow \pi^{\pm}\pi^{0}\gamma$ events the NT-PEAK signal was used to define the control sample. Figure 6.10 shows the L2 trigger efficiency for events in SS3 with different cuts applied in the T^{*}_{π} variable. In plot (a) the MFAKE efficiency for events in the range $55 < T^{*}_{\pi} < 90$ MeV is shown as a function of W. The upper T^{*}_{π} cut is just the offline version of the MBX cut. A clear dependency is seen for W < 0.3. As already mentioned, this can be explained as resolution effects. The measured global efficiency with this condition is 88.4 ± 0.7 %. In (b) the upper cut was tightened from 90 MeV to 80 MeV. A substantial improvement in the efficiency can be seen for small W values. In plot (c) the lower cut on T^{*}_{π} has been released to 0 MeV. The efficiency of the MFAKE trigger as a function of W shows a behavior compatible with flat. The global L2 efficiency has increased to 95.7 ± 0.6 %.

Therefore, in order to get rid of the observed edge effect, the T^{*}_{π} cut was set on the offline selection to $T^{*}_{\pi} < 80$ MeV. This means a reduction of $\sim 30\%$ in the number of events.

It must be noted that the region of high W values cannot be properly checked with this control sample, as it is populated with very few data events. This is a very important region for the extraction of the Direct Emission component, so the lack of statistics in the study of the L2 trigger behavior from data is not very satisfactory. However, no effects are expected from the L2 inefficiencies at high

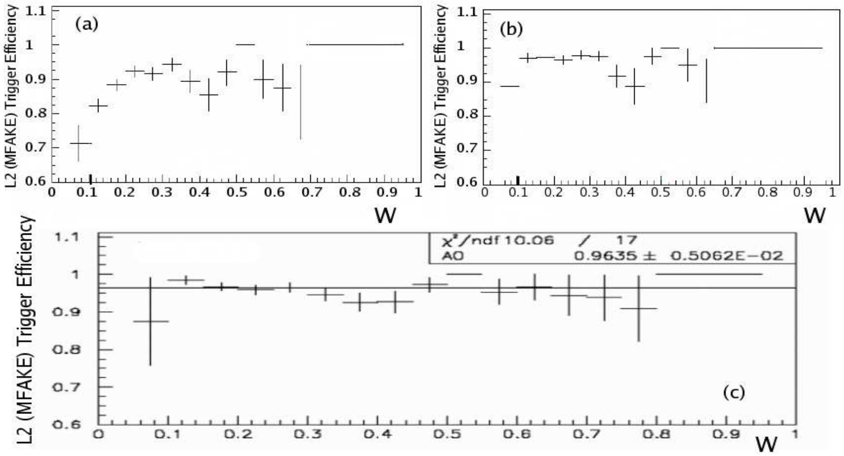

Figure 6.10: (a) L2 (MFAKE) trigger efficiency versus W for $K^{\pm} \rightarrow \pi^{\pm}\pi^{0}\gamma$ candidates in SS3 in the range $55 < T^{*}_{\pi} < 90$ MeV. A big inefficiency can be seen for small W values. (b) L2 (MFAKE) trigger efficiency versus W for $K^{\pm} \rightarrow \pi^{\pm}\pi^{0}\gamma$ candidates in the region $55 < T^{*}_{\pi} < 80$ MeV. The trigger efficiency improves for small W values with this tightened cut for high T^{*}_{π} . (c) L2 (MFAKE) trigger efficiency versus W for $K^{\pm} \rightarrow \pi^{\pm}\pi^{0}\gamma$ candidates within $0 < T^{*}_{\pi} < 80$ MeV. The shape of the MFAKE efficiency is compatible with flat in W.

W values, as they correspond to small T^{*}_{π} and these are far away from the MBX trigger cut.

In order to explore the high W region and to confirm the conclusions drawn from data, further studies on the trigger behavior have been done using simulated events.

6.3.2 L2 Studies with Simulated Events

As explained in chapter 3, the MBX processors use only information coming from the DCHs in order to compute the trigger response. In the NA48 Monte Carlo simulation all experimental conditions, like beamline magnets polarities, spectrometer magnet polarities, DCH wire efficiencies maps, bad cells in the LKr calorimeter are included in a run dependent way. In particular, the inclusion in the simulation code of the wire efficiency maps as reconstructed from data events, allows a reliable modeling of the trigger response.

The same code used online by the MBX processors to build the final trigger decision has been implemented in the Monte Carlo simulation. It produces a response in the same format as in data events. In order to compute the efficiency of one particular MBX bit, a control sample can be defined from all simulated events. Out of those, events with a positive massbox response are efficient. Different Monte Carlo samples of $K^{\pm} \to \pi^{\pm}\pi^{0}\gamma$ Inner Bremsstrahlung and Direct Emission events have been produced, and the corresponding MFAKE efficiencies calculated as function of the W variable. The results for Inner Bremsstrahlung simulation are shown in Fig. 6.11.

Plot (a) shows the MFAKE trigger efficiency as a function of W for $K^{\pm} \to \pi^{\pm}\pi^{0}\gamma$

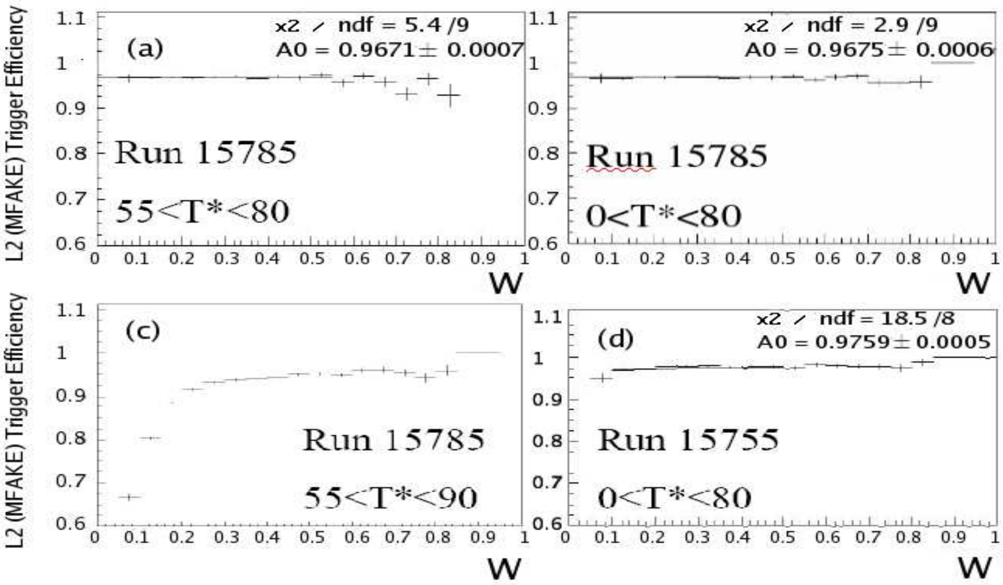

Figure 6.11: The L2 trigger efficiency for different samples of Inner Bremsstrahlung simulated events. The L2 trigger behavior is compatible with flat in W only if the cut on $T^{*}_{\pi} < 80$ MeV is applied.

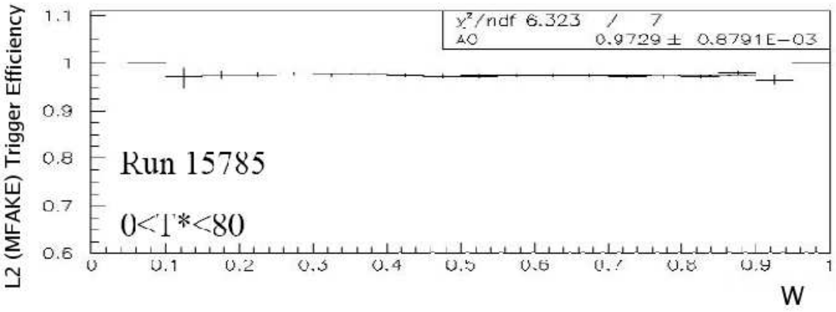

Figure 6.12: The L2 trigger efficiency for a sample of Direct Emission simulated events with $T^{*}_{\pi} < 80$ MeV. The L2 trigger behavior is flat in W, also for high values of W.

simulated IB events for run 15785 in the range of $55 < T^*_\pi < 80$ MeV. The region of W< 0.5, where most of the events lie, has been fitted to a constant. The fit quality shows that the shape of the efficiency is compatible with flat. The fitted constant is $\sim$ 97 %, which is of the same order as the efficiency measured in data. Plot (b) shows the same run in a different T^*_π region (0< T^*_π < 80 MeV). As expected, releasing the lower T^*_π cut increases the number of events at high W. The fitted constant is still $\sim$ 97 %. Plot (c) shows the behavior of the MFAKE efficiency as a function of W when the upper T^*_π cut is released to 90 MeV. A clear drop in the trigger efficiency develops for small W values. Plot (d) shows again the trigger efficiency versus W for the (0< T^*_π < 80 MeV) region, but for another run. A small dependence can still be seen for small W. However, it must be kept in mind that only events in the range of 0.2<W<0.9 have been used in the final fit, so any residual effect in the small W region will not affect the fit results.

The results for Direct Emission simulation are shown in Fig. 6.12. This is the most appropiate sample to check the MFAKE efficiency behavior for high W values. Events have been reconstructed in the $0 < T^*_\pi < 80$ MeV region. The trigger efficiency is fitted to a constant for W > 0.5. A very good fit quality is obtained, showing no dependence of the MFAKE efficiency for high W, as expected.

Chapter 7

Monte Carlo Simulation.

When studying any physical process, the original distributions are modified by the detector acceptance and response, and the selection cuts. Monte Carlo simulations are used to deconvolute these effects from the observed data distributions. The simulation allows one to extract the acceptance of the apparatus, which is usually too complex to be modeled analytically, and also the efficiency of the selection program.

The official NA48 Monte Carlo simulation [55] is based on Geant 3 [56], a CERNLIB software package which is able to propagate all particles through the defined detector, simulating their interactions with matter.

Four stages can be identified in the NA48 simulation code: beam simulation, decay simulation, simulation of the detector response and raw data format simulation. In every one of these steps considerable effort has been invested to reproduce the experimental conditions in the most accurate way.

In this work Monte Carlo simulations have been used for a number of purposes:

- Perform L2 trigger studies (chapter 6) Due to the accurate simulation of detector conditions on a run by run basis a reliable simulation of the trigger response can be implemented. This has been used to obtain confirmation of the trends seen in data for the L2 inefficiencies with higher statistical power.

- Carry out specific studies in order to estimate possible systematic effects and optimize the selection criteria (section 7.12)

- Perform background studies (chapter 8). Simulated samples of potential background decay modes have been produced to optimize the cuts rejection power and evaluate their final contribution to the sample.

- Obtain the reconstructed W distributions for Inner Bremsstrahlung , Direct Emission and Interference terms separately, after all acceptance, detector and trigger effects have been considered. These shapes are needed in order to extract the relative amounts of DE and INT with respect to IB present in the data sample using the Maximum Likelihood method (chapter 9)

In the following sections all different simulation steps, the production of different samples of simulated events and some specific studies performed on these samples are explained in detail.

7.1 Beam simulation

The transport of the kaons through the beam line is simulated using the TURTLE [57] program. All the parameters, like beam line magnets currents, are adjusted such that the relevant experimental distributions seen at the downstream detectors are reproduced. For this purpose $K^{\pm} \to \pi^{\pm}\pi^{+}\pi^{-}$ decays are used. The momentum and the COG distribution of these events at DCH1 are monitored in data on a run by run basis, and the code parameters tuned accordingly so that the beam spectrum and position are reproduced in the simulation. This is done separately for K^{+} and K^{-} beams.

7.2 Kaon decay simulation. The $K^{\pm} \to \pi^{\pm}\pi^{0}\gamma$ event generator.

In the standard NA48 simulation, only one decay mode is simulated at a time. The probability of a kaon decay occurring at a particular longitudinal position z, is given by the kaon energy and lifetime. The user can define an energy range and decay position range, for which the generated events will be tracked. Kaons with energies or decay positions outside the selected ranges will be discarded at an early stage, and the decay particles will not be tracked through the detectors. Therefore, in order to properly take into account resolution effects, it is very important that the ranges selected at generation stage are wider than those selected after reconstruction. For the generation of $K^{\pm} \to \pi^{\pm}\pi^{0}\gamma$ events the generated kaon energy was required to be within the ranges ($50 < E_{K} < 70$) GeV and ($-2200 < z_{K} < 9000$ cm).

The matrix element of the decay under study is implemented in the so-called *event generator*. For $K^{\pm} \to \pi^{\pm}\pi^{0}\gamma$ event generators for IB, DE and INT were implemented separately, so that the three terms could be independently studied. In all three cases, the decaying particles four momenta were first generated in the kaon rest frame, according to a flat 3-body phase-space distribution. For this purpose, the standard CERNLIB code GENBOD [58] was used. Then, a weight given by the corresponding matrix element was applied to the events with the hit or miss technique. Finally, the decaying particles were boosted back into the laboratory frame.

For $K^{\pm} \to \pi^{\pm}\pi^{0}\gamma$ decays the matrix element was initially coded from the expression given in [4]:

$$\begin{aligned}\frac{d^2R^{\pm}}{dE_{\gamma}dE_{\pi}} = \frac{\alpha}{4\pi^2}\frac{p_{\pi}^2}{m_K^3}sin^2(\theta)\Bigg[&\frac{|A_2^+|^2}{\left(\frac{1}{2}m_K - E_{\pi^0}\right)^2}\\ &+2cos(\pm\phi + \delta_1^1 - \delta_0^2)\frac{|A_2^+||A_0|EE_{\gamma}}{m_K^2\left(\frac{1}{2}m_K - E_{\pi^0}\right)}\\ &+(|E|^2 + |M|^2)\frac{E_{\gamma}^2}{m_K^4}\Bigg]\end{aligned} \tag{7.1}$$

The meaning of all variables in the expression has been already discussed in chapter 1. This is the same as equation 1.11 if $\frac{m_{\pi}^2 - m_{\pi^0}^2}{2m_K}$ terms are neglected.

Again, the first term in the sum, corresponding to the IB contribution, can be factorized out. The set of weights implemented for IB, DE and INT were therefore given by:

$$M_{IB} = \frac{p_{\pi}^2 sin^2(\theta)}{\left(\frac{1}{2}m_K - E_{\pi^0}\right)^2} \tag{7.2}$$

$$M_{DE} = M_{IB}W^4 \tag{7.3}$$

$$M_{INT} = M_{IB}W^2 \tag{7.4}$$

$$\tag{7.5}$$

where W is given by equation 1.13 and global multiplicative constants have been set to one.

However, it was found that the term proportional to $m_{\pi}^2 - m_{\pi^0}^2$ cannot be neglected for small values of W. If the term in $\frac{m_{\pi}^2 - m_{\pi^0}^2}{2m_K}$ is considered, the IB matrix element is singular for $E_{\pi^0} = \frac{m_K}{2} - \frac{m_{\pi}^2 - m_{\pi^0}^2}{2m_K}$, which corresponds to the kinematic limit of the $K^{\pm} \to \pi^{\pm}\pi^{0}\gamma$ decay.

At the kinematic limit, E_{π^0} and T_{π}^* are maximal, while the odd gamma energy is minimal, corresponding to small W values. Therefore, a larger number of events is generated at small W if the complete expression is used for the matrix element M_{IB}.

This is illustrated in figure 7.1 for a sample of IB events. IB events were generated, first neglecting the term in $\frac{m_\pi^2 - m_{\pi^0}^2}{2m_K}$ (called old) and then including it (called new). The ratio of the W distribution of both samples (new/old) has been plotted. The new distribution, where all terms are considered, has more events at small W.

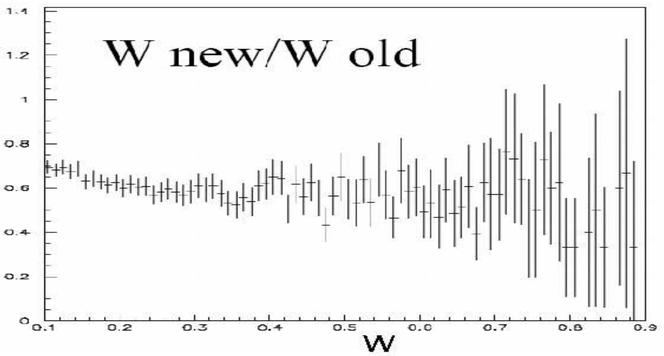

Figure 7.1: Ratio of W distributions after and before correcting the matrix element for the difference of the squares of neutral and charged pion masses. A slope is present for small W values.

The complete expression was finally used to calculate the appropriate weights:

$$M_{IB} = \frac{p_\pi^2 sin^2(\theta)}{\left(\frac{1}{2}m_K - E_{\pi^0} - \frac{m_\pi^2 - m_{\pi^0}^2}{2m_K}\right)^2} \tag{7.6}$$

$$M_{DE} = M_{IB}W^4 \tag{7.7}$$

$$M_{INT} = M_{IB}W^2 \tag{7.8}$$

7.3 Decays of π^0 and $\pi^\pm$

The $K^\pm \rightarrow \pi^\pm \pi^0 \gamma$ decay contains two unstable particles in the final state, the $\pi^\pm$ and the π^0.

The charged pion decays most of the time to a $\mu\nu$. The branching ratio of this reaction is BR($\pi \longrightarrow \mu\nu$)=(99.98770 ± 0.00004)%

As the π's mean free path is cτ= 7.8045 m, the pion decay can occur within the experimental volume, affecting the characteristics of the reconstructed track. The π decay in flight is implemented in the NA48 simulation.

The neutral pion decays most of the time to two gammas (BR($\pi^0 \longrightarrow \gamma\gamma$)= (98.798 ± 0.032)%). The second most important decay mode for the π^0 is the Dalitz decay, with a branching ratio of (1.198 ± 0.032) %. Only the pion decay to two gammas has been considered in the $K^\pm \rightarrow \pi^\pm\pi^0\gamma$ simulation.

Due to its short mean free path ($c\tau$= 25.1 nm), the π^0 travels very little before decaying. As the resolution in the longitudinal decay position in NA48 is of the order of 1 m, the distance between the π^0 decay point and the kaon decay position cannot be resolved. Therefore, in the NA48 simulation, the π^0 decay is assumed to occur at the same position as the kaon decay.

7.4 Detector response

Once the decay particles have been produced, they are boosted and traced through the detector. The complete detector geometry and matter composition has been incorporated in the simulation code. The physical processes simulated by GEANT are positron annihilation, bremsstrahlung, Compton scattering, decay in flight, δ-ray production, hadron interaction, continuous energy loss, multiple scattering and photoelectric effect. The photoelectric effect is the only process that the NA48 simulation does not require GEANT to simulate.

Conversions of photons into electron-positron pairs are therefore present in the simulation. These occur mostly in the Kevlar window and in the DCH mylar planes.

All magnetic fields measured in the decay volume, like the blue-field, have been modeled, and the measured map of the dipole magnetic field in the spectrometer has also been included.

The simulation of shower development into the NA48 calorimeters is a very time consuming task. In order to speed up the production of simulated events, a complete shower simulation is produced beforehand, and the output written into a shower library file [59]. The file contains the energy deposited channel-by-channel into the calorimeters by single particle events and can be read back by the simulation program.

Twenty of such files are available, each consisting of three shower sets: 24800 photon showers, 24800 electron showers and 10450 pion showers, with an energy spectra similar to those of data events.

When a photon, electron or pion enters the calorimeter, a shower is picked at random from the file in the corresponding energy bin and in a position inside the calorimeter cell corresponding to the impact point. The cell energy "binning" is

2 MeV for photons and electrons and 0.5 MeV for pions. The shower box in the LKr calorimeter is 51 × 51 cells for pions, and 19 × 19 cells for gammas and electrons.

A gaussian energy response of the LKr calorimeter has been simulated. The simulated DCH momentum resolution is based on the muon runs measurements and then eventually tuned to match the kaon mass resolution reconstructed in data for $K^{\pm} \to \pi^{\pm}\pi^{+}\pi^{-}$ decays, on a run-by-run basis.

7.5 Signal readout simulation and data format

After tracking the particles in the detector, the energy deposited is digitized and the reconstruction is done in the same way as for data.

DCH wire efficiencies, bad LKr calorimeter cells, etc, are included in the simulation in a run dependent way, so experimental conditions are reproduced in the most accurate way.

The DCH efficiency maps are measured from data and inserted into the simulation code. For every wire, its efficiency is given as a function of the charged particle impact position along the wire. Simulation of pathological readout cards is also implemented. This has allowed for a reliable simulation of the L2 trigger.

The format of simulated events is the same as the one of data events, but for the addition of the generated (true) quantities, and for the treatment of the time variables. For simulated events, a set of variables is available, containing the true values of the kaon and decay particles momenta, energy, decay position, etc, as produced at the time of generation by the simulation program. In the simulation, time is treated consistently within any sub detector, but absolute time values are not correlated between sub detectors in the way they are in data. This is not needed as long as accidental effects do not have to be simulated. By default accidental events are not simulated in the NA48 code. Therefore, every simulated event contains only information on one particular kaon decay, and the information given by different sub detectors is in-time by definition.

7.6 Standard Corrections

In order to get the best possible simulation of all experimental conditions, some extra effects have also been modeled. Some of these must be corrected for a posteriori, in the same way as it is done for data events.
For the LKr, the projective shape has been implemented by applying a correction to the simulated clusters energies and positions. The simulated effect has been already shown in figure 5.2.
Non-gaussian tails on the clusters energy measurement appear due to photon nuclear interaction with the LKr nuclei, tending therefore to underestimate the amount of energy deposited in the electromagnetic shower. These tails have been parameterized from data events and a correction has been implemented for simulated clusters energies modeling their effect.
In order to simulate the variations of the invariant three charged pions masses seen in data, the position of DCH4 and the spectrometer magnetic field strength have been modified in the simulation on a run by run basis. Therefore, a correction for this effect had to be calculated [60], which can be applied to simulated events in the same way as for data events.

7.7 Implementation of the L1 Trigger Correction

As already explained in chapter 6, the L1 trigger efficiency, which is maily affected by the NT-PEAK condition, is a function of the minimum photon energy in the event and has been computed from all events with three gammas in SS123.
To model the effect of the L1 trigger, the measured shape has been implemented in the simulation using a hit or miss technique. For every simulated event, the minimum gamma energy is calculated and the event is taken with a probability given by the corresponding trigger efficiency in that energy bin.
The effect of the L1 efficiency correction on the W distribution is shown in figure 7.2 (b). The ratio of W distributions after and before applying the correction is computed for simulated IB events with $E_{min}>$ 3 GeV. The correction is only significant for small W values. If the requirement in the minimum photon energy is changed to be greater than 5 GeV, the effect of the correction is much lower.
Figure 7.2 (a) shows the ratio of minimum photon energy distribution in data

and IB simulation, before (black) and after (red) applying the L1 correction. The agreement between data and simulation clearly improves after the correction is applies, especially for small energies.

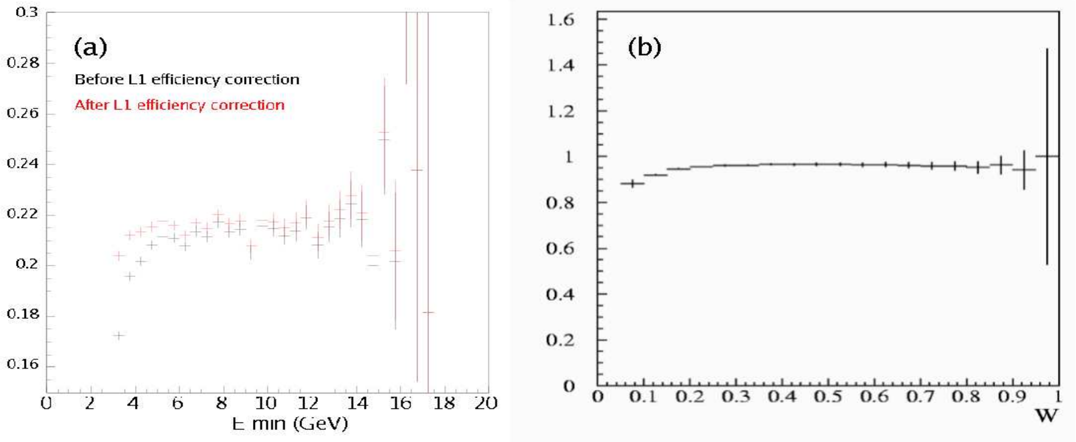

Figure 7.2: (a) Ratio of minimum photon energy distributions for data with respect to simulation. Poor agreement is found at small energies before applying the L1 trigger efficiency correction to the simulated events (black curve). The agreement improves after the correction is made (red curve). (b) Ratio of W distribution for simulated events with photon energies greater than 3 GeV, after and before applying the L1 efficiency correction. The correction is more important for small W values.

7.8 Monte Carlo productions for IB, DE and INT

Samples of simulated events have been produced for IB, DE and INT separately. This has been done on a run-by-run basis in order to properly take into account the variations of the data taking conditions.

For every run, the number of reconstructed data events was calculated, and a proportional number of simulated events was produced. This was done separately for positive and negative kaon decays.

These productions have been done at CERN, using lxbatch resources. A set of jobs was sent to the batch system per run and per kaon charge. Each job used a different seed for the random number generator and produced 200 10^3 $K^{\pm} \rightarrow \pi^{\pm}\pi^0\gamma$ decays, using one given shower library file, chosen at random among the 20 available.

For IB two samples have been produced, every one containing ~ 5 times the number of events reconstructed in the SS123 data sample. The first of these productions (IBS1) has been used to obtain the final result concerning the fractions of DE and INT with respect to IB present in the data sample. The other sample (IBS2) has been used to perform systematic checks in a statistically independent way (see chapter 9). For all studies in this chapter only IBS1 has been used.

Figure 7.3 shows the ratio of reconstructed data events to reconstructed simulated events in IBS1 for every run. To compare the IB sample with a data region dominated by Inner Bremsstrahlung events, and where the effect of Direct Emission can be neglected, the reconstructed W value is required to be less than 0.5. In addition, the minimum photon energy is 5 GeV and the L1 trigger correction has been already implemented in the simulated sample. These are the standard conditions for the comparisons between data and simulated events (see section 7.11). The plot shows that ~ 4.5 times more events are reconstructed after all cuts in the IBS1 with respect to data. This factor is constant for all runs.

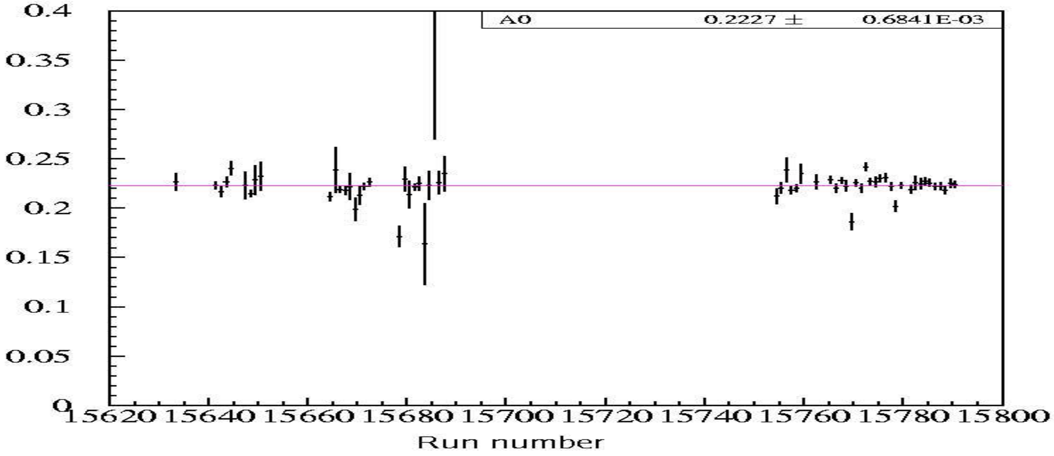

Figure 7.3: Ratio of number of reconstructed data events in SS123 to number of reconstructed events in IBS1 for every run. The L1 trigger efficiency correction has been already implemented in the simulated sample and the minimum photon energy has been set to 5 GeV. A cut on $W < 0.5$ has also been required. The number of reconstructed events in the simulation is about 4.5 times the number of reconstructed data events for every run.

For DE and INT two samples were produced, each containing ~ 10 times the number of events expected in data. For DE and INT, all the simulated statistics available has been used for the final extraction of the decay components.

A sample of 45 million $K^{\pm} \rightarrow \pi^{\pm}\pi^{0}\pi^{0}$ decays has been produced as well on a run-by-run basis. This was needed in order to study the possible background contamination from this channel (see chapter 8)

Bad NTPK periods are also excluded from the simulated data, in order not to alter the composition of the samples with respect to data.

The number of events in the samples is summarized in table 7.1. The first column contains the number of generated events in the fiducial volume; the second column, the number of reconstructed events requiring $E_{min} > 3$ GeV; the last column contains the final number of events in every sample after requiring $E_{min} > 5$ GeV and applying the L1 trigger efficiency correction. The statistics specified in the last column is used in the maximum likelihood method for extraction of the DE and INT components.

	Generated events in fiducial volume	Events after basic cuts ($E_{min} > 3$ GeV)	Events after all cuts $E_{min} > 5$ GeV, L1 eff corr
IBS1	19205282	985983	662913
DE	2230661	117116	90318
INT	2510636	134110	101127

Table 7.1: Number of generated and reconstructed events in the IB, DE and INT samples. Numbers in the last column represent the statistics used in the final fit of the DE and INT components.

For the IB samples a cut $T^{*}_{\pi} < 100$ MeV was implemented at the generation stage. For Inner Bremsstrahlung , the matrix element favours events with high T^{*}_{π} values. However, in the selection $T^{*}_{\pi} < 80$ MeV is required. Therefore, if no cut is made at generation, the program would be highly inefficient, as most events would be generated with too high values of T^{*}_{π} to pass the selection criteria. Applying a cut at 100 MeV speeds up the generation of the IB sample. However, it is important to make sure that no significant amount of events generated with $T^{*}_{\pi} > 100$ MeV would be reconstructed in the $T^{*}_{\pi} < 80$ MeV region due to resolution effects. This check has been made in a sample of 15 million IB events, generated with no T^{*}_{π} cuts. Only one event out of 110991 was reconstructed with $T^{*}_{\pi} < 80$ MeV and a true value of T^{*}_{π} greater than 100 MeV, giving an effect of 10^{-5}.

In addition, early checks have been made on the geometric acceptance. When one of the decay products would lie in a region far away from the detector, the event was not traced and therefore, not included in the output file.

7.9 Resolution of relevant variables

Storing the true values of original variables in the output file for simulated events, allows one to evaluate the experimental resolution for the different variables. This can be simply done by fitting the distributions of the difference between reconstructed and generated values for any given variable. These distributions should be gaussian (at least in a restricted range) with a sigma corresponding to the resolution of the variable.
Table 7.2 shows the resolutions for a set of the most relevant variables in the $K^{\pm} \to \pi^{\pm}\pi^{0}\gamma$ decays for the IB, DE and INT samples.

	Resolution		
Variable	IB	DE	INT
W	$(4.02 \pm 0.01)10^{-3}$	$(5.93 \pm 0.16)10^{-3}$	$(4.82 \pm 0.07)10^{-3}$
Odd γ Energy (MeV)	130.6 ± 0.5	143.5 ± 1.8	138.4 ± 1.5
T^{*}_{π} (MeV)	0.603 ± 0.002	0.536 ± 0.005	0.534 ± 0.005
Kaon Energy (MeV)	374.1 ± 1.2	364 ± 3	370 ± 3
z_{π^0} (cm)	74.6 ± 0.3	80.3 ± 1.1	77.6 ± 0.9

Table 7.2: Resolution of relevant variables measured from the IB, DE and INT samples. The distributions of the difference between reconstructed and generated values for every variable have been fitted to a gaussian in a region close to one sigma.

Variations can be observed in the variables resolutions for the different decays components. In particular, the odd gamma energy has a better resolution for IB ($\sim$ 131 MeV) than for DE ($\sim$ 144 MeV) This is due to the fact that the energy resolution is proportional to the energy, and the IB sample is richer in soft photons.
The W resolution follows the same behavior. This is illustrated in figure 7.4, where the distributions of the difference between reconstructed W values and true W values are plotted for different W bins. These distributions are narrow for small values of W and get broader as W increases.
A gaussian fit has been made to all these distributions, and the corresponding fitted sigmas have been plotted versus the mean W value for every W bin in figure 7.5 (a). The W resolution is never worse than 10^{-2}. Figure 7.5 (b) shows the percent relative resolution, which is of the order of 1 % for $0.2 < W < 0.9$.
In order to make sure that there are not important differences between resolutions estimated with simulation and those present in data, the reconstructed particle masses can be used as references. For the $K^{\pm} \to \pi^{\pm}\pi^{0}\gamma$ decays, the rel-

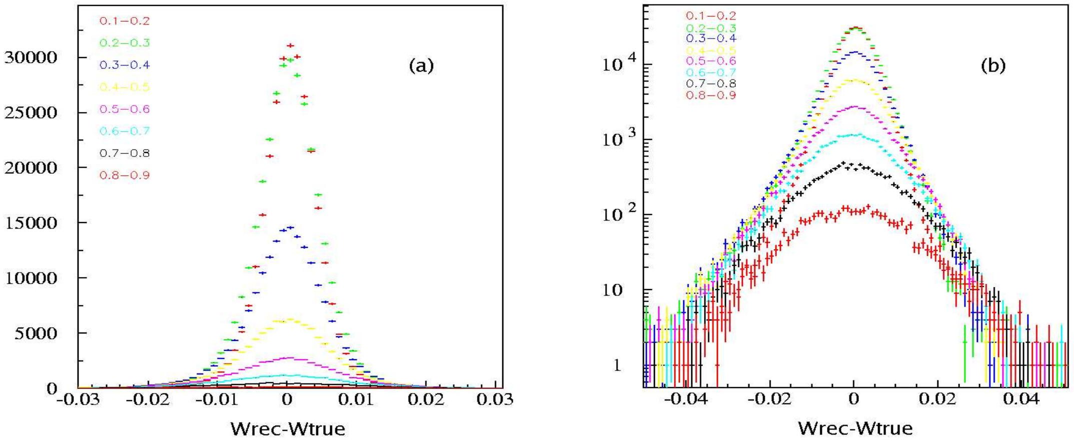

Figure 7.4: Distributions of the difference between the reconstructed value of W and its generated value in bins of W, plotted in linear (a) and logarithmic (b) scale. Distributions get broader as W increases.

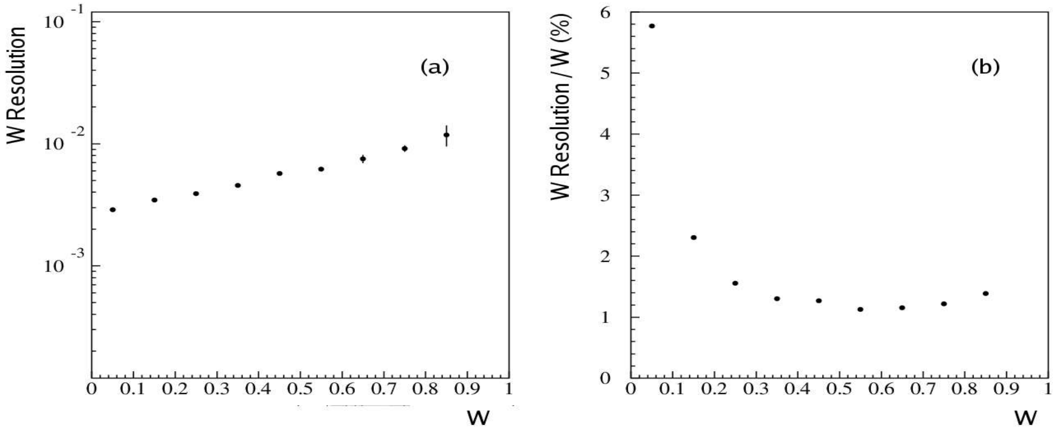

Figure 7.5: (a) Absolute W resolution as a function of W in logarithmic scale. The resolution deteriorates for high W values, reaching a maximum value of $\sim 10^{-2}$. (b) Percent W resolution with respect to the corresponding mean W value. The W resolution is $\sim$ 1 % of its value for $0.2 < W < 0.9$.

evant reconstructed invariant masses are the kaon mass and the π^0 mass. The important advantage of these variables is that their true values are constants. Therefore, the fit of the reconstructed mass distributions give directly the resolution, even for data events. This allows to check whether there are significant differences between real and simulated resolutions.

Figure 7.6 shows the gaussian fits of data and simulated kaon mass and π^0 mass distributions. The mean of the kaon mass distribution in data and simulated events is 493.61 MeV, i.e. $\sim$ 70 keV away from the nominal kaon mass. The sigma is 2.09 ± 0.02 MeV in data and 2.12 ± 0.01 MeV in the simulation, which are compatible. The mean of the neutral pion mass distribution in data is 135.10 MeV and 135.18 MeV in simulation. This offset between data and simulation will be clearly visible when making a ratio of the distributions of data over simulated events. The sigma is 1.82 ± 0.02 MeV in data and 1.82 ± 0.01 MeV in the simulation, in perfect agreement.

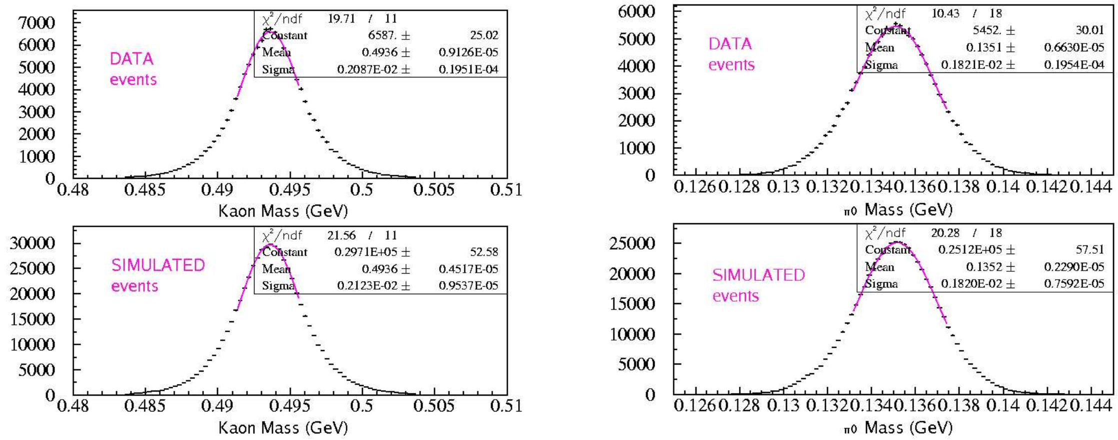

Kaon mass distributions for data and simulated events

π^0 mass distributions for data and simulated events

Figure 7.6: Kaon mass and π^0 mass distributions for Data and Simulated Events. The computed resolutions agree in data and simulation. The π^0 mass distributions shows an offset of $\sim$ 80 keV between data and simulation.

7.10 Acceptance of decay components

The analysis acceptance for a given decay is defined as the number of reconstructed events divided by the total number of events decaying in the fiducial volume.

For $K^{\pm} \to \pi^{\pm}\pi^{0}\gamma$ decays, the acceptance has been computed in bins of W. The result is shown in figure 7.7 for the different decay components. The drop of acceptance for small values of W is mainly due to the requirement that the minimum photon energy in the event is larger than 5 GeV.

Small differences in the shape of the acceptance between different components can be seen at high W values. This is due to the different shape of the W distribution for each of the terms. For the final extraction of the DE and INT components from data, only the range of $0.2 < W < 0.9$ has been considered. In this range the acceptance function is quite flat and similar for all decay terms.

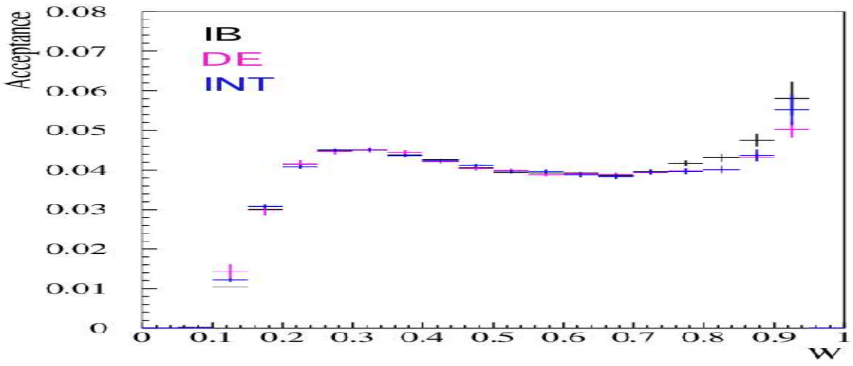

Figure 7.7: Acceptance of IB (black), DE (purple) and INT (blue) terms as a function of the W variable. Small differences in the shape of the acceptance between different components can be seen at high W values. For $0.2 < W < 0.9$, differences between components are negligible and variations as a function of W are smaller than 0.5 %

The integrated acceptance with different selection cuts is shown in table 7.3 for each of the decay components. The L1 efficiency correction has been applied in all cases. The acceptance of the IB term is smaller than that of the others because its W distribution peaks at small W values. The gain in acceptances releasing the cut in E_{min} from 5 GeV to 3 GeV is 30 % for IB, 20 % for DE and 23 % for INT. Requiring $0.2 < W < 0.9$ the acceptance is highly decreased for IB, but it almost does not change for DE and INT.

Decay component	IB	DE	INT
Acceptance standard (%) Emin > 5 GeV All W values	3.452 ± 0.004	4.049 ± 0.013	4.028 ± 0.012
Change in acceptance Emin > 3 GeV All W values	+30 (%)	+20 (%)	+23 %
Change in acceptance Emin > 5 GeV $0.2 < W < 0.9$	-21 (%)	-1.3 (%)	-5 %

Table 7.3: Acceptances for Inner Bremsstrahlung , Direct Emission and Interference $K^{\pm} \rightarrow \pi^{\pm}\pi^{0}\gamma$ simulated events, with standard cuts and relative change when different conditions on minimum energy and W range are applied.

7.11 Comparisons between Data and Monte Carlo

In order to validate the simulation results, many comparisons have been made between the predicted and the data distributions. The main problem of such a comparison is that the data is composed of undetermined amounts of IB, DE and INT; all distributions will be modified depending on the actual fractions of DE and INT components present in the sample. Therefore, comparisons between data and simulated events have been done using only a subsample with reconstructed W values smaller than 0.5. This region is dominated by the Inner Bremsstrahlung component in the data, therefore a comparison with the IB simulation only should be satisfactory.

The final comparison plots are shown in Appendix B. For every variable, the first plot represents the data distribution and the second plot its ratio with respect to IBS1 simulated events. In general a reasonable agreement has been found in all comparisons.

In addition, the ratio of W distributions of data and IB simulated events in all W range is shown in figure 7.8. For small W values, the data and the IB prediction should agree. Indeed, a fit to a constant in the range $0.2 < \mathrm{W} < 0.5$ has a good quality. The effect of Direct Emission can be clearly seen at high W values.

7.12 Specific studies using simulated events

The Monte Carlo simulation is an unique tool to test the effects of possible biases and systematic uncertainties on the relevant distributions, and to optimize the selection criteria.

Several studies have been made to achieve a better understanding of reconstruction and resolution effects in $K^{\pm} \rightarrow \pi^{\pm}\pi^{0}\gamma$ decays. These are described in the following.

7.12.1 Mistagging

The notion of mistagging has been already introduced in chapter 5, referring to a wrong assignment for the two photons coming from the π^0 decay. This implies a wrong assignment of the radiated gamma, distorting the gamma energy measurement and therefore, the W distribution.

A cut has been implemented in the selection requiring that the distance between

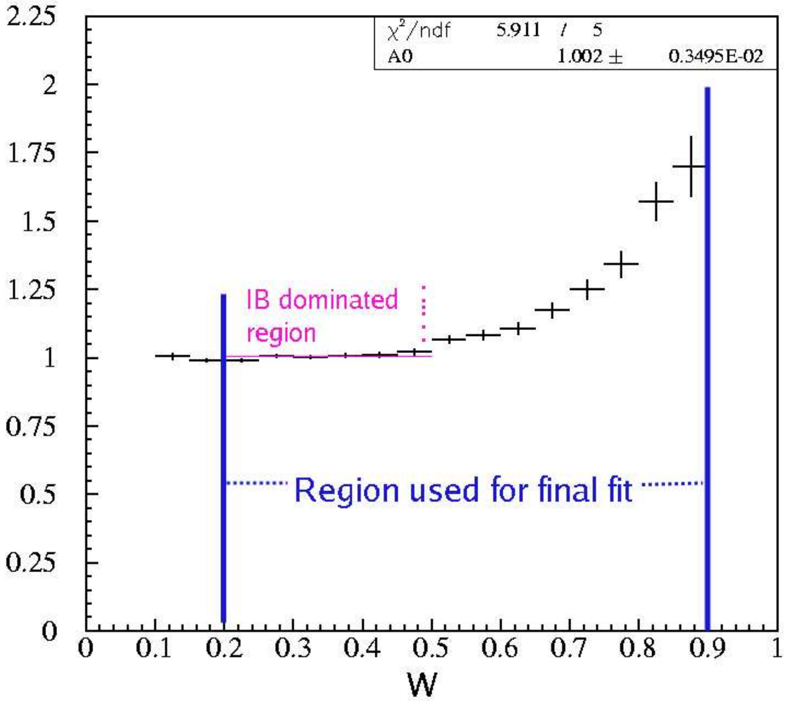

Figure 7.8: Ratio of W distributions for data events with respect to IB simulated events. The ratio is flat for small W and increases for high W, showing the presence of Direct Emission in the data sample.

the second best neutral vertex ($z_{\pi^0}^{second}$), and the charged vertex (z_{CDA}) is greater than 400 cm. The requirement that $|z_{\pi^0}^{second}$-$z_{CDA}|$ is greater than some specific quantity is called *mistagging cut*.

Let us start by studying the odd gamma energy distribution in the IBS1 sample for events passing the standard mistagging cut. Figure 7.9 (a) shows the distribution of the difference between the reconstructed odd gamma energy and the true odd gamma energy ($\Delta E = E_{rec}$-E_{true}) for these events. In the range selected in the plot, this distribution is gaussian and its sigma gives the value of the energy resolution, that is about 130 MeV. However, this distribution has long tails extending beyond the range shown in this plot, corresponding to the residual mistagged events.

In order to study this kind of events in detail, the mistagging cut was removed. In figure 7.9 (b) the analogous distribution is shown for a smaller IB sample, with no mistagging cut applied. For events located in the peak around zero, two photons have been properly assigned to the neutral pion decay, and the right odd gamma has been selected. However, for events in the tails, the wrong photon combination has been taken for the π^0 association. The odd gamma is therefore mistaken, and its assigned energy can be very different from its original value, as the measurement actually belongs to a different cluster.

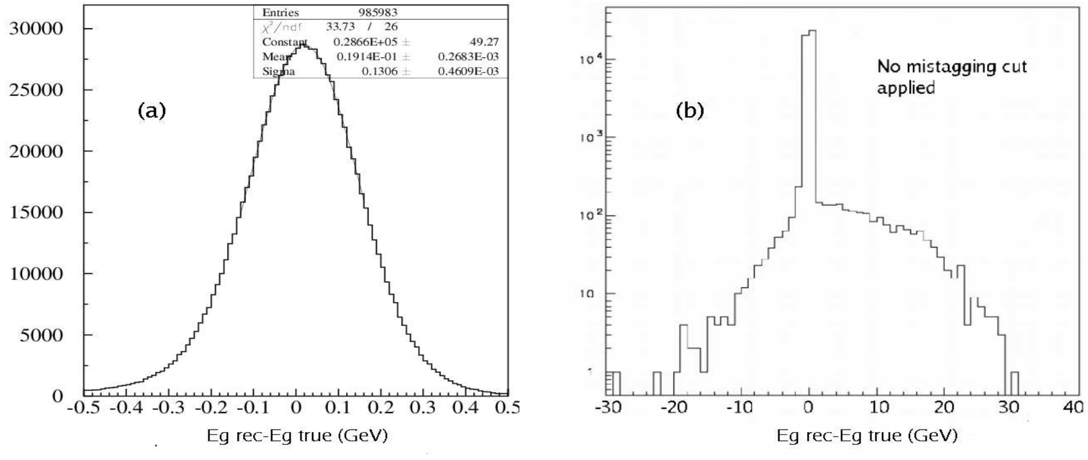

Figure 7.9: (a) Distribution of the difference between the reconstructed and the true odd gamma energy, for events for which this difference is smaller than 0.5 GeV. The whole IBS1 sample has been used in order to compute the gamma energy resolution from a gaussian fit, that is ~ 130 MeV. (b) The same distribution is shown for a reduced sample of simulated events, for which no mistagging cut was applied. Tails are shown extending up to ~ 30 GeV

As the odd gamma resolution is about few hundred MeV, a sample containing only mistagged events can be selected requiring that the reconstructed odd gamma energy differs by more than 2 GeV with respect to the generated value ($|\Delta E| > 2$ GeV). This condition is satisfied by ~ 3 % of the events in the initial sample. The W distribution for these events is shown in figure 7.10 (a). Events with wrong odd gamma assigment populate high W values, even if they belong to a pure IB simulated sample. This can be expected, as no real correlation exists between the actual measured odd gamma properties and the orginal. Therefore, the contribution from this events is very similar to a DE contribution. If this type of events is present in different proportions in data and simulation, the extraction of the Direct Emission component can be biased. Events with reconstructed odd gamma energies within 2 GeV with respect to the generated value (figure 7.10 (b)) show the expected behavior for IB events in the W distribution.

In order to minimize the potential differences in the relative number of mistagged events in data and simulation, the size of the effect itself must be minimized. To find a way of identifying mistagged events in data, the neutral vertex provided by the second best combination of two gammas to be assigned to the π^0 decay

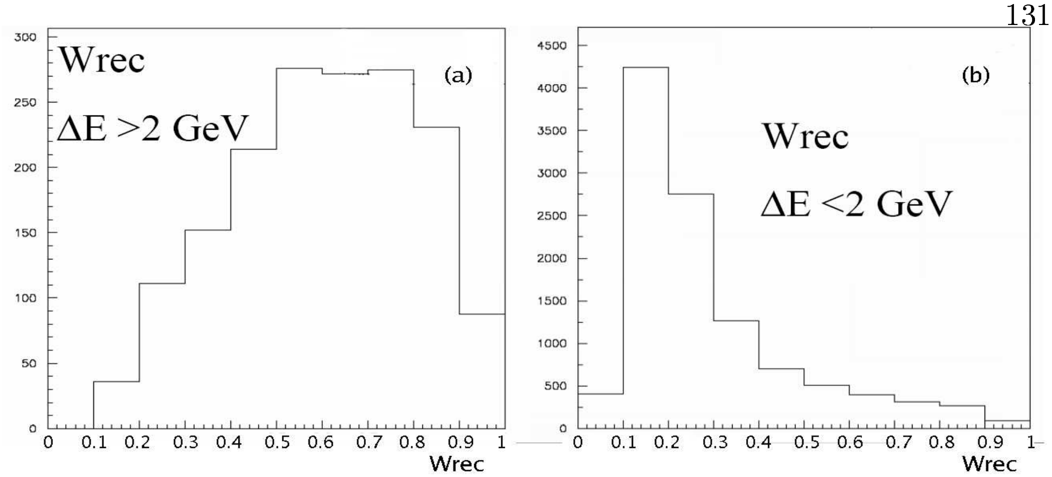

Figure 7.10: (a) W distribution for events in IBS1 for which the reconstructed odd gamma energy differs from its true value by more than 2 GeV. The shape of the W distribution for this subset is completely distorted with respect to that predicted for IB events. (b) W distribution for events in IBS1 for which the reconstructed odd gamma energy agrees within 2 GeV with its true value. For these events the shape of the W distribution is not significantly modified with respect to the IB prediction.

was studied ($z_{\pi^0}^{second}$), using the IBS1 sample. It was found that for mistagged events, there was normally a second solution for $z_{\pi^0}^{second}$ close to the charged vertex z_{CDA}. Actually, more than 97 % of the events with $|\Delta E|$ greater than 2 GeV were rejected requiring the existence of only one solution for the neutral vertex within 400 cm from the charged vertex. This reduces the mistagging effect from a $\sim$ 3 % to less than 0.1 % level.

Figure 7.11 (a) shows the W distribution for events with only one solution for the neutral vertex within 400 cm from the charged vertex (black) and the distribution for all events (red). Events passing the mistagging cut have a shaper W shape, and the number of events with high reconstructed W values has been largely reduced.

The effect of the mistagging cut can also be observed in the ratio of the reconstructed W distribution to the generated W values. When a significant amount of mistagged events is present, this ratio is not flat, and a rise is observed for large W values. This is shown in figure 7.11 (b), where the value of the mistagging cut has been changed from 0 to 800 cm. As the mistagging cut gets tighter, this ratio flattens up.

In order to quantify the effect of different values of the mistagging cut, a *mistagging probability* has been defined as the fraction of events with $|\Delta E|$ greater than

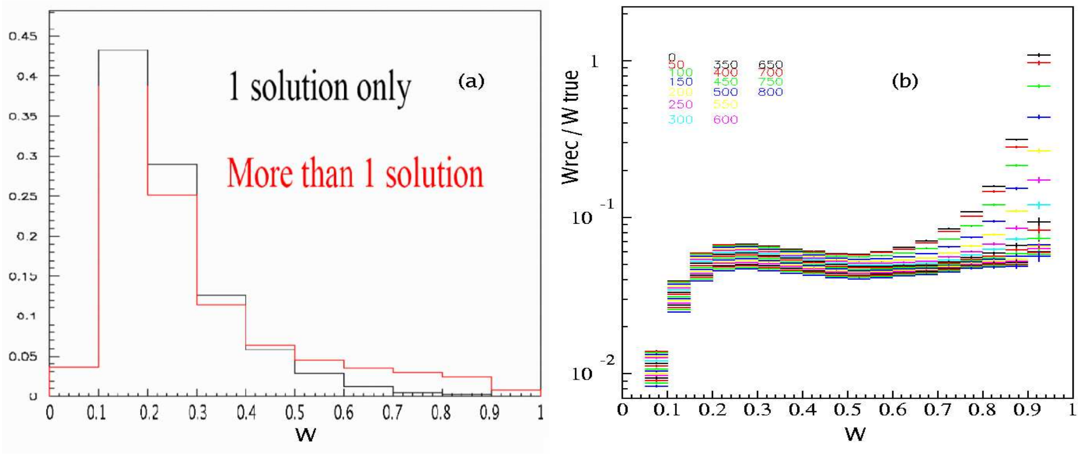

Figure 7.11: (a) W distribution for events with one solution only (black), and with more than one solution (red) for the gamma combination to be associated with the π^0 providing a z_{π^0} within 400 cm from the z_{CDA}. (b) Reconstructed W over true, for different values of the mistagging cut. As the mistagging cut gets tighter, this ratio flattens up for high W values.

2 GeV with respect to the total number of events in the sample. This quantity has been computed for $|z_{\pi^0}^{second} - z_{\mathrm{CDA}}|$ ranging from 0 to 800 cm for IB, DE and INT samples. The result is shown in figure 7.12. If no mistagging cut is applied, the mistagging probability is of order few percent for all decay components with significant differences in their values (3.2 % for IB, 2.4 % for DE and 2.8 % for INT). For mistagging cuts at 400 cm and above, the mistagging probability is smaller than 0.1 % for all decay components, and the differences in the mistagging probability between different samples are not longer significant. The standard value of 400 cm for the mistagging cut implies a loss of ~ 17.7 % of the statistics in the IB sample, 13.4 % in the DE and 15.4 % in the INT.

7.12.2 Resolution and Tails

Due to resolution effects, events can migrate from one W bin to another. As the shape of the W distribution is very steep, events tend to migrate from low to high W values. Differences in resolution between data and simulation could produce differences in the induced distortions of the W shape, potentially affecting the extraction of the DE and INT components. However, the study of kaon and pion masses distributions in data and simulation suggests a negligible difference in the resolutions.

But this is not the only potential source of distortions, and the behavior of the

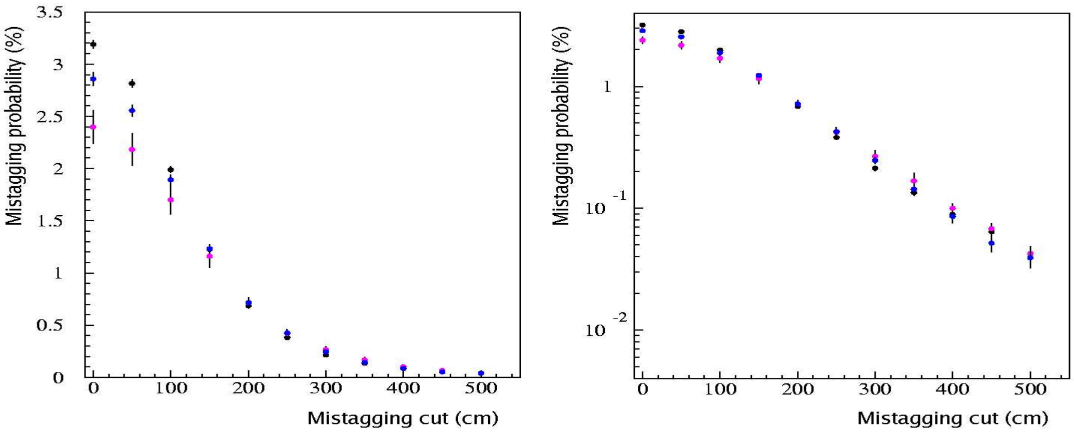

Figure 7.12: Mistagging probability versus mistagging cut in linear (a) and logarithmic (b) scale. Requiring the distance between $z_{\pi^0}^{second}$ and z_{CDA} to be greater than 400 cm, the mistagging probability is less than 0.1 % for IB, DE and INT.

tails of the distributions must be also taken into account. Some studies have been done in this respect, which results are shown in figure 7.13.

The percentage of events kept in the sample for different values of the mistagging cut was computed for data and simulated samples. First, the number of selected events in data and simulation is counted for a given value of the mistagging cut. Then, the cut is increased by 50 cm and the number of selected events is recomputed. The relative difference (%) between these two numbers is calculated, and the result is shown in figure 7.13 (a). The process is repeated for values of the mistagging cut between 100 and 800 cm. Data (black points) and simulation (blue points) behave in the same way, and no particular tendency of overestimation or underestimation of the fraction of kept events is observed in the simulation with respect to the data.

In addition, the kaon mass distribution has been also studied in detail. For this purpose, the requirement that $55 < T^*_\pi < 80$ MeV was imposed to reject background from $K^\pm \to \pi^\pm\pi^0\pi^0$ decay, so that the tails of the kaon mass distribution are clean and can be directly compared with the IB simulation. The quantity studied was the fraction of events kept for a series of cuts in the distance between the reconstructed kaon mass and the nominal kaon mass, measured in units of the kaon mass resolution. First, the number of selected events in data and simulation is counted for a given value of the kaon mass cut. Then, the cut is increased by 0.5 sigmas ($\sim 0.5 \times 2$ MeV) and the number of selected events is recomputed. The relative difference (%) between these two numbers is calculated, and the result is shown in figure 7.13 (b). The process is repeated for values of the kaon mass cut between 2.5 and 9.5 sigmas. The behavior of data (black) and simulation (blue) is very similar.

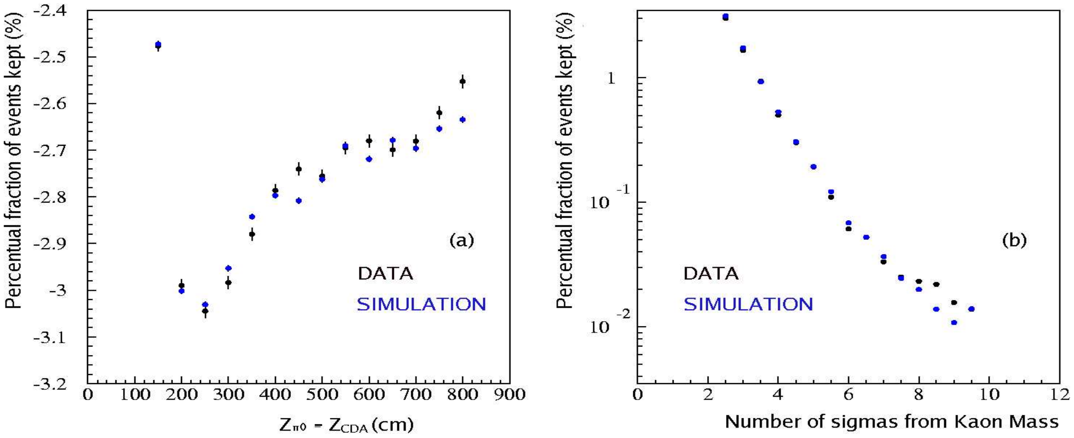

Figure 7.13: (a) Percentage of events kept in the sample with respect to previous cut, when the mistagging cut is changed from 100 to 800 cm. The IB simulation (blue) properly reproduces the behavior observed in data (black). (b) Percentage of events kept in the sample with respect to previous cut, when the kaon mass cut is varied from 2.5 sigmas ($\sim$ 5.25 MeV) to 9.5 sigmas ($\sim$ 20 MeV) from nominal kaon mass. Data (black) and simulated IB samples (blue) contain only events within $55 < T^*_\pi < 80$ MeV. The behavior observed in data is reasonably described by the simulation.

Chapter 8

Background Sources

Table 8.1 shows the potential background sources to $K^{\pm} \rightarrow \pi^{\pm}\pi^{0}\gamma$ decays. Branching ratios are taken from PDG06. Cuts applied against each of the sources are also shown in the table, and will be explained in detail in next sections.
The measured branching ration for Inner Bremsstrahlung $K^{\pm} \rightarrow \pi^{\pm}\pi^{0}\gamma$ decays is (2.75 ± 0.15)× 10^{-4} (PDG06) for $55 < T^{*}_{\pi} < 90$ MeV.

Channel	Branching Ratio (PDG06)	Cut
$K^{\pm} \rightarrow \pi^{\pm}\pi^{0}$	$(20.92 \pm 0.12)\%$	T^{*}_{π} <80 MeV cut Time cuts Mass and COG cuts Difference between $\mathrm{z_{CDA}}$ and z_{π^0}
$K^{\pm} \rightarrow \pi^{\pm}\pi^{0}\pi^{0}$	$(1.757 \pm 0.024)\%$	Cut against overlapping gammas Mass and COG cuts MUV cut
$K^{\pm} \rightarrow e^{\pm}\pi^{0}\nu_{e}$	$(4.98 \pm 0.07)\%$	E/p cut Mass and COG cuts Time cuts
$K^{\pm} \rightarrow \mu^{\pm}\pi^{0}\nu_{\mu}$	$(3.32 \pm 0.06)\%$	MUV cut Mass and COG cuts Time cuts
$K^{\pm} \rightarrow e^{\pm}\pi^{0}\nu_{e}\gamma$	$*(2.69 \pm 0.20) \times 10^{-4}$	E/p cut Mass and COG cuts
$K^{\pm} \rightarrow \mu^{\pm}\pi^{0}\nu_{\mu}\gamma$	$*(2.4 \pm 0.8) \times 10^{-5}$	MUV cut Mass and COG cuts

Table 8.1: Potential background sources to $K^{\pm} \rightarrow \pi^{\pm}\pi^{0}\gamma$. The branching ratios are taken from PDG 2006, those marked with a star do not cover the whole kinematic region. Cuts applied in the $K^{\pm} \rightarrow \pi^{\pm}\pi^{0}\gamma$ selection against each contribution are shown in the last columm.

8.0.3 Considerations on T^*_π cuts against $K^\pm \to \pi^\pm\pi^0\pi^0$ and $K^\pm \to \pi^\pm\pi^0$ decays.

Due to their big branching fractions and their topology, the most important potential background contributions to $K^\pm \to \pi^\pm\pi^0\gamma$ come from $K^\pm \to \pi^\pm\pi^0\pi^0$ and $K^\pm \to \pi^\pm\pi^0$ decays. In previous experiments a cut on $55 < T^*_\pi < 90$ MeV has been applied against these two contamination sources.

Figure 8.1 shows the shape of the theoretical p^*_π distribution for the relevant charged kaon decays. The region within $133 < p^*_\pi < 205$ MeV, equivalent to $53 < T^*_\pi < 108$ MeV, is free from contributions from $K^\pm \to \pi^\pm\pi^0\pi^0$ and $K^\pm \to \pi^\pm\pi^0$ decays.

All these distributions are smeared in the experimental data due to resolution effects. The original delta function corresponding to the two-body $K^\pm \to \pi^\pm\pi^0$ spans in reality some finite region, so that the cut in T^*_π must be tightened to $T^*_\pi < 90$ MeV. In addition, long tails in the $K^\pm \to \pi^\pm\pi^0\pi^0$ and $K^\pm \to \pi^\pm\pi^0$ distribution can originate from track misreconstruction, and in particular to π decay in flight into μ.

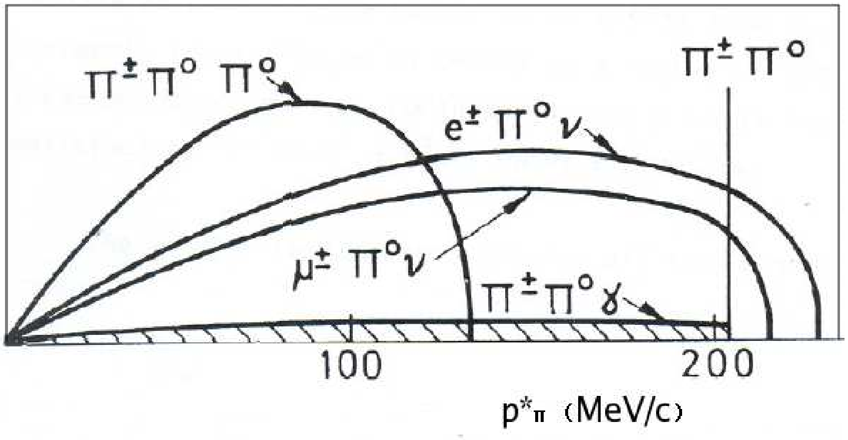

Figure 8.1: Theoretical distribution of the π momentum in the kaon center of mass for $K^\pm \to \pi^\pm\pi^0\gamma$ decays and main potential background sources. The region corresponding to $133 < p^*_\pi < 205$ MeV is free from $K^\pm \to \pi^\pm\pi^0\pi^0$ and $K^\pm \to \pi^\pm\pi^0$ contributions.

As explained in chapter 6, in NA48/2 data the upper cut on $T^*_\pi < 90$ MeV has to be replaced by a tighter cut at $T^*_\pi < 80$ MeV due to trigger effects. This further increases the rejection power for $K^\pm \to \pi^\pm\pi^0$ decays.

As mentioned above, the lower cut at $T^*_\pi > 55$ MeV is very useful against

$K^\pm \to \pi^\pm\pi^0\pi^0$ decays. However, it also cuts away a relative large amount of the $K^\pm \to \pi^\pm\pi^0\gamma$ Direct Emission component, as can be seen from figure 2.2. Therefore, enlarging the lower T^*_π cut to zero increases the sensitivity to the DE and INT components, but an alternative procedure must be found in order to supress the $K^\pm \to \pi^\pm\pi^0\pi^0$ background.

8.1 Background from $K^\pm \to \pi^\pm\pi^0\pi^0$

8.1.1 Mechanisms: One lost gamma or two overlapping.

The fundamental difference between $K^\pm \to \pi^\pm\pi^0\pi^0$ decays and $K^\pm \to \pi^\pm\pi^0\gamma$ decays is that the first has four photons in the final state and the latter has only three. Therefore, a $K^\pm \to \pi^\pm\pi^0\pi^0$ event can be reconstructed as $K^\pm \to \pi^\pm\pi^0\gamma$, if either one of the four gammas is lost (out of the detector acceptance) or two photons overlap in the LKr calorimeter. These are purely geometric effects.
There is another possible contribution, coming from $K^\pm \to \pi^\pm\pi^0\pi^0$ decays with one very soft gamma in the final state. However this type of events is very much supressed by phase space.
All these effects can be adequately studied using a Monte Carlo simulation. A sample of 45 million $K^\pm \to \pi^\pm\pi^0\pi^0$ events has been generated, out of which 37 million lay within the fiducial volume[1] .
To insure a background contamination level in the data sample smaller than 1 % of the DE component, the fraction of $K^\pm \to \pi^\pm\pi^0\pi^0$ events reconstructed as $K^\pm \to \pi^\pm\pi^0\gamma$ out of all $K^\pm \to \pi^\pm\pi^0\pi^0$ decays occurring in the fiducial volume must smaller than 2.4 10 $^{-7}$. This fraction (F) can be simply calculated from equation 8.1.

$$\frac{F * BR_{Background}}{(Acc_{DE} * BR_{DE})} < 10^{-2} \tag{8.1}$$

The meaning of F is simply the acceptance of background events to be reconstructed as signal.

---

[1] The fiducial volume is defined by kaon decays with true longitudinal decay position in the range -1000 < z < 8000 cm, and true total energy within 54 < E < 66 GeV

8.1.2 Mass and COG cuts against lost gammas

In general, cuts on the reconstructed invariant mass of the event and on the event COG are useful to reject events with inappropriate (either too low or too big) total energy. If energy has not been reconstructed in the event, the COG and total invariant mass cuts will, in principle, not be satisfied.

The effect of one photon being out of acceptance in the reconstructed invariant mass of $K^{\pm} \to \pi^{\pm}\pi^{0}\pi^{0}$ events has been shown already in figure 5.5.

For this study, a kaon mass cut of 0.47 GeV together with a requirement on the COG $<$ 3 cm were implemented in the selection. In addition, the T^{*}_{π} should lie in the region of $55 < T^{*}_{\pi} < 80$ MeV. The rejection power for $K^{\pm} \to \pi^{\pm}\pi^{0}\pi^{0}$ obtained in this way was not as high as desired, therefore tighter cuts on the final invariant mass and COG needed to be implemented. A summary of the results is shown in table 8.2.

First, the difference between the invariant mass of the event and the nominal kaon mass was required to be less than 10 MeV, gaining a factor of ~ 3 in the rejection power. Then, a cut on COG $<$ 2 cm was added. After this, the final fraction of $K^{\pm} \to \pi^{\pm}\pi^{0}\pi^{0}$ decays reconstructed as $K^{\pm} \to \pi^{\pm}\pi^{0}\gamma$ is smaller than 2.4 10^{-7}, as required.

Applied cut	Fraction of surviving events (out of 37 10^{6})
COG$<$ 3cm and $\mathrm{M}_{\pi\pi^{0}\gamma} > 0.47$ GeV and $55 < T^{*}_{\pi} < 80$ MeV	8×10^{-7}
$\mid \mathrm{M}_{\pi\pi^{0}\gamma} - M_{K} \mid < 10$ MeV	3×10^{-7}
COG $<$ 2cm	1.6×10^{-7}

Table 8.2: Fraction of surviving $K^{\pm} \to \pi^{\pm}\pi^{0}\pi^{0}$ events in the region $55 < T^{*}_{\pi} < 80$ MeV, after different cuts on reconstructed kaon mass and COG have been applied.

8.1.3 Algorithm to reject overlapping gammas

$K^{\pm} \to \pi^{\pm}\pi^{0}\pi^{0}$ events with two gammas overlapping in the LKr have the same signature as the signal in all detectors. Moreover, the reconstructed values of kaon mass and COG satisfy the selection criteria, as there is no energy loss for this kind of events.

By releasing the T^{*}_{π} cut in the selection described in previous section, about 60 times more $K^{\pm} \to \pi^{\pm}\pi^{0}\pi^{0}$ events are accepted, all of them satisfying the tight COG and kaon mass cuts. These events are shown in figure 8.2 (a).

An algorithm can be implemented testing the overlap hypothesis for all three gamma clusters in the event. Let us consider the three reconstructed gamma clusters with energies E_1, E_2, E_3 and assume that the first one, with energy E_1, is really the overlap of two gammas of energies $E = xE_1$ and $E' = (1-x)E_1$. Let us now suppose that the photon with energy E comes from the decay of the same π^0 as the second gamma cluster of energy E_2. Then the decay vertex for that π^0 would be:

$$z^{1}_{\pi^0} = \frac{\sqrt{(Dist_{1-2}EE_2)}}{M_{\pi^0}} = \frac{\sqrt{(Dist_{1-2}xE_1E_2)}}{M_{\pi^0}} \tag{8.2}$$

where $\mathrm{Dist}_{1-2} = \sqrt{(x_1 - x_2)^2 + (y_1 - y_2)^2}$ is the distance between the gamma clusters at the Lkr, and M_{π^0} is the nominal π^0 mass.

In the same way, let us suppose that the photon with energy E' comes from the decay of the same π^0 as the third cluster of energy E_3. The decay vertex for this second π^0 is given by:

$$z^{2}_{\pi^0} = \frac{\sqrt{(Dist_{1-3}E'E_3)}}{M_{\pi^0}} = \frac{\sqrt{(Dist_{1-3}(1-x)E_1E_3)}}{M_{\pi^0}} \tag{8.3}$$

As the two neutral pions originate from the same kaon decay, they must satisfy the constraint $z^{1}_{\pi^0} = z^{2}_{\pi^0} \equiv z^{overlap}_{\pi^0}$. This allows to solve for x, i.e. for the fraction of energy shared by the overlapping gammas in the event.

Once x is known, $z^{overlap}_{\pi^0}$ can be computed. The procedure is repeated for all three gamma clusters.

The event is finally rejected if there is at least one solution for x with a π^0 decay vertex $z^{overlap}_{\pi^0}$ compatible with the charged vertex. The actual cut was given by the requirement that all three $|z^{overlap}_{\pi^0} - z_{CDA}| > 400$ cm.

The action of the overlapping gamma cut is shown in figure 8.2 (b). The cut T^{*}_{π} > 55 MeV rejects 355 events out of the 360, while the algorithm just described is able to reject 352.

The overlapping gamma cut allows therefore to drop the lower T^{*}_{π} cut, keeping the required rejection power for $K^{\pm} \to \pi^{\pm}\pi^{0}\pi^{0}$ decays.

8.1.4 Track misreconstruction and π decay into μ: cut on MUV hits.

Due to misreconstruction of the track it is possible that $K^{\pm} \to \pi^{\pm}\pi^{0}\pi^{0}$ events, with one photon out of acceptance, can still satisfy the kaon mass and

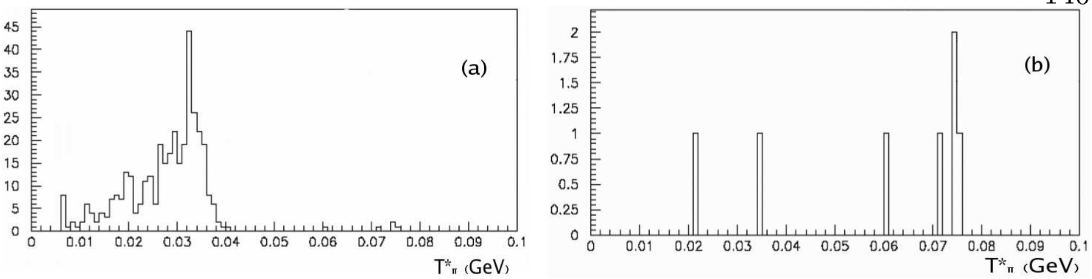

Figure 8.2: (a) Distribution of T^*_π for simulated $K^\pm \to \pi^\pm\pi^0\pi^0$ events passing through the $K^\pm \to \pi^\pm\pi^0\gamma$ selection. (b) Same distribution for events with no overlapping photons on the Lkr calorimeter. More than 98 % of the potential background events are rejected with this requirement.

COG requirements. This happens in particular when the π decays in flight into a μ. This kind of events are rejected in the standard $K^\pm \to \pi^\pm\pi^0\gamma$ selection requiring no associated hits in the MUV detector. If the MUV cut is released the number of $K^\pm \to \pi^\pm\pi^0\pi^0$ simulated events reconstructed as $K^\pm \to \pi^\pm\pi^0\gamma$ decays increase by a factor of four.

8.2 Backgroud from $K^\pm \to \pi^\pm\pi^0$

8.2.1 Mechanisms: Conversions and Accidentals

The fundamental difference between $K^\pm \to \pi^\pm\pi^0$ decays and $K^\pm \to \pi^\pm\pi^0\gamma$ decays is that the first has only two photons in the final state and the later has three. Therefore, in order for a $K^\pm \to \pi^\pm\pi^0$ event to be reconstructed as $K^\pm \to \pi^\pm\pi^0\gamma$, there must be an extra cluster faking a third gamma.

This extra cluster can be of different natures. In the first place, one of the photons from the π^0 decay can convert into an e$^-$, e$^+$ pair. In that case the $K^\pm \to \pi^\pm\pi^0$ decay could produce three clusters in the LKr calorimeter (one from the non-converted photon, one from the electron and one from the positron). If the conversion is produced before the magnet, two tracks would be seen in the spectrometer, and the event would be rejected. Therefore, only conversions occurring in the last plane of DCH2 can contribute to a potential background.

In addition, due to accidental activity, there can be an extra reconstructed cluster in the LKr. The presence of accidentals can be studied by releasing the time requirements in the selection and looking at the tails of the clusters' time distributions.

Clusters from the π shower could also be reconstructed as gamma clusters. A cut requiring the gammas to be at a distance greater than 35 cm from the extrapolated π track at the LKr minimizes this effect.

8.2.2 Mass and COG cuts

The mass and COG cuts help in the rejection of $K^{\pm} \rightarrow \pi^{\pm}\pi^{0}$ decays, with one photon cluster faked by either accidentals or clusters from the pion shower. This type of events has indeed too high a value of the reconstructed total energy, as an extra amount is added by the faked photon to the initial value from the $K^{\pm} \rightarrow \pi^{\pm}\pi^{0}$ decay itself. Events of this kind can be observed as tails in the high kaon mass region.

If the added energy is very small it could happen that the COG and kaon mass cuts are still satisfied. Accidental photons are typically very soft, and clusters belonging to the π shower can also be of low energies. However, the requirement that the minimum photon energy is greater than 5 GeV excludes this possibility.

8.2.3 Vertex difference $|z_{\pi^0} - z_{\mathrm{CDA}}|$ cut and $\mathrm{Y}_{\mathrm{LKr}}$ difference cut.

For $K^{\pm} \rightarrow \pi^{\pm}\pi^{0}$ decays with photon conversions in last plane of DCH2 there is no extra energy added to the original kaon decay. Therefore, these kind of events lie in the appropiate range of invariant masses and COGs.

To study in detail this type of background, $K^{\pm} \rightarrow \pi^{\pm}\pi^{0}\gamma$ candidates have been selected in the SS3 data sample, using very loose criteria. In particular the kaon mass, projection cut, T^{*}_{π} and $|z_{\pi^0} - z_{CDA}| < 400$ cm cuts have not yet been applied to the initial sample. In addition, the value of COG cut was set to 3 cm. The reconstructed kaon mass for these events is shown in figure 8.3 (a), where contributions from $K^{\pm} \rightarrow \pi^{\pm}\pi^{0}\pi^{0}$ and $K^{\pm} \rightarrow \pi^{\pm}\pi^{0}$ are observed at low and high kaon mass values respectively. In order to specifically study $K^{\pm} \rightarrow \pi^{\pm}\pi^{0}$ decays, events with kaon mass greater than 0.47 GeV have been selected. The p^{*}_{π} for these events is shown in figure 8.3 (b). The presence of $K^{\pm} \rightarrow \pi^{\pm}\pi^{0}$ events in the sample can be spotted from the shape of the the p^{*}_{π} distribution as a clear peak at around 205 MeV.

In order to test whether the source of this background comes from $K^{\pm} \rightarrow \pi^{\pm}\pi^{0}$ decays with photon conversions, a simple check has been done. When photons convert in the last plane of DCH2, the e^{-} and e^{+} tracks are bent by the spectrometer magnet, such that their impact position in the Lkr has the same Y coordinate. Therefore, these events can be rejected requiring that the distance between any two photons (i,j) in y be greater than 2 cm (the value of 2 cm is given by the LKr cell size). The effect of adding this cut is illustrated in figure 8.3 (c). The disappearance of the peak at $\mathrm{p}_{\pi}^{*} \sim 205$ MeV after requiring $\Delta \mathrm{y}_{(\mathrm{i,j})} > 2$ cm confirms the hypothesis that the background is from photon conversions.

Alternatively to the cut on $\Delta \mathrm{y}_{(\mathrm{i,j})}$, another cut can be made in order to reject these events. If conversions occured, either the e^{-} or the e^{+} cluster is paired to the real photon cluster and used to reconstruct the π^0 vertex and mass. The electron (or positron) cluster does not have the same energy and position as the photon that converted. Therefore, the π^0-related quantities are misreconstructed.

In particular, the agreement between the longitudinal position of the decay vertex reconstructed with the π track ($\mathrm{z}_{\mathrm{CDA}}$) and the one reconstructed with the neutral variables (z_{π^0}) will not be compatible. The cut $|z_{\pi^0} - z_{\mathrm{CDA}}| < 400$ cm rejects the $K^{\pm} \to \pi^{\pm}\pi^0$ contribution, with almost no effect on the signal. In the final selection the $\Delta \mathrm{y}_{(\mathrm{i,j})} > 2$ cm has not been implemented, conversions have been rejected using only the $|z_{\mathrm{CDA}} - z_{\pi^0}| < 400$ cm condition.

8.2.4 Accidental activity.

Accidental activity in the detectors can be produced by beam particles or simultaneous kaon decays contributing to the event under consideration. A significant contribution from accidentals in the final sample would distort the photon energy spectrum, as accidentals are dominantly soft.

Time distributions have been checked in SS123 data releasing the time cuts. For this study, no cuts have been applied in the time difference between clusters or in the time difference between the track and the clusters. This is a general check, valid not only for $K^{\pm} \to \pi^{\pm}\pi^0$ decays, but for any other background source requiring accidental clusters to fake one of the gammas. The result of the test can be seen in figure 8.4 (a), where the maximum time difference between all three photons in the event is plotted for all reconstructed $K^{\pm} \to \pi^{\pm}\pi^0\gamma$ decays. This distribution shows that essentially no contribution from accidental activity can be seen in this sample.

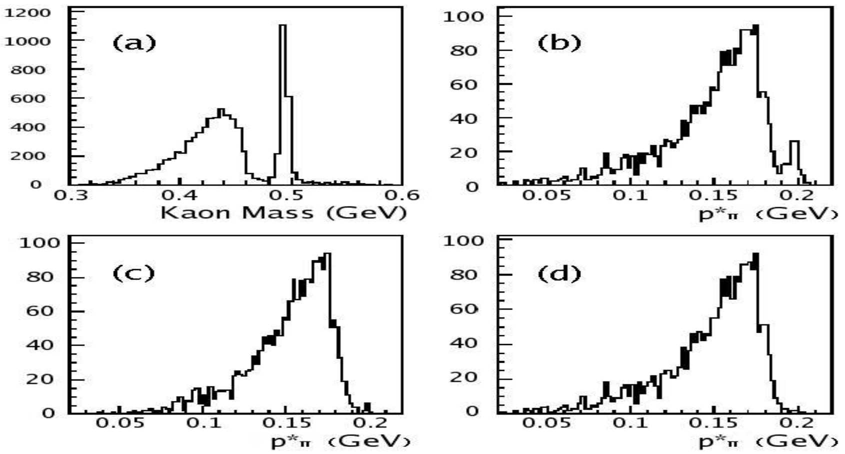

Figure 8.3: (a) Reconstructed kaon mass for candiate events in a small subsample of SS3 data, at an early selection stage. Low mass events correspond to $K^{\pm} \to \pi^{\pm}\pi^{0}\pi^{0}$ decays with one photon not reconstructed. Tail at high kaon mass values correspond to $K^{\pm} \to \pi^{\pm}\pi^{0}$ decays with one extra cluster. (b) p^{*}_{π} distribution for events with kaon mass greater than 0.47 GeV. A small peak in the vicinity of 205 MeV reveals the presence of $K^{\pm} \to \pi^{\pm}\pi^{0}$ events in the sample. (c) Same distribution after requiring the distance between clusters in the y coordinate at the LKr to be greater than 2 cm. The peak from $K^{\pm} \to \pi^{\pm}\pi^{0}$ decays is clearly decreased, confirming the background source to be $K^{\pm} \to \pi^{\pm}\pi^{0}$ decays with photon conversions in DCH2. (d) p^{*}_{π} for events satidfying $|z_{\pi^0} - z_{CDA}| < 400$ cm, with no requirement on y distance between clusters. There is no evidence from $K^{\pm} \to \pi^{\pm}\pi^{0}$ background after this cut.

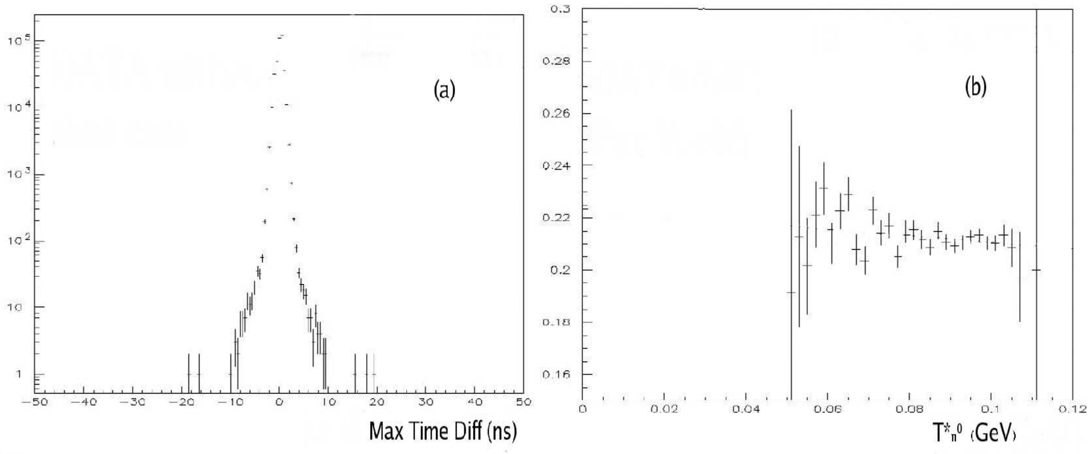

Figure 8.4: (a) Distribution of the maximal time difference between photons in $K^{\pm} \to \pi^{\pm}\pi^{0}\gamma$ decays. No contribution from accidental clusters is observed. (b) Ratio of $T^{*}_{\pi^0}$ distributions for Data over Simulated events. No presence of $K^{\pm} \to \pi^{\pm}\pi^{0}$ contamination can be seen in data.

8.2.5 Final $T^*_{\pi^0}$ distribution.

A final check can be made, specific to $K^{\pm} \to \pi^{\pm}\pi^0$ decays. As $K^{\pm} \to \pi^{\pm}\pi^0$ is a two-body decays, the $T^*_{\pi^0}$ distribution is a delta function at 110 MeV (if resolution effects are not considered). In case of contamination from $K^{\pm} \to \pi^{\pm}\pi^0$ in the sample, this could be detected as a peak in the ratio of the $T^*_{\pi^0}$ distributions of $K^{\pm} \to \pi^{\pm}\pi^0\gamma$ data events over simulated events. This ratio is shown in figure 8.4 (b). No signal of $K^{\pm} \to \pi^{\pm}\pi^0$ background can be seen from this picture.

The application of all mentioned cuts makes negligible the $K^{\pm} \to \pi^{\pm}\pi^0$ contribution to the final sample.

8.3 Background from decays with neutrino in final state

There is a set of potential background sources to the $K^{\pm} \to \pi^{\pm}\pi^0\gamma$ decays with neutrinos in the final state: radiative and non-radiative semileptonic decays. As indicated in table 8.1, the branching fractions of non-radiative decays are of the order of few percent, and those of radiative decays are of the order of 10^{-4} for the electron channel, and 10^{-5} for the muonic channel.

Radiative branching ratios have been measured in a restricted region of radiated photon energies and angles between the radiated gamma and the charged particle, in order to avoid infrared and collinear singularites of the bremsstrahlung matrix elements.

Table 8.3 summarizes the possible mechanisms through which semileptonic decays can fake the $K^{\pm} \to \pi^{\pm}\pi^0\gamma$ signal.

In general, for all these decay modes there is a variable amount of energy lost in the event. This is due to the presence of the neutrino, that cannot be detected. Therefore, COG and kaon mass cuts will not be satisfied unless the neutrino is very soft. This is, however, very much suppressed by phase space.

In addition, particle mis identification is required in all cases. For electrons, mis identification is suppressed by the cut on E/p and for muons, by the cut on the MUV response. The probability of mis identifying an electron as a pion for E/p < 0.85 has been evaluated to be ~ 0.4 %[61], and the efficiency of the MUV response is greater than 99.5 %.

For non radiative decays, accidental activity is required in order to fake one extra photon. As shown in previous section, no sign of accidental activity was found in the $K^{\pm} \rightarrow \pi^{\pm}\pi^{0}\gamma$ sample.

After all cuts, the final background contribution from semileptonic decays is expected to be negligible.

Decay mode	Mechanism
$K^{\pm} \rightarrow e^{\pm}\pi^{0}\nu_{e}\gamma$	Soft ν emission and Miss ID e with π
$K^{\pm} \rightarrow e^{\pm}\pi^{0}\nu_{e}$	Same as previous plus accidental activity
$K^{\pm} \rightarrow \mu^{\pm}\pi^{0}\nu_{\mu}\gamma$	Soft ν emission and Miss ID μ with π
$K^{\pm} \rightarrow \mu^{\pm}\pi^{0}\nu_{\mu}$	Same as previous plus accidental activity

Table 8.3: Summary of mechanisms needed for semileptonic decays in order to fake a $K^{\pm} \rightarrow \pi^{\pm}\pi^{0}\gamma$ event. For a given decay mode, all specified conditions must be concurrently satisfied.

This has been checked with simulated $K^{\pm} \rightarrow e^{\pm}\pi^{0}\nu_{e}\gamma$ and $K^{\pm} \rightarrow \mu^{\pm}\pi^{0}\nu_{\mu}\gamma$ events. Large Monte Carlo samples have been produced for the study of semileptonic decays [62], using the PHOTOS package [63]. At generation level, the energy of the radiated photon in the kaon center of mass was required to be greater than 3 MeV.

For the electron channel, 5.5 10^{6} events were generated in the decay fiducial volume. A basic selection, with no cut on E/p, has been implemented. Zero events have been selected after requiring that the recontructed invariant mass is greater than 470 MeV and that the T_{π}^{*} is smaller than 90 MeV.

As already mentioned, the kaon mass cut is expected to be highly efficient in rejecting decays with neutrinos, because of the loss of detected energy. In addition, as the reconstructed track is assumed to be generated by a π, the computed T_{π}^{*} does not lie on the required range.

For the muon channel, 6.4 10^{6} events were generated in the decay fiducial volume. A basic selection, with no cut on the MUV response, has been implemented. Zero events have been selected after requiring that the T_{π}^{*} is smaller than 90 MeV and that the reconstructed invariant mass of the event is within 10 MeV with respect to the nominal kaon mass. In addition, releasing these cuts and requiring no hits in the MUV, the number of selected events is zero as well.

8.4 Final background estimation from Data and Simulation.

The conclusion from the studies carried out on the different data and Monte Carlo samples, is that all physical background to $K^{\pm} \rightarrow \pi^{\pm}\pi^{0}\gamma$ decays can be attributed to $K^{\pm} \rightarrow \pi^{\pm}\pi^{0}\pi^{0}$ decays only.
The final confirmation of this statement is shown in figure 8.5, where data from SS123 and simulated $K^{\pm} \rightarrow \pi^{\pm}\pi^{0}\gamma$ and $K^{\pm} \rightarrow \pi^{\pm}\pi^{0}\pi^{0}$ events have been plotted. $K^{\pm} \rightarrow \pi^{\pm}\pi^{0}\gamma$ events have been reconstructed using the final selection criteria, releasing only the kaon mass cut. The invariant mass distribution of data events is shown in the plot as black dots with errors. Simulated distributions for $K^{\pm} \rightarrow \pi^{\pm}\pi^{0}\gamma$ IB events (green) and $K^{\pm} \rightarrow \pi^{\pm}\pi^{0}\pi^{0}$ events (yellow) have been superimposed to these data, applying a proper normalization. Good agreement is found between the distribution of data events and the addition of the two simulated contributions. In the region of ± 10 MeV around the nominal kaon mass, the relative amount of background from $K^{\pm} \rightarrow \pi^{\pm}\pi^{0}\pi^{0}$ decays is negligible.

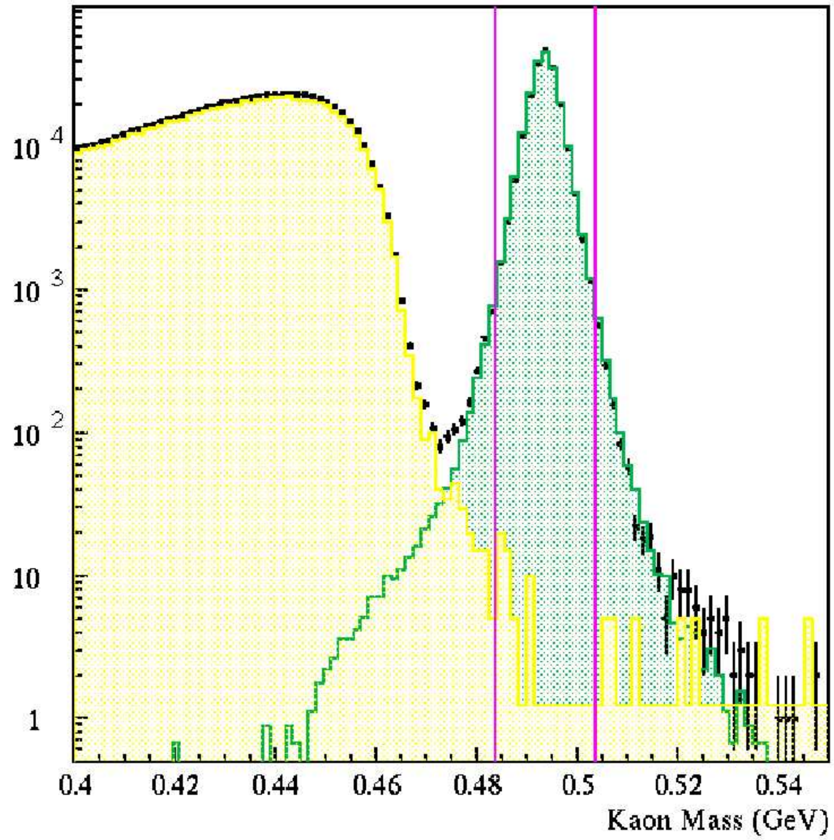

Figure 8.5: Mass distribution of $K^{\pm} \rightarrow \pi^{\pm}\pi^{0}\gamma$ candidates reconstructed in SS123. Dots represent data events. $K^{\pm} \rightarrow \pi^{\pm}\pi^{0}\gamma$ simulated events are plotted in green. $K^{\pm} \rightarrow \pi^{\pm}\pi^{0}\pi^{0}$ simulated events are superimposed in yellow. The data distribution is compatible with the addition of these two contributions. Purple lines delimit the region of $|m_k - M_K| < 10$ MeV, where the amount of background from $K^{\pm} \rightarrow \pi^{\pm}\pi^{0}\pi^{0}$ decays is negligible with respect to the total sample.

Chapter 9

Results and Conclusions

The main result of this work is the extraction of the DE and INT fractions with respect to IB for $K^{\pm} \rightarrow \pi^{\pm}\pi^{0}\gamma$ decays in the range $0 < T^{*}_{\pi} <$80 MeV.
As already mentioned, these results can be obtained in two different ways, using either the Shape or the Maximum Likelihood methods. A general description of each one of them has been already given in chapter 2. The actual implementation of the Maximum Likelihood approach used in this work is discussed in detail in appendix B.
Checks have been done in order to test the reliability and robustness of both methods. For this purpose, samples of pseudo-data have been produced using simulated events. Given proportions of DE and INT events have been added to subsets of the IBS2 sample, and fitted using the same samples of simulated events used to extract the results for real data. Fits using the Maximum Likelihood approach have been able to recover the input fractions. However, the Shape Method was found to be highly sensitive to the region chosen for normalization, the binning in W and the initial proportions of DE and INT. Therefore, only the ML approach has been used to obtain the final results.
The W distributions used in the fit are shown in figure 9.1. In the fitting range $0.2 < \mathrm{W} < 0.9$ they contain 117627 data events, and 711743 simulated events (526751 IB, 89144 DE, 95848 INT).

9.1 Results from a Maximum Likelihood fit to DE and INT terms.

The Maximum Likelihood method has been used to fit three free parameters: the fractions of DE and INT with respect to the total number of events in the sample, and a global normalization factor. The results from this fit are

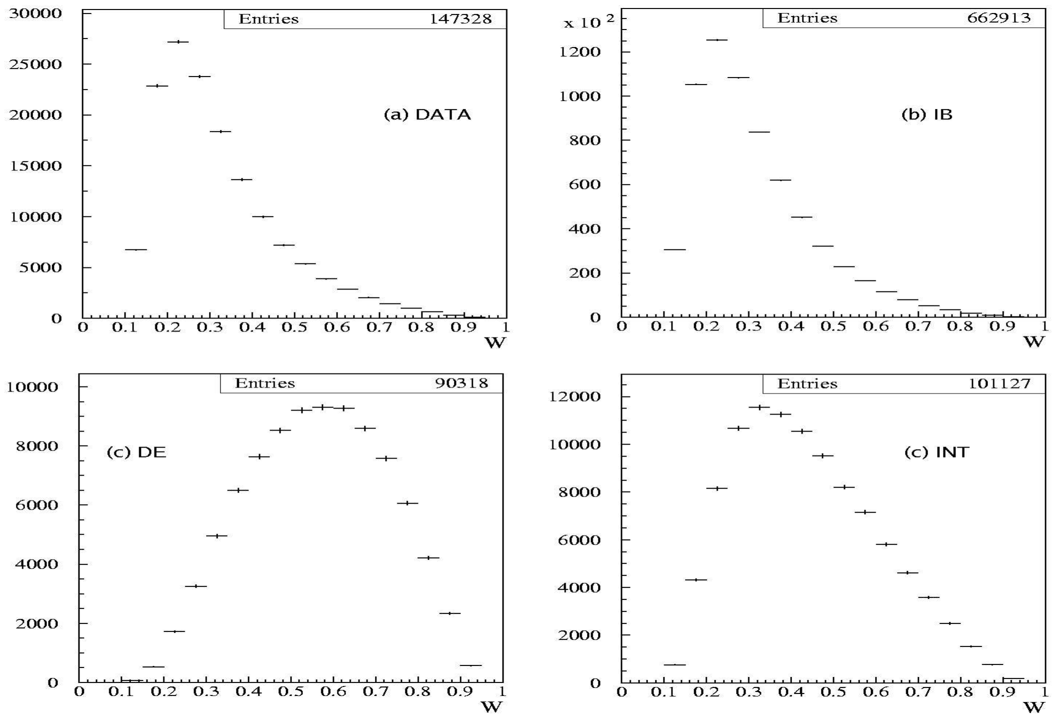

Figure 9.1: Final W distributions for Data (a), IB (b), DE (c) and INT (d).

summarized in table 9.1.

	Frac(DE)$_{\mathrm{TOT}}$	Frac(INT)$_{\mathrm{TOT}}$	Normalization
Result	0.0453	-0.033	117.68 10^3
Positive MINOS error	0.0049	0.011	0.34 10^3
Negative MINOS error	-0.0048	-0.011	-0.34 10^3
Parabolic error	0.0046	0.010	0.34 10^3

Table 9.1: Results and errors from ML fit.

The DE fraction has been obtained with a relative statistical error of the order of ~ 10 %. The INT component has been found to be negative and about 3 sigmas away from zero. This is the first evidence for the existence of an INT term in $K^{\pm} \to \pi^{\pm}\pi^{0}\gamma$ decays.

Errors computed using the likelihood derivatives at the maximum (Parabolic errors) or scanning the likelihood function (MINOS errors) are very similar. This means that no significant non-linearities are present in the likelihood function.

The full error matrix is given in table 9.2 and the correlation coefficients between the parameters are shown in table 9.3. A very high negative correlation of -93

% is observed between the DE and the INT fractions.

	EXTERNAL ERROR MATRIX		
PARAMETER	$\mathrm{Frac(DE)_{TOT}}$	$\mathrm{Frac(INT)_{TOT}}$	Normalization
$\mathrm{Frac(DE)_{TOT}}$	$0.210\ 10^{-4}$	$-0.443\ 10^{-4}$	$0.108\ 10^{-3}$
$\mathrm{Frac(INT)_{TOT}}$	$-0.443\ 10^{-4}$	$0.109\ 10^{-3}$	$-0.265\ 10^{-3}$
Normalization	$0.108\ 10^{-3}$	$-0.265\ 10^{-3}$	$0.118\ 10^{6}$

Table 9.2: Error matrix

	CORRELATION COEFFICIENTS		
PARAMETER	$\mathrm{Frac(DE)_{TOT}}$	$\mathrm{Frac(INT)_{TOT}}$	Normalization
$\mathrm{Frac(DE)_{TOT}}$	1.000	-0.927	0.000
$\mathrm{Frac(INT)_{TOT}}$	-0.927	1.000	0.000
Normalization	0.000	0.000	1.000

Table 9.3: Correlation matrix

At this point, the obtained results represent the fractions of DE and INT components with respect to all accepted events. These must therefore be corrected in order to take into account the fact that different decay components have different acceptances. The original fractions of Direct Emission and Interference with respect to Inner Bremsstrahlung can be computed from the following equations:

$$\mathrm{Frac(IB)_{TOT}} = 1 - \mathrm{Frac(DE)_{TOT}} - \mathrm{Frac(INT)_{TOT}} \tag{9.1}$$

$$\mathrm{Frac(DE)} = \frac{\mathrm{Frac(DE)_{TOT}}}{\mathrm{Frac(IB)_{TOT}}} \times \frac{\mathrm{Acc(IB)}}{\mathrm{Acc(DE)}} = (3.14 \pm 0.32)\ \% \tag{9.2}$$

$$\mathrm{Frac(INT)} = \frac{\mathrm{Frac(INT)_{TOT}}}{\mathrm{Frac(IB)_{TOT}}} \times \frac{\mathrm{Acc(IB)}}{\mathrm{Acc(INT)}} = (-2.39 \pm 0.76)\ \% \tag{9.3}$$

$$\tag{9.4}$$

Where the values of the acceptances for every term correspond to the last row of table 7.3.

In order to evaluate the quality of the ML fit, the residuals have been calculated for every W bin from the difference between the number of data events and the Monte Carlo prediction from the fitted DE and INT fractions. These are shown in figure 9.2. A fit of the residuals to a constant has a χ^2 of ~10 for 13 degrees of freedom, and the constant value is compatible with zero.

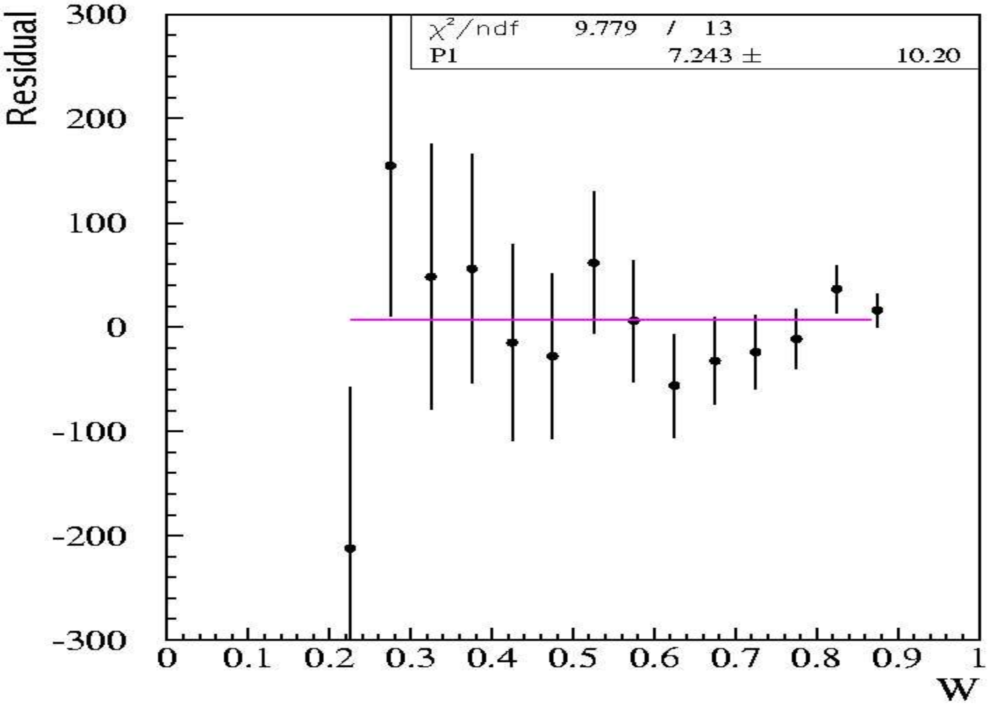

Figure 9.2: Residuals for ML fit to DE, INT and normalization.

9.2 Studies of cut variation

The stability of the result has been checked varying the value of the main selection cuts within a reasonable range. The ML fit has been repeated for every set of Data and Simulated samples obtained with the modified cut value, in order to study the differences in the resulting DE and INT fractions with respect to the standard (reference) ones. The relevant plots are shown in Appendix C. In every figure the results for the corrected fractions of DE and INT with respect to IB are shown as a function of the cut value. For the reference point, the error bars show the total statistical error assigned by the ML fit. For all other points (j), uncorrelated errors with respect to the reference have been calculated for this application as:

$$\mathrm{Uncorrelated\,Error(j)} = \sqrt{\left(1 - 2\frac{\mathrm{Num(j)}}{\mathrm{Num(Ref)}}\right)\mathrm{Error(j)}^2 + \mathrm{Error(Ref)}^2} \qquad (9.5)$$

where Num(j) represents the number of events that pass the cut value (j), Num(Ref) the number of events passing the standard selection, Error(j) the statistical error given by the ML fit to the result for cut value j, and Error(Ref) the statistical error assigned to the reference point.

A number of cuts have been checked using this procedure and for most of them no significant variation of the results was observed. However, the variation of some specific cuts showed a potentially significant effect. For these, the results for the DE and INT fractions obtained for every value of the cut have been plotted together with the DE-INT contour curves. A summary of these studies is given in the following:

- **COG.** The COG cut was varied from 1 to 5.5 cm, to check the effect of possible residual background contamination in the sample. The reference point is situated at 2 cm. No significant effect has been observed in the ML results from varying this cut.

- **Distance between charged and neutral vertex $|\Delta \mathbf{z}| = |\mathbf{z}_{\pi^0}\text{-}\mathbf{z}_{\mathrm{CDA}}|$.** The standard value of the cut is 400 cm, and it was varied from 200 to 650 cm. The results are compatible within uncorrelated errors.

- **Kaon mass** The reference cut value in the difference between the reconstructed kaon mass and the nominal kaon mass is set at 10 MeV, corresponding to $\sim$ 4 sigmas (4×2.2 MeV). This value has been changed between 2.5 and 9.5 sigmas. It is expected that releasing this cut background from $K^\pm \to \pi^\pm\pi^0\pi^0$ decays enters the sample. However, the background is separated well enough from the signal, so that no effect can be seen up to $\sim$ 7 sigmas.

- **E/p** In the selection this cut is made at 0.85, in order to reject background from $K^\pm \to e^\pm\pi^0\nu_e$ and $K^\pm \to e^\pm\pi^0\nu_e\gamma$ decays. This condition was varied from 0.75 to 1, with negligible effect observed in the result.

- **Distance between pion impact point at LKr and gamma clusters.** Gamma clusters were defined to lie outside a radius of 35 cm from the charged pion impact point at the LKr front face in order to minimize a possible contamination from the pion shower. This was modified from 20 to 50 cm. The results are in agreement within uncorrelated errors.

- **Charged pion momentum** A cut at 10 GeV is implemented to maintain a high efficiency for the MUV response, needed for background rejection. The value of this cut was varied from 5 to 15 GeV. A significant effect can be observed when requiring high values for the minimum pion momentum allowed. However, it must be noted that these imply big statistical losses. In order to better disentangle the statistical effects from a possible systematic uncertainty, the results obtained for every cut value (green points) have been plotted together with the contour curves associated to the reference point. All points fall within the first contour, meaning that they are statistically compatible. Therefore, no systematic uncertainty has been associated to this effect.

- **Mistagging** The mistagging cut was varied from 0 to 800 cm. From the contour plot it can be seen that all results are statistically compatible.
- **Minimum photon energy** The value of this cut was varied from 3 to 10 GeV. The reference point is defined as 5 GeV. For high values of the minimum energy cut many events are lost in the sample. The contour plot shows that the observed effect could be due to statistical fluctuations, as only the points with smaller statistics lie outside of the first contour, and all points are within the second contour. However, it was decided to assign to this effect a systematic uncertainty of half of the maximum difference observed. The absolute total difference amounts to ± 0.52 % for the DE fraction and ± 1.33 % for the INT fraction.

The negative correlation between the fraction of DE and the fraction of INT is clear from all these plots.
More cuts have been checked, without any effect on the results:

- **Photon position at DCH1** The requirement that the photons cannot come from the vicinity of the DCH1 flange was released. No change was observed in the result within uncorrelated errors.
- **Radial track position at the DCHs**. The standard cut for the track impact point at DCH1,2 and 4 is set to a minimum radius of 12 cm and a maximum of 150 cm. These values were tightened requiring a minimum radius of 16, 16, 20 cm and a maximum radius of 90, 150, 150 cm in DCH1,2 and 4 respectively. The new values imply statistical losses of the order of few %. The results for DE and INT fractions did not change within uncorrelated errors with respect to the standard cut values.

9.3 Systematic Effects

In addition to varying the relevant cuts, other types of effects have been studied.

- **L1 trigger efficiency correction.** The effect of applying or not applying the L1 trigger efficiency correction for $E_{min} > 5$ GeV is 0.09 % for DE and 0.28 % for INT. The correction itself is computed with high precision and no systematic uncertainty has been assigned to it.

- **Energy scale.** The absolute neutral energy scale is known to a precision of 0.1 %. In order to evaluate the effect of this uncertainty, the data clusters energies have been multiplied by 1.001. The results of the ML fit changed by 0.09 % for the DE fraction and by 0.21 % for the fraction of INT. Half of this difference has been assigned as systematic uncertainty to the result.

- **Non linearity.** The shape of the non-linearity correction has been changed within a reasonable range. The results of the ML fit did not change with respect to the reference within the uncorrelated errors.

- **Residual L2 trigger effects.** The effect of a possible residual L2 trigger inefficiency has been studied changing the upper T^*_π limit from 80 MeV to 75 and 70 MeV. The results of the corresponding ML fits are shown in table 9.4. To make a comparison with the standard measurement, all results have been extrapolated to the $T^*_\pi < 80$ MeV region, using the factors shown in table 9.5. A significant change in the result is observed changing the T^*_π from 80 to 75 MeV. The absolute total difference is 0.21 % for DE and 0.87 % for the INT term. However, the results with $T^*_\pi < 75$ MeV and $T^*_\pi < 70$ MeV are compatible within uncorrelated errors. This behavior is in agreement with the hypothesis of an edge effect from the MBX response. Half of the observed difference has been assigned as systematic uncertainty to the final result.

The values of the relevant systematic uncertainties from different sources are summarized in table 9.6

9.4 Final results for fit to DE and INT

The final result obtained on the fractions of Direct Emission and Interference with respect to Inner Bremsstrahlung for $T^*_\pi < 80$ MeV in SS123 is:

$$\text{Fraction of DE} = (3.14 \pm 0.32 \pm 0.29)\% \tag{9.6}$$

$$\text{Fraction of INT} = (-2.39 \pm 0.76 \pm 0.81)\% \tag{9.7}$$

	DE fraction (%)	INT fraction (%)
$T^*_\pi < 80$ MeV (direct measurement)	3.14 ± 0.32	-2.39 ± 0.76
$T^*_\pi < 75$ MeV (ext. to $T^*_\pi < 80$ MeV)	3.35 ± 0.33	-3.26 ± 0.80
$T^*_\pi < 70$ MeV (ext. to $T^*_\pi < 80$ MeV)	3.38 ± 0.36	-3.41 ± 0.87

Table 9.4: Results for the DE and INT fractions from ML fits to samples with different cuts on the T^*_π .All results have been extrapolated to the $T^*_\pi < 80$ MeV region, so they can be directly compared with the direct measurement. Half of the maximum difference has been assigned as systematic uncertainty.

	Fraction of events.		
T^*_π range	IB	DE	INT
0-75	0.2480	0.8065	0.6167
0-80	0.3189	0.8691	0.6949
0-70	0.1927	0.7345	0.5388
55-90	0.4862	0.4910	0.5469
55-80	0.2372	0.3950	0.3845
	Extrapolation factors.		
55-90/55-80	2.0490	1.2430	1.4198
55-80/0-80	0.7436	0.4545	0.5533
55-90/0-80	1.5241	0.5650	0.7870

Table 9.5: Fraction of IB, DE and INT events within different T^*_π ranges. Extrapolation factors between different T^*_π ranges for IB, DE and INT events.

Effect	Systematic effect on DE (%)	Systematic effect on INT (%)
Energy Scale	±0.05	±0.11
Minimum photon energy	±0.26	±0.67
L2 trigger	±0.11	±0.44
Total systematic error	±0.29	±0.81

Table 9.6: Systematics uncertainties in the measurements of the fractions of DE and INT with respect to IB.

$$\tag{9.8}$$

The result is based on 117627 data events and 711743 simulated events in the range $T^*_\pi < 80$ with $0.2 < \mathrm{W} < 0.9$.

The correlation coefficient between the DE and INT fractions is -0.93.

Contour plots have been computed requiring the logarithm of the log-likelihood to change by 0.5, 2 and 4.5 units. These correspond to probabilities in the DE-INT fractions plane of 39.3 %, 86.5 % and 98.9 % respectively. Contour curves are shown in figure 9.3, showing only statistical uncertainties. The green thick bars show the statistical errors, and the black bars the total (systematic plus statistical) error. This result can be extrapolated to the region $55 < T^*_\pi < 90$ MeV making use of the values in table 9.5.

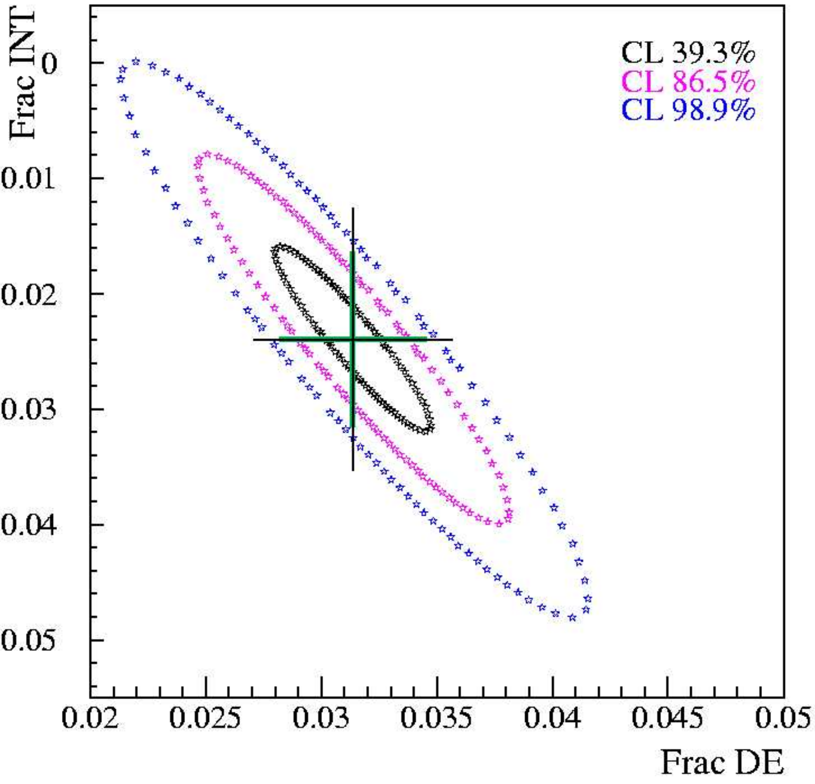

Figure 9.3: Contour plot for final result. Contour curves show statistical uncertainties only. For the result, green thick bars show statistical error and black bars show total (statistical + systematic) error

$$\text{Fraction of DE}(55 < T^*_\pi < 90\,\text{MeV}) = (1.16 \pm 0.12 \pm 0.11)\% \tag{9.9}$$

$$\text{Fraction of INT}(55 < T^*_\pi < 90\,\text{MeV}) = (-1.23 \pm 0.39 \pm 0.42)\% \tag{9.10}$$

$$\tag{9.11}$$

9.4.1 Preliminary Extraction of $\mathbf{X}_E$ and $\mathbf{X}_M$

As already mentioned, the simultaneous measurement of the DE and INT terms in $K^{\pm} \to \pi^{\pm}\pi^{0}\gamma$ decays allows one to separate the electric and magnetic contributions. The quantities X_E and X_M:

$$X_E = \frac{E}{|A_2^+|m_K^4}, \quad X_M = \frac{M}{|A_2^+|m_K^4} \tag{9.12}$$

are often used for this purpose. Using these variables, equation 1.15 becomes:

$$\begin{aligned} \frac{\partial^2\Gamma}{\partial T_\pi^* \partial W} &= \frac{\partial^2\Gamma^+}{\partial T_\pi^* \partial W} + \frac{\partial^2\Gamma^-}{\partial T_\pi^* \partial W} \\ = 2\frac{\partial^2\Gamma_{IB}}{\partial T_\pi^* \partial W} \Big[1 &+ 2cos(\phi)cos(\delta_1^1 - \delta_0^2)m_\pi^2 m_K^2 X_E W^2 + \\ & m_\pi^4 m_K^4 (X_E^2 + X_M^2) W^4 \Big] \end{aligned} \tag{9.13}$$

The Direct Emission term defines a circle in the X_E, X_M plane, and the Interference sets the X_E value.
Assuming a negligible amount of CP violation in the $K^{\pm} \to \pi^{\pm}\pi^{0}\gamma$ decays, the ϕ angle can be set to zero, and therefore $\cos(\phi) \sim 1$. As explained in chapter 1 the difference between the two strong rescattering phases δ_1^1, δ_0^2 can be set to 10^0 under certain hypothesis, so that the $\cos(\delta_1 - \delta_0)$ can be also approximated to 1. The relations between the measured DE and INT fractions with respect to IB and X_E, X_M are given by equations 2.4, where a= $2m_\pi^2 m_K^2 X_E$ and b= $m_\pi^4 m_K^4 (X_E^2 + X_M^2)$. The values of the required integrals have been evaluated using Monte Carlo techniques:

$$\frac{\int \partial T_\pi^* \int W^4 \frac{\partial^2\Gamma_{IB}}{\partial T_\pi^* \partial W} \partial W}{\int \partial T_\pi^* \int \frac{\partial^2\Gamma_{IB}}{\partial T_\pi^* \partial W} \partial W} = 2.2710^{-2} \tag{9.14}$$

$$\frac{\int \partial T_\pi^* \int W^2 \frac{\partial^2\Gamma_{IB}}{\partial T_\pi^* \partial W} \partial W}{\int \partial T_\pi^* \int \frac{\partial^2\Gamma_{IB}}{\partial T_\pi^* \partial W} \partial W} = 0.105 \tag{9.15}$$

The values obtained for X_E and X_M are:

$$X_E = (-24 \pm 11)\, GeV^{-4} \tag{9.16}$$

$$X_M = (246 \pm 16)\, GeV^{-4} \tag{9.17}$$

A graphic representation of the extraction of X_E and X_M is shown in figure 9.4. The purple arc shows the measured Direct Emission contribution with its experimental error (dark band corresponds to one sigma and light band to two sigma).

The green band shows the value of X_E from the measurement of the INT component. The crossing of these two regions defines the allowed experimental region for X_M. The blue line shows the theoretical prediction for X_M, assuming that the chiral anomaly is the only source of magnetic amplitudes in $K^{\pm} \to \pi^{\pm}\pi^{0}\gamma$ decays. This has been calculated as follows:

The prediction for the Direct Emission branching ratio under the assumption that the chiral anomaly is the only source of direct terms is taken from [17] to be BR(DE)= 0.35 10^{-5} for $55 < T^{*}_{\pi} < 90$ MeV. This is equivalent to a fraction of DE equal to 1.34 10^{-2}, where the value of the BR(IB) has been taken from [23]. This has been extrapolated to the region $T^{*}_{\pi} < 80$ MeV obtaining Frac(DE)= 3.61 10^{-2}. The theoretical prediction for the value of X_M coming from the chiral

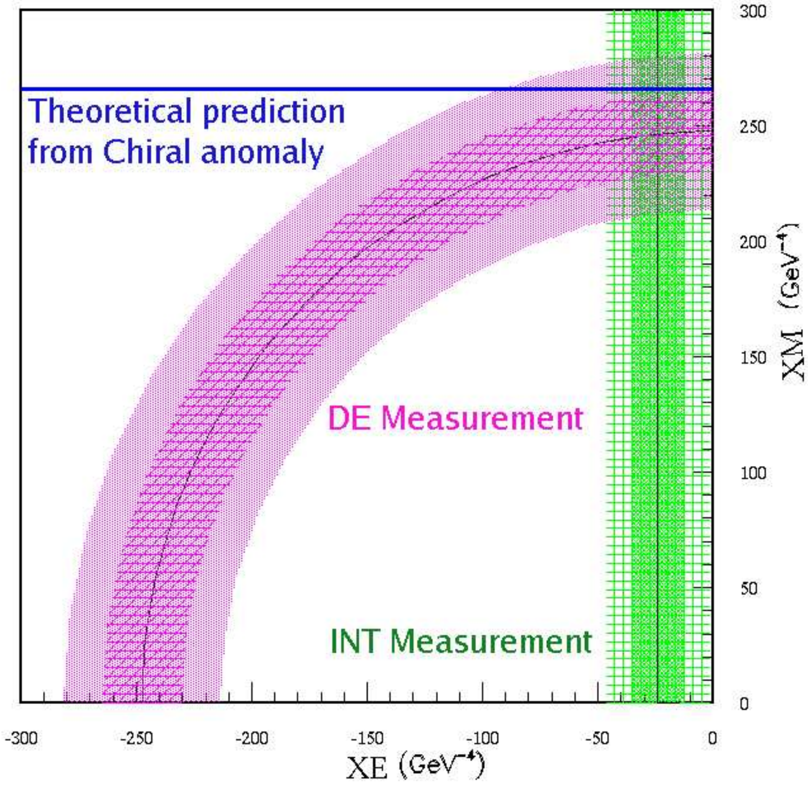

Figure 9.4: Graphic representation of the X_E and X_M extraction. Dark bands show one sigma errors, ligth bands two sigma errors. Measurements are compatible with the chiral anomaly being the only source of magnetic amplitudes in $K^{\pm} \to \pi^{\pm}\pi^{0}\gamma$ decays. Correlations between parameters have not been taken into account for this plot.

anomaly for $T^*_\pi < 80$ MeV can be therefore calculated as:

$$X_M = \sqrt{\frac{Frac(DE)}{2.2710^{-2} m_\pi^4 m_K^4}} = 265.63\,\mathrm{GeV}^{-4} \quad \text{for}\, T^*_\pi < 80\mathrm{MeV} \tag{9.18}$$

Therefore, the obtained result for X_M= 246 ± 16 is in agreement with the hypothesis that the chiral anomaly is the only source of magnetic amplitudes in the Direct Emission term.

It must be noted that the correlation between the parameters has not been taken into account in these calculations.

9.5 Final Results for ML fit with INT=0

In order to compare the obtained results with those from previous experiments, the ML fit has been redone setting the Interference term to zero. As already mentioned, previous measurements used the region $55 < T^*_\pi < 90$ MeV, which cannot be done in NA48/2 due to L2 trigger issues. Therefore, events were selected with $0 < T^*_\pi < 80$ MeV, and the result extrapolated to $55 < T^*_\pi < 90$ MeV.

The result obtained for the fraction of Direct Emission with respect to Inner Bremsstrahlung for T^*_π< 80 MeV, when the Interference term is set to zero is:

$$\text{Fraction of DE(INT} = 0) = (2.25 \pm 0.13_{stat} \pm 0.05_{syst})\% \tag{9.19}$$

The residuals of the fit are shown in figure 9.5. The χ^2 is ~ 17 for 13 degrees of freedom.

The systematic error assigned to this measurement corresponds to half of the difference observed in the result varying the upper T^*_π cut. The value of other cuts has been also varied in order to check the stability of the result. Related plots are shown in appendix D. No systematic effect has been found from these studies.

Extrapolating to $55 < T^*_\pi$< 90 MeV:

$$\text{Fraction of DE(INT} = 0) = (0.83 \pm 0.05_{stat} \pm 0.02_{syst})\% \tag{9.20}$$

Using the prediction from [23] for the BR(IB) in $55 < T^*_\pi$< 90 MeV, the BR(DE) can be calculated:

$$\text{BR(DE)(INT} = 0) = (2.17 \pm 0.13_{stat} \pm 0.05_{syst})10^{-6} \tag{9.21}$$

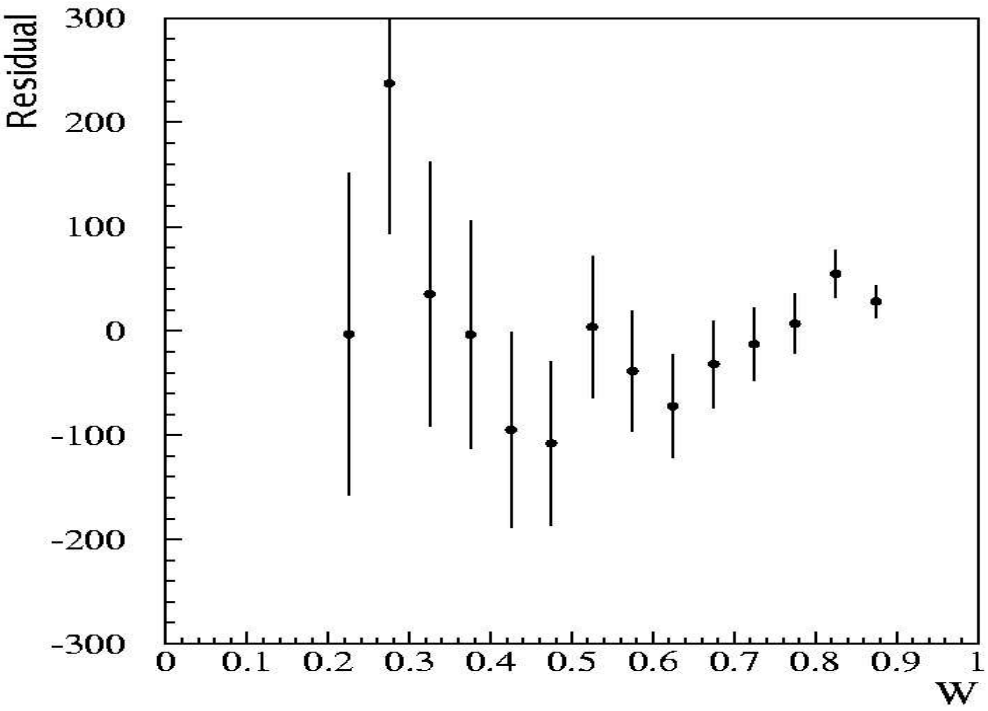

Figure 9.5: Residuals for the 2 parameter fit (INT=0)

This can be compared with results of previous experiments, that were summarized in table 2.1. The value of the measured Direct Emission branching ratio is significantly lower than previous. The error on the result has been improved by a factor of ∼ 6 with respect to the best precedent measurement.
In addition, the measurement was also performed in the range $55 < T^*_\pi < 80$ MeV. A prediction can be made for the result in this region by extrapolating the one obtained for $T^*_\pi < 80$ MeV. Both direct and extrapolated results are compatible:

$$\text{Predicted Fraction of DE(INT} = 0) = (1.38 \pm 0.07_{stat})\ \% \tag{9.22}$$

$$\text{Fraction of DE(INT} = 0) = (1.36 \pm 0.11_{stat})\ \% \tag{9.23}$$

9.6 Checks using the shape method

Even if the shape method has not been used to extract the final results, it has been used to verify the need of an interference component to fit the data sample. Figure 9.6 shows the ratio of the reconstructed W variable in data with respect to the IB simulation, normalized to the total number of events in the data sample.

Figure (a) shows the fit to the Direct Emission parameter only. Significant deviations are observed between the points and the fit value, especially for high W values and in the intermediate W region. The χ^2 of the fit is ~ 22 for 13 degrees of freedom.

Figure (b) shows the same ratio, now fitted to both Direct Emission and Interference parameters. The agreement between the points and the fit is clearly improved and the χ^2 is now ~ 8 for 12 degrees of freedom.

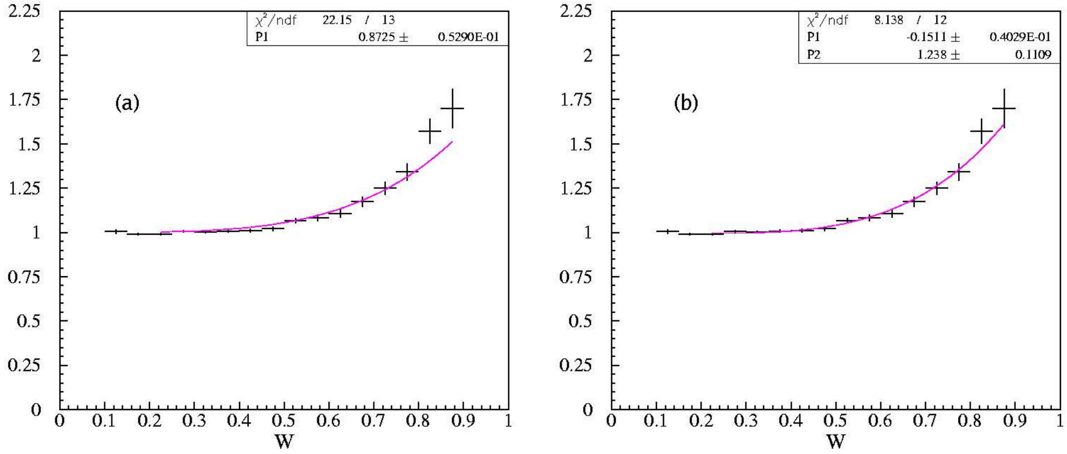

Figure 9.6: Shape fit to DE only (a) and to DE and INT (b).

9.7 Preliminary studies on CP violation

Some preliminary studies on CP violation have been done on this data sample. It must be noted that the described selection has not been optimized for this purpose, however the design of the experiment is such to suppress apparatus-related differences between K^+ and K^- decays.

To check CP violation in $K^\pm \to \pi^\pm \pi^0 \gamma$ decays events were separated depending on the reconstructed kaon sign. The most simple observable that has been computed is the asymmetry on the total number of events A_N

$$A_N = \frac{N_+ - rN_-}{N_+ + rN_-} \tag{9.24}$$

where N_+, N_- are the number of K^+, K^- decays to $\pi\pi^0\gamma$ in the data sample, and r is the ratio of the number of K^+, K^- events computed from another channel for which no CP violation is present.

The NA48/2 data has shown no CP violation in $K^{\pm} \rightarrow \pi^{\pm}\pi^{0}\pi^{0}$ decays at the level of 10^{-4} [11]. A large number of $K^{\pm} \rightarrow \pi^{\pm}\pi^{0}\pi^{0}$ decays has been collected, allowing to extract the ratio of K^{+} to K^{-} in SS123[1] with high accuracy r=1.798 ± 0.001.

The acceptances for K^{+} and K^{-} to $\pi\pi^{0}\gamma$ decays have been checked using simulated samples, and found to be Acc(K^{+})= 3.537 ± 0.005 % and Acc(K^{-})= 3.548 ± 0.007 %.

Table 9.7 summarizes the number of K^{+} and K^{-} to $\pi\pi^{0}\gamma$ collected events with different achromat and spectrometer magnet polarities.

Achromat polarity	A^{+}		A^{-}	
Spectrometer magnet polarity	B^{+}	B^{-}	B^{+}	B^{-}
Number of $K^{+} \rightarrow \pi^{+}\pi^{0}\gamma$ decays	30956	25777	16574	21440
Number of $K^{-} \rightarrow \pi^{-}\pi^{0}\gamma$ decays	17185	14385	9263	11748

Table 9.7: Number of reconstructed $K^{+} \rightarrow \pi^{+}\pi^{0}\gamma$ and $K^{-} \rightarrow \pi^{-}\pi^{0}\gamma$ decays for positive and negative achromat polarities (A^{+} and A^{-}) and for different signs of the spectrometer magnetic field (B^{+} and B^{-}).

The total number of reconstructed $K^{+} \rightarrow \pi^{+}\pi^{0}\gamma$ decays in SS123 is 94747 and the number of $K^{+} \rightarrow \pi^{+}\pi^{0}\gamma$ is 52581, resulting in a value for A_{N} = (1.1 ± 2.7) 10^{-3}. This measurement sets a limit on the difference of the branching ratios of $< 4.5\ 10^{-3}$ at 90 % confidence level, which is one order of magnitude more accurate than previous measurements [27].

The difference on the number of events can be related to the CP violating phase ϕ (see chapter 1) by equation 1.16

$$\frac{B_{+}-B_{-}}{B_{+}+B_{-}} \sim \frac{B_{+}-B_{-}}{2B_{IB}} = 2\left(\frac{\int \partial T_{\pi}^{*} \int W^{2} \frac{\partial^{2}\Gamma_{IB}}{\partial T_{\pi}^{*}\partial W} \partial W}{\int \partial T_{\pi}^{*} \int \frac{\partial^{2}\Gamma_{IB}}{\partial T_{\pi}^{*}\partial W} \partial W}\right) X_{E} m_{K}^{2} m_{\pi}^{2} sin(\phi) sin(\delta_{1}-\delta_{0}) \tag{9.25}$$

Using the value of 0.105 for the ratio of W integrals (9.15), X_{E} from the present measurement $X_{E} = -24 \pm 11$ (9.17) and $\delta_{1}-\delta_{0}$ =$10^{0} \pm 0.3$ from reference [5] a measurement for sin(ϕ)=-0.27 ± 0.65 is obtained. The smallness of the X_{E} term and sin($\delta_{1}-\delta_{0}$) drastically reduces the sensitivity to the ϕ angle.

---

[1] Bad NT-PEAK periods 1 and 2 are excluded from the $K^{\pm} \rightarrow \pi^{\pm}\pi^{0}\pi^{0}$ sample used to compute the value of r, but bad NT-PEAK period 3 is still present. However this cannot make a significant difference as the number of collected neutral events in period three is lower due to the malfunctioning of the trigger chain.

In addition, the fit in the range $0.2 < \mathrm{W} < 0.9$ was repeated separately for K^+ and K^- events, yielding results compatible within statistical accuracy. This is summarized in table 9.8

	K^+	K^-
Number events $0.2 < \mathrm{W} < 0.9$	75745	41932
$\mathrm{Frac(DE)_{TOT}}$	4.07 ± 0.57	4.67 ± 0.77
$\mathrm{Frac(INT)_{TOT}}$	-2.34 ± 1.30	-3.34 ± 1.77

Table 9.8: Results and errors from ML fit for K^+ and K^- events separately.

9.8 Conclusions

A subsample of 2003 NA48/2 data has been studied in detail. About 120 10^3 $K^\pm \to \pi^\pm\pi^0\gamma$ decays, with negligible background contamination have been reconstructed in the ranges $0.2 < \mathrm{W} < 0.9$ and $T^*_\pi < 80$ MeV. This statistics is more than five times larger than that of previous experiments.

Thanks to the development of an algorithm for rejecting $K^\pm \to \pi^\pm\pi^0\pi^0$ decays with two gammas overlapping in the detector, the lower cut on T^*_π could be released. This is a major achievement with respect to previous measurements, as it increases the sensitivity to Direct photon emission and Interference terms. In addition, the photon mistagging has been kept smaller than the per mil level for all decay components.

The fractions of Direct Emission and Interference (with respect to the Inner Bremsstrahlung component) present in the data sample have been obtained using a maximum likelihood method. Stability of the results with variation of selection cut values and a number of sources of systematic uncertainties have been studied. The total relative error in the Direct Emission result is ~ 15 %. A negative INT term has been found with a significance of more than two sigmas. Preliminary extraction of magnetic and electric amplitudes show that the magnetic Direct Emission component is compatible with being saturated by the chiral anomaly.

In addition, a CP violating asymmetry in the K^+ and K^- branching ratios for this channel has been obtained to be less than 4.5 10^{-3} at 90 % confidence level.

List of References

[1] F. E. Low, *Bremsstrahlung of Very Low-Energy Quanta in Elementary Particle Collisions.* Phys. Rev. **110** (1958) 974.

[2] M. E. Peskin, D. V. Schroeder, *An Introduction to Quantum Field Theory.* Addison-Wesley, (1996)

[3] M. MacGuigan and A.I. Sanda, $K \longrightarrow \pi\pi^0\gamma$ *in the six-quark model.* Phys. Rev. D **36** (1987) 1413.

[4] N. Christ, *Possible CP Violation in* $K^\pm \to \pi^\pm\pi^0\gamma$. Phys. Rev. **159** (1967) 1292.

[5] E. Chell and G. Olsson, *.Phase of direct CP violation from threshold pion production.* Phys. Rev. D **48** (1993) 4076.

[6] J. L. Lucio M. *Short-distance contribution to* $K \longrightarrow \pi\pi^0\gamma$ *and the* $\Delta I = 1/2$ *rule.* Phys. Rev. D **24** (1981) 2457.

[7] A. Lai et al., *A precise measurement of the direct CP violation parameter Re* (ϵ'/ϵ) Eur. Phys. J. C **22** (2001) 231.

[8] A. Alavi-Harati et al., *Measurements of direct CP violation, CPT symmetry, and other parameters in the neutral kaon system.* Phys. Rev. D **67**, 012005 (2003)

[9] A. Lai et al., *Observation of the rare decay* $K^0_S \to \pi^0 e^\pm e^\mp$ Phys. Lett. B **576** (2003) 43.

[10] J. R. Batley et al., *Search for direct CP violation in the decays* $K^\pm \to \pi^\pm\pi^+\pi^-$ Phys. Lett. B **634** (2006) 474.

[11] J.R. Batley et al., *Search for CP violation in* $K^\pm \to \pi^\pm\pi^0\pi^0$ *Decays.* Phys. Lett. B **638** (2006) 22.

[12] H. Y. Cheng, *Radiative kaon decays* $K^\pm \to \pi^\pm\pi^0\gamma$ *and direct CP violation.* Phys. Rev. D **49** (1994) 3771.

[13] H.-Y. Cheng, S.-C. Lee and H.-L. Yu, $K \longrightarrow \pi\pi^0\gamma$ *and Chiral Pertubation Theory.* Z. Phys. C **41** (1987) 72.

[14] H. Y. Cheng, *Large-N_c higher order weak chiral Lagrangians coupled to external electromagnetic fields: Applications to radiative kaon decays.* Phys. Rev. D **42** (1990) 72.

[15] G. Ecker, A. Pich, E. De Rafael, *Radiative Kaon Decays and CP Violation in Chiral Perturbation Theory.* Nucl. Phys. B **303** (1988) 665.

[16] G. Ecker, H. Neufeld, A. Pich, *Anomalous non-leptonic Kaon Decays.* Phys. Lett. B **278** (1992) 337.

[17] G. Ecker, H. Neufeld, A. Pich, *Non-Leptonic Kaon Decays and the Chiral Anomaly.* Nucl. Phys. B **413** (1994) 321.

[18] S. Gasiorowicz and D.A. Geffen Rev. Mod. Phys. **41** (1969) 531;

[19] J. Gasser and H. Leutwyler, *Chiral Perturbation Theory: Expansions in the Mass of the Strange Quark* Ann. Phys. **158** (1984) 142; Nucl. Phys. **B250** (1985) 465.

[20] J. Kambor et al., Nucl. Phys. **B346** (1990) 17.

[21] J. Wess and B. Zumino, *Consequences of Anomalous Ward Identities.* Phys. Lett. **B37** (1971) 95.

[22] E. Witten, *Global Aspects of Current Algebra.* Nucl. Phys. **B223** (1983) 422.

[23] G. D'Ambrosio, M. Miragliuolo and P. Santorelli, *Radiative non-leptonic kaon decays.* The Daϕne Physics Handbook, Eds. L. Maiani, G. Pancheri and N. Paver (1992)

[24] V. P. Efrosinin, *About radiative kaon decay $K^+ \longrightarrow \pi^+\pi^0\gamma$.* arXiv:hep-ph/0606216 (2006).

[25] G. Cowan, *Statistical Data Analysis.* Oxford University Press (1998)

[26] R.J. Abrams et al., *Evidence for Direct Emission in the Decay $K^\pm \to \pi^\pm\pi^0\gamma$.* Phys. Rev. Lett. **29** (1972) 1118.

[27] K.M. Smith et al., *A search for CP violation in $K^\pm \to \pi^\pm\pi^0\gamma$ Decays.* Nucl. Phys. **B109** (1976) 173.

[28] V.N. Bolotov et al., *Experimental Study of the structure radiation in the decay $K^- \longrightarrow \pi^-\pi^0\gamma$* Yad. Fiz., **45** (1987) 1652, Sov. J. Nucl. Phys. **45** (1987) 1023.

[29] S. Adler et al.,E787 Collaboration, *Measurement of Direct Photon Emission in $K^+ \to \pi^+\pi^0\gamma$ Decay.* Phys. Rev. Lett. **85** (2000) 4856.

[30] M.A. Aliev et al., KEK-E470 Collaboration, *Measurement of direct photon emission in $K^+ \to \pi^+\pi^0\gamma$ decay using stopped kaons.* Phys. Lett. B **554** (2003) 7.

[31] V.A. Uvarov et al., ISTRA Collaboration, *Experimental study of direct photon emission in* $K^- \to \pi^-\pi^0\gamma$ *decay using ISTRA+ detector.* Phys. Atom. Nucl. **69** (2006) 26.

[32] M.A. Aliev et al., KEK-E470 Collaboration, *New result of the measurement of the direct photon emission in* $K^+ \to \pi^+\pi^0\gamma$ *decay.* hep-ex/0511060 v1 30 Nov 2005

[33] T. Tsunemi, E787 Collaboration, *New results on* $K^+ \to \pi^+\pi^0\gamma$ *from E787.* Talk given at KAON 2005, Chicago, June 2005.

[34] R.J. Abrams et al., *Test of CP Noninvariance in the Decay* $K^\pm \to \pi^\pm\pi^0\gamma$*.* Phys. Rev. Lett. **30** (1973) 500.

[35] R. Batley et al., *Addendum III (to Proposal P253/CERN/SPSC) for a Precission Measurement of Charged Kaon Decay Paramenters with an Extended NA48 Setup* CERN/SPSC 2000-003 (2000)

[36] B. Peyaud on behalf of M.Boyer et al., *KABES: A novel beam spectrometer for NA48.* Proceedings to VCI04.

[37] I.Mandjavidze, B.Vallage, *Implementation Options for the KABES Read-Out System.* NA48 Note-2002-01 (2002)

[38] E. Griesmayer et al., *Comparisons of field calculations and measurments of a spectrometer magnet.* Nucl. Instrum. Methods **A361** (1995) 466.

[39] B. Bédérède et al., *High resolution drift chambers for the NA48 experiment at CERN.* Nucl. Instrum. Methods **A367** (1995) 88.

[40] I. Agustin et al., *A drift chamber electronics and readout for the NA48 experimentat the CERN SPS.* Nucl. Instrum. Methods **A403** (1998) 472.

[41] R. Arcidiacono et al., *The Drift Chamber Electronics for the NA48 Experiment.* IEE Trans. Nucl. Sci. **51** (2004) 1470.

[42] NA48 collaboration, presented by P.Buchholz, *The NA48 liquid krypton calorimeter.* Nucl. Instrum. Methods **A316** (1992) 1.

[43] NA48 collaboration, presented by M. Jeitler, *The NA48 liquid krypton calorimeter.* Nucl. Instrum. Methods **A494** (2002) 373.

[44] G. Fischer et al., *A 40-MHz pipelined trigger for* $K^0 \to \pi^0\pi^0$ *decays for the CERN NA48 experiment.* Nucl. Instrum. Methods **A419** (1998) 695.

[45] S. Anvar et al., *The Charged Trigger System of NA48 at CERN.* Nucl. Instrum. Methods **A419** (1998) 686.

[46] R. Arcidiacono et al., *The Trigger Supervisor of the NA48 experiment at CERN SPS.* Nucl. Instrum. Methods **A443** (2000) 20.

[47] C. Biino et al., *Compact 7.2 User Guide.* NA48 documentation. (2005)

[48] J.B. Chèze, *NA48 Drift Chamber Reconstruction User's Guide.* NA48 documentation. (1999)

[49] J.B. Chèze, *NA48 spectrometer: Vertex calculation.* NA48 internal note. NA48-02-02 (2002)

[50] G. Unal, *Reconstruction program for the LKr.* NA48 internal note. NA48-98-02 (1997)

[51] G. Unal, *Neutral reconstruction.* NA48 internal note. NA48-95-10 (1995)

[52] W.-M. Yao, et al., *Review of Particle Physics.* Journal of Phys. G **33** (2006) 1.

[53] L. Di Lella. *Alignment and corrections to the momenta.* Talk at NA48 meeting (08.03)

[54] S. Balev, *Data Quality and Trigger Systematics for Neutral Asymmetry.* Talk at NA48 meeting (03.05.2005)

[55] De Beer, M. and Derue, F., *NASIM User's Guide.* NA48 internal note. NA48-00-23 (2000)

[56] Application Software Group (CERN), *GEANT, detector description and simulation tool.* GEANT user's guide. CERN program library long writeup W5013 (1993)

[57] D. C. Carey, *TURTLE (Trace Unlimited Rays Through Lumped Elements): A computer program for simulating charged particles beam transport systems.* FERMILAB-NAL-064 (1971)

[58] F. James, *N-BODY Monte Carlo Event Generator.* CERN Program Library Short Writeup W515 (1975)

[59] Calafiura, P. and Talamonti, C., *The new NA48 shower library User's guide.* NA48 internal note. NA48-94-26 (1994)

[60] B. Bloch-Devaux, *Alpha and Beta corrections for NA48/2 Simulated Events.* NA48 internal note. NA48-05-05 (2005)

[61] V. Kozhuharov, private communications.

[62] E. Marinova, private communications.

[63] P. Golonka and Z. Was, *PHOTOS Monte Carlo: A precision tool for QED corrections in Z and W decays.* Eur. Phys. J **C107** (2006) 45.

[64] A. Nappi, *Fitting linear combinations of known distributions to binned data. Some mathematical subtlety.* NA48 internal note. NA48-06-02 (2006)

[65] F. James and M. Roos, *MINUIT a system for function minimization and analysis of the parameter errors and correlations.* Comp. Phys. Comm. **10** (1975) 343.

Appendix A

Maximum Likelihood.

A fitting program was developed for this work, based on a Poissonian Maximum Likelihood Method, for extraction of the IB, DE and INT fractions present in the data sample. This problem can be treated both with poissonian and multinomial approaches, and the only differences that could show up are of numerical nature. This is discussed in detail in [64]

The input information consisted on the reconstructed W distributions of data and simulated IB, DE and INT samples. For each of them, 14 bins were considered in the range 0.2<W<0.9. The data W distribution is determined by the set $\{d_1,d_2,...,d_n\}$, n=14, where d_i is the number of data events in bin i. For source j (j=1,2,3=IB, DE, INT) a_{ij} is the corresponding number events in W bin i.

If the Poissonian distribution is considered, the probability of finding a particular number of events d_i in bin i is given by:

$$P(d_i) = e^{-f_i} \frac{f_i^{d_i}}{d_i!} \tag{A.1}$$

where f_i represents the expected value.

If the data distribution of the W variable is a mixture of unknown proportions of the IB, DE and INT sources, then the predicted number of events on every bin i is given by a function of these proportions, $f_i(P_{IB},P_{DE},P_{INT})$ such that:

$$f_i = N_D \sum_{j=1}^{m} P_j a_{ji}/N_j \tag{A.2}$$

where N_D is the total number of events in the data and N_j the total number of events in the sample for source j. Note that the proportions P_j must add up to one, as they can be thought as the fractions of the different sources contributing to the data distribution.

The estimates of the proportions P_j are found by maximising the logarithm of the likelihood (lnL). Omitting constant terms that are irrelevant for maximization this can be written as:

$$ln\mathcal{L} = \sum_{i=1}^{n} d_i ln f_i - f_i \tag{A.3}$$

This procedure does not account the fact that the simulated samples used are also of finite size, leading to statistical fluctuations. However, when the simulated samples have much more events than the data sample, fluctuations on the number of events in one bin in the simulated distributions are negligible with respect to the corresponding fluctuations in data, and do not contribute considerably to the error estimation of the relevant parameters.

The final expression used for f_i in this work is:

$$f_i = \text{Norm}(\text{frac}_{DE}\delta_i + \text{frac}_{INT}\gamma_i + (1 - \text{frac}_{DE} - \text{frac}_{INT})\beta_i) \tag{A.4}$$

where δ_i, γ_i and β_i are the relative number of events in bin i of DE, INT and IB samples, normalized to the total number of events on that sample, and frac$_{DE}$ and frac$_{INT}$ and Norm are considered as free parameters.

The result of maximizing (A.3) with f_i given by A.4, provides estimations for the values of the three free paramenters: frac$_{DE}$ and frac$_{INT}$, that represent the proportions of DE and INT present in data with respect to the total number of events in the data sample, and for Norm, a global normalization parameter that should come out from the fit compatible with the total number of data events in the sample.

The MIGRAD routine of the MINUIT software package [65] has been used for minimization of -ln(L). MIGRAD performs a numerical minimization and provides an estimation of the parameters' errors. These so-called parabolic errors are computed assuming that -ln(L) is a parabola around the minimum. The value of the error is given by the difference between the value of the parameter at -ln(L$_{max}$) and at the point -ln(L)= -ln(L$_{max}$) + 0.5.

Another routine, MINOS, provides an estimate for the errors that does not assume a parabolic behavior for the ln(L), but instead scans the log-likelihood function. If there are no significant non-linearities involved in the problem, parabolic and MINOS errors should be of comparable sizes.

Contour curves for any pair of parameters are also provided by the MINUIT package. These are given by sets of points in the two parameter space where the value of the log-likelihood function is constant, and differs from the -ln(L$_{max}$) by a given amount m. Contour curves are calculated using a procedure analogous to that used by MINOS. These curves are very useful for visualizing the effects of correlations. For this work contours in the frac$_{DE}$ - frac$_{INT}$ plane have been often computed for values of m = 0.5, 2 and 4.5, corresponding to 39.3 %, 86.5 % and 98.9 % coverage.

In addition, another version of the program was implemented with only two free parameters: the global normalization and the DE fraction.

Appendix B

Plots. Comparisons Data and IB Simulation.

Distributions of data events and ratio of data over simulated IBS1 events for different variables. The L1 efficiency correction has been applied to the simulation. Only events with $E_{min} > 5$ GeV and $W < 0.5$ have been considered. For every variable, first plot represents the data distribution and second plot its ratio with respect to IBS1 simulated events.

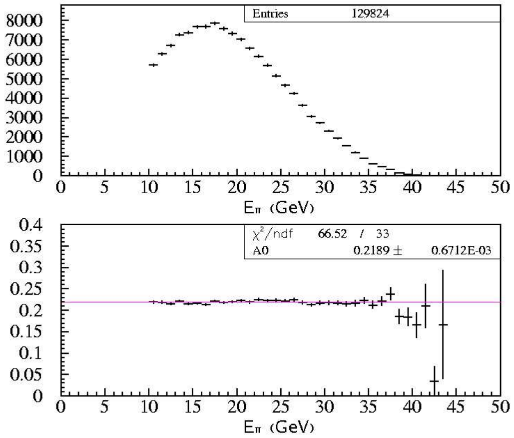

Charged pion energy.
Drop at high energies could be due to residual L2 inefficiencies.

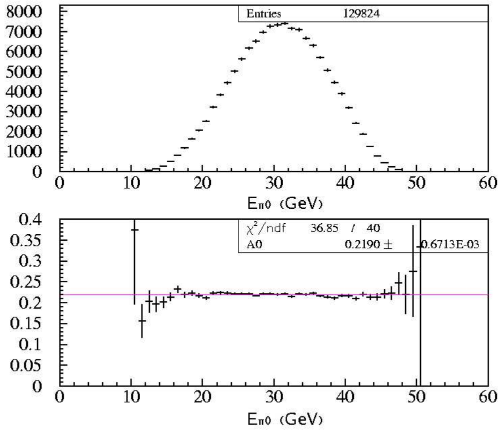

Neutral pion energy.
Good agreement.

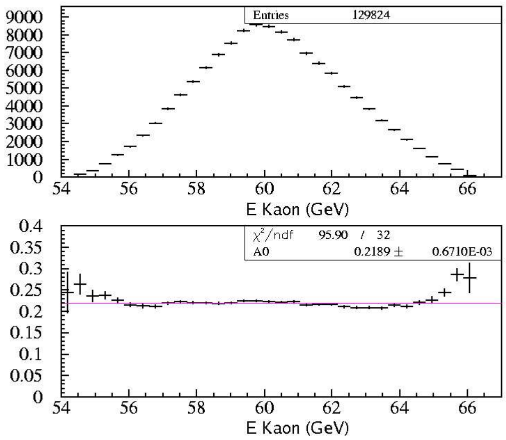

Kaon energy.
Mismatch at edge of spectrum could be due to residual beam tunning problems

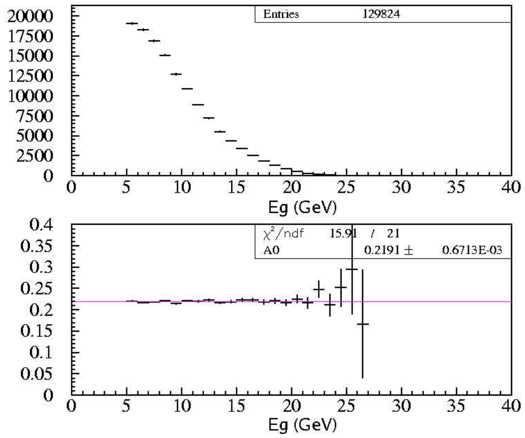

Odd Gamma energy.
Good agreement after L1 efficiency corrections.

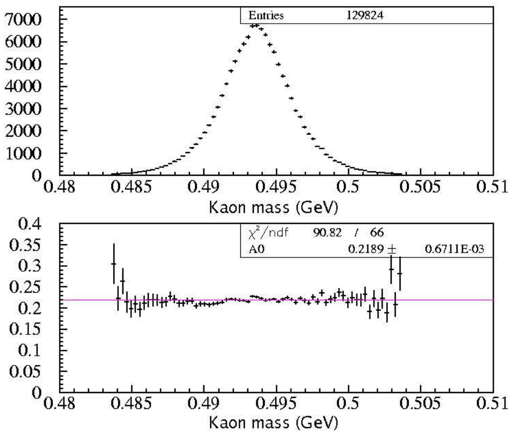

Kaon mass.
Good agreement.

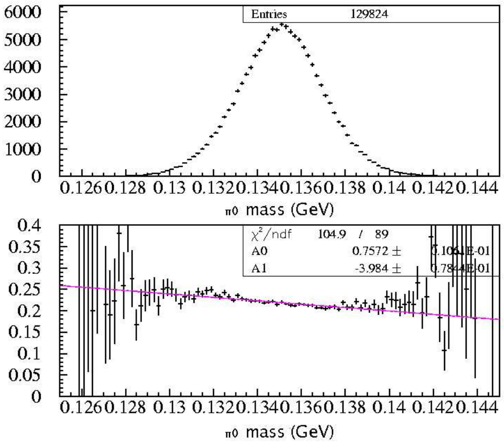

π^0 mass.
Offset in mean values for Data and Simulation produces slope in the ratio.

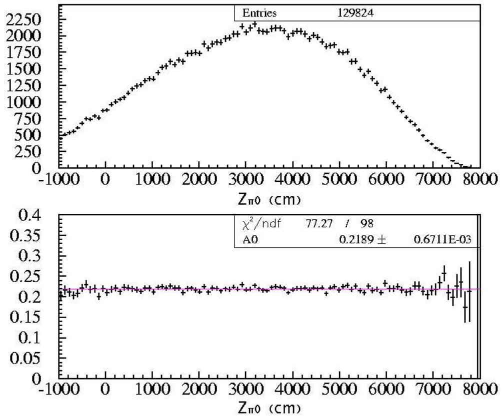

Neutral vertex
Good agreement

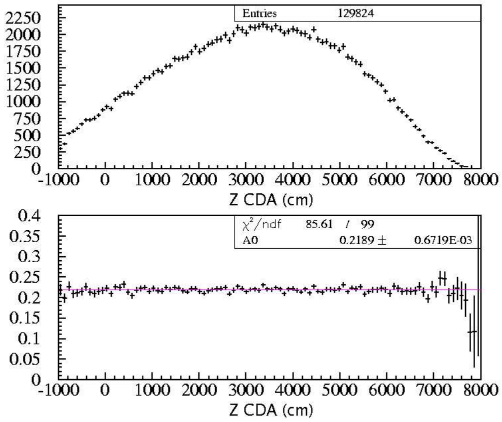

Charged vertex.
Drop at high values could be due
to residual beam tunning problems.

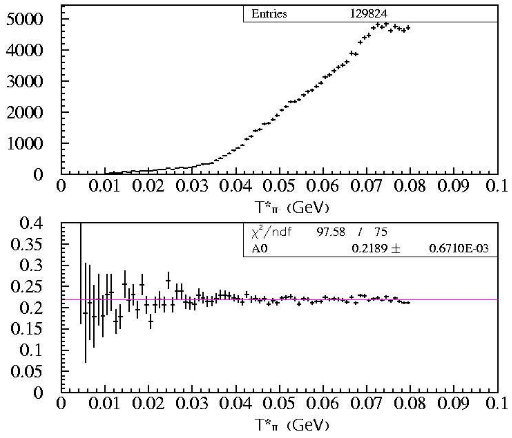

Charged pion kinetic energy
in the Kaon COM system.
Drop at high values could be due
to residual L2 inefficiency.

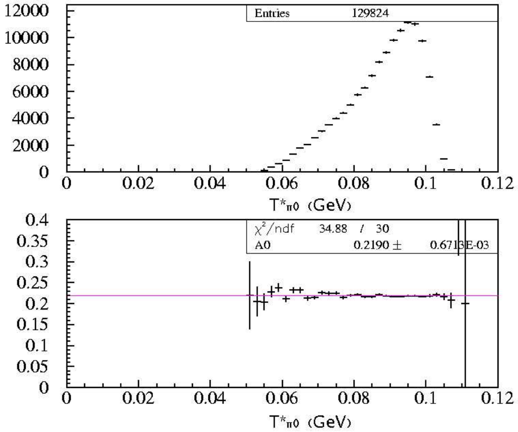

Neutral pion kinetic energy
in the Kaon COM system.
Good agreement. No sign of
$K^{\pm} \to \pi^{\pm}\pi^{0}$background.

Appendix C

Plots. Variation of cuts for 3 parameter ML fit.

Plots showing the variation of the results for the DE and INT fractions with respect to IB when cut values are varied within a reasonable range. Error bars on reference point show total statistical error, for the other points uncorrelated errors with respect to reference are plotted. A negative correlation between variations of the DE fractions and variations of the INT fraction can be observed. Note change in scale when studying minimum photon energy cut. Only for this cut a significant effect is seen.

Results of cuts variations are also shown within contour plots for the kaon mass cut, the charged pion momentum cut, the mistagging cut and the minimum photon energy cut.

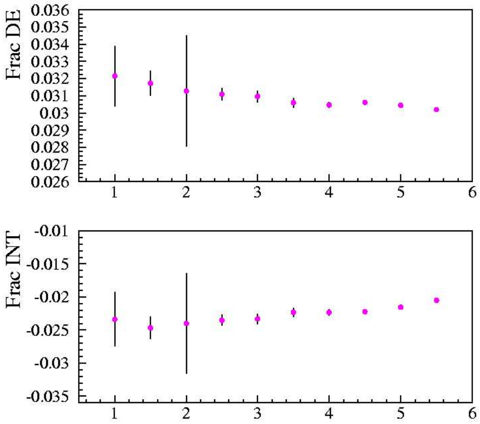

COG cut (cm)
No effect found
within uncorrelated errors

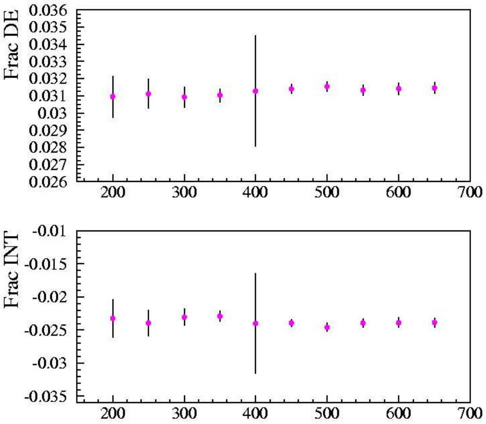

$|z_{\pi^0} - z_{\rm CDA}|$ **cut (cm).**
No effect found
within uncorrelated errors

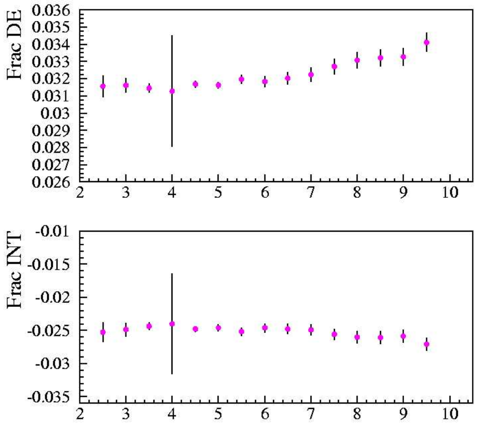

Kaon mass cut (number of sigmas).
No effect found up to ∼ 7
sigmas within uncorrelated errors

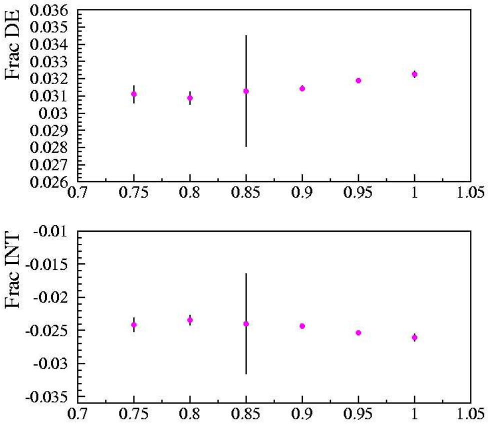

E/p for pion track cut.
No effect found
within uncorrelated errors

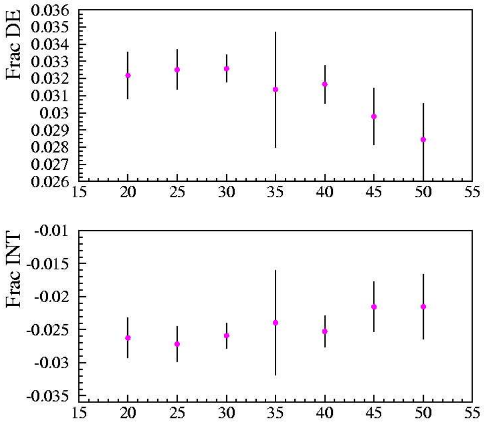

Distance γ-π at LKr (cm)
No effect found
within uncorrelated errors

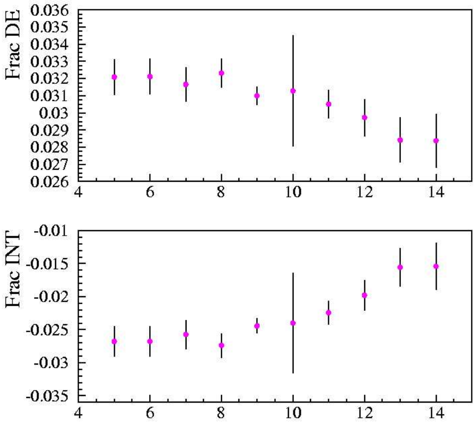

π momentum cut (GeV)
No effect found
within uncorrelated errors
(see contour plot)

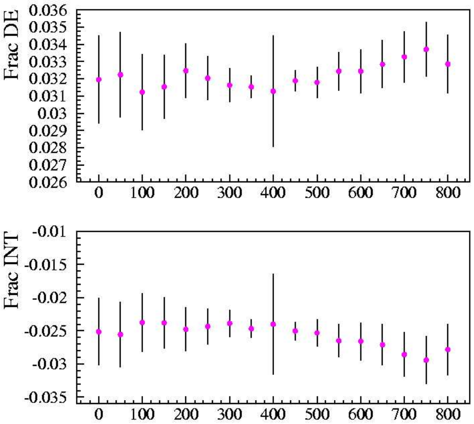

Mistagging cut (cm)
No effect found
within uncorrelated errors
(see contour plot)

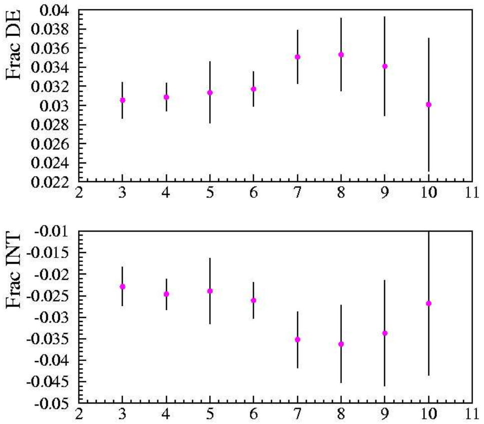

Minimum photon energy (GeV)
Systematic uncertainty
assigned to this effect.
(see contour plot)

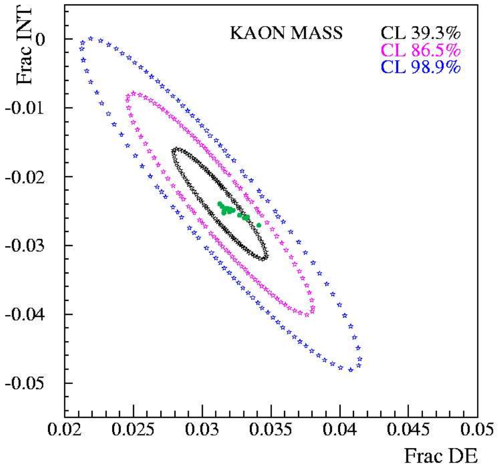

Kaon Mass cut
Variations compatible with
statistical fluctuations

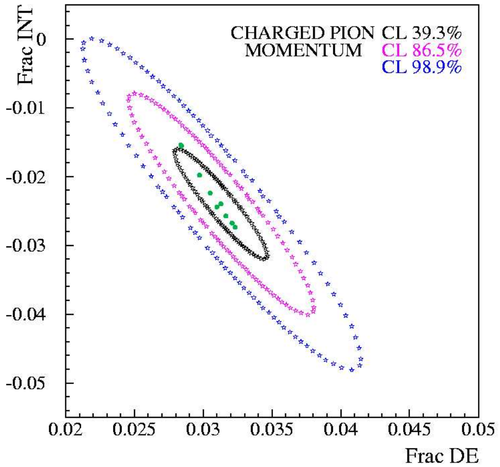

Charged pion momentum cut
Variations compatible with
statistical fluctuations

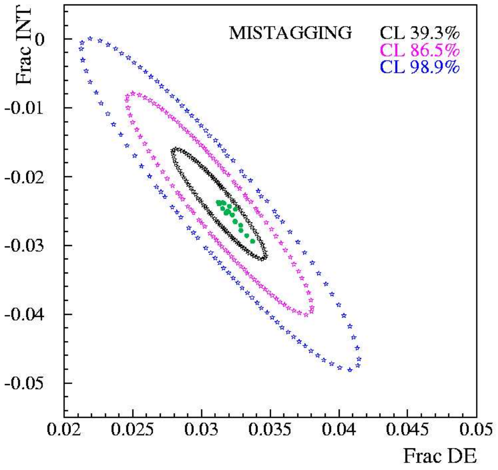

Mistagging cut

All points within first contour.

Compatible with statistical fluctuations

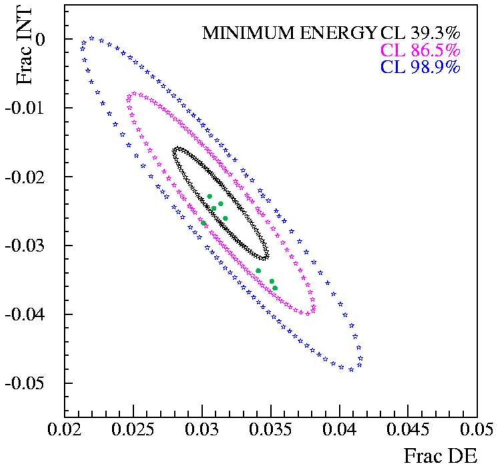

Minimum photon energy cut

Four points outside first contour

All within second contour.

Appendix D

Plots. Variation of cuts for 2 parameter (INT=0) ML fit.

Plots showing the variation of the results for the DE fraction with respect to IB when cut values are varied within a reasonable range. Error bars on reference point show total statistical error, for the other points uncorrelated errors with respect to reference are plotted. No systematics effect has been found for any of the cuts considered.

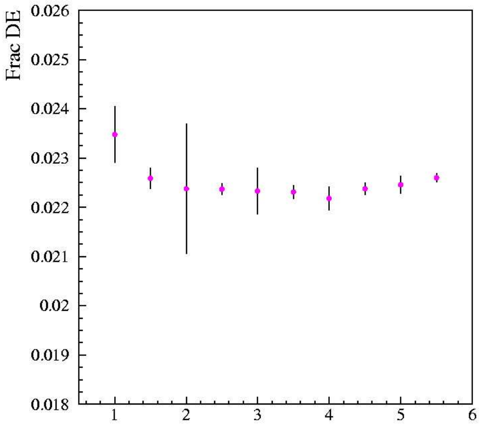

COG cut (cm)
No effect found
within uncorrelated errors

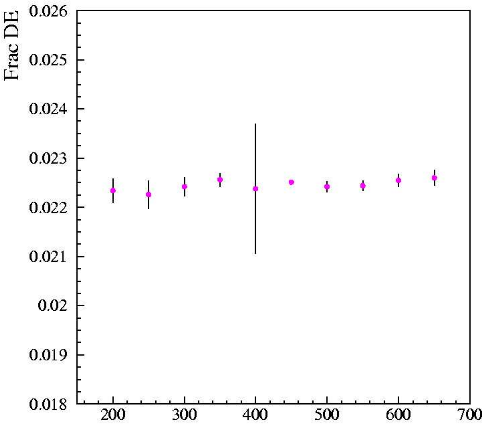

$|z_{\pi^0} - z_{\mathrm{CDA}}|$ **cut (cm).**
No effect found
within uncorrelated errors

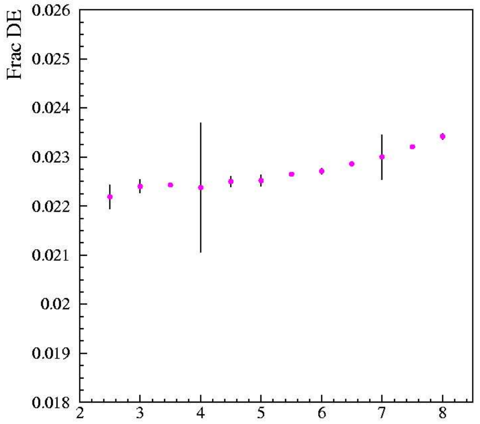

Kaon mass cut (number of sigmas).
No effect found up to ~ 6
sigmas within uncorrelated errors

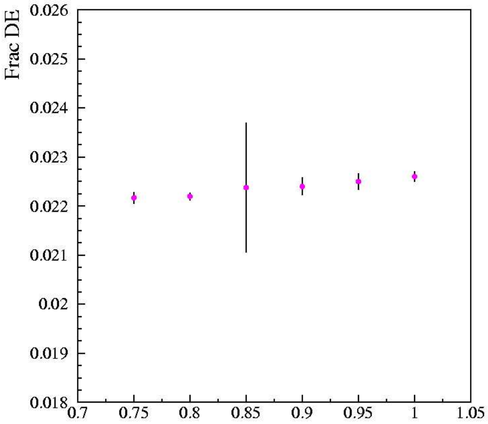

E/p for pion track cut.
No effect found
within uncorrelated errors

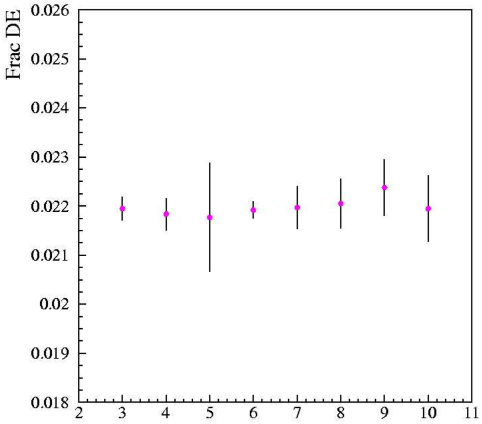

Minimum Odd Photon Energy (GeV)
No effect found
within uncorrelated errors

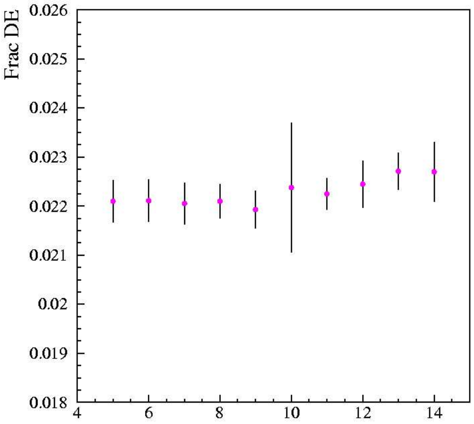

π momentum cut (GeV)
No effect found
within uncorrelated errors

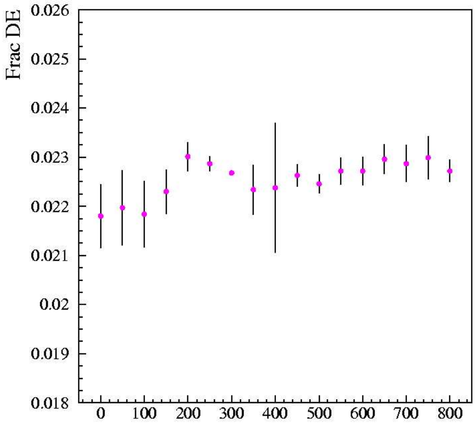

Mistagging cut (cm)
No effect found
within uncorrelated errors

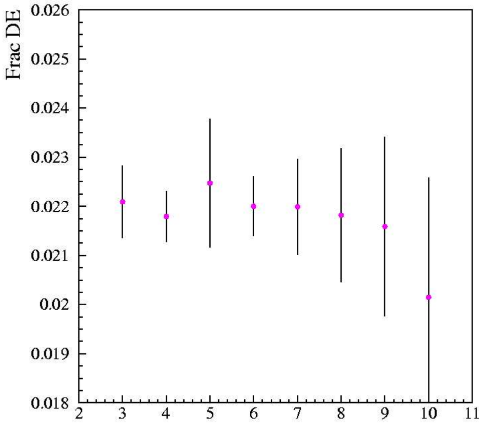

Minimum photon energy (GeV)
No effect found
within uncorrelated errors